Novel Methods of Enhanced Hydrocarbon Recovery

Dimitrios Spanakos

Supervised by Prof. Sean Rigby, Prof. Richard Wheatley & Prof. Richard Graham

A thesis submitted for the degree of Doctor of Philosophy

University of Nottingham

Department of Chemical Engineering

September 2021

Abstract

Carbon dioxide (CO_2) is considered as the major anthropogenic greenhouse gas and its voluminous emission to the atmosphere leads to undesirable environmental impacts, particularly global warming. According to the EIA Annual Energy Outlook (EIA, 2021), the atmospheric CO_2 concentration has increased by approximately 50% since the pre-industrial era. In addition, fossil fuels (oil, natural gas, coal) will still predominate in global energy systems, contributing between 40% and 65% over the next three decades (BP, 2020). Injection of CO_2 into reservoirs offers the potential to both enhance oil and gas recovery while simultaneously sequestering CO_2. Hence, CO_2 injection into reservoirs is a promising technology which will facilitate the meeting of worldwide oil and gas demand, as well as the challenge of greenhouse gas emissions.

Extraction of natural gas (mainly methane) from shale reservoirs via CO_2 injection techniques has received a great attention over the past decade. The main reasons are the greater sorption affinity of CO_2 compared to that of methane, meaning it readily displaces methane, and the potential of shale gas to supply the world with an immense amount of energy. In this research, low-pressure gas adsorption isotherms and helium pycnometer experiments were applied to determine pore size distribution and estimate porosity for a series of Marcellus shales from different depths. In addition, Mineral Liberation Analyser and Rock Eval Analysis experiments were conducted to characterise the mineralogy and TOC content, respectively. Results showed that both the pore volume of the microporosity and the fractal dimension decreased with increasing depth of the shale sample, leading to a lower surface area. The reason for this lower surface area was a combination of the change in content of both TOC and illite. It was also observed that the samples were heterogeneous, and the clay minerals must have undergone a complete transformation. Calorimetry experiments revealed that the heat of adsorption had a positive correlation with illite, TOC content and the surface fractal dimension, while its correlation with quartz content was negative.

Previous investigations have indicated that surface diffusion is much more significant than the bulk gas transport in shale gas reservoirs due to the larger fraction of adsorbed phase found in the nanopores of shales. Most publications to date have used a theoretical model to predict surface diffusion coefficient in a low-pressure condition. In this research, gravimetric experiments were conducted to measure surface diffusivities of CO_2 on different shales, at various temperatures. A fractal theory for predicting the Arrhenius parameters of the surface diffusivity of molecules on heterogeneous surfaces has been applied to the surface diffusion of CO_2 in shales. In line with the theory, it was found that both the pre-exponential factor and the activation energy are functions of the surface fractal dimension. Hence, the surface diffusivity, around a monolayer coverage, on shales could be established from an equilibrium gas adsorption isotherm, once the Arrhenius parameters have been calibrated for the specific chemical species. This work is the first to apply the fractal theory and effectively predict, *a priori*, surface diffusivity parameters for highly heterogeneous natural materials as shales.

The surface diffusion parameter obtained from gravimetric experiments was added to an established apparent permeability model, which was then applied for the first time to numerical reservoir simulations to model CO_2 injection techniques (CO_2 flooding, CO_2 huff and puff). Shale reservoirs, with different reservoir and petrophysical properties, were generated to investigate the efficiency of transport of CO_2 via surface diffusion. The proposed fractal model for surface diffusion was also used to investigate the impact of rock surface roughness on methane (CH_4) production. In cases where the average pore radius was less than 2 nm, simulation results showed that surface diffusion make an important contribution to CH_4 production as well as CO_2 adsorption. It was also observed that reservoirs exhibiting high surface fractal dimension in the matrix of shale, may enhance CH_4 production and should not be neglected. From the geostatistical reservoir simulations, it was concluded that increasing the reservoir heterogeneity is not favourable to methane recovery via CO_2 injection techniques, except for the Barnett shale reservoir. This work can provide a better understanding of the effectiveness of surface diffusion on CH_4 recovery via CO_2 injection techniques at shale reservoir scale.

A fluid characterization model was constructed based mainly on laboratory-measured data from an oil sample. The oil sample was representative of the Prinos reservoir in northern Greece which can serve as a potential site for high capacity as well as cost-effective CO_2-storage. The fluid characterization model was implemented into a reservoir simulator to model CO_2 injection techniques and investigate their impact on cumulative oil production and CO_2 storage efficiency in the Prinos reservoir. Simulation results revealed that CO_2-Water Alternating Gas (CO_2-WAG) injection is the most favorable scenario. It was also found that the CO_2 storage efficiency is greatly affected by the CO_2-WAG slug ratio and the reservoir permeability heterogeneity. From an economic analysis, it was concluded that the effect of miscibility and

CO_2-WAG slug ratio are of major importance for the Net Present Value and should not be overlooked. This work can provide insights into the potential of CO_2 injection techniques for Enhanced Oil Recovery (EOR) and CO_2 sequestration for the Prinos oil reservoir.

Dedication

To my parents, Evgenia Leoutsakou and Nikolaos Spanakos,

To my brother, Spyridon Spanakos.

Acknowledgements

First and foremost, I would like to thank my supervisor, Professor Sean Rigby. During my doctoral study period, Professor Sean Rigby has been tirelessly helped me to improve myself in all aspects over the years. This thesis would not have been feasible without his excellent guidance, consistent support, encouragement, and inspiration. No words can fully express my gratitude to him. It is truly a privilege and indeed a great honour to work under his supervision. Sean, I will always see you as my boss, but also as a good friend.

I would also like to sincerely acknowledge Professor Richard Wheatley, Professor Richard Graham and Professor Matthew Hall, for their support, guidance, and advice during this project. I am also deeply indebted to Professor Colin Snape for his critically constructive comments and feedback over the past years of this work. I want to specially thank Dr Aleksandra Gonciaruk and David Mee. Their tremendous knowledge and friendliness helped me to understand the fundamental principle of gas adsorption.

Furthermore, I would like to gratefully acknowledge the Engineering and Physical Sciences Research Council for the funding of this project. I owe many thanks to Hiden Isochema for technical assistance. I am thankful to the Computer Modelling Group (CMG) for supplying the licence to access their reservoir simulators and for their technical support. I would also like to extend my appreciation to Dr Elisabeth Steer and Jason Greaves for their assistance in running SEM-MLA and TGA experiments, respectively.

Thank you to my great officemates Baris Gungordu, Kerem Derelizade, Mohamed Adam and Davin Arifin for being readily collaborative and, thus, tremendously supportive. With utmost sincerity, I extend my deepest thanks to my family and two people who are gone from my sight, but never from my heart. Last but surely not least, I would like to dedicate this dissertation to my parents and my brother, for being there for me all these years. This PhD thesis stands as a testament to your unconditional love and enduring support. Thank you for letting me be myself and encouraging me to work hard towards my dreams.

Table of Contents

4. CHAPTER FOUR: PREDICTING SURFACE DIFFUSIVITIES OF GAS MOLECULES IN SHALE 62

5. CHAPTER FIVE: EVALUATION OF IMPACT OF SURFACE DIFFUSION ON METHANE RECOVERY VIA CARBON DIOXIDE INJECTION IN SHALE 91

6. CHAPTER SIX: CO_2 INJECTION FOR ENHANCED OIL RECOVERY AND CO_2 SEQUESTRATION IN PRINOS OIL RESERVOIR 126

List of Figures

List of Tables

List of Publications

- Spanakos, D., Rigby, S.P., 2020. Predicting Surface Diffusivities of Gas Molecules in Shale. *Energy & Fuels* 34, 12417–12428.

- Spanakos, D., Rigby, S.P., 2022. Evaluation of impact of surface diffusion on methane recovery via carbon dioxide injection in shale reservoirs. *Fuel* 307, 121928.

1. Chapter One: Introduction

1.1 General Overview

Global energy consumption is expected to increase by approximately 50% by 2050 (EIA, 2020). From technical and economic points of view, the renewable energy resources may not be capable of replacing the use of fossil fuels (oil, natural gas, coal) and meeting the global energy needs. According to BP (2020), it is predicted that there will be a decline in the share of fossil fuels from 81% of total primary energy demand in 2018 to between 40% and 65% by 2050. Despite this apparent decline, fossil fuels will continue to play a dominant role in global energy systems. In past years, hydrocarbon sources from conventional reservoirs have decreased rapidly, leading to increased interest in enhanced oil and gas recovery from unconventional reservoirs. As shown in Figure 1.1, these unconventional reservoirs include tight oil, oil shale, shale oil, tight gas, shale gas and coal bed methane.

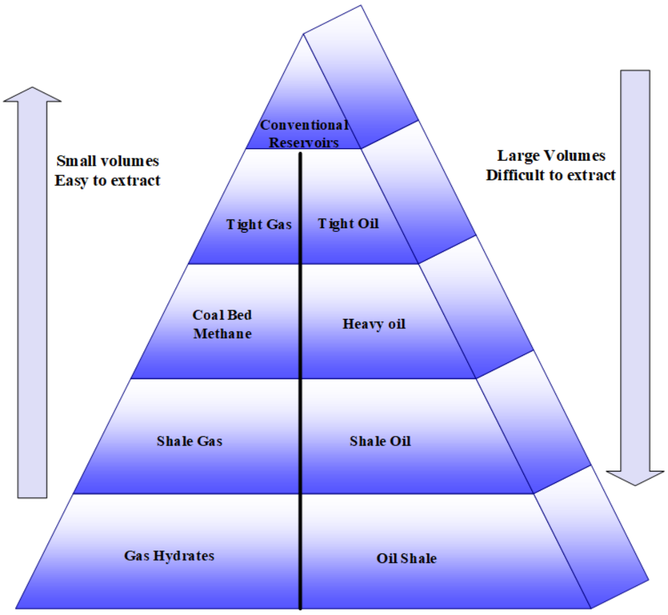

Figure 1.1 Worldwide resource pyramid of hydrocarbons. Reprinted from Aguilera (2014)

Of all fossil fuels, natural gas has played a prominent role due to its relative environmental friendliness. Figure 1.2 depicts the geologic nature of most significant sources of natural gas (EIA, 2010). At the time of writing, shale gas resources have received great attention because of their abundance across the globe and their potential to supply the world with an immense amount of energy. According to the U.S. Energy Information Administration report (EIA, 2020), dry shale gas production is the largest contributor, rising from 29.2 trillion cubic feet in 2020 to 36.5 trillion cubic feet in 2040. In general, shale gas production is expected to contribute approximately 30% of world natural gas production by 2040 (EIA, 2020). In contrast to conventional reservoirs, shale gas reservoirs (SGRs) consist of shale matrix with extremely low permeability and conductive natural fractures that influence the well performance. In shale reservoirs, methane molecules are stored as free state and/or as adsorbed state on the surface of the matrix particle and natural fractures (Kang et al., 2011). Notably, a significant portion of the total gas volume (20% - 80%) is present as adsorbed state in the pore media (Chalmers and Bustin, 2007; Ross and Bustin, 2007; Zhang et al., 2012). Hydraulic fracturing is usually applied to exploit ultra-low permeability reservoirs by inducing fracture networks around the wellbore. These fracture networks exhibit enormously high permeability. Hence, SGRs exhibit a variety of gas mass transfer mechanisms, which are of major importance in the apparent permeability, and, thus in the the assessment of the production and gas storage potential of SGRs.

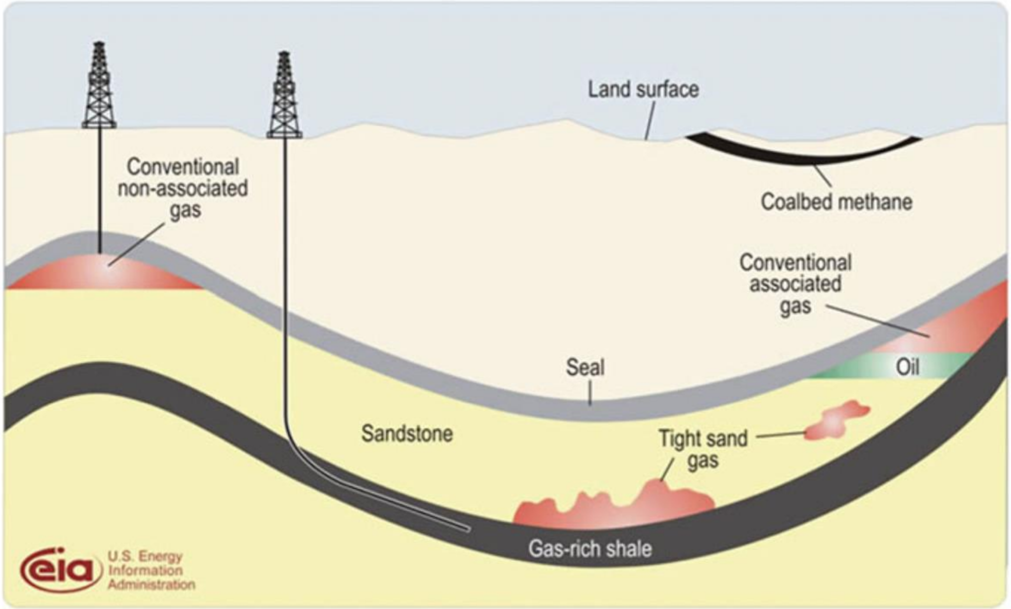

Figure 1.2 Schematic geology of natural gas resources (EIA, 2010)

Since the beginning of the industrial revolution, the carbon dioxide (CO_2) concentration in the atmosphere has been substantially increasing. Presently, the atmospheric CO_2 concentration has reached approximately 410 ppm, whereas in the pre-industrial era, the CO_2 concentration was about 280 ppm (EIA, 2021). The reason for this CO_2 increase is mainly due to the combustion of fossil fuels for energy production (Keeling et al., 1995). One of the most promising methods to reduce CO_2 emissions in the atmosphere is the application of CO_2 in gas injection processes. CO_2 injection can be utilised as a means of both enhancing oil and/or gas recovery and sequestering CO_2 in reservoirs. Consequently, CO_2 injection addresses the growing worldwide gas demand, as well as the challenge of greenhouse gas emissions. In past years, interest in enhanced gas recovery via CO_2 injection in SGRs has increased rapidly, especially throughout North America. In the United States, dry shale gas production was equal to approximately 78% of the total U.S. dry natural gas production in 2020 (EIA, 2020). Previous researchers (Zhao and Wang, 2019; Liu et al., 2020) have shown that the surface of the shale matrix shows stronger affinity for CO_2 compared to that of CH_4. In general, adsorption capacity of pure CO_2 is consistently greater than that of CH_4 (Kang et al., 2011; Heller and Zoback, 2014; Hong et al., 2016). A study conducted by Nuttal et al. (2005) showed that the adsorption capacity of pure CO_2 is approximately 5 times higher than that of CH_4 in Devonian black shales. As mentioned previously, SGRs exhibit a variety of gas transfer mechanisms. These gas transfer mechanisms in SGRs exhibit a significant rate difference compared to that seen in conventional gas reservoirs. The gas transfer regimes, occurring within the SGRs, consist of bulk gas transfer and surface diffusion mechanisms.

Previous work (Wu et al., 2016) has shown that the mass transport flux in shales is dominated by the surface diffusion mechanism due to the greater fraction of adsorbed phase found in the nanopores of shales. However, the surface diffusion tends to have been overlooked by previous researchers (Yu et al., 2016; Kim et al., 2017), who have conducted reservoir simulations to investigate the practical feasibility of use of CO_2 for CH_4 extraction and CO_2 storage in shale reservoirs. Greater mobility of CO_2 within the shale improves the displacement efficiency of the originally present CH_4, as well as increasing the CO_2 penetration of the shale formation. Thence, surface diffusion of adsorbed gas is of major importance in the apparent permeability of SGRs and must be considered to ensure accurate prediction of gas recovery and storage, despite being omitted in previous work. CO_2 injection is also considered one of the most effective methods for enhanced oil recovery (EOR) in both conventional and unconventional reservoirs (Jarrell et al., 2002; Li et al., 2019).

According to a previous research (Hawthorne et al., 2013), a minor improvement in oil recovery factor such as 1% could yield 1.6 to 9 billion barrels of additional oil. Assuming that the crude oil price is \$80 per barrel, the additional 1% in oil recovery factor could bring a revenue of \$128 to \$720 billion (Yu and Sepehrnoori, 2018). The implementation of CO_2 enhanced oil recovery (CO_2-EOR) method may recover up to 20% of the original oil in place (Yongmao et al., 2004) thereby prolonging the reservoir life for 15-20 years. At the time of writing, the Gorgon Project is one of the world's largest natural gas projects where CO_2 injections commenced in 2019. The Gorgon CO_2 Injection Project, located on Barrow Island in Western Australia, will be the world's largest CO_2 injection plant, with an ability to store up to 4 million tons of CO_2 per year. Furthermore, The Weyburn-Midale CO_2 Project located in Midale, Saskatchewan, Canada, started CO_2 injection in 2000 and continues to produce oil from Weyburn and Midale oil fields. In particular, the CO_2 injected is captured at a lignite-fired synfuels plant in Beulah, North Dakota, U.S., and transported to the fields via a 320 km pipeline. However, CO_2-EOR is not suitable for all reservoirs (Verma, 2015). For instance, CO_2 is not fully miscible in heavy oil reservoirs. Rojas et al., (1991) showed the partially dissolved CO_2 can reduce the heavy oil viscosity only by a factor of 10, leading to a limitation of oil flow through the porous media. Hence, the oil recovery in heavy oil reservoirs is sufficiently small in comparison with oil recovery in medium to light oil reservoirs. Moreover, a variety of factors, namely swelling effect, heterogeneity, viscous fingering, minimum miscibility pressure, reservoir geology and petrophysical properties need to be examined before applying the CO_2-EOR technique in oil reservoirs. Although pipelines have been identified as the primary means of transporting CO_2 from point-of-capture to site, a CO_2 source (i.e. refinery, coal plant etc.) needs to be at close proximity to field in case the pipeline infrastructure is not extensive. It is thus reasonable to say there remain significant technical challenges and uncertainties that need to be evaluated to provide insights into a better understanding of the potential of CO_2-EOR techniques.

1.2 Aims and Objectives

From the literature reviewed, the aim is to assess the effectiveness of CO_2 recovery methods in shale gas and oil. The objectives of this thesis are outlined as follows:

- Highlight the advantages of the CO_2 injection method over other recovery techniques, especially in shale gas and medium to light oil reservoirs.

- To estimate the surface diffusivity of CO_2 at different temperatures on various shale samples with different properties (i.e. adsorption capacity, mineralogy, organic content, heat of adsorption, fractal dimension etc.).
- To apply the fractal theory and effectively predict, *a priori*, surface diffusivity parameters for structurally and chemically heterogeneous natural samples as shales.
- To generate and validate numerical reservoir models of shale reservoirs against existing field data.
- To implement an apparent permeability model within a numerical reservoir simulator to investigate the impact of surface diffusion on methane recovery via CO_2 injection techniques at various shale reservoirs.
- To conduct numerical reservoir simulations in a geologically realistic reservoir.

1.3 Thesis Outline

This thesis is structured as follows:

Chapter two presents a review of the different oil and gas recovery techniques. It also provides comprehensive detail on gas adsorption phenomena and the mechanisms of gas flow within shale gas reservoirs.

Chapter three outlines experimental methods to obtain surface area, pore size distribution and gas uptake kinetics to obtain key rock void space parameters prior to reservoir simulation of shale reservoirs. It also summarises the governing equations required to accurately simulate fluid flow in fractured shale gas reservoirs.

Chapter four describes low pressure gas adsorption isotherms and helium pycnometer experiments to investigate the pore size distribution and estimate porosity on various shale samples. The surface fractal dimension is estimated via the low-pressure nitrogen adsorption measurements. Then, total organic carbon (TOC) and mineralogy is determined via Rock Eval Analysis and Mineral Liberation Analysis (MLA), respectively. Subsequently, gravimetric gas uptake experiments are conducted to estimate the Arrhenius parameters for surface diffusivity on each shale sample. Conclusions on the validity of theory are drawn by testing the applicability of the fractal theory to highly structurally and chemically heterogeneous natural materials.

Chapter five involves the generation of numerical reservoir models of shale reservoirs (i.e. Marcellus, Barnett, New Albany) based on existing geological data. Existing experimental measurements of methane and carbon dioxide from shale core samples are analyzed using the Langmuir adsorption model. Thereafter, properties, namely the bulk porosity, free gas saturation, and connate water saturation of the models are corrected, *a priori*, to avoid overestimation of the volume of free gas and the original gas in place. Uncertain parameters such as fracture height, fracture half-length, and fracture conductivity were found by obtaining a good history match with gas field data. Afterwards, the surface diffusivities estimated in Chapter four are implemented into an established apparent permeability model, which was then applied to numerical reservoir simulations to model CO_2 injection techniques. The efficiency of transport of CO_2 via surface diffusion is investigated assuming various pore radii. The fractal model proposed in Chapter 4 is also applied to examine the impact of rock surface roughness on CH_4 production and CO_2 adsorption. The Chapter closes by investigating the effect of larger-scale reservoir heterogeneity on gas production via geostatistical reservoir simulations.

Chapter six presents the construction of a fluid characterization model for the Prinos oil reservoir. The fluid characterization model is based on both existing experimental studies and laboratory-measured data for live oil samples. Then, the fluid characterization model is implemented into a numerical reservoir simulator and the simulated reservoir model is history matched with real field scale oil production data. Subsequently, several CO_2 injection techniques are simulated and compared with waterflooding, as a base case. Similar to Chapter five, a geostatistical approach is applied to assess the effect of reservoir heterogeneity on oil production and CO_2 storage efficiency. In order to select the best development strategy for the Prinos field, an economic analysis is performed for each case.

Chapter seven draws the general conclusions from the research findings, as well as provides some recommendations for future research.

2. Chapter Two: Literature review

2.1 Introduction

The first section of this chapter presents a comprehensive review of the different oil and gas recovery techniques. Critical assessment of their merits and demerits is also made. The aim of the review is to identify the superiority of carbon dioxide injection over the other recovery techniques, mainly, in unconventional reservoirs. The following are identified to be among the realisable advantages of carbon dioxide (CO_2) injection over the other methods:

i. It extracts heavier components (C_5 - C_{30}) from the oil reservoir compared to other gas injection methods.
ii. It is soluble in water.
iii. It increases oil density.
iv. It has significantly lower minimum miscibility pressure (MMP) value compared to other gas injection methods.
v. It can be utilized for a wide depth range of oil reservoirs.
vi. It promotes oil swelling. The greater the methane amount within the oil, the less the swelling.
vii. It reduces oil viscosity, thereby improving oil mobility, and, thus the oil recovery factor.
viii. It reduces the difference between water and oil density, thereby reducing the change for gravity segregation.
ix. Miscible CO_2 -Enhanced Oil Recovery (EOR) reduces the surface tension of oil and water due to absence of capillary forces, which results in a more effective displacement and increase of oil recovery factor.
x. It has greater sorption affinity than that of methane in shale gas reservoirs, thereby enhancing gas recovery and simultaneously reducing greenhouse gas emissions from the use of fossil fuels.

The review of oil and gas recovery methods is then followed by a critical review of the characteristics of unconventional shale gas reservoirs. The aim of this, is to investigate the mechanisms of gas adsorption phenomenon since a significant portion of the total gas volume in shale reservoirs exists in the adsorbed phase. The Chapter closes by discussing the multiple flow mechanisms within shale reservoirs which play a major role in comprehending and forecasting the production of gas.

2.2 Oil and Gas Recovery Processes

Oil and gas production in reservoirs consists of three distinct phases, namely primary, secondary, and tertiary recovery. Primary recovery is the initial stage for extracting oil and gas from the reservoir. It relies on the natural rise of hydrocarbons due to the pressure difference between the underground reservoir and the surface, combined with artificial lift techniques (rod pumps) to force oil to the surface. However, only approximately 10% of original oil in place is typically produced at this stage (Tzimas et al., 2005). Subsequently, secondary and tertiary (enhanced) recovery methods are implemented with the intent of extending a field’s productive life and reducing the residual oil saturation. The secondary recovery method involves the waterflooding process, whereas the tertiary recovery methods consist of three major categories, namely, gas injection, chemical injection and thermal recovery. As will be explained later in this chapter, these methods improve both the displacement and sweep efficiency, thereby enhancing oil and gas production.

2.2.1 Waterflooding

Waterflooding, also known as secondary recovery, follows the primary recovery stage (Figure 2.1). It is the process whereby water is injected into the reservoir to displace the remaining oil (Taber and Seright, 1992). The waterflooding process has also been successfully applied as a primary method in some heavy oil reservoirs across the world, namely the Continental Shelf in the United Kingdom (Etebar, 1995; Jayasekera and Goodyear, 1999). During the recovery process, water is injected into injector wells to push the oil towards the production wells. At the production wells, submersible pumps are utilized to bring the oil to the surface.

Once the waterfront reaches the production well, a greater amount of water is produced, making the whole process thereafter uneconomical. The recovery factor varies within the range of 10% to 30% depending on oil and reservoir characteristics (Muggeridge et al., 2014; Istchenko and Gates, 2014). It should be noted that the greater the viscosity, the lower the recovery factor due to channelling of the waterflood front, and, thus poor sweep efficiency.

Despite the fact that the waterflooding technique has been widely used in conventional reservoirs, its application in unconventional reservoirs with low permeability is challenging. The reason for this challenging issue in unconventional reservoirs, is a combination of the low injectivity, along with the clay swelling problems and the poor sweep efficiency in the fracture networks.

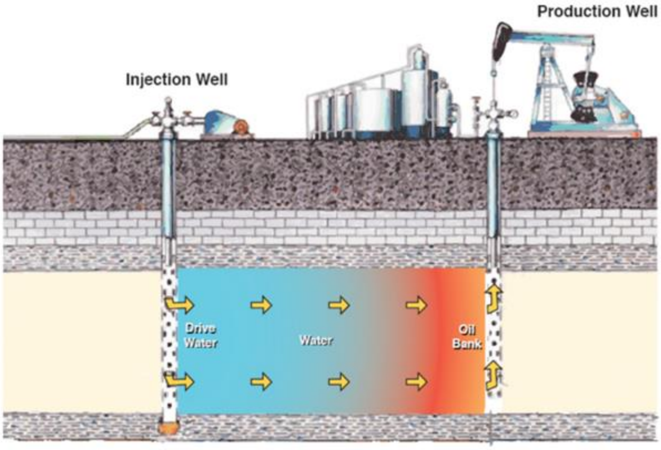

Figure 2.1 Schematic of waterflooding process (NETL, 2010)

2.2.2 Gas Injection

The gas injection method used as a tertiary method, has been found to be one of the most cost-effective methods amongst all the different methods of EOR. When compared to waterflooding, the gas injection method attains higher displacement efficiency, hence its wide range of applicability to various reservoirs. Gas injection is the most suitable technique in unconventional and conventional medium to light oil reservoirs (Verma, 2015). Gas injection is used as a tertiary method in oil recovery involves the injection of non-hydrocarbon gases (i.e. nitrogen, carbon dioxide) or hydrocarbon gases (i.e. natural gas, liquified petroleum gases) to displace reservoir oil under miscible or immiscible conditions.

Gas injection reduces the interfacial tension (IFT) leading to higher oil recovery. The reason for this IFT reduction is a combination of oil swelling, along with the mass transfer between the displaced and displacing phases. In addition, it has been observed that oil viscosity is reduced, leading to reservoir repressurization and decrease of the capillary forces (Firoozabadi and Aziz, 1986; Christensen et al., 1998). The application of gas injection as an EOR method is generally categorised as either an immiscible or miscible technique.

Minimum miscibility pressure (MMP) and gas injection pressure determine the utilization of either miscible or immiscible flood. The MMP refers to the lowest pressure at which crude oil becomes miscible with the injected gas. It should be noted that miscibility is achieved after a dynamic multiple contact between the two phases (i.e. injected gas and crude oil) at reservoir temperature (Stalkup, 1987).

In immiscible flooding, the reservoir pressure is below the MMP, and the injected CO_2 will not form a single phase with the crude oil. The immiscible CO_2 injection technique was initially utilized for reservoir pressure maintenance and is dominated by the process of oil swelling. An interface between the injected fluid and the crude oil is developed, leading to the establishment of a capillary pressure. In immiscible flooding, the residual oil saturation is higher compared to the miscible flooding (Tewari et al., 2010) since the CO_2 is not completely dissolved in crude oil and the interfacial tension values between the oil and the injected gas are low.

In miscible flooding, the reservoir pressure should be maintained above the MMP. Miscible CO_2 flooding is a multiple-contact process where the CO_2 will vaporize the lighter oil fractions into the injected CO_2-rich phase. The vaporization makes the CO_2 phase denser to be soluble in the oil phase. In addition, the phases involved in the process can be mixed with each other at any ratio, leading to the absence of the interface between the two phases and the reduction of the capillary forces to a minimum value (Green and Willhite, 1998). It has been observed that miscibility, attained via vaporization and/or condensation process (Johns et al., 1993), enhances the mobility of great amounts of trapped oil (Oren et al., 1992; Ayirala and Rao, 2006). Hence, the oil recovery factor in miscible flooding is higher when compared to the immiscible flooding.

2.2.2.1 Nitrogen Injection

The mechanism of nitrogen (N_2) injection is similar to the mechanism of carbon dioxide injection as will be explained in Section 2.2.2.3. N_2 injection is a more economical method when compared to other gas injection methods due to the low cost of nitrogen. In addition, nitrogen is easier to capture since it is abundant in air (78%) and less corrosive than CO_2. The low cost of N_2 makes the N_2 option even more economical besides facilitating large volumes of gas being injected at a higher pressure. For example, the Cantarell offshore reservoir in Mexico is the largest nitrogen flood project with a daily production of 500,000 barrels of oil

(Sanchez et al., 2005). However, N_2 injection is not as efficient as CO_2 injection due to the MMP pressure. In particular, N_2 gas has a high miscibility pressure (~ 9000 psi). In certain cases, the MMP of nitrogen is even greater than the fracture pressure of the reservoir. Consequently, N_2 gas will be injected at high pressures to achieve miscibility. At high pressures, the vaporization of lighter components (C_2 to C_6) occurs to generate miscibility. These high pressures limit the N_2 injection method to reservoirs having a depth deeper than 5,000 feet (Bougre and Gamadi, 2021). Nitrogen injection is thus suggested to be applied as an immiscible flood at lower pressures.

2.2.2.2 Hydrocarbon Injection

Various gas drive methods have utilized light hydrocarbons as the injection gas (Lyons, 1996). These light hydrocarbons involve the injection of natural gas (methane) or a liquefied petroleum slug (e.g. propane) driven by natural gas and enriched natural gas. Enriched or condensing natural gas drive consists of higher hydrocarbons (ethane to hexane) and is transferred from gas to oil, leading to the reduction of viscosity and an increase of miscibility of the oil. The inverse of the enriched natural gas process is called the vaporizing gas process. This process entails the injection of dry methane at high pressure, which results in the vaporization of the ethane to hexane components. In addition, reservoir mobility is increased due to the expansion of vapour. Despite the fact that hydrocarbon gas injection is costly, high pressure is required for the vaporizing gas drive. Consequently, hydrocarbon gas injection is limited to reservoirs having depth deeper than 5,000 feet.

2.2.2.3 Carbon dioxide Injection

Carbon dioxide injection has been proposed as a promising EOR method (Figure 2.2). Over the past three decades, the number of CO_2 injection projects in the United States has risen by 300% (Manrique et al., 2010). According to previous researchers miscible CO_2-EOR may enhance oil recovery by up to 20%, whereas immiscible CO_2 -EOR may enhance oil recovery by up to 8% (Perera et al., 2016). In addition, Rao (2001) showed that implementation of carbon dioxide increases the oil recovery factor of water-flooded projects by 30%. CO_2 injection to recover oil and gas also has the advantage of simultaneously sequestering carbon dioxide, thereby concurrently addressing the issue of increased greenhouse gas emissions from the use of fossil fuels.

CO_2 injection has been widely applied in conventional oil reservoirs (Jarrell et al., 2002; Kong et al., 2015) and the main mechanisms involved in the process have been well understood. These mechanisms mainly include oil viscosity, oil swelling, vaporisation of crude oil and oil density change (Holm and Josendal, 1974). In general, CO_2 extracts light to intermediate components within the range of C_5 and C_{30} from the reservoir oil. Once miscibility is developed after multiple contacts, the oil volume significantly expands, whereas both the surface tension and viscosity are reduced. As a result, residual oil becomes more mobile and flows easier in porous media (Taber and Martin, 1983; David Martin and Taber, 1992; Lambert et al., 1996).

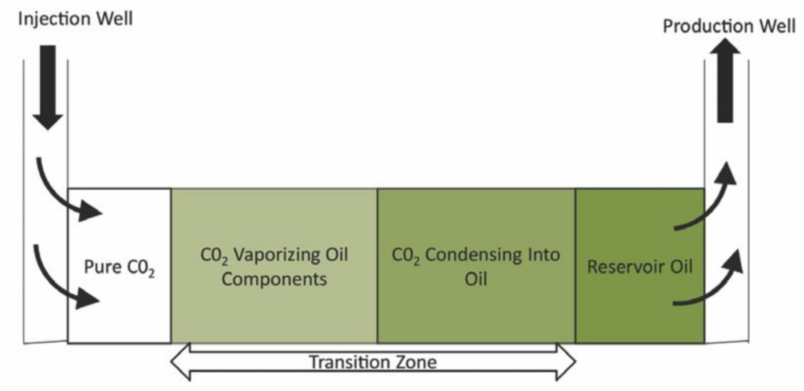

Figure 2.2 Schematic of continuous CO_2 injection method (Jarrell et al., 2002)

Nonetheless, a distinct limitation that needs to be taken into account is the poor mobility control of CO_2 due to its low viscosity. This leads to viscous fingering (Figure 2.3), gravity overriding and early breakthrough to the producer well. To counter this problematic behavior of CO_2 and reduce the viscous instabilities in oil reservoirs, the CO_2-Water Alternating Gas process (CO_2-WAG) is usually implemented, as will be explained in Section 2.2.3.

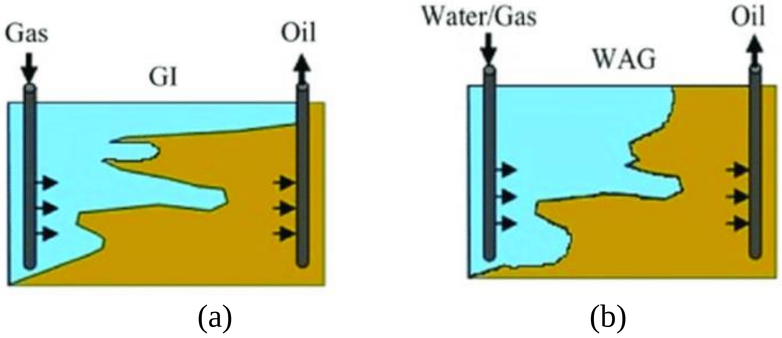

(a) (b)

Figure 2.3 Schematic of fingering via (a) continuous CO_2 method and (b) CO_2-WAG method (Afzali et al., 2018)

In cases where a CO_2 source is available, the process is more economical compared to natural gas flooding. Previous studies (Stalkup, 1987; Holm, 1987) showed that, CO_2 has a significantly lower MMP compared with nitrogen and hydrocarbon gas. In addition, hydrocarbon extraction depends on the CO_2 density, implying that the greater the CO_2 density, the higher the oil extraction density (Holm and Josendal, 1982; Orr et al., 1983; Sigmund et al., 1984).

When reservoir temperature is greater than the critical temperature of CO_2 (31°C), the CO_2 density ranges from 0.1 to 0.8 g/cm^3 at pressures between 1000 and 4000 psi (Holm and Josendal, 1982). Hereafter, a purification of source CO_2 is necessary since it determines the sweep efficiency (Zhang et al., 2004).

The global demand for natural gas is predicted to increase by 35% by 2040, and approximately 30% of its supply is expected to come from shale gas (EIA, 2020). Consequently, there has been a paradigm thinking towards shale gas production, especially over the past decade.

In a normal production process for shale gas, the free gas in large pores and fractures usually comes out first and its production usually lasts for just under two years (Pan and Connell, 2015). Subsequently, after few years of production from the shale gas well, the gas rate declines steeply. Thus, there has been a growing interest in enhanced shale gas recovery (ESGR) via CO_2 injection scenarios, namely CO_2 huff and puff injection and continuous CO_2 flooding.

Even though rare field tests are reported for the CO_2-ESGR injection technique (Nuttal et al., 2005; Louk et al., 2017), there are both experimental and numerical studies conducted to assess its suitability in the exploration and production of shale (Kim et al., 2013; Fathi and Akkutlu, 2014; Heller and Zoback, 2014; Li and Elsworth, 2015; Yu et al., 2015). In shale gas reservoirs, Kim et al. (2013) showed that cumulative gas production via CO_2 huff and puff and CO_2 flooding was 6%, and 24%, respectively, higher than for the no CO_2 injection.

Furthermore, CO_2 sorption affinity to the shale is greater than that of CH_4 in the subsurface situation (Busch et al., 2008; Shi and Durucan, 2008). A study conducted by Liu et al. (2019) showed that 95% of the injected CO_2 is effectively sequestered. Consequently, in shale gas reservoirs, CO_2 injection does not just improve the production of CH_4 but also enables CO_2 sequestration.

2.2.3 CO_2-WAG injection

CO_2-WAG injection is considered as a tertiary method in oil recovery processes. It was first implemented in the 1950s, and is the most widely used CO_2 -EOR technique, especially in fields where waterflooding has been previously applied (Alvarado and Manrique, 2010; Ghedan, 2009; Rogers and Grigg, 2000; Taber and Martin, 1983). In addition, CO_2-WAG has been applied in over 90% of CO_2 injection projects (Aghdam and Ghorashi, 2017; Merchant, 2017; Afzali et al., 2018). Previous studies have shown that CO_2-WAG injection has improved the sweep efficiency, and thence the recovery factor of CO_2 injection method, especially in conventional light-oil reservoirs (Bhatia et al., 2014; Ligero and Schiozer, 2014). According to Holm (1987) and Ghedan (2009) , typical incremental oil recovery by CO_2-WAG varies in the range of 5% and 25%.

The initial aim of the CO_2-WAG process was the reduction of the CO_2 injected, and the simultaneous enhancement of both the macroscopic and microscopic sweep efficiency. In order to achieve this enhancement, CO_2-WAG combines two recovery processes, waterflooding and CO_2 injection method.

Similar to gas injection, discussed in Section 2.2.2, CO_2-WAG is categorized as either a miscible or immiscible displacement process (Green and Willhite, 1998; Christensen et al., 1998). In CO_2-WAG injection method, the MMP needs to be lower than the reservoir pressure to achieve miscibility. As shown in Figure 2.4, a miscible zone is generated at the front, which consists of the injected CO_2 slugs and the oil bank. Once miscibility is achieved, the CO_2-induced interfacial tension (IFT) and oil viscosity reduces, similar to CO_2 injection in Section 2.2.2.3. As a result, the oil bank expands and becomes better able to flow to the production wells. In contrast, in the immiscible CO_2-WAG process, the injected gas is immiscible with the oil and maintains its gaseous state during the displacement process.

Moreover, water injection efficiently controls the mobility of the injected gas by reducing the gas relative permeability. In contrast to the CO_2 injection method, water injection during the half cycle of a CO_2-WAG process, results in an increase in water saturation, reduction of gas relative permeability, and thus effective control of the mobility of the injected gas. It should be noted that, effective control of the injected gas prevents early gas breakthrough (BT) in the production wells. The reason for an early BT in the production wells is a combination of viscous fingering and gravity overriding (Dellinger et al., 1984).

Nonetheless, CO_2-WAG method is not suggested as a recovery method in unconventional reservoirs. Due to the low permeability in unconventional reservoirs, water adsorbs in the internal shale matrix and channels via the fracture networks, inhibiting CO_2 migration. Consequently, CO_2 injection is considered as a more efficient oil and gas recovery method in unconventional reservoirs.

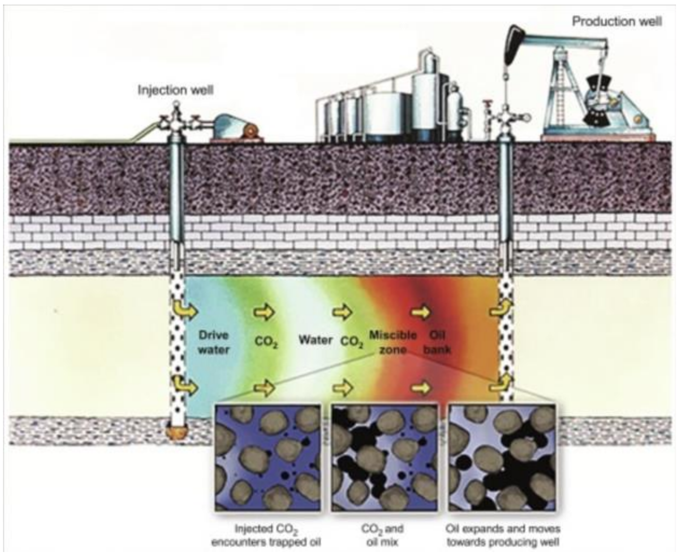

Figure 2.4 Schematic of CO_2-WAG method (NETL ,2010)

2.2.4 Chemical flooding

Chemical flooding is also used as a tertiary method where chemicals are utilised to reduce the interfacial tension and enhance the sweep efficiency (Thomas and Farouq Ali, 1999). Chemical flooding entails three main categories, surfactant, polymer and alkaline flooding (Figure 2.5). A combination of the main categories of chemical flooding can yield the best characteristics of each. This means that slugs of different composition and size are injected sequentially into the reservoir to enhance the performance of the chemicals. According to previous studies, chemical flooding may increase the oil recovery factor up to 40% (Shah et al., 2010). However, the use of this method has been restricted due to the high cost of the chemicals, except for reservoirs in China.

Furthermore, reservoir characteristics limit the performance of chemicals. For instance, the adsorption capacity of chemicals (e.g. surfactants) on the surface of carbonates and sandstones is high. The reason for this high adsorption is that the surface of carbonate rocks is positively charged whereas the surfactants are negatively charged after ionization in water. Consequently, the loss of surfactant during the propagation process leads to higher economic costs and a reduction in the mobility ratio of water. In addition, reaction of alkali with clays causes an increase in swelling, which results in permeability reduction.

Chemical flooding in unconventional reservoirs is not recommended due to the low fracture density. It should be noted that, the imbition rate is inversely proportional to the characteristic length (linearly or squared), which leads to a significantly slow recovery rate (Mattax and Kyte, 1962; Kazemi et al., 1992; Cuiec et al., 1994).

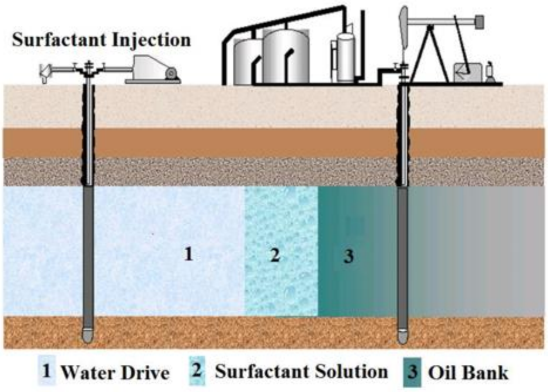

Figure 2.5 Schematic of surfactant flooding mechanism (International Energy Outlook, 2008)

2.2.5 Thermal Recovery Processes

Thermal EOR methods are mostly applied to enhance the recovery of heavy oil, or bitumen by injecting heat generated at the surface or in situ from steam or hot water to reduce oil viscosity. Subsequently, oil becomes more mobile and better able to flow to the production wells (Speight, 1999). Over the past few decades, thermal techniques, namely cyclic steam stimulation (CSS), toe-to-heel air injection (THAI), steam flooding, steam assisted gravity drainage (SAGD) and *in situ* combustion (ISC) have been investigated.

Briefly, the general basic procedure of thermal EOR methods is described as follows: In the case of cyclic steam stimulation, steam is periodically injected to heat the reservoir around the wellbore. This process is also called huff and puff and the oil recovery can be up to 40% (Shah et al., 2010). In particular, a certain amount of steam is injected to the well to assist the heavy oil to flow more easily into the production or injection well. Afterwards, the process stops in order to allow the steam to heat the formation around the well. Then, the wells are put back in the production and heat is exhausted with the produced fluid. This thermal process is recommended for extra-heavy oil production due to its high investment rate of return (Bahadori, 2018).

The SAGD process is more efficient when compared to CSS, yielding between 60% and 70% recovery of oil (Speight, 2014). The SAGD process was initially introduced for bitumen extraction and is more economic when applied to thick reservoirs, in comparison to CSS. Two uneven horizontal wells are drilled, where the upper well is the injector and the lower the producer. A continuous stream of high-pressure gas is injected into the upper well. In that way oil viscosity reduces and the heated oil moves towards the producer. It should be mentioned that no vapour is produced since the gases are accumulated within the upper well due to density (Holdaway, 2014). Despite the fact that less reservoir damage would occur due to lower pressures, SAGD leads to generation of greenhouse gases.

The steam flooding method is analogous to waterflooding, where steam is continuously injected into the oil layer in order to enhance the production of viscous crude oil by reducing the viscosity of the heavy oil. Typical oil recovery factors range from 50% to 60% (Bahadori, 2018). The injection well pattern around the production well must be carefully considered. Nonetheless, the excessive heat lost during the steam flooding method, leads to high energy costs, increasing the cost of the process.

The in-situ combustion method is also applied to high viscous oils with high oil recovery. The process involves exothermic reactions which increase the final temperature of the reservoir (i.e. 300-400^{o}C) and may reach phase change. In the ISC process, air is injected into the reservoir in order to oxidize a small fraction of hydrocarbons. Subsequently, heat and gas are generated, leading to a greater drive energy and a viscosity reduction (Prats, 1982). Despite the high efficiency of ISC (~75% oil recovery factor) (Zhang et al., 2019), the process has led to few successful field experiences since the heat front is challenging to control (Turta et al., 2005). In addition, the combustion reactions (i.e. oxidation, cracking) increase the complexity of the process.

The horizontal production well and *in situ* combustion concept are integrated in the THAI method. In particular, the THAI method plays two major roles in terms of oil displacement. First, the oil viscosity is reduced, increasing the mobility of the oil. Second, the thermal cracking of the immobile oil plays a critical role in upgrading the heavy oil and achieving high oil recovery (Greaves et al., 2000). Experimental modelling has shown that recoveries up to 85% are feasible (Greaves et al., 2000), which is significantly higher compared to other thermal methods. THAI experiments conducted at the University of Bath (Xia et al., 2005) have shown that THAI overcomes problems associated with ISC. As shown in Figure 2.6, THAI involves at least one vertical air injector and a horizontal production well which controls the flow regime in the reservoir. The vertical well is perforated in the upper part of the oil layer whereas the horizontal well is located at the lowest part of the oil layer and the toe faces the injector. In THAI, the heavy oil flows to the surface via a combination of procedures, namely mass-, heat, and gas- momentum transfer, gravity drainage and coke combustion reaction (Xia and Greaves, 2002; Turta and Singhal, 2004; Xia et al., 2005; Greaves et al., 2008). The zone around the wells is initially heated to establish communication between the wells. Then the oil is ignited, but as combustion proceeds some of the oil-in-place acts as the fuel for the process. This fuel is essential for the combustion front and propagation. Subsequently, air is continuously injected to the formation via the injector well, generating a large temperature gradient. The mobile oil zone drains to the horizontal producer whereas the highly viscous material is deposited in the cracking zone. In contrast to ISC, mobile oil does not travel over a long distance due to the well arrangement (short well displacement). Of all the thermal methods, THAI is the safest and most stable oil recovery technique. The full description of the main advantages of THAI are summarized elsewhere (Turta and Singhal, 2004; Xia et al., 2005; Greaves et al., 2008). Moreover, a significant advantage of the THAI process is the addition of catalytic upgrading process in-situ (CAPRI) where in-situ further upgrading is achieved. The full experimental work on the CAPRI is described in great detail elsewhere (Xia and Greaves, 2002). Despite the fact that thermal EOR methods are applicable to all types of crude oil, the high energy consumption limits the methods for the high viscosity oils (i.e. heavy oils, sand oils) to be economically successful.

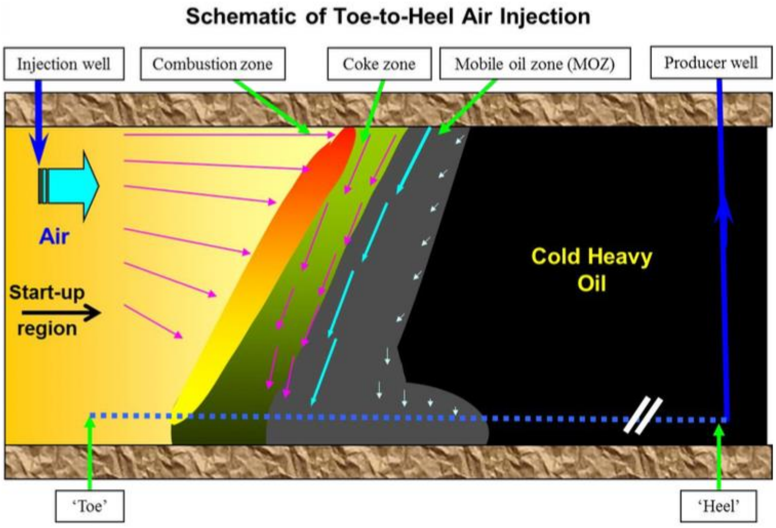

Figure 2.6 Schematic arrangement in THAI (Xia and Greaves, 2002)

2.3 Characteristics of Unconventional Shale Reservoirs

The world today is faced with a scarcity of conventional energy sources and the global energy consumption is expected to increase by approximately 50% by 2050 (Bellani et al., 2021). Current renewable resources may not be capable to relieve the pressure exerted on conventional resources. Hence, gas shales are an increasingly exploited resource across the world. According to Liu et al. (2019), gas reserves in unconventional shale are estimated at nearly 719 trillion cubic metres. Shales can be the seal, the reservoir, and/or the hydrocarbon source. Typically, the properties of gas shale include a very low permeability, of the order of nano-Darcy (10^{-6} mD), a very small grain size, increased total organic carbon (TOC), and a small porosity. Gas hold-ups in shale reservoirs are mainly made up of bulk gas within the pore space and gas adsorbed on the internal shale matrix (Crosdale et al., 1998; Curtis, 2002; Pan and Wood, 2015). According to past studies, a significant portion of the total gas volume (20% - 80%) is present as adsorbed state in the nanopores of organic matter and clay minerals (Chalmers and Bustin, 2007; Ross and Bustin, 2007; Zhang et al., 2012)

2.3.1 Gas Adsorption Phenomenon

Adsorption is the adhesion of molecules (the adsorbate, or the adsorptive) to the surface of the solid (the adsorbent) (Figure 2.7). Adsorption is a reversible process, because it involves weak attractive forces. The adsorption process is also exothermic ($\Delta H<0$) due to the substantial loss of entropy ($\Delta S<0$), for the formerly dispersed adsorbate molecules, on being adhered at the surface. Adsorption initiates when, the number of molecules that accumulate at the surface is greater compared to the number of molecules that leave the surface. Subsequently, adsorption is a dynamic equilibrium process where molecules are both accumulating at the surface and departing at all times. Equilibrium is achieved when the size of accumulation flux equals that of the departing flux. The adsorption process can be divided into two main categories depending on the strength of the interaction: Physisorption (physical adsorption) and Chemisorption (chemical adsorption).

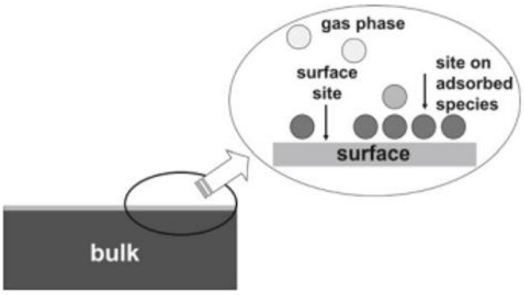

Figure 2.7 Schematic of gas adsorption phenomenon at the surface of solid material (Bolis, 2013)

Isotherms are utilized to describe adsorption indicating the amount of adsorbate on the adsorbent as a function of concentration at constant temperature. Key information about the mechanism of physisorption and the energy interaction between gas and solid is obtained from the isotherm shape and the hysteresis pattern. The shape of the isotherm is used in the determination of the types of pores found in the adsorbent. Pressure is normalized to the saturation vapour pressure p_o when the temperature is below the critical temperature and the adsorbed amounts are so referred to the dimensionless relative pressure, p/p_o.

According to the International Union of Pure and Analytical Chemistry (IUPAC) recommendation (Sing, 1985), the pores in porous materials are categorized into three different kinds:

i. Macropores, pores with pore-width greater than 50 nm
ii. Mesopores, pores with pore-widths between 2nm and 50 nm
iii. Micropores, pores with pore-widths below 2 nm

It should be noted that it has become popular to refer to micropores and mesopores as nanopores. In 2015, Thommes et al., refined the original IUPAC recommendations (Sing, 1985) of physisorption isotherms. The proposed updated classification of physisorption isotherms were grouped into six characteristic types of isotherms which are closely related with certain pores structures (Figure 2.8).

As shown in Figure 2.8, Type I (a) and I (b) isotherms are reversible and are concave to the relative pressure axis. At low relative pressure the curves rise sharply and as the pressure increases, they reach a plateau implying that the amount adsorbed approaches the limiting value ($p = 1$). The Type I (a) curve corresponds to the filling of the narrow micropores while Type I (b) isotherms is an indication of the existence of wider micropores and probably narrow mesopores (< ~ 2.5 nm). Hence, Type I isotherms represent microporous materials (i.e. shale, coal) or monolayer adsorption. Type II isotherms are also reversible and refer to multi-layer adsorption on non-porous or macroporous adsorbents. At point B where the linear middle section starts is an indication of the completion of the monolayer coverage. Type III isotherms are characterised by a convex shape to the relative pressure axis over the whole range. It represents the weak interaction between the adsorbent and adsorbate on the non-porous or macroporous adsorbent. Mesoporous adsorbents typically demonstrate Type IV [(a) and (b)] isotherms. In the low p/p_o range, the Type IV isotherm shape is very similar to that of Type II. At high relative pressure, the isotherms are flat with a characteristic saturation plateau. Capillary condensation is observed for Type IV (a) isotherms and is often indicated by the presence of hysteresis as will be explained in more detail at Section 2.3.4. Hysteresis refers to the gap between the two isotherm branches. The reason for this gap is due to the lack of thermodynamic reversibility of the capillary condensation. It should be noted that the pore width depends on temperature and adsorption system. For instance, hysteresis for nitrogen in cylindrical pores occurs when the pore width is wider than ~ 4 nm at 77 K (Lowell et al., 2004; Landers et al., 2013; Thommes et al., 2015). Reversible Type IV (b) isotherms are obtained for adsorbents having mesopores of smaller width. Type V isotherms are similar to Type III isotherms at low relative pressures. This is due to weak interactions between adsorbent and adsorbate on microporous or mesoporous solid. Initially, the Type V isotherm is convex to relative pressure axis but at higher relative pressures the shape becomes similar to type IV isotherms. The presence of a hysteresis loop is indicated, and this is attributed to pore filling via capillary condensation. Layered build-up of adsorption on a highly uniform nonporous surface characterizes Type VI isotherms. Type VI isotherms are reversible, and each layer is completed before the next starts. The generated steps represent the capacity of each adsorbed layer. The adsorption system and temperature determine the sharpness of steps.

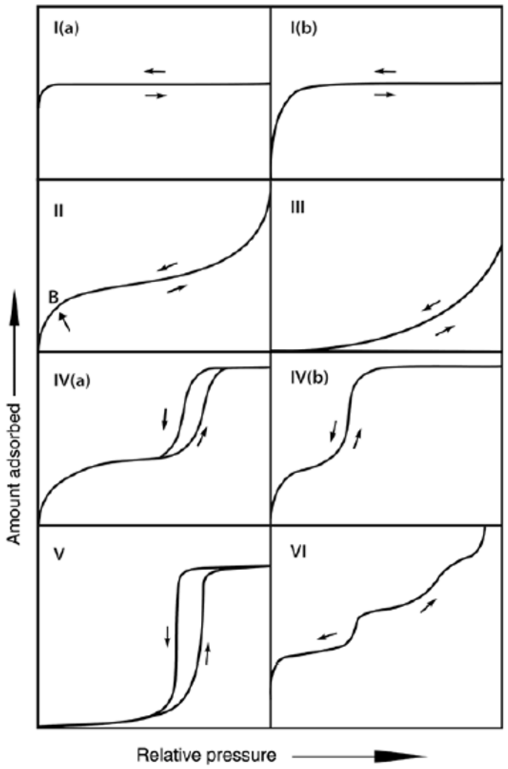

Figure 2.8 IUPAC classification scheme of physisorption isotherms (Thommes et al., 2015)

The thermodynamic properties of gas within nanopores are significantly different from the equivalent bulk gas properties (Koga et al., 2001; Alba-Simionesco et al., 2006; Holt, 2006; Köfinger et al., 2008; Giovambattista et al., 2009; Pellenq et al., 2009; Petropoulos and Papadokostaki, 2012). A gas molecule changes from a free gas to the adsorbed film when adsorbed on a surface. Thereupon, heat is released due to loss of potential energy. One of the most fundamental thermodynamic quantities used in the description of the physisorption phenomena is the heat of adsorption. The heat of adsorption relates the strength of interaction between the solid adsorbent and the gas adsorbate.

At equilibrium, the isosteric heat of adsorption (ΔH_{ads}) refers to the change in enthalpy of the system due to adsorption at a specific state of surface occupancy. Heat of adsorption varies as a function of system conditions, the quantity of adsorbate and the pore properties. In the first stages of the adsorption process, the released heat of adsorption increases the delay to achieve an equilibrium between the bulk phase and adsorbed phase. High heat of adsorption leads to slow gas desorption. The reason for this, is the strong interaction induced between the adsorbed molecules and the adsorbent. Previous studies (Xiong et al., 2017; Zhang et al., 2012) have shown that the methane adsorption capacity could be reflected by the heat of adsorption of methane.

The isosteric heat of adsorption can be measured indirectly via Clausius-Clapeyron relationship. The Clausius-Clapeyron is applied on the isothermal data at two or more different temperatures, and is given by the expression:

$$\Delta H_{ads} = RT^2 \left[\left(\frac{\partial (\ln P)}{\partial T} \right)_{n_a} \right] \tag{2.1}$$

The equilibrium data provided by the isotherms is used for the evaluation of the heat of adsorption. A plot of the equilibrium pressure as a function of the adsorption temperature at constant coverage θ is applied to determine the isosteric heat of adsorption. After the integration of Eq. (2.1), the isosteric heat of adsorption, for a given constant coverage θ, can then be expressed as:

$$\ln \left(\frac{p_1}{p_2} \right) = \frac{\Delta H_{ads}}{R} [\left(\frac{1}{T_2} \right) - \left(\frac{1}{T_1} \right)] \tag{2.2}$$

It should be emphasized that Eq. (2.2) can be applied only when the gas behaves like an ideal gas. In addition, Eq. (2.2) is valid when the impact of the adsorbed phase can be ignored. It is thus suggested that the foregoing equation is not applicable in cases where the impact of the adsorbed phase cannot be neglected or the gas behavior deviates from ideal gas. However, it is applicable in the low-pressure condition (Henry’s range).

Adsorption calorimetry can be utilized to directly determine the heat of adsorption since it measures the heat evolved (differential enthalpies of adsorption) when a certain amount of gas adsorbs onto the pore surface. For both theoretical and experimental reasons, adsorption calorimetry is the most suitable method to measure accurately the heat of adsorption, especially in micropore region.

2.3.2 Pore filling processes

At low relative pressures, in the pre-capillary condensation range of a physisorption isotherm, filling of micropores of width less than 2nm occurs (Figure 2.9). This process is referred to as primary micropore filling and is due to enhanced interactions between adsorbent – adsorbate in smaller pores. The impact of the wall extends to the centre of the pore due to overlapping of interaction with opposite walls. If the width of the pore falls within the ultramicropore range (pore width less than 0.7 nm), then the pore filling occurs at very low relative pressures. At higher relative pressures, a secondary process fills the wider micropores (pore width between 0.7 nm and 2 nm) extending into the multilayer region. Adsorbate molecules start to bind to already adsorbed molecules creating a continuous film of adsorbate. This film of adsorbate has a greater density when compared to the un-adsorbed fluid. The reason for this increase in density, is that the attractive force of the wall potential leads to close packing of the adsorbate. The saturation of gas storage is demonstrated by the smaller nanopores as a result of overlapping of the fields of opposite walls of the pores (Dubinin, 1960; 1975). For meso- and larger pores, the adsorbate gas molecules are adsorbed onto the surface of the pore wall in a mono- or multiple layers (Langmuir, 1916; Brunauer et al., 1938), as will be explained in Sections 2.3.3.1 and 2.3.3.2. In multilayer adsorption, more than one layer of molecules will accumulate over time whereas a small amount of adsorbed molecules come in direct contact with the adsorbent surface. In this case the overlapping effect disappears since the impact of the pore wall is negligible on the centre of the pore. Moreover, the densities between the bulk phase and the adsorbed phase in the pore space are more pronounced.

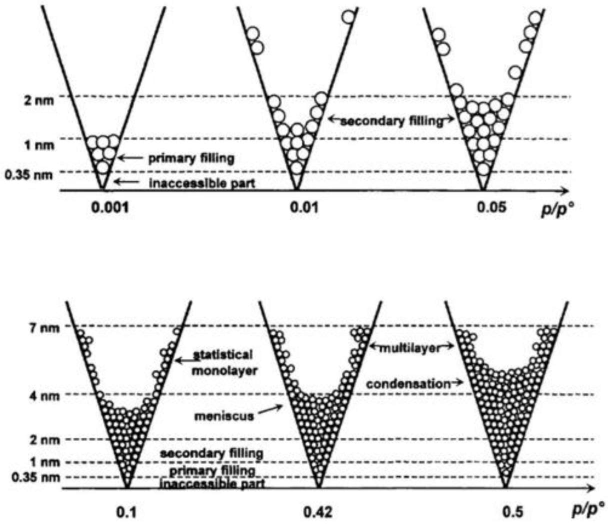

Figure 2.9 Successive filling of micropores and mesopores during adsorption (Rouquerol et al., 1999)

2.3.2.1 Langmuir Theory

The Langmuir isotherm (Langmuir, 1916) is the most widely used model because of its simplicity and effectiveness. The Langmuir equation was developed by Irving Langmuir and describes the dynamic equilibrium between the adsorbed phase and bulk phase. The model describes gas storage capacity on an adsorbent as a function of pressure at a given temperature. The model is based on certain assumptions. First, the Langmuir model assumes that the equilibrium has been reached, an assumption which plays a critical role in experimental conditions. Second, it is assumed that the adsorbent consists of definite number of active surface sites where each adsorbate molecule occupies one site on the adsorbent (localized adsorption). Third, the model is based on the assumption that the surface is homogeneous and flat. Hence, the adsorption sites are energetically equivalent (homogeneous) where the heat of adsorption is constant and independent of surface coverage. Fourth, the model assumes no lateral interactions between the adjacent adsorbed molecules. Lastly, the adsorption sites are identical and monolayer. This means that adsorbate molecules do not bind to already adsorbed molecules, and, thus adsorption only arises in a monolayer (Figure 2.10). The Langmuir isotherm can be expressed as:

$$\theta = \frac{q_e}{q_m} = \frac{bP}{1+bP} \tag{2.3}$$

where θ is the surface coverage, q_e is the amount adsorbed amount, q_m is the maximum adsorbed capacity (monolayer), P is the pressure, and b is an empirical constant related to heat of adsorption of monolayer and is assumed to be equal for all adsorption sites. The Langmuir isotherm can be expressed as:

$$b = A_o e^{\left(\frac{E_o}{RT}\right)} \tag{2.4}$$

where A_o is the prefactor, E_o is the activation energy, R is the universal gas content and T is the temperature. The shape of plot of Langmuir isotherm is similar to Type I isotherms (Figure 2.8). Eq. (2.3) can be written in the linear form as:

$$\frac{1}{q_e} = \frac{1}{q_m b}\frac{1}{\mathrm{P}} + \frac{1}{q_m} \tag{2.5}$$

Eq. (2.5) implies that if one plots $1/q_e$ versus $1/q_{m}$,, a straight line will be thereby obtained, whose intercept ($1/q_m$) and slope ($1/q_e$) are related to monolayer capacity and constant b, respectively. It should be mentioned that the specific surface area can be obtained by multiplying the capacity by the effective cross-sectional area of a single molecule. Langmuir's model reduces to Henry's model at the low limit pressure:

$$q_e = \lim_{P \to 0} \left(\frac{q_m bP}{1+bP} \right) = K_h P \tag{2.6}$$

where K_h is the Henry's constant. It should be noted that Henry's constant is a function of the binding energy and temperature and has a linear form.

The Freundlich equation which is one of the empirical equations of equilibrium data does not mathematically have Henry's law as a limit. In addition, it does not have a finite limit at high pressures. The Freundlich isotherm can be expressed as:

$$C_\mu = KP^{1/n} \tag{2.7}$$

where K and n are constants which depend on temperature.

Arri et al. (1992) extended the Langmuir isotherm for mixtures. The isotherm can be expressed as:

$$q_i = \frac{(q_s)_i b_i P_i}{1+\sum_{i=1}^{n} b_i P_i} \tag{2.8}$$

where q_{si} and b_i are the Langmuir constants for pure gas sorption. P_i is the partial pressure of adsorbate i and is given by Dalton's law of partial pressures:

$$P_i = Py_i \tag{2.9}$$

where y_i is the gas content of each component. It should be noted that no binary sorption constant is utilized and only the Langmuir constants are needed.

Numerous analyses of experimental data for gas in shale and coal have utilized the Langmuir model (Bustin and Clarkson, 1998; Yu et al., 2016; Tang et al., 2017). The model is routinely applied in modelling of the adsorption of methane in coal and shale for the estimation of the adsorbed methane at reservoirs of the shale gas industry and coalbed methane.

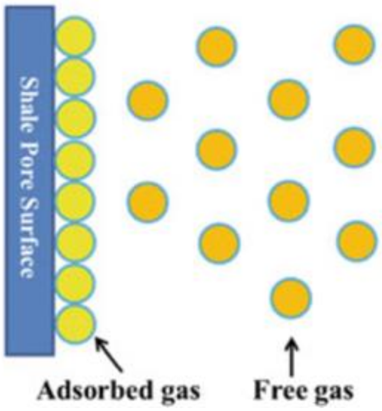

Figure 2.10 Schematic of Langmuir monolayer gas adsorption (Yu et al., 2014)

2.3.2.2 BET Theory

Brunauer, Emmet and Teller (BET) developed a theory of multilayer adsorption theory in 1938. The BET theory was based on the Langmuir model but also incorporated the concept of adsorption of gas molecules as multiple layers on a pore surface. As shown in Figure 2.11, additional adsorbate molecules can bind to already adsorbed molecules. The BET model was based on the assumption that the forces active for the condensation of gases are responsible for the binding energy in multilayer adsorption. Similar to the Langmuir model there are no lateral interactions between adjacent adsorbed molecules. Hence, molecules in second and subsequent layers interact with molecules vertically. In addition, the number of layers may approach infinity while the uppermost layer is in equilibrium with the vapor phase. In particular, it is assumed that molecules in the second and higher layers adsorb directly on top of previously adsorbed molecules. It should be noted that the van der Waals forces at the surface of the adsorbent are stronger when compared to the van der Waals forces between gas molecules. Subsequently, the heat of adsorption of the first layer will be greater than the higher layers. Except for the first layer, the additional layers will have equivalent heat of adsorption. The BET model is used for the interpretation of Type II isotherms and the reversible part of Type IV isotherms. In cases where the empirical constant is low, the BET model will also reproduce Type III and V isotherms. The BET isotherm can be expressed as:

$$\frac{q_e}{q_m} = \frac{Cx}{1-x}\frac{1-(N+1)x^N+Nx^{N+1}}{1+(C-1)x-Cx^{N+1}} \tag{2.10}$$

where N is the maximum number of adsorbed layers, x is the relative pressure, and C an empirical constant, expressed approximately by:

$$C \approx e^{q_1 - q_L/RT} \tag{2.11}$$

Where q_1 is the heat of adsorption and q_L is the latent heat of vaporisation of the adsorptive. When the empirical constant (C) exhibits low values (< 50), the shape of plot of BET isotherm is similar to Types III and V isotherms, while greater values are associated with Types II and IV isotherms. When N is equal to 1, then Eq. (2.10) reduces to the Langmuir equation. When N approaches infinity Eq. (2.10) reduces to the standard form of the BET equation:

$$\frac{x}{q_e(1-x)} = \frac{1}{q_m c} + \frac{C-1}{q_m C} x \tag{2.12}$$

Eq. (2.12) suggests that if one plots $x/[q_e(1-x)]$ against x, a straight line with the slope $(C - 1)V_m C$ and the intercept $1/ V_m C$ is expected. Hence, the monolayer capacity can be obtained. Similarly to Langmuir model, the surface area of the sample can also be determined by multiplying the capacity by the cross-sectional area of a single molecule.

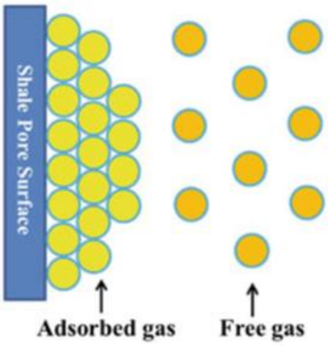

Figure 2.11 Schematic of BET multilayer gas adsorption (Yu et al., 2014)

For mesoporous materials, the range of linearity of the BET plot is limited to a certain part of isotherm, usually between 0.05 and 0.35 relative pressure. However, this relative range of BET plot is not applicable to complex materials with micropores, namely shale or coal.

2.3.2.3 Theory for adsorption on fractal surfaces

According to previous researchers (Yang et al., 2014; Sakhaee-Pour and Li, 2016; Li et al., 2019), the Frenkel-Halsey-Hill (FHH) model has been extensively used to quantitively characterize pore structure of shales. The fractal dimension of the pore wall is estimated via low-pressure nitrogen adsorption measurements such that:

$$\ln\left(\frac{V}{V_m}\right) = C_F + S\ln\left[\ln\left(\frac{P_0}{P}\right)\right] \tag{2.13}$$

where V is the equivalent volume of adsorbed gas at equilibrium pressure P, P_0 is the saturation pressure and V_m is the equivalent volume of gas in a monolayer. S is a power law exponent dependent on the surface fractal dimension (d), whereas the constant C_F is a pre-exponential factor.

Two limiting cases arise (Pfeifer and Liu, 1997): It has been determined that at the beginning of the multilayer build-up, the film-gas interface is subjected to van der Waal's forces, which act between the solid and the gas, thereby causing the film-gas interface to assume the same shape as the surface roughness. The value of the constant S is then given by:

$$S = \frac{d-3}{3} \tag{2.14}$$

However, generally for thicker surface films, the form of the interface is influenced by the gas-liquid surface tension, thereby causing it to migrate away from the surface, which eventually results in the reduction of the upper external surface area of the film. In this case, S is given by:

$$S = d - 3 \tag{2.15}$$

2.3.3 Mechanism of Capillary Condensation

Capillary condensation indicates the presence of a non-equilibrium process where the vapor phase in a porous medium condenses to a liquid like phase at a pressure p less than the saturation pressure p_o of the bulk liquid. As explained in Section 2.3.1 capillary condensation is often accompanied by hysteresis loops where a gap between two isotherm branches (i.e.

Type IVa and V isotherms) is observed (Haul, 1982). Since high Van der Waals forces exist between the particles in the capillary tube, less pressure is required for the condensation to occur.

Figure 2.12A, shows that gas molecules bind to the walls of the capillary tube due to adhesive forces. A multilayer adsorption is formed since more gas molecules enter the capillary tube (Figure 2.12B). Figure 2.12D shows that a meniscus has been formed at the liquid-vapour interface. Evaporation of the adsorbate occurs from the liquid meniscus leading to the formation of a hemispherical shape (Figure 2.12E). Typically, the contact angle for nitrogen is assumed to be zero and the curvature radius at that point is related to the pore radius (i.e. basis of the Kelvin equation). Figure 2.12F illustrates the formation of multilayer adsorption at low relative pressure, which is in equilibrium. At that point hysteresis does not exist.

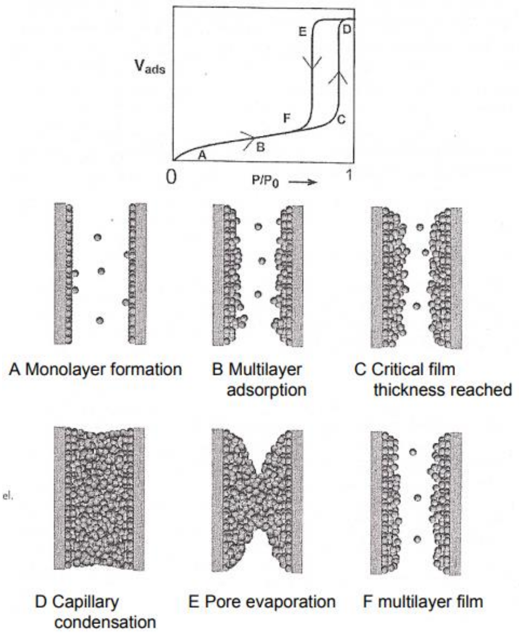

Figure 2.12 Mechanism of capillary condensation (Rouquerol et al., 1999)

Thommes et al. (2015) identified the major types of hysteresis loops (Figure 2.13). Each of these six characteristic types in Figure 2.13, are an extension of the original IUPAC classification of 1985, which included Types H1, H2(a), H3 and H4. In addition, these main types of hysteresis loops are closely related to particular characteristics of pore structure and adsorption mechanism.

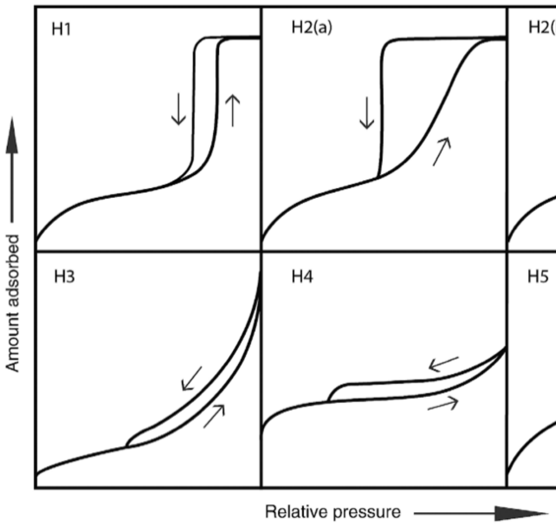

Figure 2.13 IUPAC classification scheme of Hysteresis Loops (Thommes et al., 2015)

For the Type H1 hysteresis loop, the network effect is minimal. In addition, the narrow and steep loop is an indication of delayed condensation on the adsorption branch. Hysteresis loops of type H1 are common in materials having uniform mesopores, namely, templated silicas, ordered carbons and controlled pore glasses. Hysteresis loop of Type H1 is also obtained in disordered silica where the onset of condensation in one pore sets off advanced condensation in rest (Hitchcock et al., 2014). In addition, Thommes and Cychosz (2014) observed that Type H1 hysteresis can also be found in pores where the width of the neck size distribution is similar to the width of the pore distribution (i.e. ink-bottle). In Type H2 hysteresis loop, the pore structure is more complex compared to Type H1. Moreover, the network effect is now more pronounced. In particular, the steep desorption branch in Type H2(a) loop is mainly due to cavitation-induced evaporation or pore blocking in pore necks with narrow width. For instance, desorption is delayed in ink-bottled shaped pores because the wide body of the pore will remain filled until the pore at the neck evaporates at lower vapor pressure. Thus, interconnected larger pores must empty through pores with a smaller diameter as a result of the pore network effect. Hysteresis loops of H2(a) is common in materials, such as porous glasses (i.e. vycor) and silica gels. In cases where materials consist of greater neck width, Type H2(b) is observed. Similarly to Type H2(a), the Type H2(b) loop is also related to pore blocking.

In the Type H3 loop, the adsorption branch is similar to a Type II isotherm while the lower limit of the desorption branch is situated at the cavitation induced relative pressure. Hysteresis loop H3 is mainly observed in non-rigid aggregates with slit-shaped pores (i.e. clays) where the pore network (usually macropores) is not completely filled with gas condensate.

In hysteresis loops of Type H4, the two branches are horizontal and parallel over a wide range of relative pressure. In particular, the Type H4 loop is a combination of Type I and II isotherms. At low relative pressure the gas uptake is related to the filling of the micropores. Type H4 loops commonly arise for mesoporous zeolites and micro-mesoporous carbons. Lastly, the Type H5 loop is common in pore structures which include open as well as blocked mesopores (e.g. plugged hexagonal templated silicas). However, this type of hysteresis loop is rare.

In general, condensation of gas in pores with different diameters will occur at different pressures, implying the pore size distribution of the sample. Sudden closure of the desorption branch at a relative pressure (i.e. Tensile strength effect) between 0.35 and 0.45 indicates the presence of pores with width less than 4 nm (Groen et al., 2003). The reason for this sudden disappearance of the hysteresis is that surface tension forces are stronger than the tensile strength of the liquid, leading to spontaneous evaporation of the bulk liquid and collapse of the hemispherical meniscus.

It is thus reasonable to consider hysteresis loops can be a useful source regarding pore shape and width. However, it is challenging to characterize materials with pore size distribution of narrow mesopores and micropores, since the Kelvin equation cannot be applied. The reason for this, is that the Kelvin equation is derived using bulk thermodynamics and there are limitations when applied to pores where the adsorbate density becomes greater than the bulk gas phase (i.e. walls overlap substantially). In these cases, microscopic treatments, namely molecular simulation models and density functional theory (DFT) can bridge the gap between macroscopic approaches and molecular level.

2.3.4 DFT Theory

Previous researchers (Landers et al. 2013) have shown that the Kelvin-Cohan equations cannot be applied to pores of width less than 20 nm. However, other researchers (Kruk et al., 1999) have suggested that, with minor corrections, it can describe accurately pore size distribution down to a few nanometers. At the time of writing, the most widely-used models are based upon density functional theory (DFT). Seaton et al. (1989) first reported the pore size distribution from nitrogen adsorption isotherms on porous carbons, using DFT theory. The theory was formed on the basis of the local mean field approximation (Evans and Tarazona, 1984; Evans et al., 1985; Evans et al., 1986).

The general basic procedure of DFT is described as follows. DFT can be used to estimate adsorption for pores of a particular surface chemistry, geometry and size, at a particular pressure. The density profile from DFT is converted to an amount adsorbed at the molecular level, and thus describing efficiently the sorption behavior of inhomogeneous fluids confined to porous media. It is important to mention that this procedure is repeated for different pressures, leading to the construction of a full isotherm for a particular size. Once this procedure is completed for a single characteristic size, it is repeated for a variety of pore sizes. The complete series of theoretical isotherms for various pore sizes, of a specific surface chemistry and geometry, is called the "kernels". Afterwards, the kernels are fitted to the experimental isotherm in order to obtain the pore size distribution of a porous material. Despite the fact that kernels determine the fluid-solid interaction potential, they can be used as a reference for a particular class of adsorbent/adsorptive system. Different DFT kernels (e.g. slit, cylinder, spherical) have been developed for materials such as silicas, carbons and zeolites.

The pore size distribution function *f(D)* depends on a solution of the general adsorption isotherm (GAI) equation. The GAI relates the kernel of the theoretical sorption isotherms to the experimental sorption isotherms. The GAI is given by the expression:

$$N\left(\frac{p}{p_0}\right) = \int_{D_{min}}^{D_{max}} N\left(\frac{p}{p_0}, D\right) f(D) dD \qquad (2.16)$$

where $N(P/P_o)$ is the experimental sorption isotherm data, D is the diameter of the pore, $N(P/P_0, D)$ is the kernel of the theoretical isotherms of different pore width D, and $f(D)$ is the PSD function, and D_{max} and D_{min} are the maximum and minimum pore sizes in the kernel, respectively.

A further improvement was the non-local density functional theory (NLDFT). Lastoskie et al. (1993) was the first to utilize NLDFT to initially estimate simple slit geometries for activated carbon. Despite the fact that NLDFT theory enhanced the accuracy of pore size distribution for microporous materials, the theory was based on smooth density approximation (Landers et al. 2013; Lowell, 2004; Thommes et al., 2015). This means that NLDFT assumes that the surface of the pores is flat and homogeneous, leading to spurious step-like multilayer build-up and artificial gaps in the PSD. Hence, NLDFT is not representative for real materials with heterogeneous chemistry and surface roughness, which tend to have smooth build-up of adsorbate. In particular, for pores with width less than 5 nm, NLDFT isotherms deviate from the experimental adsorption isotherms since the NLDFT does not account for the nucleation phenomenon (Landers et al. 2013). For pores below the hysteresis critical pore size (~ 4nm), capillary condensation becomes reversible and matches the equilibrium kernel.

Quenched solid density functional theory (QSDFT) incorporated the impact of pore wall surface roughness and heterogeneity to address this issue. In particular, the inner part of the pore wall has a constant gradient in solid density with roughness parameter δ. The parameter δ is equal to the half-width of the molecular level geometrical heterogeneity of pore walls, known as the “corona”. The roughness parameter δ can be either approximated by using XRD data or as a free-fitting parameter. A complete description of the equation can be found in Landers et al. (2013). Therefore, QSDFT theory is suitable for pore size analysis of geometrically and chemically disordered silicas/zeolites and carbons. The solid density profile equation can be found in Landers et al. (2013). In QSDFT, the parameters of solid-fluid potential are different compared to NLDFT, since different approaches were proposed for accounting for intermolecular interactions. For instance, in QSDFT, the pairwise Lennard-Jones (LJ) potentials were applied, instead of Steel potential in NLDFT carbon kernels and integrated LJ potentials in NLDFT silica kernels. Consequently, the PSD might not be comparable.

2.4 Multiple Mechanisms of gas flow in shales

Mass transport models based upon conventional continuum flow equations (i.e. Darcy’s law) neglect certain gas transfer mechanisms that exist within the matrix of shale gas reservoirs (SGRs) (Figure 2.14). Hence, gas production from SGRs may be significantly overestimated, or underestimated, when the apparent permeability, which is the transport parameter that includes provision for these additional mechanisms, is not used. The reason that standard mass transfer models cannot be utilized for predicting the physics of fluid flow in shale reservoirs is due to the presence of organic matter and particular nano-scale phenomena. Previous studies have indicated that organic matter contributes approximately 40% of the total gas volume (Firouzi et al., 2014; Xiong et al., 2017). Moreover, the diameter of nanopores is comparable to the order of the gas molecular mean free path at reservoir conditions. Consequently, increased consideration has been given to modify the continuum flow, or Darcy flow, by coupling with additional different mass transfer mechanisms to accurately predict gas production in SGRs. The gas transfer mechanisms, occurring within the matrix of SGRs, include both bulk gas transfer and surface diffusion mechanisms. Previous researchers (Wu et al., 2016, 2015; Wang et al., 2016a) established approaches to articulate the mass transfer processes in the nanopores of SGRs.

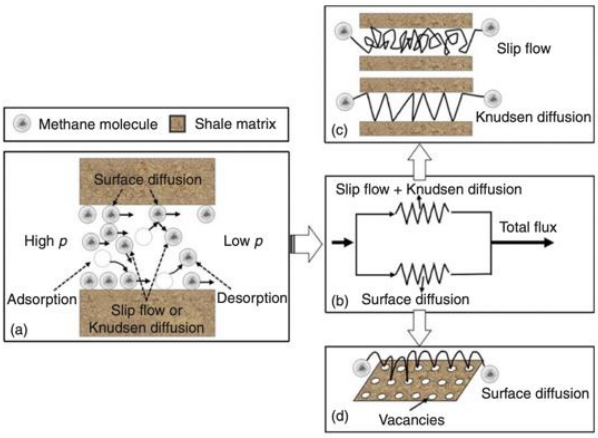

Figure 2.14 Schematic diagram of gas transfer mechanism in nanopores of shale gas reservoirs (Wu et al., 2015)

2.4.1 Continuum Flow of Free Gas

Continuum no-slip flow, or Darcy flow, occurs when the Knudsen number (Kn) < 10^{-3}. The collisions between molecules then dominate, and, thus the gas flow is continuum flow, which can be expressed according to the Hagen-Poiseuille equation (Choi et al., 2001):

$$J_v = -\zeta_{mb} \frac{r^2 P}{8\mu RT} \frac{\mathrm{d}p}{\mathrm{d}l} \tag{2.17}$$

where

$$\zeta_{mb} = \frac{\varepsilon}{\tau} \tag{2.18}$$

where J_v is the continuum-flow, ζ_{mb} is a dimensionless correction factor of apparent permeability, μ is the gas viscosity, P is the pressure, l is the gas transport distance, T is the temperature, ε is the porosity, τ is the tortuosity, and r is the nanopores radius.

2.4.2 Slip Flow of Free Gas

Slip flow occurs when $10^{-3}<Kn<10^{-1}$, where gas molecules slip on the nanopore wall. In this case, both the intermolecular collisions, and collisions between gas molecules and nanopore walls, are similarly dominant. The slip boundary condition was achieved by modifying the no-slip boundary condition in continuum flow (Karniadakis et al., 2005):

$$J_{vs} = -\frac{1}{1+Kn}\zeta_{mb}\omega_s\omega_m\frac{r^2P}{8\mu RT}(1+\alpha Kn)\left(1+\frac{4Kn}{1-\psi Kn}\right)\frac{\mathrm{d}P}{\mathrm{d}l} \tag{2.19}$$

where

$$\omega_m = \left[1+\frac{(\alpha_f-\alpha_s)}{(1+Kn_{avg}/E_s)}\frac{s(p-p_{\mathrm{int}})}{b_{\mathrm{int}}E_s}\right]^3 \tag{2.20}$$

and

$$\omega_s = \left[1-\frac{3}{\phi}\frac{\varepsilon_L p_L(p-p_{\mathrm{int}})}{(p+p_L)(p_{\mathrm{int}}+p_L)}\right]^3 \tag{2.21}$$

where ψ is the dimensionless gas-slip constant (takes a value of -1), α the dimensionless rarefaction coefficient, ω_m is the poromechanical response coefficient and ω_s is the sorption-induced swelling response coefficients of the shale matrix. a_f is the dimensionless Biot's number for microfracture, a_s is the dimensionless Biot's coefficient for shale matrix, E_s is the shale matrix Young's modulus, Kn_{avg} is the average microfracture normal stiffness, b_{int} is the initial microfracture aperture, p_{int} is the initial pressure, ε_L is the dimensionless Langmuir strain and p_L is the Langmuir pressure. According to previous molecular-simulation results (Karniadakis et al., 2005), the relationship between the Knudsen number and the rarefaction coefficient is depicted in Figure 2.15.

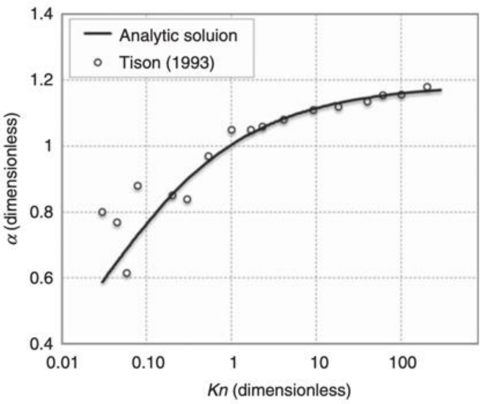

Figure 2.15 Experimentally data (symbols) conducted by Tison (1993) and fits to molecular simulation results (Karniadakis et al., 2005)

2.4.3 Knudsen Diffusion of Free Gas

Knudsen diffusion arises for Kn≥1, when collisions between gas molecules and nanopore walls dominate. Assuming that the pore is circular in cross-section, with a radius *r*, and taking into account the wall roughness, the Knudsen equation can be expressed as (Choi et al., 2001; Darabi et al., 2012):

$$J_k = -\frac{1}{1+1/Kn}\frac{2}{3}\zeta_{mb}\,\omega_s\omega_m r\delta^{D_f-2}\left(\frac{8}{\pi RTM}\right)^{0.5}\frac{\mathrm{d}P}{\mathrm{d}l} \tag{2.22}$$

where

$$D_k = \frac{2}{3}\zeta_{mb}\left(\frac{8RT}{\pi M}\right)^{0.5} \tag{2.23}$$

where D_k is the Knudsen diffusion coefficient, δ the ratio of the gas molecule diameter, D_f is the fractal dimension of the pore wall and *M* the gas molar mass. Researchers have shown the importance of Knudsen diffusion to the pore transport mechanism in nanopores and a study conducted by Darabi et al. (2012) showed that Knudsen diffusion contributes around 20% of the total produced gas at typical SGR conditions.

2.4.4 Surface Diffusion of Adsorbed Gas

Surface diffusion plays a significant role in mass transport within the nanopores of shale, wherein there is organic matter with a large surface area, and, thence, in the overall gas mass transfer (Etminan et al., 2014; Fathi and Akkutlu, 2014; Xiong et al., 2017; Kang et al., 2011). Experimental investigations have also indicated that, in comparison to bulk gas transport, surface diffusion, is more significant where the pore network is not yet well-evolved within shale gas reservoirs (Rigby and Gladden, 1999; Rigby, 2003a). During gas phase mass transfer in nanopores, the surface diffusion of adsorbed gas is characterised by a large concentration gradient, which plays a crucial role in this process (Darabi et al., 2012). Surface diffusion is a physical process that entails a random hopping mechanism, such that the adsorbed particles periodically escape from, and move between, lower-energy adsorption sites. The activated molecules can, thence, jump between fixed sites with a specific velocity, which leads to surface migration in the adsorbed phase. Once a molecule acquires enough energy to fully escape from the surface, it returns to the gaseous state.

2.4.4.1 Surface diffusivity at low pressure

Previous studies have shown that it is more appropriate to investigate shale gas sorption by using the Langmuir isotherm which is based on single-layer adsorption (Cui et al., 2009; Ambrose et al., 2010). Thus, the hopping model can be most appropriate to surface diffusion of adsorbed gas in shales. Various researchers established different classical hopping models. For instance, a widely used analytical model was developed by Hwang and Kammermeyer (1966) and Guo et al. (2008) for low-pressure conditions where the equation of the surface diffusion coefficient is influenced by temperature, adsorbent and adsorbate.

$$D_s^0 = \Pi T^m \exp\left(-\frac{\mathrm{E}}{RT}\right) \tag{2.24}$$

where

$$E = \Delta H^{0.8} \tag{2.25}$$

where E is the gas activation energy, Π is the constant that relates to gas molecule weight, ΔH is the isosteric heat of adsorption and m is a dimensionless constant which takes a value of 0.5.

It should be emphasized the combination of Eqs. (2.24) and (2.25), experimental data for methane/activated-carbon adsorption was fitted to obtain the surface diffusion coefficient (Guo et al., 2008):

$$D_s^0 = 8.29 \times 10^{-7} T^{0.5} \exp\left(-\frac{\Delta H^{0.8}}{RT}\right) \tag{2.26}$$

2.4.4.2 Surface diffusivity at high pressure

The impact, on surface flow of surface occupancies above the zero limit, was obtained using the Chen and Yang (1991) model. These authors established a surface diffusion model describing the influence of adsorbed-gas coverage from a hopping model. In particular, a kinetic method was applied to derive the surface diffusion coefficient under a high-pressure condition such that:

$$D_s = D_{so} \frac{(1-\theta)+\frac{k}{2}\theta(2-\theta)+[H(1-\kappa)](1-\kappa)\frac{k}{2}\theta^2}{\left(1-\theta+\frac{\kappa}{2}\theta\right)^2} \tag{2.27}$$

$$H(1-\kappa) = \begin{cases} 0, & \kappa \geq 1 \\ 1, & 0 \leq \kappa \leq 1 \end{cases} \tag{2.28}$$

$$\kappa = \frac{\kappa_b}{\kappa_m} \tag{2.29}$$

where D_s is the gas surface diffusion coefficient, θ is the dimensionless gas coverage; $H(1-\kappa)$ is the dimensionless Heaviside function, κ is the ratio constant for blockage to the rate constant for forward migration and takes a value of 0.5 (Wu et al., 2015), κ_b and κ_m are the coefficients for surface-gas molecules for the blocking velocity and forward velocity, respectively.

2.5 Summary

From the literature reviewed, the EOR technique that is gaining prominence in recent years, is CO_2 gas injection. The reason that CO_2 injection is an attractive method, is mainly due to the increasing pressure for countries to reduce their emissions of greenhouse gases (i.e. CO_2). Subsequently, CO_2 can be utilized as a means to address the challenge of greenhouse gas emissions by sequestering carbon, mainly in shales. Despite the fact that CO_2 injection is an environmentally friendly technique, it is also an efficient method for oil and gas recovery, especially in medium to light oil reservoirs. In particular, implementation of CO_2 injection in oil reservoirs promotes oil swelling and reduces the oil viscosity. Hence, residual oil becomes more mobile and flows easier to the production wells. However, previous studies have determined a distinct limitation that needs to be considered. For instance, continuous CO_2 injection produces an early CO_2 breakthrough (BT) due to viscous fingering and gravity overriding. This results to leaving large areas of the reservoir unswept. To overcome this problematic behavior of CO_2, CO_2-WAG process is applied to effectively control the mobility of the injected CO_2 by reducing the gas relative permeability. As a result, gas BT is delayed in the production wells.

There has been a paradigm shift in thinking towards shale gas production to relieve the pressure exerted on conventional resources. Gas adsorption phenomenon plays a major role in shale gas reservoirs since a significant portion of the total gas volume exists in the adsorbed state (20% - 80%). The isotherm equations presented are utilized to efficiently describe adsorption data in shale reservoirs. Moreover, the isotherm shape and hysteresis pattern are closely related to pore sizes and pore structures. The BET equation, building upon the Langmuir equation, is the most popular equation for determining the surface area of porous solids. When condensation occurs in reduced relative pressures (0.4-0.995), the Kelvin equation is applied for the determination of pore size distribution as well as pore width. However, Kelvin equation is only valid down to approximately 10nm and is not used to characterize systems with pore size distribution including narrow mesopores and micropores, such as shales. Thus, models based upon DFT theory were developed to determine both mesoporosity and microporosity. Furthermore, the Clausius-Clapeyron (CAC) method may lead to an overestimation of isosteric adsorption heat since it utilizes the ideal gas law and assumes that the heat does not depend upon temperature. Hence, adsorption calorimetry is the most suitable method to precisely measure heats of adsorption.

This chapter has presented the mass transfer processes within shale-gas reservoirs compared to conventional gas reservoirs. Previous researchers have modified the continuity equation, or Darcy equation, to include the gas transfer regimes in SGRs. The gas transfer regimes in SGRs include bulk gas transfer as well as surface diffusion mechanisms. The Knudsen diffusion in the bulk gas transfer regime, contributes significantly to the total produced gas (~20%) at typical SGR conditions and should not be overlooked. Previous experimental investigations have also shown that surface diffusion probably plays the major role because of the greater amount of adsorbed gas, especially within the abundant nanopores within the organic matter of shale gas reservoirs. Subsequently, surface diffusion of adsorbed gas and the Knudsen diffusion of the free gas, can increase the apparent permeability of the SGRs. Hence, these regimes should not be omitted to ensure accurate prediction of shale gas recovery.

3. Chapter Three: Experimental and Numerical Methods

3.1 Introduction

Shales are unconventional gas systems which have the potential to be the major source of natural gas across the globe. The surface area and pore size distribution in the shale matrix (predominantly composed of micro- to meso-pores) are significant parameters for assessing gas adsorption capacity and gas-transport mechanism in shales. As outlined in Section 2.3 of Chapter 2, gas molecules in shale reservoirs are present as free state and/or as adsorbed state in the pore media, where the latter state makes up the larger part of the total gas volume. Elucidating the pore structure and surface area of shales via gas adsorption experiments is important in comprehending the gas-in-place for these plays and modelling gas flow in shale matrix. Carbon dioxide (CO_2) injection method can be utilised as a means of both enhancing gas recovery from shales and sequestering carbon, as explained in Section 2.2.2.3. Greater mobility of CO_2 within the shale matrix improves the displacement efficiency of the originally present CH_4, as well as, increasing the CO_2 penetration of the shale formation. Hence, CO_2 uptake kinetics in the shale matrix provides a key criterion for numerically simulating CO_2 injection in field applications. Furthermore, shale gas reservoirs consist of natural fractures which are of major importance in hydraulic fracture propagation and gas production. In order to simulate the fluid flow in fractured reservoirs mathematical formulations need to be applied via a reservoir simulator. This Chapter primarily contains experimental methods to obtain surface area, pore size distribution and gas uptake kinetics prior to reservoir simulating shale reservoirs. Thereafter, this Chapter presents numerical reservoir application and the summary of the methodology employed to accurately simulate fluid flow in fractured shale gas reservoirs.

3.2 Experimental Methods

Gas adsorption techniques are widely used to characterize the pore structure and surface area of fine microporous materials (i.e. zeolites, activated carbons, catalysts etc.) and powders. Various gases, namely nitrogen, argon and carbon dioxide are used to quantify the interaction processes at the gas/liquid-shale interface. The accurate measurement of an equilibrium isotherm is essential for the determination of surface area, pore size distribution or other parameters estimation from gas sorption. In certain machines, gas uptake kinetics can also be obtained for each isotherm data point as will be explained later in Section 3.2.2. In order to ensure that each individual point in the isotherm has reached equilibrium, enough time is allowed for the adsorptive to enter the void space. In general, gas sorption isotherms are obtained via a pressure table which consists of a set of pressure points. The capabilities of the machine used will determine the range of these pressure points. The majority of sorption measurements are conducted via volumetric or gravimetric methods.

3.2.1 Volumetric Analysis

The volumetric method provides a way to estimate the surface area and pore size distribution. Figure 3.1 illustrates a schematic diagram of a generic volumetric adsorption analyzer. In particular, the adsorptive gas supply valve is initially closed while the sample and vacuum valves open. Subsequently, the manifold and sample tube are evacuated (degassed). The reason for the degassing procedure is due to the fact that the adsorbents (i.e. shales, coals) adsorb contaminants from the air when exposed to the atmosphere. Typically, heat is applied to the sample tube to enhance the contaminant desorption process. Once vacuum is achieved, the vacuum and sample valves close simultaneously. Then, the cold bath reservoir is raised bringing the sample to the analysis temperature. The adsorptive gas supply valve opens to charge the manifold to a pressure which is above vacuum. In that way the instrument is ready to dispense a dose of adsorptive onto the sample. The known quantity of gas added in the manifold is determined from the universal gas law. Afterwards, sample valve is opened to allow gas to enter the sample tube. Thus, the dosing cell is connected to the uptake cell which contains the adsorbent (i.e shale, coal). Equilibration pressure and adsorption quantity are calculated once the pressure is stabilized. It should be mentioned that pressure is monitored at all stages throughout the experiment.

The total number of moles in the system before and after the sample valve is opened, can be expressed respectively as:

$$n_{Tot} = (V_u - V_S)\frac{P_{uo}}{z_u R T_u} + V_d \frac{P_{do}}{z_d R T_d} + V_S q_0^{ex} \tag{3.1}$$

$$n_{Tot} = (V_u - V_S)\frac{P_{u1}}{z_u R T_u} + V_d \frac{P_{d1}}{z_d R T_d} + V_S q_1^{ex} \tag{3.2}$$

where P_{uo} is the pressure in uptake cell before valve is opened, P_{u1} is the pressure in uptake cell after valve is opened, P_{do} is the pressure in dosing cell before valve is opened, P_{d1} is the pressure in the dosing cell after the valve is opened, q_{ex} is the excess adsorbed phase concentration, V_s is the volume of solid, and V_u is the volume of uptake cell. It should be noted that the non-accessible (dead) volume of the adsorbent has been estimated by charging the system with a known amount (moles) of non-adsorbing gas, such as helium. In that way, the excess amount adsorbed is estimated. In particular, the excess mass of gas adsorbed is equal to the mass of the adsorbed layer minus the mass of an equivalent volume of non-adsorbed gas (helium). As discussed in Section 2.3.4 of Chapter 2, the excess amount adsorbed is due to the Van der Waals' forces. Notably, excess adsorption may be considered equal to the absolute adsorption at low pressures (< 10 bar) since the difference between the two quantities is of the order of less than one percent (Myers and Monson, 2014).

In cases where the temperature of the reservoir bath is different from the ambient temperature, the temperature profile varies along the sample tube. The reason for this, is that one portion of the sample tube is at ambient temperature, and another is at the temperature of the cold bath (i.e. liquid nitrogen). In order to characterize the sample tube volume with regard to "warm" and "cold" temperature, a free-space measurement of the sample tube is typically conducted at ambient temperature and the temperature of the reservoir bath. Consequently, the quantity of gas remaining in the sample tube as well as in the manifold volume can be accurately estimated through the universal gas law.

Once the point on the isotherm is estimated, the sample valve closes while the adsorptive gas supply valve re-opens and charges the manifold to a pressure higher than P_{u1}. The dosing and equilibration processes are repeated over a number of cycles until the analysis pressure is near the saturation pressure. At that point, the desorption isotherm is measured by a stepwise reduction in pressure where the physically adsorbed molecules will desorb from the adsorbent.

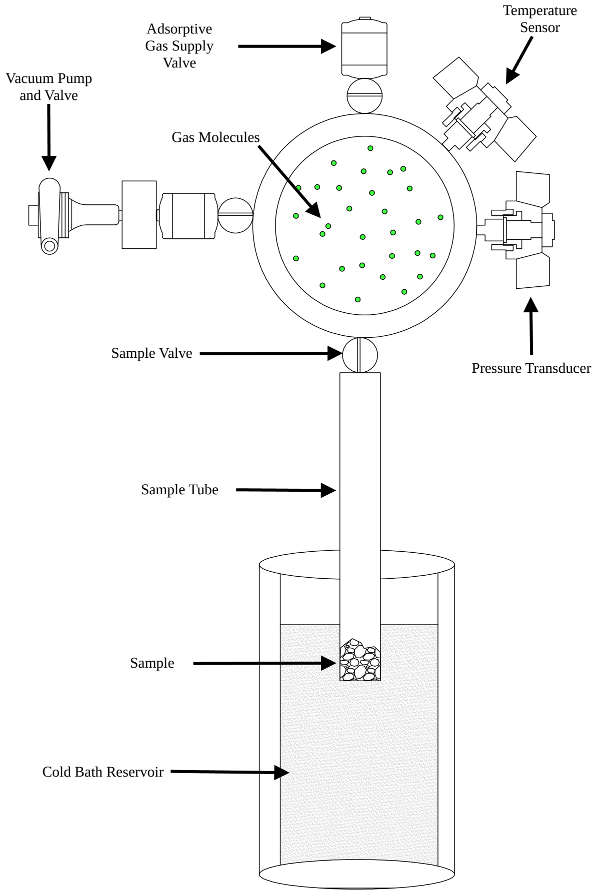

Figure 3.1 Schematic diagram of the Micromeritics 3Flex volumetric analyser

3.2.2 Gravimetric Analysis

In addition to volumetric analysis, suitable for structural characterization, gravimetric analysis is used to obtain information on mass transport. A Hiden XEMIS (gravimetric apparatus) was used to obtain kinetic gas uptake data against time, and a schematic diagram of this apparatus is shown in Figure 3.2. The XEMIS microbalance by Hiden incorporates a magnetically coupled balance which allows operation at high pressures (200 bar) and over a broad temperature range (77-77 3K). Due to the symmetric design, buoyancy effects are reduced, and measurement accuracy is improved. A pair of admit and exhaust valves are used to regulate the pressure. Similar to volumetric analysis, adsorbents (i.e. shales, coals) are initially degassed at elevated temperatures (110 ^{o}C) to remove excess moisture and contaminants from the air. The vacuum system includes an oil-free backing pump which reduces the system pressure down to 10^{-8} bar. Subsequently, a water bath is raised to reach the required temperature and adsorptive gas is dosed onto the sample in controlled increments via the admit valve. The pressure is equilibrated and excess mass of gas adsorbed is estimated after each step of dosing increment. It is essential to ensure that enough time is allowed for each individual data point in the isotherm to reach equilibrium. The XEMIS is equipped with multiple sensors to accurately measure high (up to 200 bar) and low pressures (up to 1 bar).

In addition, the control system provides the interface to Hiden's HIsorp software which has real-time processor functions. Hence, it is possible to observe whether equilibrium has been reached and analyze experimental data against time. In a gravimetric system the force acting on the sample is measured. Thereafter, the amount adsorbed is determined via a force balance wherein the buoyancy forces acting on the microbalance components must be corrected for. Table 3.1 shows a summary of the components within the XEMIS microbalance. These components are constructed from materials with known densities.

The sample's buoyancy is governed by Archimedes' principle, which states that the upward buoyant force exerted on the sample immersed in a fluid, is equivalent to the volume of the displaced fluid. Archimedes' principle can be expressed as:

$$F_b = -V_i \rho_g g = -\frac{m_i}{\rho_i} \rho_g g(T, P) \tag{3.3}$$

where F_b is the buoyant force, V_i the volume of the object, ρ_g the density of the gas surrounding the sample at known temperature and pressure, and g the gravitational acceleration. NIST refpropo database was utilized to determine the gas phase density.

The general force balance applied to correct the buoyancy forces acting on each microbalance component is expressed as:

$$\text{balance reading} * \text{g} = \sum_i m_i * g(\text{ sample side }) - \sum_j m_j * g(\text{ counterweight side }) \tag{3.4}$$

$$\begin{aligned}\text{balance reading} = {} & \sum_{i=1} m_i - \sum_{j=1} m_j - \sum_{i=1} \frac{m_i}{\rho_i} \rho_g(T_i, P) + \sum_{j=1} \frac{m_j}{\rho_j} \rho_g(T_i, P) \\ & + m_s + m_a - \frac{m_s}{\rho_{s(T_s)}} \rho_g(T_i, P) - \frac{m_a}{\rho_{a(T_a)}} \rho_g(T_i, P) - C_f(T_s, P)\end{aligned} \tag{3.5}$$

where m_s is the mass of the sample, m_a is the mass of the adsorbed gas and C_f is a balance correction factor for nonideal changes.

Table 3.1 Xemis microbalance components applied for buoyancy correction

Subscript	Component	Material
s	Sample	Variable
a	Gas	Variable
i1	Sample container	Pyrex
i1	Lower hangdown wire	Tungsten
i3	Upper hangdown chain	22 Ct. gold
i4	Sample side balance hook	Tungsten
j1	Counterweight (CW)	316 SS
j2	CW hook	Tungsten
j3	CW hangdown chain	22 Ct. gold
j4	CW balance hook	Tungsten

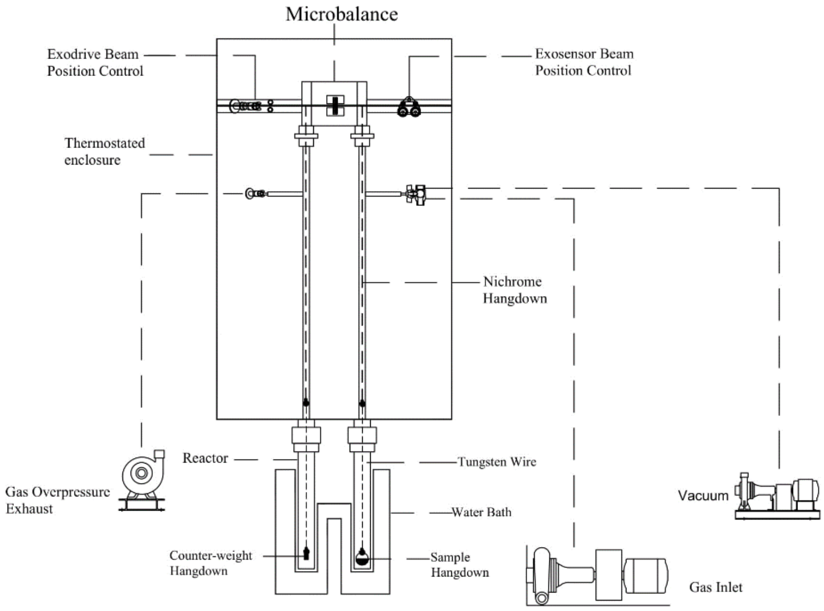

Figure 3.2 Schematic diagram of the Xemis gravimetric analyser

A typical example of gas uptake data against time in shale sample, obtained via XEMIS gravimetric apparatus, is shown in Figure 3.3. It should be noted that the pressure has reached equilibrium. Hereafter, the temperature variation which is closely related with the diffusivity should be examined. When adsorbate enters the sample container most of the gas is likely to be adsorbed. This means that there will be an exotherm due to the adsorption phenomenon, as highlighted in Section 2.3.1 of Chapter 2. In cases where the heat does not escape the sample, a steep rise in temperature, and, thus in the diffusivity can be observed. This rise in temperature leads to two different diffusion components in the gas uptake data, a fast uptake followed by a slower uptake.

Typically, a variety of equations can fit the gas uptake data. Notably, the Linear Driving Force (LDF) model (Do, 1998) is the most widely used model to approximate the solution to the diffusion equation. The model can be expressed as:

$$\frac{M(t)}{M(\infty)} = 1 - \exp\left(-kt\right) \tag{3.6}$$

where $M(t)$ is the measure of uptake at time t, $M(\infty)$ is the amount adsorbed at infinite time, and k is the mass transfer coefficient.

Nonetheless, certain samples may experience some sort of patchwise heterogeneity, implying two different media for adsorption. For this reason, a composite LDF model may be implemented to better fit the gas uptake data:

$$\frac{M(t)}{M(\infty)} = p\big(1 - \exp\left(-k_1 t\right)\big) + (1-p)\big(1 - \exp\left(-k_2 t\right)\big) \tag{3.7}$$

where p is the fraction of component 1.

In cases where the LDF model cannot fit the uptake data, a more complex analysis is utilized (Crank, 1975). In particular, Crank (1975) proposed spherical as well as cylindrical geometry solutions to the diffusion equation which give the rate of uptake at time t. The cylindrical geometry solution to the diffusion equation is given by:

$$\frac{M_{\mathrm{t}}}{M_\infty} = 1 - \sum_{n=1}^{\infty} \frac{4\alpha(1+\alpha)}{4+4\alpha+a^2 q_{\mathrm{n}}^2} \exp\left(-D q_n^2 t/a^2\right) \tag{3.8}$$

where a is the characteristic diffusion length (radius) of the cylindrical adsorbent, and q_n are positive non-zero roots of:

$$\alpha q_n J_o(q_n) + 2J_1(q_n) = 0 \tag{3.9}$$

The spherical geometry solution to the diffusion equation is given by:

$$\frac{M_t}{M_\infty} = 1 - \sum_{n=1}^{\infty} \frac{6\alpha(1+\alpha)}{9+9\alpha+a^2 q_n^2} \exp\left(-D q_n^2 t/a^2\right) \tag{3.10}$$

where a is the characteristic diffusion length (radius) of the spherical adsorbent, and q_n are positive non-zero roots of:

$$\tan\, q_n = \frac{3q_n}{3+\alpha q_n^2} \tag{3.11}$$

It should be noted that the foregoing equations are suitable for homogenous samples.

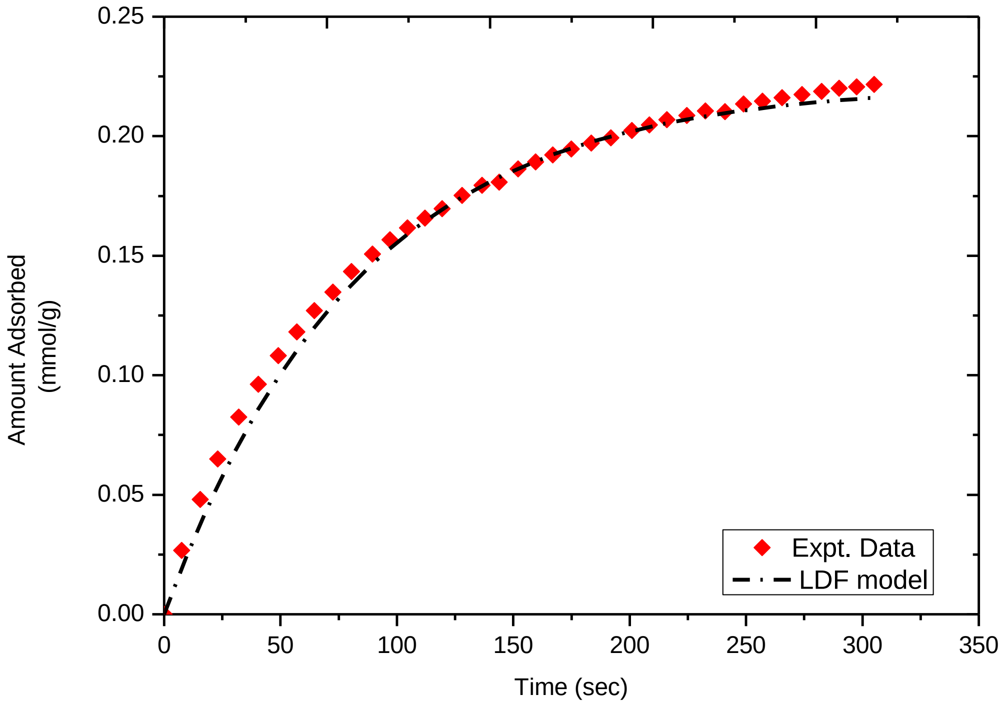

Figure 3.3 Experimentally measured (symbols) uptake curves, and fits to the LDF model (dashed lines) for the Marcellus shale 7834-7837 ft

3.3 Numerical Modelling

Reservoir simulators are constructed using a set of mathematical equations that govern the flow of fluid within porous media. These mathematical equations are in the form of strongly non-linear partial differential equations (PDEs). In order to establish a correlation between the fluid, the porous medium, and the system's flow conditions, these PDEs are formulated according to physical principles (i.e. equation of state, continuity equation etc.). Due to the analytical intractability of these equations, they must be solved numerically. This entails discretizing the equations in order to find an approximate solution on the finite set of difference points (i.e. mesh or grid points). In addition, a system of algebraic equations replaces the PDEs since they are more easily solved. The discretization of any PDE can be achieved via three techniques, namely the Finite Difference or Taylor series method, the Spectral or the Variational method, and the Finite Volume or the Integral method (Aziz and Settari, 1979). Of all these methods the finite difference method is usually applied in reservoir simulations (Appau et al., 2019).

3.3.1 Modeling of Shale Gas Reservoirs

Mass transfer processes within organic-rich shale gas reservoirs (SGRs) are significantly different compared to conventional reservoirs, as explained in Section 2.3 of Chapter 2. The main reason is that gas in conventional reservoirs migrates into porous and permeable rock formations. In particular, conventional gas has migrated from a source rock (unconventional reservoir) and is trapped under a seal. By contrast, with unconventional gas, the source rock (i.e shale) where gas is trapped, has low porosity and extremely low permeability (Figure 3.4). The poor permeability in shale reservoirs implies that gas, either free in natural fractures or adsorbed on the surface of shale matrix, is unable to flow through the porous media easily. A combination of horizontal drilling and artificial stimulation techniques, such as multi-stage hydraulic fracturing, is applied to enhance gas flow by improving reservoir permeability. In order to capture all the processes and simulate the fluid flow in fractured reservoirs, mathematical formulations were applied.

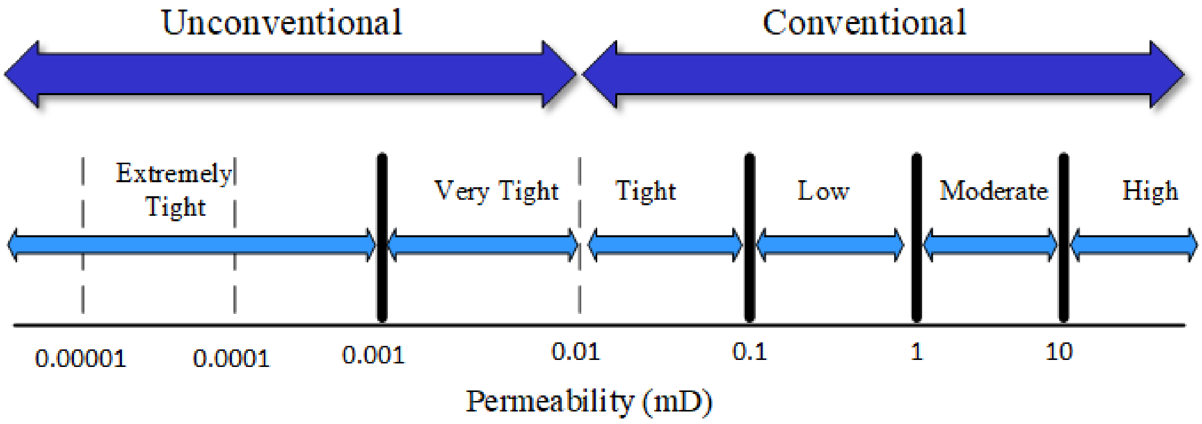

Figure 3.4 Permeability diagram of conventional and unconventional reservoirs

Numerous studies have been presented (Cipolla et al. 2010; Rubin 2010; Yu et al. 2013; Lee et al. 2014; Kim et al. 2014, 2015; Kim and Lee 2015) using a variety of numerical models to simulate fluid flow in SGRs. These numerical models often include the equivalent continuum (single porosity), dual porosity, dual permeability, and multiple interaction continua (MINC) models (Figure 3.5).

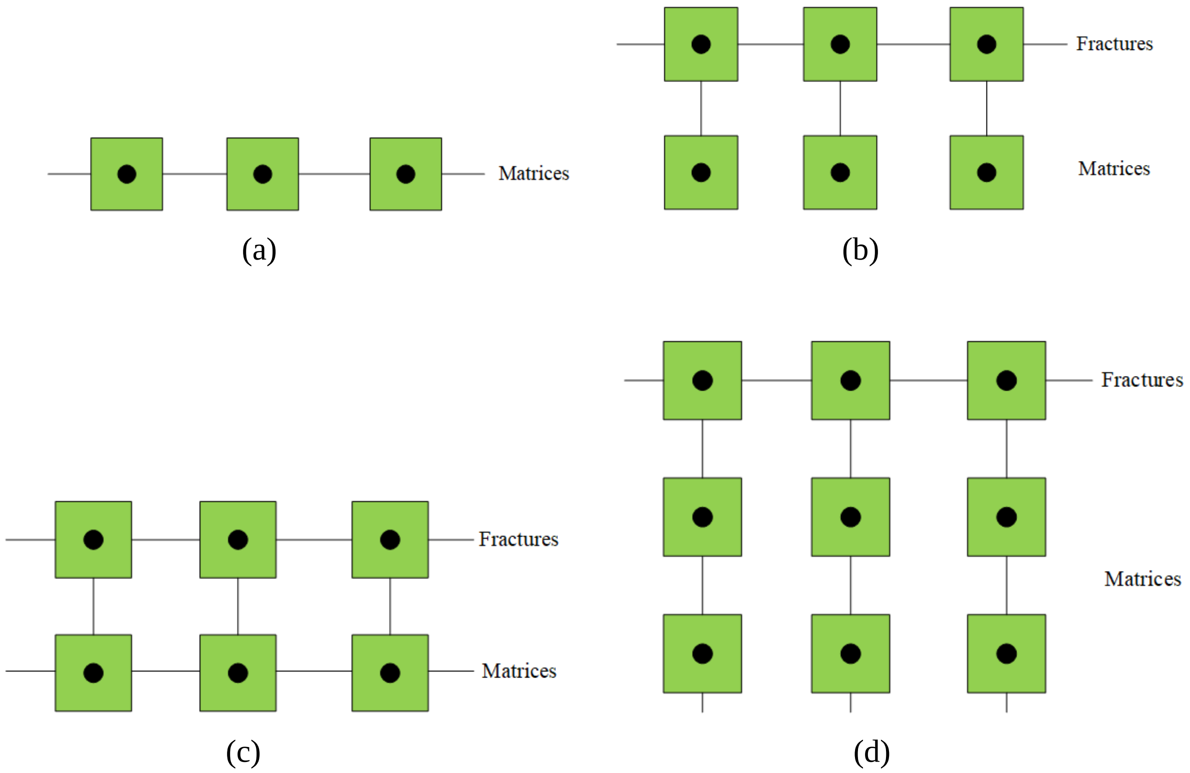

(a) (b) (c) (d)

Figure 3.5 Schematic conceptualizations for handling matrix-fracture interactions a) single porosity model, b) dual porosity model, c) dual permeability model, d) multiple interaction continua model

The single porosity model is where the properties of the fracture arrays (i.e. porosity, permeability etc.) are averaged over the entire porous medium. Consequently, the fractured porous media is considered as a continuum media and the fluid behavior is predicted via a single block in naturally fractured shale reservoirs. Hence, this model is not suitable to describe the mass transport in fractured SGRs since it is extremely challenging to obtain an averaged value for the reservoir permeability and porosity.

Warren and Root (1963) presented the dual porosity model (Figure 3.6) where the flow of fluids is assumed to occur between matrix blocks and fractures (Figure 3.7). In addition, the fracture system in SGRs is the only pathway connected to the wellbore. In contrast to the single porosity model, two sets of reservoir properties (porosity and permeability) per grid block are defined. This entails that each simulator block has two interacting media (i.e. matrix blocks, fracture network) with one set of reservoir properties in the matrix and one in the fractures. It should be noted that the matrix blocks with high porosity have either low or high permeability, whereas the natural fractures have low porosity and high conductivity.

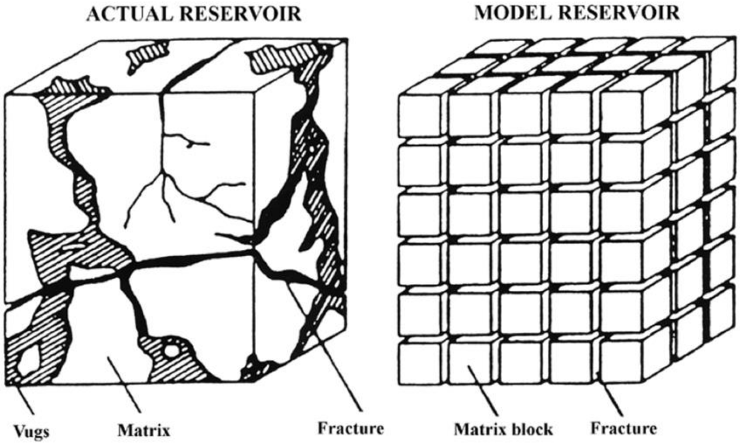

Figure 3.6 Idealization of a fractured system (Warren and Root, 1963)

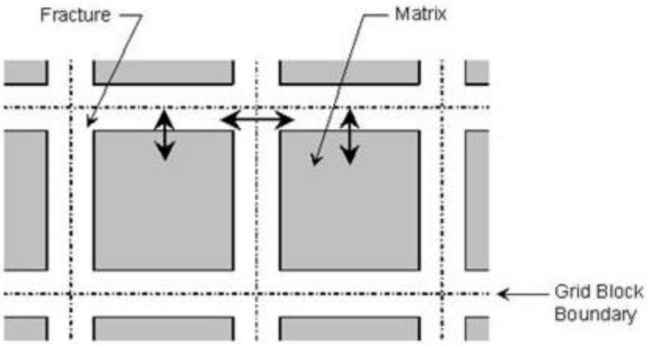

Figure 3.7 The schematic concept of dual porosity model (Warren and Root, 1963)

The dual porosity model was enhanced by the dual permeability model (Kazemi et al., 1978). Similar to dual porosity model, each simulation grid block has two distinct sets of reservoir properties in the matrix and fracture. However, in the dual permeability model, fluid can flow via the matrix and fracture system to the wellbore since both matrix and fractures are connected to the wellbore. In addition, the dual permeability model allows both matrix-to-matrix and fracture-to-fracture flow between gridblocks (Figure 3.8).

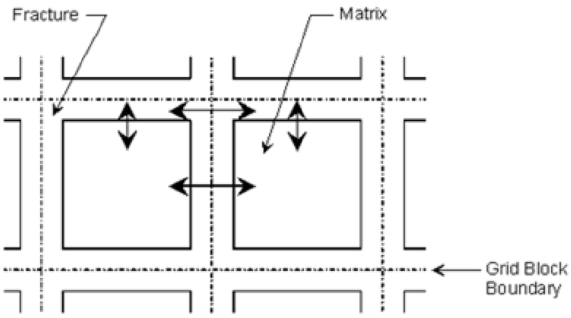

Figure 3.8 The schematic concept of dual permeability model (Kazemi et al., 1978)

Pruess and Narasimhan (1985) proposed the Multiple Interaction Continua method as an extension of the dual porosity model. In general, the MINC method yields better numerical approximations for the fracture-matrix interaction when compared to the dual porosity model. Despite the fact that MINC approach is more suitable for handling SGRs, it is more computationally intensive since the method subdivides the matrix system into a sequence of nested rings (Figure 3.9). Previous studies (Moridis et al., 2010) have also shown that the MINC approach is not suitable to reservoirs where the fracture system is sparse and cannot be approximated as a continuum.

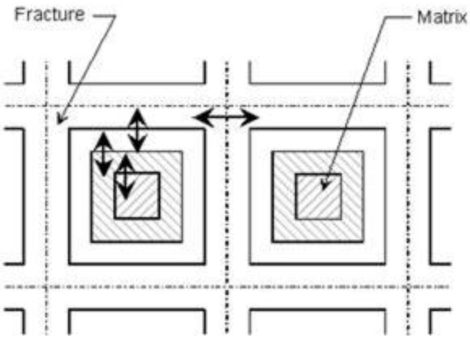

Figure 3.9 The schematic concept of multiple interaction continua model (Pruess and Narasimhan, 1985)

Over the last few years, researchers have developed the Discrete fracture modeling (DFM) to explicitly simulate the fracture geometries and complexities (Rubin, 2010; Gong et al., 2011; Karimi-Fard and Durlofsky, 2016). When applying DFM in SGRs, each fracture is characterized as a geometrically well-defined entity (Figure 3.10). Despite the fact that these models are able to capture detailed geometry of each fracture, DFM is considered as the most rigorous method due to its computational intensity. In addition, DFM is limited due to the incompatibility with existing reservoir simulators and lack of detailed knowledge of fracture-matrix properties and spatial distribution in reservoirs (Civan et al., 2011; Fumagalli et al., 2017).

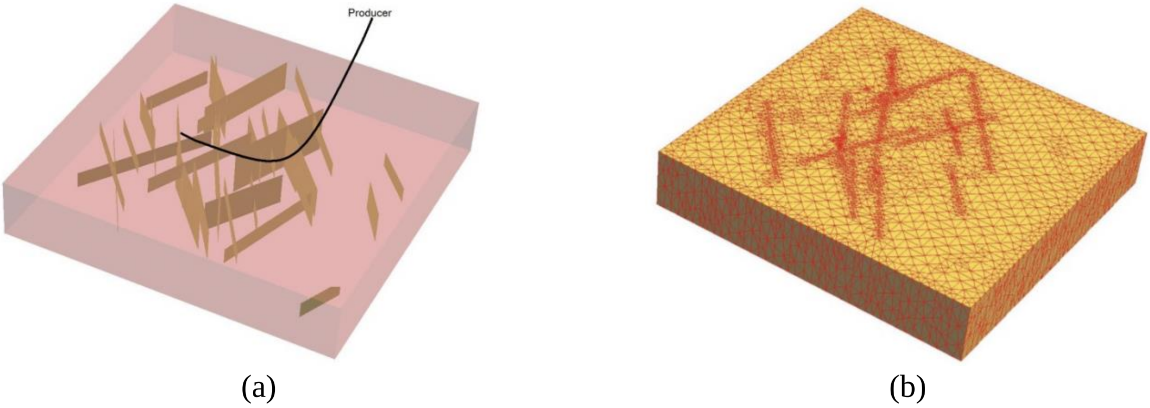

(a) (b)

Figure 3.10 The schematic concept of unstructured discrete fracture model that corresponds to a) natural and b) hydraulic fractures (Civan et al., 2011)

Amongst the foregoing models, studies (Ho, 2000; Moridis et al., 2010; Guo et al., 2018) have shown that the dual permeability model is the main approach for modelling fluid flow in fractured SGRs. Despite the fact that it is less computationally demanding compared to MINC and DFM, it accurately characterizes the interacting media (i.e. matrix blocks, fracture network), which results in more reliable outcomes for shale reservoir analysis.

3.3.1.1 Dual-Permeability Formulation

The governing equations of the dual permeability model are similar to those of the dual porosity model. However, additional channels for fluid flow exist due to communication between matrix gridblocks, as explained in Section 3.3.1. It should be noted that the governing equations of dual-permeability and dual-porosity models are an extension of the equations for single porosity systems. According to Kazemi et al. (1978), the representation of the matrix acts as boundaries to matrix elements, whereas the fractures are assumed orthogonal in the three co-ordinate directions. Dual permeability formulations in the matrix (Eqs. (3.12) and (3.13)) and fracture (Eqs. (3.14) and (3.15)) can be given by the expressions:

$$\begin{aligned}\psi_{im} &= \Delta T_{om}^{s} y_{iom}^{s} (\Delta p^{n+1} - \gamma_o^s \Delta D)_m + \Delta T_{gm}^{s} y_{igm}^{s} \left(\Delta p^{n+1} + \Delta p_{cog}^{s} - \gamma_g^s \Delta D\right)_m \\ &\quad - \tau_{iomf} - \tau_{igmf} - \frac{V}{\Delta t}\left(N_i^{n+1} - N_i^{n}\right)_m = 0 \qquad i = 1, \dots, n_c \end{aligned} \tag{3.12}$$

$$\psi_{n_c+1,m} = \Delta T_{wm}^{s}(\Delta p^{n+1} - \Delta p_{cwo}^{s} - \gamma_w^s \Delta D)_m - \tau_{wmf} - \frac{V}{\Delta t}\left(N_{n_c+1}^{n+1} - N_{n_c+1}^{n}\right)_m = 0 \tag{3.13}$$

$$\begin{aligned}\psi_{if} &= \Delta T_{of}^{s} y_{iof}^{s}(\Delta p^{n+1} - \gamma_o^s \Delta D)_f + \Delta T_{gf}^{s} y_{igf}^{s}\left(\Delta p^{n+1} + \Delta p_{cog}^{s} - \gamma_g^s \Delta D\right)_f \\ &\quad + q_i^{n+1} + \tau_{iomf} + \tau_{igmf} - \frac{V}{\Delta t}\left(N_i^{n+1} - N_i^{n}\right) = 0, \qquad i = 1, \dots, n_c\end{aligned} \tag{3.14}$$

$$\psi_{n_c+1,f} = \Delta T_{wf}^{s}(\Delta p^{n+1} - \Delta p_{cwo}^{s} - \gamma_w^s \Delta D)_f + q_w^{n+1} + \tau_{wmf} - \frac{V}{\Delta t}\left(N_{n_c+1}^{n+1} - N_{n_c+1}^{n}\right)_f = 0 \tag{3.15}$$

where ψ is the material balance equation, Δt is the time step, y_i is the mole fraction of component i, τ_{iomf} is the matrix-fracture transfer in the oil phases for component i, τ_{igmf} is the matrix-fracture transfer in the gas phases for component i, τ_{wmf} is the matrix-fracture transfer for water, V is the grid block volume, N_i are the moles of component i per unit of grid block volume, N_{nc+1} are the moles of water per unit of grid block volume, T is the transmissibility, y_{io} is the mole fraction of component i in the oil phase, γ is the gradient, D is the depth, p_{cog} is the oil-gas capillary pressure, and p_{cwo} is the water-oil capillary pressure. The subscripts f and m correspond to the fracture and matrix respectively. The subscript n_c+1 is the water component and the subscript i with $i = 1, ..., nc$ is the hydrocarbon component. Subscripts o, g, and w refer to oil, gas, and water, respectively.

The superscripts n and $n+1$ correspond to the old- and new-time step, respectively. The superscript s corresponds to n for explicit blocks and to $n+1$ for implicit blocks.
Eqs. (3.12) and (3.13) are the same as those in dual porosity formulation.

Assuming that the matrix and fracture blocks are at the same depth, the matrix-fracture transfer is given by the expressions:

$$\tau_{omf} = \sigma V \frac{k_{ro}\rho_o}{\mu_o}\left(p_{om} - p_{of}\right) \tag{3.16}$$

$$\tau_{gmf} = \sigma V \frac{k_{rg}\rho_g}{\mu_g}\left\{\left(p_{om} - p_{of}\right) + \left[S_{gm} + \frac{\sigma_z}{\sigma}\left(\frac{1}{2} - S_{gm}\right)\right]\left(\tilde{p}_{cog,m} - \tilde{p}_{cog,f}\right)\right\} \tag{3.17}$$

$$\tau_{wmf} = \sigma V \frac{k_{rw}\rho_w}{\mu_w}\begin{Bmatrix}\left(p_{om} - p_{of}\right) - \left(p_{cwo,m} - p_{cwof}\right) \\ -\left(\frac{1}{2}\frac{\sigma_z}{\sigma}\right)\left[\left(\tilde{p}_{cwo,m} - \tilde{p}_{cwo,f}\right) - \left(p_{cwo,m} - p_{cwof}\right)\right]\end{Bmatrix} \tag{3.18}$$

where σ is the transfer coefficient (shape factor) and is given by:

$$\sigma = 4\left(\frac{1}{l_x^2} + \frac{1}{l_y^2} + \frac{1}{l_z^2}\right) \tag{3.19}$$

Eqs. (3.16), (3.17), and (3.18) account for the pseudo capillary pressure and partially immersed matrix element in either gas or water.

3.3.2 Non-Darcy Flow

One of the most fundamental equations in the oil and gas industry was developed by Henry Darcy in 1856. Darcy conducted experiments to examine the flow of water through sand pack configurations by varying the inlet and outlet pressures. After multiple experiments for a variety of test cases, a single expression correlating ground water flow and pressure loss was generated. Darcy's law is given by the expression:

$$\frac{q}{A_c} = -\frac{k}{\mu}\frac{dp}{dx} \tag{3.20}$$

where q is the flow rate, k is the permeability, A_c is the cross-sectional area of the rock, μ is the viscosity, and dp/dx is the pressure gradient in the direction of flow. Eq. (3.20) has been utilized to linearly relate pressure gradient and fluid-flow rate across the porous media. This linear proportionality simplifies its implementation in the numerical reservoir simulations and reservoir engineering analysis.

Nonetheless, Forchheimer (1901) observed deviation from the linearity of Eq. (3.20) in hydraulic fractures making Darcy's law not applicable. The reason for this deviation, is the increased turbulent flow, which leads to an additional pressure drop inside the hydraulic fractures so that production rate is maintained. Hence, an additional proportionality constant was induced. Forchheimer equation is given by:

$$-\frac{dp}{dx} = \frac{\mu v}{k} + \beta\rho v^2 \tag{3.21}$$

where β is the non-Darcy flow coefficient. Various researchers addressed different correlations for the non-Darcy flow coefficient (Cooke, 1973; Geertsma, 1974). However, the most widely used correlation was developed by Evans and Civan (1994) and can be expressed as:

$$\beta = \frac{1.485 \times 10^9}{\phi k^{1.021}} \tag{3.22}$$

It should be noted that, this correlation is determined from a large variety of porous media (consolidated and unconsolidated) under different conditions where the quality of fit is high (R=0.974). Hence, this correlation of the non-Darcy coefficient is expected to yield reasonable estimations and is implemented in numerical reservoir simulations.

3.3.3 Reservoir Modelling with Hydraulic Fractures

The local grid refinement (LGR) technique was implemented to accurately model flow within the hydraulic fractures, within shale, and from shale to hydraulic fractures (Figure 3.11). Local grid refinements, which are either cartesian or cylindrical, aim to provide improved accuracy of the transient effects (i.e. rapid pressure drops, condensate dropout, undulating horizontal wells etc.), especially in the region around the hydraulic fracture. In general, cells increase in size logarithmically away from the hydraulic fracture. This means that, the region around the hydraulic fracture is discretized to a much finer degree compared to the region further away from the hydraulic fractures, which is more coarsely gridded. In particular, this approach has been extensively used by previous researchers (Cipolla et al., 2010; Yu et al., 2016; Kim et al., 2017) to simulate transient fluid flow in hydraulically fractured shale gas reservoirs. In these studies, the fracture width was set to a small value (0.01ft) with a large permeability. An LGR-based, logarithmically spaced, dual-permeability grid approach accurately models shale-gas reservoirs using orders of magnitude less CPU time than finely gridded equivalent models, as has been suggested (Rubin, 2010; Cipolla et al., 2010).

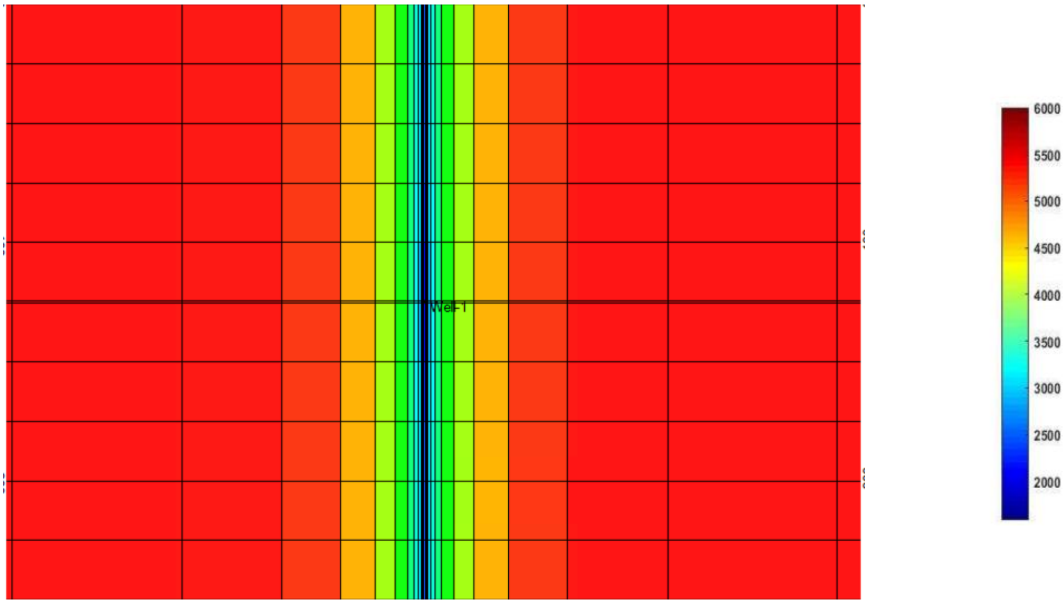

Figure 3.11 Local grid refinement for one fracture network. The scale bar is the pressure (psi)

3.3.4 Multicomponent Adsorption

According to previous studies, adsorbed methane could be responsible for 5–30% of the entire gas production in shale gas reservoirs (Cipolla et al., 2010; Mengal and Wattenbarger, 2011; Thompson et al., 2011). Adsorption trapping is also a dominant means for storing CO_2, because the adsorption interaction of CO_2 with a highly organic shale is five times stronger than that of CH_4 (Nuttal et al., 2005). To formulate a model that includes competitive multi-component adsorption/desorption, the extended Langmuir isotherm has been identified as providing a good description of the binary gas sorption of CO_2 and CH_4, and, thus is applied in the current dissertation. The generalised multi-component Langmuir isotherm is given as (Arri et al., 1992; Hall et al., 1994):

$$\alpha_\zeta = \frac{\alpha_{\zeta max} b_i \gamma_{\zeta g} P}{1+P\sum_{\xi} b_j \gamma_{\xi g}} \tag{3.23}$$

where α_ζ represents the quantity of adsorbed component ζ in moles per unit rock mass, $\alpha_{\zeta max}$ [gmole/lb] represents the highest quantity of adsorbed component ζ in moles for each unit mass of rock, b_i represents the energy of interaction parameter for the Langmuir isotherm relation, $\gamma_{\zeta g}$ represents the molar fraction of adsorbed component i in the gas phase, and P represents the pressure. $\alpha_{\zeta max}$ and b_i depend upon the total organic content (TOC) of the shale and must be measured experimentally for core samples.

3.3.5 Thermodynamic Equilibrium

When designing CO_2 injection in field applications, it is required to describe the phase behavior of reservoir fluids under reservoir conditions as CO_2 is injected. It is assumed that the gas phase and the aqueous phase are in thermodynamic equilibrium:

$$g_i = f_{ig} - f_{iw} = 0, i = 1, \dots, n_c \tag{3.24}$$

where f_{ig} is the fugacity of component i in the gas phase, f_{iw} is the fugacity of component i in the aqueous phase and n_c is the number of gaseous components. The Peng-Robinson (1976) equation of state (PR-EOS), used throughout this thesis, is the principle method used to determine the fugacity f_{ig}. Previous work (Yu et al., 2015; Yu et al., 2016; Kim et al., 2017) has shown that the PR-EOS accurately describes the volumetric and phase behavior of both pure components and their mixtures, while only the critical properties and the acentric factor of each component are required. The PR-EOS model can be expressed as:

$$\ln \frac{f_{ig}}{y_i p} = \ln \phi_{ig} = \frac{B_i}{B}(z-1) - \ln(z-B) + \frac{A}{2\sqrt{2}B} \ln\left(\frac{B_i}{B} - \frac{2}{A}\sum_{j=1}^{N} y_j A_{ij}\right) ln\left(\frac{z+(1+\sqrt{2})B}{z-(1-\sqrt{2})B}\right) \tag{3.25}$$

where A is the attraction parameter between molecules and B is the repulsion parameter between molecules. The complete procedure for the determination of the fugacity and explanation of the corresponding parameters in the PR-EOS, can be found in Appendix A.

Furthermore, Henry's law is utilized to calculate the fugacity f_{iw} of gaseous components soluble in the reservoir fluid (Li and Nghiem, 1986):

$$f_{iw} = y_{iw} H_i \tag{3.26}$$

where y_{iw} is the mole fraction of component i in the aqueous phase and H_i the Henry's constant of component i. The Henry's constants H_i can be expressed as (Stumm and Morgan, 1996):

$$\ln H_i = \ln H_{ir} + \frac{\overline{V}_i (p-p_r)}{RT} \tag{3.27}$$

where H_{ir} is the Henry's constant for component i at pressure p_r, $\overline{V}_i$ is the partial molar volume of component i and p_r is the reference pressure.

3.3.6 Solution Technique

Fluid flow in an underground porous medium where oil or gas are trapped stratigraphically and/or structurally, is a complex phenomenon. Reservoir simulation is often the only tool to obtain reliable solutions for many complex fluid problems. In general, reservoir simulators are described by a set of mathematical equations that govern the flow of fluid in porous media. These mathematical equations are in the form of strongly non-linear partial differential equations (PDEs). In order to establish a correlation between the fluid, the porous medium and the system's flow conditions, these PDEs are formulated by obeying to physical principles (i.e. equation of state, continuity equation, Darcy's law etc.). Due to the complexity of these equations, they must be solved numerically. This entails discretizing the equations in order to find an approximate solution on the finite set of different points (i.e. mesh or grid points).

As outlined in the equations above (Section 3.3.1.1), a system of algebraic equations has replaced the PDEs since they were easier to be solved. The discretization of any PDE can be achieved via three techniques, namely the Finite Difference or Taylor series method, the Spectral or the Variational method, and the Finite Volume or the Integral method (Aziz and Settari, 1979). Of all these methods, the finite difference approach is the most widely used numerical method in reservoir simulations to discretize the reservoir (Appau et al., 2019). In general, the nonlinear PDEs are, usually, discretized using central finite difference method with the time discretized using backward finite difference method. Thereafter, a fully implicit discretized equation is obtained which is solved via Newton-Raphson's method. Figure 3.12 depicts the development of a reservoir simulator, where the finite difference equations of a mathematical model to describe the fluid flow are initially established. Afterwards, numerical modelling and computer programming is applied, and, finally, reservoir simulation software is generated.

The discretization of the nonlinear equations using the finite difference approach is not discussed here as these are not the subject of this thesis. The mathematical derivations and solutions in discretizing the nonlinear PDEs are given elsewhere (Thomas, 1977; Peaceman, 1978; Aziz and Settari, 1979; CMG-GEM, 2019). This is justified given that the reservoir simulator, GEM (CMG-GEM, 2019), implemented and utilised throughout this thesis, solves the above equations. It should be mentioned that GEM, which is a compositional reservoir simulator, is suggested for unconventional reservoirs and gas flooding techniques (i.e. CO_2

injection) since it provides more accurate results compared to thermal and black oil simulators. The reason for this accuracy, is that GEM solves both the fluid flow equations and the equation of state, whereas the black-oil and thermal simulators solve only the fluid flow equations.

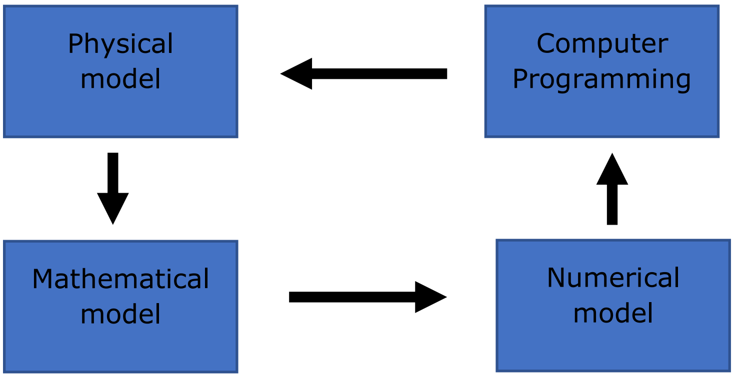

Figure 3.12 Reservoir simulation process

3.4 Summary

Textural parameters of shales, namely the pore size distribution, and the surface area can be experimentally measured via the volumetric method. A gravimetric analyser (Hiden XEMIS) is used to obtain CO_2 uptake kinetics in shale matrix prior to numerically simulating the CO_2 injection process. The dual permeability model is suggested to accurately simulate the naturally fractured shale reservoirs, while the logarithmic refinement is required to capture the transient effects around the hydraulic fractures. The Peng-Robinson equation of state is applied to accurately model the phase behavior of reservoir fluids as CO_2 is injected in reservoirs. In shale reservoirs, the extended Langmuir isotherm is utilized to describe the binary gas sorption of CO_2 and CH_4.

4. Chapter Four: Predicting Surface Diffusivities of Gas Molecules in Shale

4.1 Introduction

Gas shales are an increasingly exploited resource across the world due to the depletion of conventional reservoirs and their potential to supply the world with an immense amount of energy. Gas reserves in unconventional shale are estimated at nearly 719 trillion cubic metres (Liu et al., 2019). Gas recovery from shales can be enhanced greatly by injection of carbon dioxide (Kim et al., 2017;Godec et al., 2013;Yu et al., 2015). CO_2 injection to recover methane also has the advantage of simultaneously sequestering carbon, thereby concurrently addressing the issue of increased greenhouse gas emissions from the use of fossil fuels. The displacement efficiency of the CH_4 and the carbon sequestration potential is much enhanced by greater mobility of the CO_2. Previous work (Wu et al., 2016) has shown that the mass transport flux in shales is dominated by the surface diffusion mechanism because of the large internal surface area-to-volume ratio of shale rocks. Hence, a better understanding of the structure-transport relationship for surface diffusion in shale rocks will greatly improve the assessment of the production and storage potential of shale gas reservoirs.

Surface diffusion probably plays the major role to gas transfer mechanisms due to the greater amount of adsorbed gas, particularly within the abundant nanopores within the organic matter of shale gas reservoirs. Surface diffusion is a complex physical phenomenon, which is characterized by an activated process (Riekert, 1971; Yeh and Yang, 1989). It is a physical process that entails random hopping, as the adsorbed particles move between adsorption sites, that requires a minimum activation energy and experiences an activated transition state. During transport, the adsorbed gas is characterised by a large concentration gradient, and the occupation of a large specific surface area gives rise to a large flux (Yi et al., 2009; Clarkson et al., 2013). In the presence of surface diffusion, the apparent permeability can be ten times higher than when compared to without (Darabi et al., 2012).The high magnitude of the surface diffusion contribution to overall mass transport, leads to challenges in the prediction of long-term production for shale gas reservoirs since the structure transport relationship for surface diffusion in shales is not well understood (Majumder et al., 2005; Holt, 2006). Some experimental investigations have also indicated that, in comparison to the bulk gas transport, surface diffusion, is more significant in particular circumstances (Do and Wang, 1998), as in the case where the pore network is not yet well-developed within shale gas reservoirs (Akkutlu and Fathi, 2012). Hence, it is reasonable to say that surface diffusion is considered as an essential mechanism for transport in shale gas resources.

Surface diffusivity depends upon the concentration of the adsorbate on the porous solid and the non-linearity of the isotherm. The particular value of surface diffusivity derived from experimental measurements depends upon how the surface flux is defined, and this is usually achieved by subtraction, whereby the pore diffusion rate is isolated from the overall rate observed. One procedure, for isolating the pore diffusion contribution, is usually conducted by increasing the temperature until it reaches a point whereby the effects of surface diffusion are greatly reduced. Surface diffusion is rendered negligible at high temperatures because the surface diffusion flux is a product of the surface diffusivity and the surface loading. An increase in temperature results in an increase in surface diffusivity but this is, relatively, much less than the decrease of the surface loading; hence, overall, the surface flux decreases (Schneider and Smith, 1968; Mayfield and Do, 1991). However, this particular technique, has several disadvantages. Firstly, it may not be practical to attain the temperature at which surface diffusion is no longer of any matter since this value may be very high. Secondly, when the pore diffusion rate is compared with the surface diffusion rate, it is usually found that the latter only becomes negligible as the temperature is increased if the adsorption isotherm is linear. This problematic high-temperature method can be avoided by using the half-time method that allows for the extraction of surface diffusivity through a simple physical analysis without the need to resort to the use of the mass balance equation, which is always complicated and computationally intensive (Do, 1990; Do and Rice, 1991). The half-time is the period that it takes for the quantity of adsorbate on the porous solid to attain half of the equilibrium amount.

A simple diagram of the inverse of half time of adsorption against concentration factor can be plotted (Do and Rice, 1991). The pore diffusivity can be obtained from the intercept of the anticipated linear plot, while the surface diffusivity can be calculated from the slope. The application of this particular technique to the mass transport of butane within Ajax carbon has been demonstrated. This study utilized the theory proposed by Do for the derivation of surface and pore diffusivities, to obtain these parameters for highly heterogeneous adsorbents, namely shales. It will be seen that this technique reveals that surface diffusion is the predominant mass transport mechanism for CO_2 in a series of Marcellus shales.

The relationship between surface mass transport and the nature of a surface is poorly understood. Further, the surface of shale rocks is particularly complex, possessing both chemical and geometric heterogeneities, given they are composed of a variety of mineral types, including clays, quartz and carbonaceous materials. The use of fractal models to describe the structural heterogeneity in shales has become increasingly common (Zgrablich, 1997; Fan et al., 2018), since fractals enable the discernment of hidden patterns in the face of seemingly intractable disorder. Indeed, it has been found that fractals can provide good structural models for a number of different types of shales (Daigle et al., 2015; Ojha et al., 2017; Wang et al., 2019). However, the implications for mass transport have been much less studied (Ojha et al., 2017), and for surface diffusion not at all. In the past, a fractal theory for surface diffusion, applicable to a variety of molecular species, has been found to be successful for predicting surface diffusivity on relatively homogeneous materials like activated carbons, precipitated silica and porous glasses (Rigby, 2005). It was found that both of the Arrhenius parameters, characterising the variation of the diffusivity on these surfaces with temperature, were directly related to the surface fractal dimension and some other structural parameters of the pore network of the material. The fractal theory was also found to directly predict the compensation effect observed experimentally for surface diffusivity (Rigby, 2003a; Rigby, 2005). It is the purpose of this work to determine whether this fractal theory for surface diffusion can be applied successfully to more heterogeneous materials like shales, and, thereby, offer a way to predict the variation in surface diffusion flux found in a series of different shales.

In this study, low-pressure gas adsorption isotherms and helium pycnometer experiments will be primarily conducted to investigate pore size distribution and estimate porosity for a series of Marcellus shales from different depths. However, the low-pressure nitrogen adsorption-desorption measurements are also analysed to estimate surface fractal dimension, according to the Frenkel-Halsey-Hill method. In addition, Rock Eval Analysis and Mineral Liberation Analyser experiments are also applied to determine the TOC and mineralogy, respectively. Furthermore, gravimetric experiments are performed to effectively measure the half-time, and, thereby, pore-surface diffusivities could be derived according to Do's theory. Subsequently, gravimetric gas uptake experiments are reported at three different temperatures, in order to estimate the Arrhenius parameters for surface diffusivity on each shale sample. These data will be used to test the applicability of the fractal theory to highly structurally and chemically heterogeneous natural materials.

4.2 Theory

4.2.1 Fractal theory for surface diffusion

In an activated process of surface diffusion, where the rate of diffusion varies with temperature, the diffusivity can be represented using the Arrhenius expression:

$$D = D_0 \exp\left(\frac{-E_D}{RT}\right) = \frac{k\lambda_0^2}{\tau_0} \exp\left[\frac{-(2E_\lambda - E_\tau)}{RT}\right] \quad (4.1)$$

where D_0 is the pre-exponential factor and E_D the activation energy for diffusion, and the surface diffusion proceeds by a series of activated jumps of range λ occurring on a characteristic timescale of τ, that each have Arrhenius dependence such that τ_o is the pre-exponential factor and E_τ is the activation energy for the correlation time and, similarly, λ_o is the pre-exponential factor and E_λ is the activation energy for jump length.

The pre-exponential factor in the Arrhenius expression is the entropic term related to the difference in entropy between the initial and final states of a diffusional hop. This entropy change relates to the number of possible configurations of the migrating molecule in the initial and final states. Past studies (Alexander and Gladden, 1997; Cheah et al., 1997) have determined that the pre-exponential factor of the correlation time has an inverse relationship with the number of available sites to which a molecule can hop, where this space was estimated to be within a jump range of R. For a fractally rough surface, the quantity of accessible destinations to which it is feasible for a molecule of linear extent r to hop to is equivalent to the quantity of molecular sized boxes, N, expected to fill the surface within the characteristic upper length scale R:

$$N(R, r) \propto \left(\frac{R}{r}\right)^d r^2 \quad (4.2)$$

where d is the scaling law exponent referred to as the fractal dimension of the surface (Avnir et al., 1984). Therefore, $(R/r)^d$ is the number of boxes of size r^2 needed to cover an area A within an upper length scale R.

By using Eq. (4.2), to adapt an expression previously (Alexander and Gladden, 1997) obtained for zeolites to fractal surfaces, Rigby (1999) showed that the pre-exponential factor for the correlation time for the motion of a molecule on a surface characterised by a fractal dimension d is given by the expression:

$$\tau_0 = \tau_{0r}\left(\frac{R_\infty}{r}\right)^{(d_r-d)} \tag{4.3}$$

where r is the cross-sectional area of the molecule, R_∞ is the apparent limiting upper length scale cut-off for the area as the temperature tends to infinity (related to the upper limit of the jump length), and d_r and τ_{or} are the fractal dimension and pre-exponential factor, respectively, for a reference material. The correlation times in Eq. (4.3) are predicted correctly for the surface diffusion of benzene adsorbed on a variety of silica surfaces (Rigby, 1999). Combining Eqs. (4.1) and (4. 3) means that:

$$\ln\,D_0 \quad = [\ln\,D_{0r} - d_r\ln\,(\tfrac{R_\infty}{r})] + d\ln\,(\tfrac{R_\infty}{r}) \tag{4.4}$$

Thus, a linear relationship exists between the natural logarithm of pre-exponential factor for the surface diffusivity and the fractal dimension. In deriving Eq. (4.4) it is assumed that the Arrhenius parameters for the jump length are independent of the surface fractal dimension (Rigby, 2003a).

For a fractal dimension to be valid it must hold over a wide range of length-scales. In this surface diffusion model the fractal dimension referred to above, which holds at the jump range of the molecule, must also be the same fractal dimension that holds for shorter length-scales, just above that of the single molecule, occupied by its nearest neighbours. Hence, the condition for a valid fractal dimension is also essential to this theory of surface diffusion. The theory behind the derivations below will be given briefly, since it is described in more detail in a previous paper (Rigby, 2005). The activation energy is the enthalpy term and can also be directly related to surface fractal dimension. In prior studies, it was proposed that the total interaction energy, comprising such as the activation energy for the correlation time or the heat of adsorption, originates from the individual contributions from each of the adjacent adsorption sites and from directly beneath the adsorbed molecule. The convolutions of rougher surfaces mean that they have a higher connectivity, which results in more contributions from the nearby sites. On a fractal surface, the particular number of nearby sites is a function of the surface fractal dimension.

In past work (Rigby, 1999; 2003a; 2003b), it was accepted that just closest neighbor interactions were significant. Hence, it has been shown that the surface fractal dimension is related to total interaction energy E_i by the expression:

$$E_i = (E_{\mathrm{S}i} - \varepsilon_i) + \pi\varepsilon_i \left(\frac{R_n}{r}\right)^d \tag{4.5}$$

where the subscript i denotes the particular surface of interest, and $E_{\mathrm{S}i}$ the contribution from the surface site directly below the adsorbed molecule, ε_i the contribution from a single neighbouring site, and R_n a characteristic length-scale. In cases where only the interactions from the closest neighbors are deemed significant, then the distance from the middle of a molecule to the furthest edge of an immediately adjacent site can be denoted by R_n. In this particular case, R_n/r then equals 1.5. From Eq. (4.5), it can be observed that a linear relationship exists between E_i and $(R_n/r)^d$. Eqs. (4.2) and (4.5) can be combined to give:

$$E_{\mathrm{D}} \quad = w + x(\frac{R_n}{r})^d \tag{4.6}$$

where $w(= 2E_\lambda - E_{\mathrm{S_r}} + \varepsilon_{\mathrm{r}})$ and $x(= -\pi\varepsilon_\tau)$ are terms composed only of constants. Eq. (4.6) demonstrates that the activation energy for the surface diffusivity is a linear function of the group $(R_n/r)^d$. Rigby (2002) showed that a compensation effect results when both the natural logarithm of the pre-exponential factor and the activation energy depend on surface fractal dimension as described above, such that:

$$\ln\ D_0 = mE_{\mathrm{D}} + h \tag{4. 7}$$

where m and h are constants.

As outlined in Section 2.3.3.3, the Frenkel–Halsey–Hill (FHH) model has been used extensively by researchers to quantitively characterize pore structure of shales based on N_2 adsorption isotherms (Yang et al., 2014; Sakhaee-Pour and Li, 2016; Li et al., 2019). Hence, the surface fractal dimension factor in Eqs. (4.4) and (4.6) can be measured independently using Eqs. (2.13) and (2.15) from Chapter 2, for the analysis of gas adsorption data (Pfeifer and Liu, 1997).

It is noted that the heat of adsorption and the surface fractal dimension are independent parameters since they are obtained from different parts of the isotherm data. The adsorption heat is derived from the sub-monolayer region, while the surface fractal dimension is determined from the multilayer region.

4.2.2 Theory for obtaining surface diffusivity

As mentioned above, Do proposed a theory whereby surface diffusivity may be obtained from gas uptake measurements (Do and Rice, 1991). The diffusion fluxes of the free (J) and adsorbed (J_s) species are expressed as (Barrer, 1987):

$$J = -\varepsilon_M D_p \frac{\partial C}{\partial r} \tag{4.8}$$

$$J_s = -(1-\varepsilon_M) D_s \left[\frac{\partial C_\mu}{\partial r}\right] \tag{4.9}$$

where ε_M is the voidage of the particle (cc void volume/cc of total particle envelope volume), C_μ is the concentration in the adsorbed phase (mole/cc), C is the bulk fluid concentration (mole/cc), D_s is the surface diffusivity, and D_p is the pore diffusivity. It is noted that the Do and Rice (1991) analysis uses equations for standard Fickian diffusion, rather than those of anomalous diffusion associated with pore fractals (Havlin and Ben-Avraham, 1987). The use of the standard Fickian equations for data analysis here is justified as follows. The theory presented in Section 4.2.1 is for the rate-controlling step in surface diffusion, namely the rate of individual molecular jumps, and thus is sensitive to the characteristic length-scales of this process (ie of the order of the molecular jump length). In contrast, the CO_2 uptake experiments, by which the surface diffusivity will be measured, have characteristic timescales and length-scales (i.e. diffusion path length is ~size of shale particles) that are much bigger than the correlation time of individual molecular jumps and the size of pores in shale (<100 nm), respectively. The shale is not a pore fractal over these length-scales (i.e. >100 nm to 100s microns) so diffusion is not anomalous in uptake experiments. For example, mercury intrusion porosimetry data exhibits no macroporosity. Hence, the random walk of the surface diffusing molecules is not anomalous over long times, and normal diffusion equations are applicable.

The fluxes are determined from the overall surface area of the cross-section, while their units are based on the number of moles transported across a unit section within a unit time. The material balance equations can then be written as follows:

$$\varepsilon_M \frac{\partial C}{\partial t} + (1-\varepsilon_M)\frac{\partial C_\mu}{\partial t} = (\varepsilon_M D_P)\frac{1}{r^s}\frac{\partial}{\partial r}\left(r^s \frac{\partial C}{\partial r}\right) + (1-\varepsilon_M) D_s \frac{1}{r^s}\frac{\partial}{\partial r}\left(r^2 \frac{\partial C_\mu}{\partial r}\right) \tag{4.10}$$

The symmetry condition always applies at the centre of the particle, while continuity of flux at the exterior boundary of the pellet is maintained, such that:

$$r = 0; \quad \frac{\partial C}{\partial r} = \frac{\partial C_\mu}{\partial r} = 0 \tag{4.11}$$

$$r = R_d; \quad (\varepsilon_M D_p)\frac{\partial C}{\partial r} + (1-\varepsilon_M) D_s \frac{\partial C_\mu}{\partial r} = k_m(C_b - C) \tag{4.12}$$

If the pore diffusion is the only diffusion mechanism and the adsorption isotherm is linear, then the half time of adsorption is given by (Crank, 1975):

$$\frac{\varepsilon_M D_p t_{0.5}}{R_d^2[\varepsilon_M + (1-\varepsilon_M)K]} = 0.03055 \tag{4.13}$$

By carrying out numerical simulation of intermediate cases for a Langmuir isotherm (Eq. (4.13)), Do (1990) derived the following expression for the half time for the pore diffusion model with local adsorption equilibrium:

$$\frac{\varepsilon_M D_p t_{0.5}}{R_d^2[\varepsilon_M + (1-\varepsilon_M)(C_{\mu 0}/C_0)]} = 0.03055\left[1 - \frac{0.3\delta}{1+3\delta/4}\right] \tag{4.14}$$

where $C_{\mu o}$ (mole/volume of solid), is the adsorbed amount in equilibrium with the bulk concentration C_o (mole/volume of fluid). The overall adsorption rate is considered to happen faster than pore and surface diffusion. Local adsorption equilibrium is thus attained within a short time. Therefore, the equilibrium data can be described using the local Langmuir isotherm.

$$\mathrm{C}_{\mu 0} = \mathrm{C}_{\mu s}\frac{\mathrm{bC_0}}{1+\mathrm{bC_0}} \tag{4.15}$$

where $C_{\mu s}$ is its maximum concentration, and *b* is the Langmuir constant. The justification for the continued use of the Langmuir isotherm, as employed by Do and Rice (1991), in the analysis of CO_2 uptake data for the fractal shales studied here is as follows. It should be noted that all isotherm model predictions (Langmuir, BET, fractal BET and fractal FHH) look very similar up to around point B (the first knee of the isotherm corresponding roughly to a statistical monolayer coverage) since the influence of multilayer adsorption (which distinguishes the others from Langmuir) only becomes evident beyond that point. Since we are only considering the surface diffusion of CO_2 up to the region of point B, then the Langmuir model is sufficient to characterise the CO_2 isotherm in this region. The surface fractality enters the adsorption isotherm models via two separate effects. First, the surface roughness at short length-scales affects the heat of adsorption for individual molecules, which determines such model parameters as the Langmuir and BET constants. Second, multi-layer build-up is affected by the decline in number of adsorption sites in successive adsorbed layers on fractal surfaces, which is the effect also incorporated into the fractal BET and fractal FHH models, but which is only manifest in experimental data well beyond point B. Further, it is noted that if the surface fractal dimension tends towards a value of 3 (as it does in this study), then the overall forms of the fractal BET and fractal FHH isotherms tend towards that of the Langmuir isotherm.

Now, allowing for the pore and surface diffusion being in parallel, and that the isotherm is linear, the half time of adsorption is then given by:

$$\frac{[\varepsilon_M+(1-\varepsilon_M)KD_s]t_{0.5}}{R^2[\varepsilon_M+(1-\varepsilon_M)K]} = 0.03055 \tag{4.16}$$

Finally, when the surface diffusion is the controlling mechanism, the half time will be:

$$\frac{\mathrm{D_s t_{0.5}}}{\mathrm{R^2}} = 0.03055 \tag{4.17}$$

no matter what the isotherm nonlinearity is, and the Langmuir isotherm can be used. Thus, by combining the behaviour of the half time at various limits (Eqs. (4.13) - (4.17)), the following general equation for the half time for parallel pore and surface diffusion and any nonlinearity of the isotherm is obtained (Do and Rice, 1991):

$$\varOmega = \varepsilon_M D_p + (1-\varepsilon_M)D_s\varXi \tag{4.18}$$

where:

$$\varOmega = \frac{\alpha R^2[\varepsilon_M+(1-\varepsilon_M)\frac{C_{\mu 0}}{C_0}](1-\frac{\beta b C_0}{1+\gamma b C_0})}{t_{0.5}} \tag{4.19}$$

and

$$\varXi = (1-\frac{\beta b C_0}{1+\gamma b C_0})(\frac{C_{\mu 0}}{C_0}) \tag{4.20}$$

This equation suggests that if one plots $\varOmega$ versus $\varXi$, a straight line with the slope $(1-\varepsilon_M)D_s$ and the intercept $\varepsilon_M D_p$ is expected. Eq. (4.18) is valid for any of the three possible shapes (as expressed via the geometrical parameters α, β, γ) of the particle. The only difference between the three particle shapes is the values of the parameters α, β, and γ given in Table 4.1. The samples used in this study have a spherical shape and will be analysed in Section 4.4.

Table 4.1 Parameters values for shape particle

Shape of particle	α	β	γ
Slab	0.19674	0.25	0.686
Cylinder	0.0631	0.26	0.663
Sphere	0.03055	0.3	0.75

4.3 Materials used and Experimental Methods

4.3.1 Materials

Three core shale samples from the Marcellus Formation were obtained during exploratory drilling of a borehole located in the Appalachian basin, Ohio, USA. The core samples were collected from three different depths: 7804-7807ft, 7834-7837ft and 7864-7867ft. Due to commercial confidentiality reasons, a more detailed location cannot be disclosed. The Marcellus Shale lies within a total area of greater than 100,000 miles, and its depth ranges between 4000 and 8500 ft, having an average thickness of 50–200 ft. (NETL, 2013). The formation contains 1500 trillion cubic feet (tcf) of original gas in place (OGIP) and has 141 TCF of technically recoverable gas (NETL, 2013).

Each shale specimen was ground and sieved using 0.15-0.18 mm metal sifters and placed in a drying oven at 110 °C for 16 h to dehydrate. Subsequently, helium pycnometer experiments were performed to obtain the skeletal density, and, thus the solid volume of the dried shale samples. Once the skeletal density of the samples was determined, the samples were then stored in a desiccator prior to gas (N_2 and CO_2) sorption measurements.

The porosity can then be calculated as:

$$\varphi = \frac{V_p}{V_p + V_s} \tag{4.21}$$

where φ is the absolute porosity, V_p is the total pore volume obtained from gas sorption experiments and V_s is the solid volume obtained from helium pycnometer experiments.

The physical parameters of the shale samples are summarized in Table 4.2.

Table 4.2 Results of Marcellus Shale characterisation

Depth(ft)	BET(m^2/g)	TOC(%)	Illite(%)	Quartz(%)	Density (g/cm^3)	Porosity(%)	Tortuosity
7804-7807	43.2 ± 1.17	7.22	70	6.88	2.63	7.7	1.74
7834-7837	34.6 ± 0.81	4.39	68.31	7.01	2.68	7.6	2.69
7864-7867	28.8 ± 1.76	6.11	38.12	37.46	2.69	7.6	1.99

4.3.2 Scanning Electron Microscopy (SEM) and Mineral Liberation Analysis (MLA)

Scanning electron microscopy - Mineral liberation analysis (SEM-MLA) experiments were conducted on an FEI Quanta 600 which was equipped with mineral liberation analysis software by JKTech/FEI. The MLA software enables the quantification of sample mineralogy by taking several energy dispersive X-ray (EDX) points. The mineral identification was achieved by matching the EDX points from SEM to a known mineral database. It should be noted that the EDX points were related with a specific dispersive X-ray spectrum. Afterwards, the modal mineralogy (area % of the sample) was calculated by the computer software. Artificial colours were associated to minerals and the process was repeated until all possible minerals were identified (Sylvester, 2012).

The Marcellus shale samples were embedded in epoxy resins in different orientations (i.e. parallel and perpendicular) to the bedding plane. Afterwards, the samples were placed in a vacuum oven for 16 h to remove the air bubbles. In order to obtain the best energy dispersive X-ray analysis, the samples were polished with decreasing coarseness of polishing pads. This led to smoother surfaces and greater exposure of the samples. It should be mentioned that the samples were carbon coated in a thick coat of carbon (10-20 nm) prior to analysis. It should be mentioned that SEM is not a good technique to determine PSDs for samples including a great amount of microporosity and molecular scale pores. The reason is that SEM allows areas between 1 cm and 5 μm to be viewed and features at a scale of 50-100 nm to be seen (Fandrich et al., 2007). However, SEM is a good technique to determine mineralogy and mineral distribution in the sample.

4.3.3 Volumetric Analysis

A Micromeritics 3Flex volumetric analyzer was used to automatically determine the gas sorption isotherms. The sample preparation process involved the crushing of the samples to powder particle sizes between 150 and 180 mesh, followed by degassing, using a VacPrep Degasser, for 16 hours at 110 ^{o}C. The adsorbates used were nitrogen (N_2) at 77 K, and carbon dioxide (CO_2) at 273K. These gases were used to determine the overall pore volume from the Micromeritics 3Flex volumetric analyser. 2-2.5 grams of shale samples were used for each N_2 isotherm, and a filler rod was utilized in all the experiments. 1-1.5 grams of each shale sample were used for the CO_2 isotherms. The sample tubes containing these shale samples were then submerged in 50% ethylene glycol solution. These solutions were contained in an isothermal controller maintained at 0 ^{o}C. The pressure measurement approach was used to measure the equilibrium isotherm of each sample tested; the partial pressure fluctuation was within 0.1%. Non-Local Density Functional Theory (NLDFT) was used to obtain the pore size distribution (Ravikovitch et al., 2000). This technique was adopted since it is considered that this is the most appropriate for shales because the pore sizes are so small, and various carbon DFT kernels have been successively used previously in experiments involving organic materials like carbons (Ravikovitch et al., 2000; Landers et al., 2013). In this study, the carbon slit pore model of NLDFT kernel was applied for meso- and macro-porosity determination using N_2 adsorption data, and the CO_2-DFT model was applied for microporosity using CO_2 adsorption data. The determination of the bulk density for each sample was performed using helium pycnometry.

4.3.4 Heat of Adsorption

The measurement of the heats of adsorption (such as in Figure 4.1) has been done using simultaneous calorimetry, as opposed to the method of isosteres and the Clausius-Clapeyron equation. The Clausius-Clapeyron (CAC) method cannot be used because it may lead to an overestimated isosteric adsorption heat because it utilizes the ideal gas law and assumes that the heat does not depend upon temperature. Both of these common assumptions do not apply in this case.

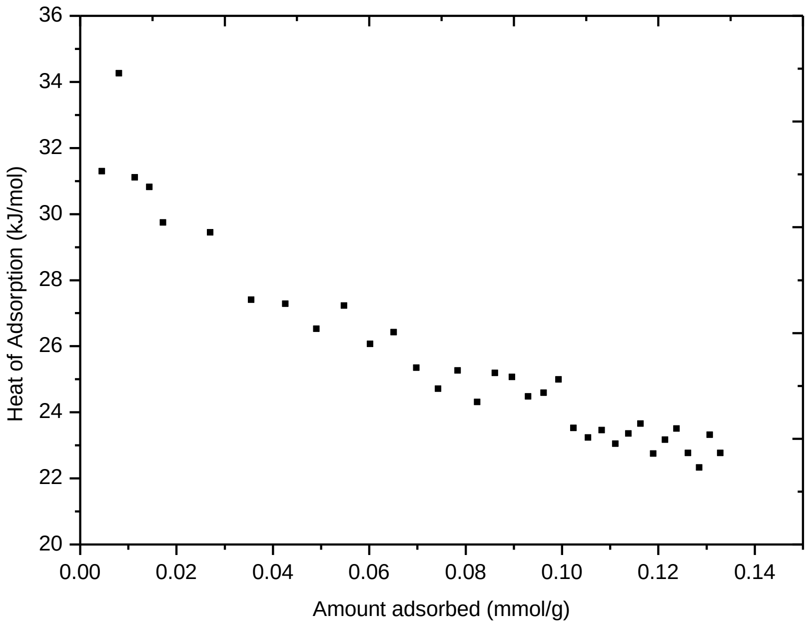

Figure 4.1 Variation of heat of Adsorption of CO_2 with coverage for Marcellus Shale 7804-7807 ft

The adsorption was performed in a Quantachrome Autosorb iQ. In order to precisely measure the real heats of adsorption for the duration of equilibration and the adsorption process, a Sensys Evo Tian-Calvet heat flux calorimeter was used. The calorimeter had to be placed as close as possible to the analysis station of the Autosorb iQ, with the aim of minimizing the length of the tube between the calorimeter cell and the analysis station. All the calorimeter results have been pre-calibrated with an indium standard.

4.3.5 Gravimetric Analysis

A Hiden XEMIS (gravimetric analyser) was used to obtain kinetic gas uptake data, and a schematic diagram of this apparatus is shown in Figure 3.2. In the case of each sample, a series of experiments was conducted with a range of sizes of steps in exterior bulk pressure from vacuum to different ultimate pressures. In the uptake experiments the set of values chosen for ultimate pressures in the pressure steps were close to that required to achieve a statistical monolayer according to the carbon dioxide adsorption isotherms. Even though experiments were carried out at different bulk concentrations over the isotherm, the range of bulk gas concentrations steps was consistent for all shale samples.

Gravimetric measurements were conducted using a sensitive microbalance which measured the change in mass of an adsorbent sample subjected to a step change in adsorbate concentration. This represents a direct indicator for the adsorption rate onto the solid. In the kinetic measurements case, only a small sample (usually of the order of ten milligrams) was used.

The adsorbents to be used were initially degassed overnight to remove the excess moisture. On completion of degassing the adsorbent is brought to the adsorption temperature by immersing in an isothermal water bath. At this point the system is ready for commencing adsorption. At time zero adsorbate gas passes through the ceramic tube and the sample weight change was monitored until constant mass was observed indicating that equilibrium had been attained. The adsorbent was then degassed again until constant mass was achieved and the gas that was initially injected had been desorbed. This procedure was repeated for all the points. Between twelve to eighteen data points were normally acquired to characterise an uptake curve. Lastly, data correction for buoyancy effects was also made.

4.4 Results and Discussion

In order to characterise the inorganic mineral content of the shale samples, Mineral Liberation Analysis (MLA) was used. The information thereby obtained for the samples is listed in Table 4.2. From Table 4.2 it can be seen that the samples are heterogeneous, being predominantly composed of illite, quartz, and carbonaceous phases. It is further noted that no kaolinite or smectite were detected in the Marcellus shale samples, which shows that these particular clay minerals must have undergone a complete transformation. Typically, the overall transformation of the clay takes place in two stages; kaolinite first transforms to smectite, and, then, smectite transforms into illite. The densities for the shale samples were obtained from helium pycnometry, and the values given in Table 4.2 are similar to those reported previously (Yu et al., 2016) for Marcellus shale of 2.63 g/cc, and shales in general (Manger, 1963) of 2.06-2.75 g/cc.

Figure 4.2 and Figure 4.3 show the adsorption isotherms for nitrogen and carbon dioxide, respectively, on Marcellus Shale samples from three different depths. It is highlighted that the pore volume of the microporosity decreased with depth, which also resulted in lower surface area (Figure 4.4). The reason for this decrease in the micropore volume was a combination of the change in content of both TOC and illite, as can be seen in Table 4.2.

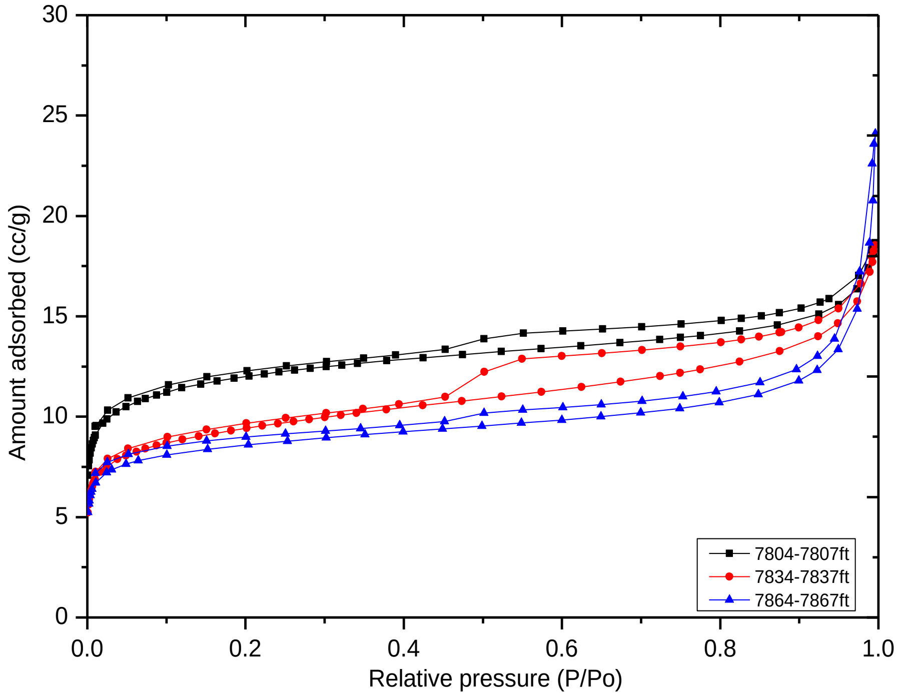

Figure 4.2 Adsorption isotherms for N_2 on Marcellus shale

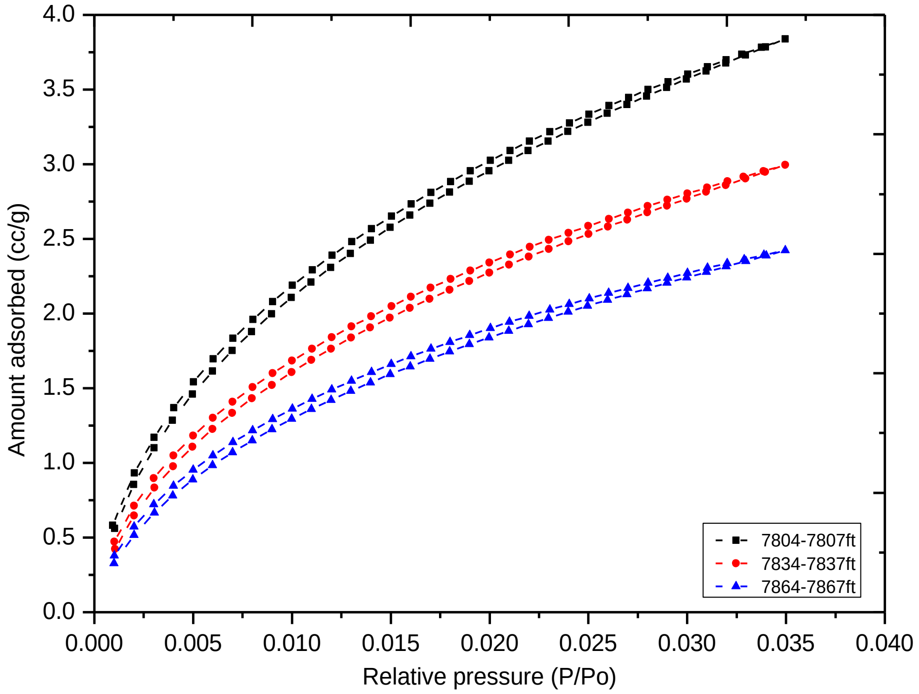

Figure 4.3 Adsorption isotherms for CO_2 on Marcellus shale

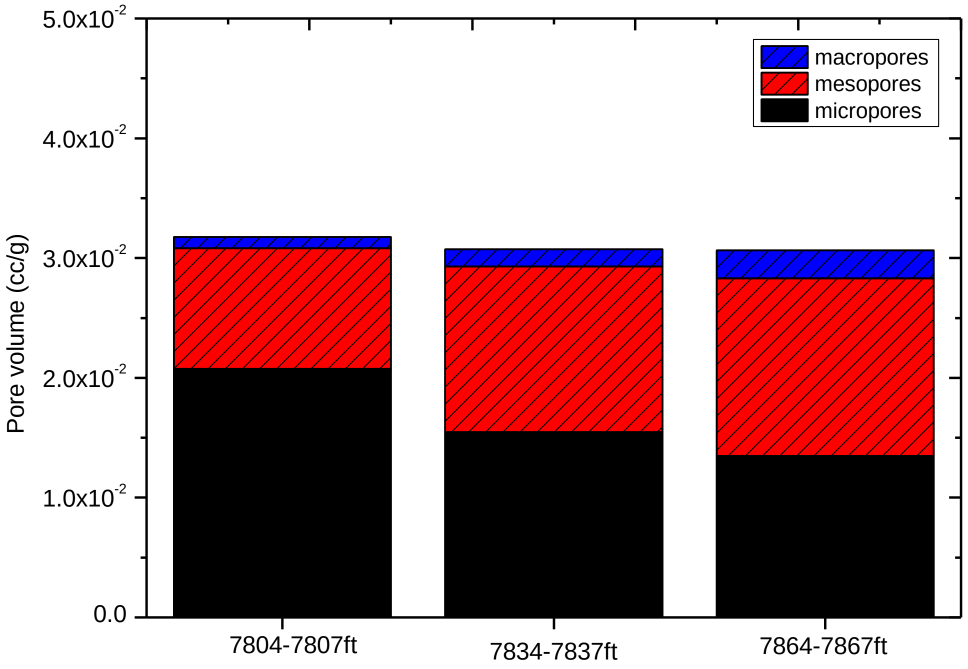

Figure 4.4 Pore size distribution of Marcellus Shale

Figure 4.5 shows an example of a fractal FHH plot obtained using one of the sets of nitrogen adsorption isotherm data given in Figure 4.2. The parameters obtained from such fits (using Eqs. (2.13) and (2.15)) to all the nitrogen isotherm data above a statistical monolayer coverage are given in Table 4.3. It can be seen that the surface fractal dimension tends to decline with increasing depth of the shale sample.

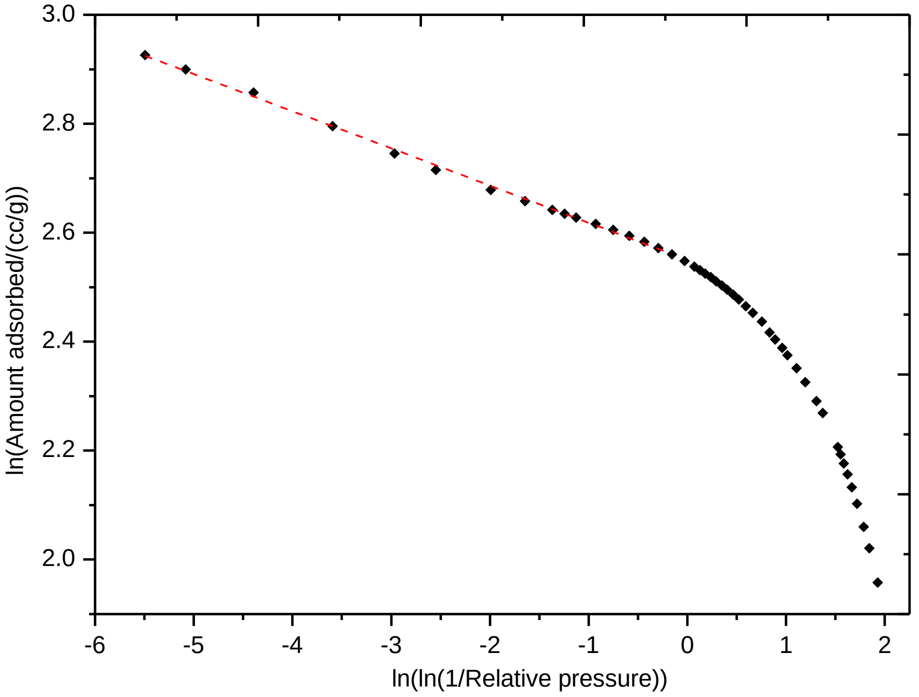

Figure 4.5 Fit of Fractal FHH Eq. (2.13) (dashed line) to the adsorption isotherm data (symbols) for nitrogen on Marcellus shale 7804-7807 ft

Table 4.3 Parameters obtained from fractal FHH analyses of the N_2 gas adsorption isotherms

Depth(ft)	Fractal dimension (d)	r^2 (FHH plot)	Fitted relative pressure range for FHH plot	$(R_n/r)^d$
7804-7807	2.937±0.003	0.996	0.42-0.996	3.29 ± 0.0033
7834-7837	2.893±0.001	0.996	0.43-0.996	3.23 ± 0.0014
7864-7867	2.847±0.005	0.995	0.44-0.995	3.17 ± 0.007

Examples of the isotherm data for CO_2 on the three shale samples, obtained via the gravimetric method, can be seen in Figure 4.6(a-c). Since the local adsorption equilibrium is reached quickly, these isotherm data were reasonably fitted to a Langmuir isotherm expression by using a non-linear regression technique for the selected temperatures of 10 °C,20 °C, and 30 °C. The agreement between the experimental data and Langmuir isotherm model was good, and the parameters, $C_{\mu s}$ and b, thereby obtained from this non-linear regression are given in Table 4.4 for the three temperatures. From Figure 4.6(a-c), it can be seen that the Langmuir isotherm fits the experimental data well for the three temperatures.

Table 4.4 Langmuir isotherm parameters for CO_2 on Marcellus shale derived from isotherms measured at the indicated different temperatures

Depth(ft)	Property	Temperature(°C)		
		10	20	30
7804-7807				
	$C_{\mu s}$ (mol/cm^3)	0.000534	0.000491	0.000443
	b(cm^3/mol)	49836	40855	35445
7834-7837				
	$C_{\mu s}$ (mol/cm^3)	0.000349	0.000332	0.000292
	b(cm^3/mol)	42527	33481	31649
7864-7867				
	$C_{\mu s}$ (mol/cm^3)	0.000279	0.000246	0.000229
	b(cm^3/mol)	40629	37290	31097

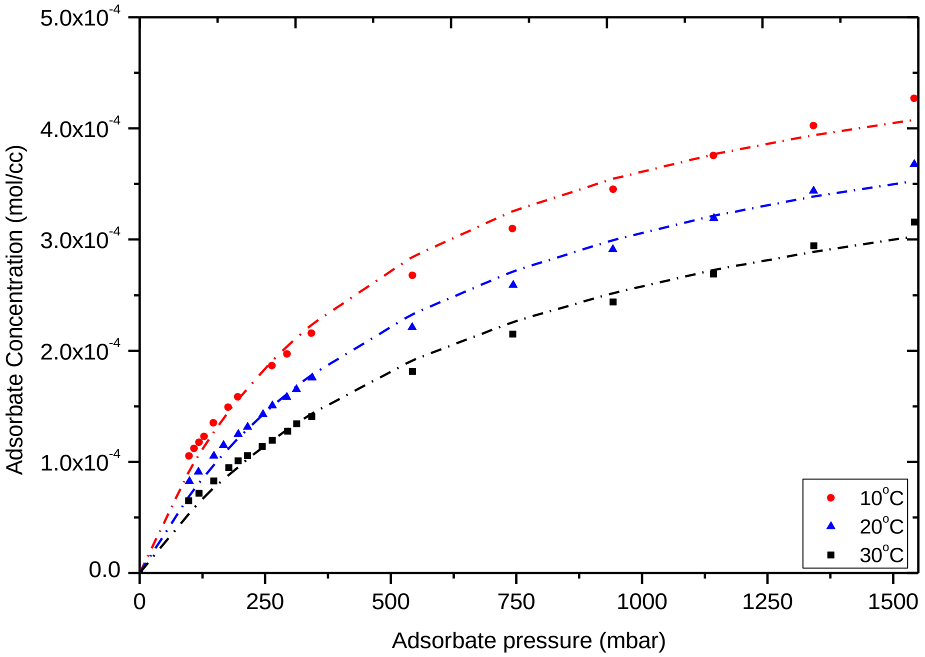
Adsorbate Concentration (mol/cc)
5.0x10^{-4}
4.0x10^{-4}
3.0x10^{-4}
2.0x10^{-4}
1.0x10^{-4}
0.0
0
250
500
750
1000
1250
1500
Adsorbate pressure (mbar)
10°C
20°C
30°C

(a)

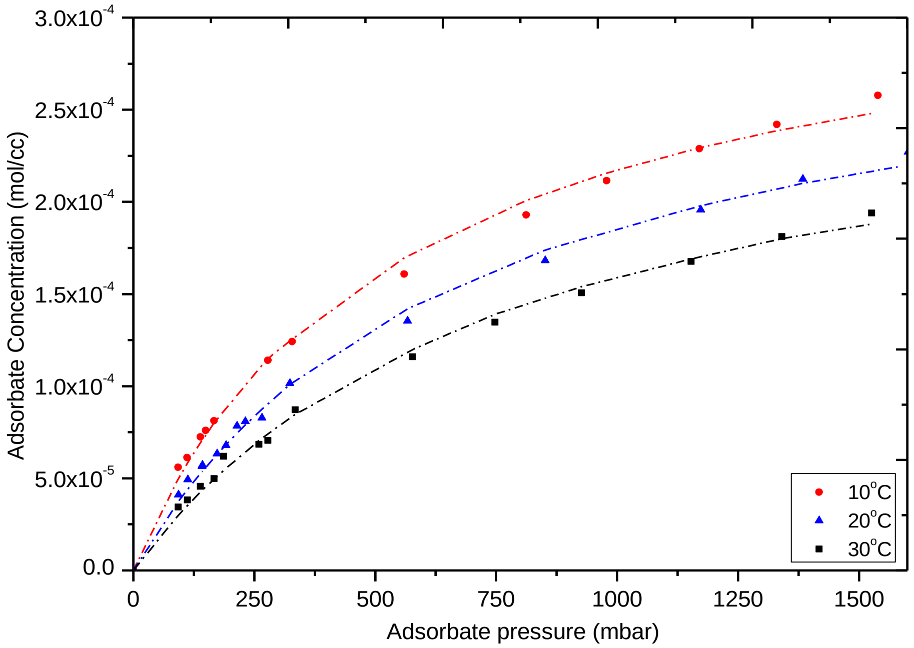
Adsorbate Concentration (mol/cc)
3.0x10^{-4}
2.5x10^{-4}
2.0x10^{-4}
1.5x10^{-4}
1.0x10^{-4}
5.0x10^{-5}
0.0
0
250
500
750
1000
1250
1500
Adsorbate pressure (mbar)
10°C
20°C
30°C

(b)

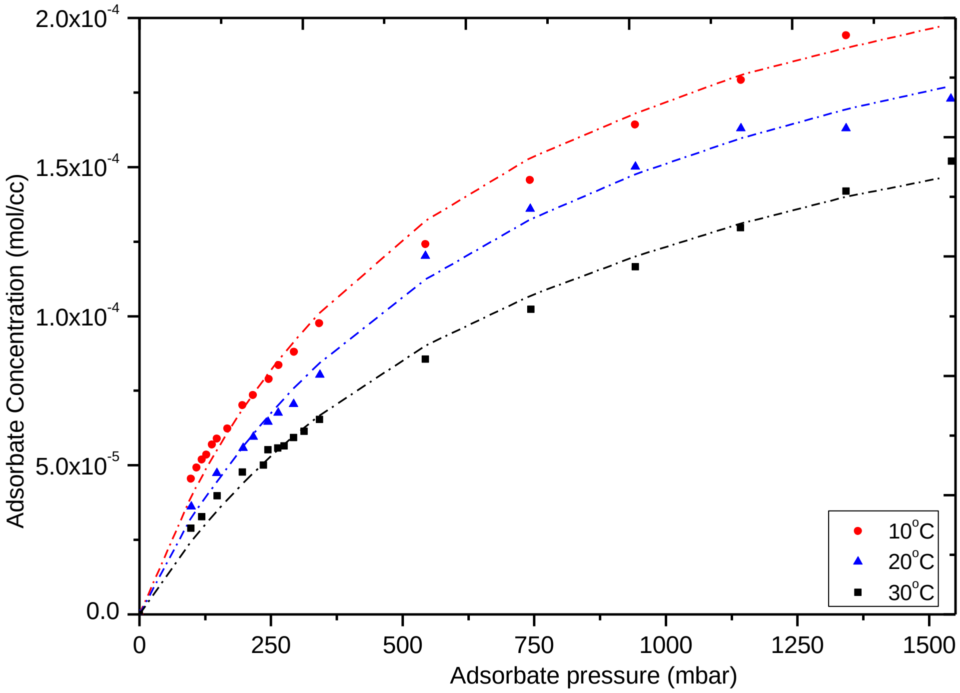

(c)

Figure 4.6 Isotherms for CO_2 adsorption onto Marcellus Shale from a) 7804-7807 ft b) 7834-7837 ft c) 7864-7867 ft measured at 100 °C , 200 °C, 300 °C using Xemis apparatus. The lines shown are fits to the Langmuir isotherm model using parameters given in Table 4.4

Figure 4.7 shows examples of the fractional uptake of CO_2 with time which was obtained via the gravimetric method at various different ultimate bulk concentrations of CO_2. When the initial bulk gas concentration is lower, the adsorption equilibrium time will also be shorter. A single exponential Linear Driving Force (LDF) model was used in order to fit the experimental data and thereby obtain the rate constant to find the half time of adsorption (Do, 1998). The measured half-times were ultimately used in Eq. (4.19) to estimate the surface diffusion.

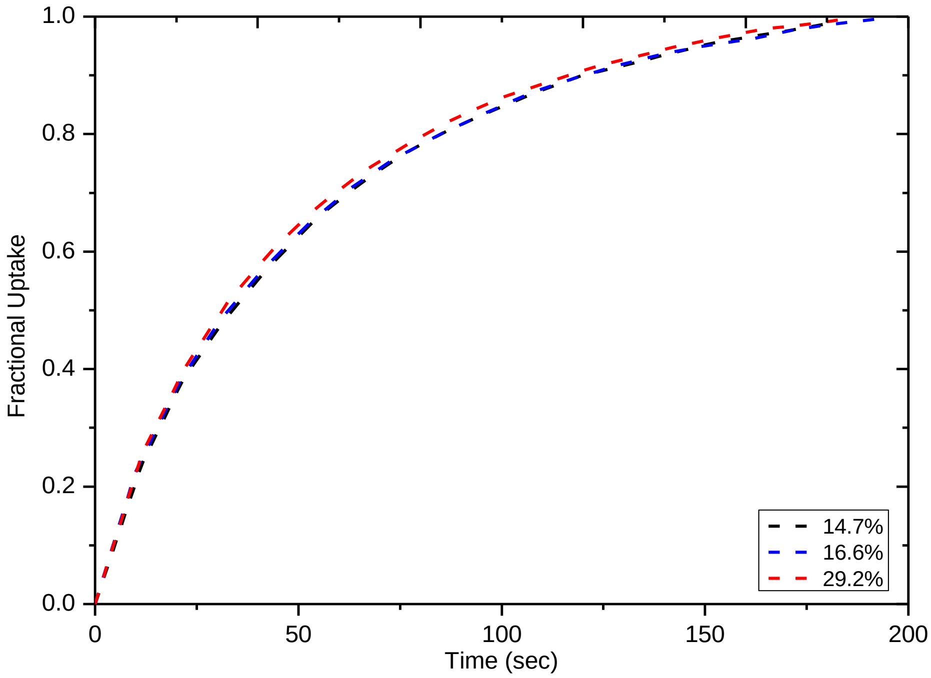

Figure 4.7 Plot of fractional uptake of CO_2 onto Marcellus shale 7804-7807 ft at three different bulk concentrations at 20 °C as listed with the legend

Figure 4.8(a-c) show the experimental fractional uptakes at three similar bulk concentrations of CO_2 for samples of spherical particles of shale having a radius of 0.00825 cm. It is noted that the half-time is decreasing with temperature for all three bulk concentrations and for all samples; that is the time to attain equilibrium is reduced at higher temperatures. These results are in agreement with past findings of Do for a spherical particle (Do, 1998). At this point, it should be emphasized that higher gas mobility systems do not necessarily mean that they will reach equilibrium at a much faster rate. The time to reach equilibrium is also dependent upon the ultimate adsorbed quantity that the solid can accommodate at the equilibrium state. The speed with which a system approaches equilibrium is determined by two factors: capacity and mobility. Given the same concentration of the bulk gas at the initial stages, it is considered that when the temperature is higher, the adsorption equilibrium time will be shorter.

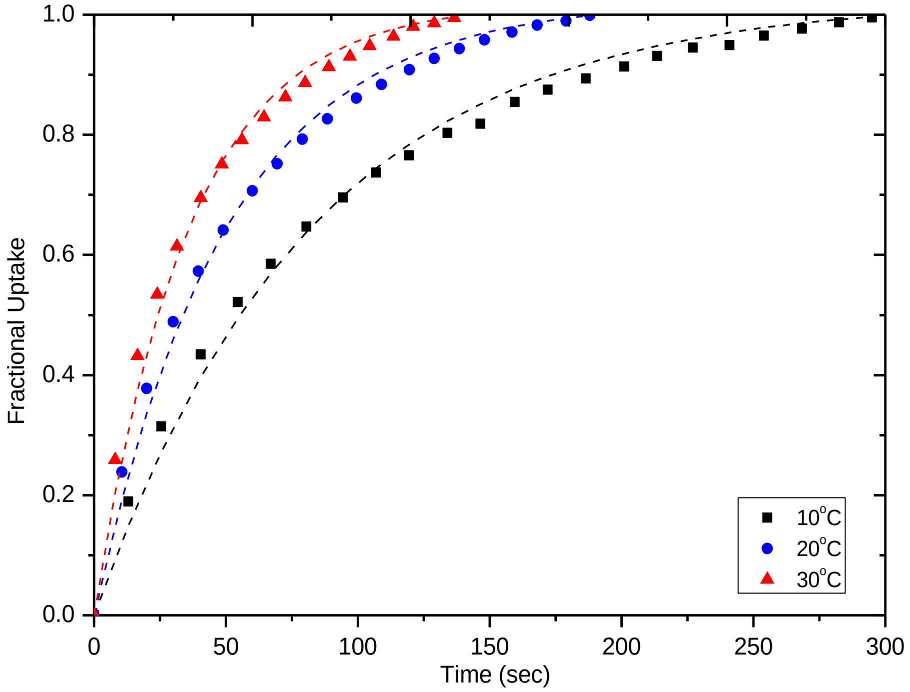
1.0
0.8
0.6
0.4
0.2
0.0
Fractional Uptake
0
50
100
150
200
250
300
Time (sec)
■ 10^oC
● 20^oC
▲ 30^oC

(a)

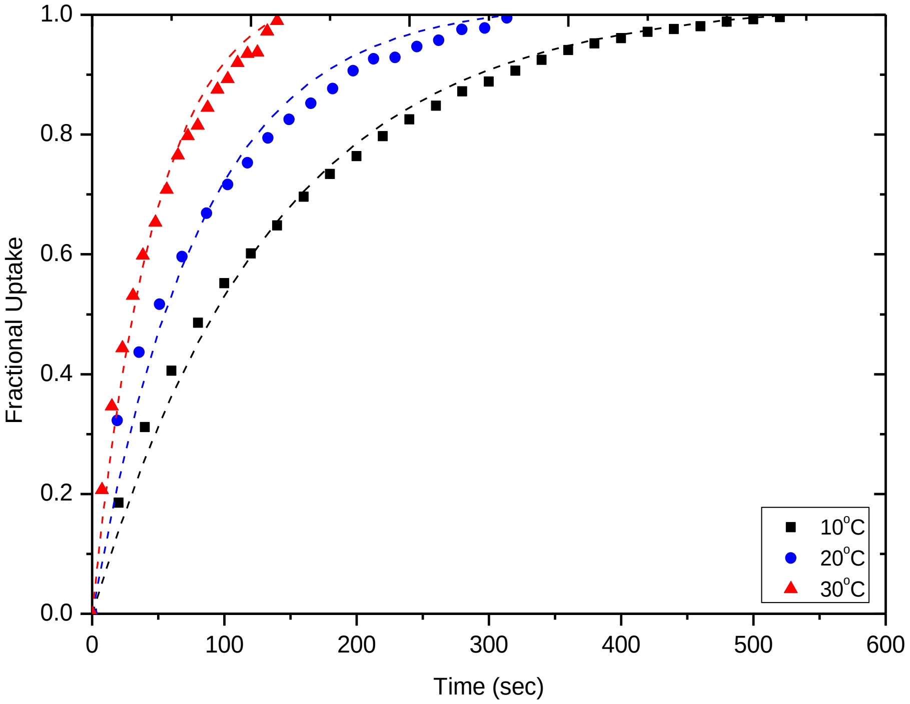
1.0
0.8
0.6
0.4
0.2
0.0
Fractional Uptake
0
100
200
300
400
500
600
Time (sec)
■ 10^oC
● 20^oC
▲ 30^oC

(b)

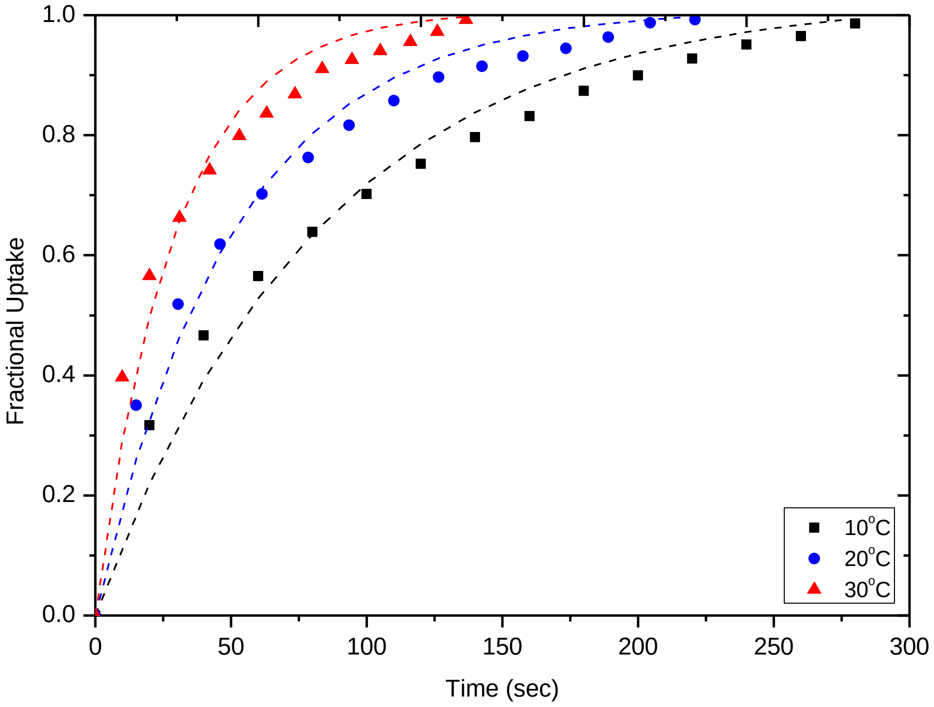

(c)

Figure 4.8 Experimentally measured (symbols) uptake curves, and fits to the LDF model (lines) for Marcellus shale a) 7804-7807 ft, b) 7834-7837 ft, c) 7864-7867 ft

The effectiveness of the Do technique (1991) for surface diffusion parameter determination was tested with the sorption data for CO_2 into the shale samples. Adsorption dynamics were measured at different bulk gas concentration steps but for the same range as explained in Section 4.4.4. Plotting the parameter Ω from Eq. (4.18) versus the parameter Ξ, as shown in Figure 4.9(a-c) for all the samples gave rise to straight lines, which were then used to estimate the slopes and the intercepts. From Eq. (4.18) the intercept and the slope correspond to $\varepsilon_M D_p$ and $(1-\varepsilon_M)D_s$ respectively. Figure 4.9(a-c) show that the data gave rise to good fits to the various expressions for the Do technique.

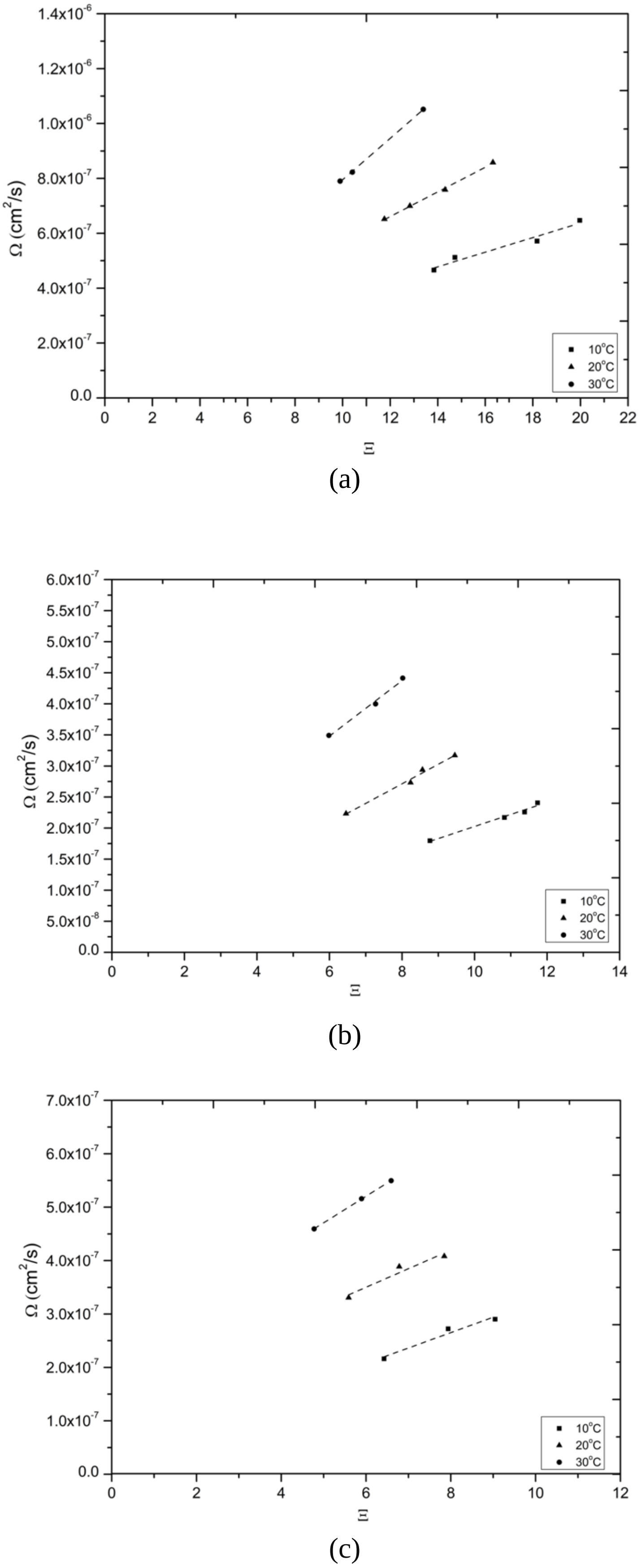

(a)

(b)

(c)

Figure 4.9 Plot of the term Ω versus Ξ given in Eq. (4.18) for Marcellus shale a) 7804-7807 ft b) 7834-7837 ft c) 7864-7867 ft. It can be noted that if dashes are extrapolated the intercept is positive

It should be noted that, if there was no surface diffusion occurring in the system, then a linear plot of the Eq. (4.18) must then have zero slope, with the intercept being the pore diffusivity. The CO_2 sorption data on the three Marcellus shale samples in the laboratory have indicated a good fitting to the theoretical uptake model. Therefore, this finding supports the implementation of the Do’s theory (1991) in heterogeneous systems like shales in which pore diffusion and surface diffusion may be determined within the system.

Figure 4.10 shows Arrhenius plots for the surface diffusivities of CO_2 on the three shale samples. The values of the surface diffusivities obtained in this work are similar in size to those obtained in previous studies in the literature, such as those found, by Karacan and Mitchell (2003), for CO_2 in coal. The values of pore diffusivities obtained here for CO_2 in the shales are ~10^{-6} cm^2/s. It should be noted that these results are consistent with previous findings (Karacan and Mitchell, 2003). In this study, pore diffusivity was not several orders of magnitude higher than surface diffusivity but of similar order of magnitude or only ten times larger. The reason is probably due to the existence of small pores restricting the entrance of CO_2 molecules into the shale. The resultant fitted Arrhenius parameters for the surface diffusivity at a monolayer coverage are shown in Table 4.5.

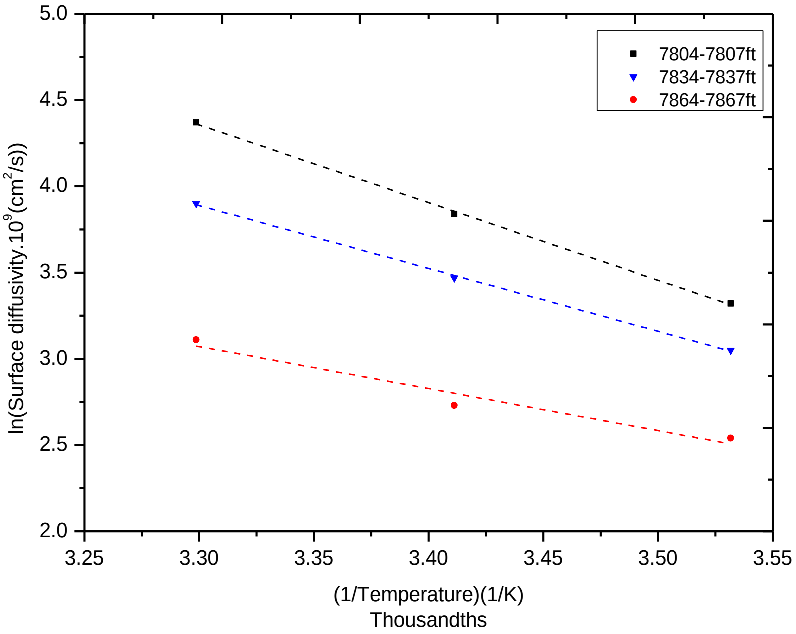

Figure 4.10 Arrhenius plot of the surface diffusivities for CO_2 on Marcellus shale from various depths

Table 4.5 Arrhenius parameters for the surface diffusivity of CO_2 on Marcellus shale samples

Depth(ft)	Heat of Adsorption(kJ/mol)	ln (pre-exponential factor 10^9(cm^2/s))	Activation Energy(kJ/mol)
7804-7807	26.5 ± 0.35	19.22 ± 0.47	37.45 ± 0.87
7834-7837	24.7 ± 0.33	15.80 ± 0.14	30.03 ± 0.28
7864-7867	22.7 ± 0.53	11.12 ± 0.54	20.27 ± 0.86

The characteristic isosteric heat of adsorption, ΔH, for each shale listed in Table 4.5 was calculated from the iQ-calorimeter. From Table 4.2 and Table 4.5, it can be seen that the heat of adsorption and surface area had a positive correlation with illite and the TOC content, while their correlation with quartz content was negative.

Figure 4.11 shows the correlation of the characteristic heat of adsorption of CO_2 with the group $(R_n/r)^d$ for the various depths of Marcellus Shale. The coefficient of determination for the fit to the data shown in Figure 4.11 was 0.999, and thus, a good fit between the fractal parameter $(R_n/r)^d$ and the heat of adsorption was obtained. The good quality of fit to a straight line shows that the data are consistent with the theoretical prediction given in Eq. (4.5).

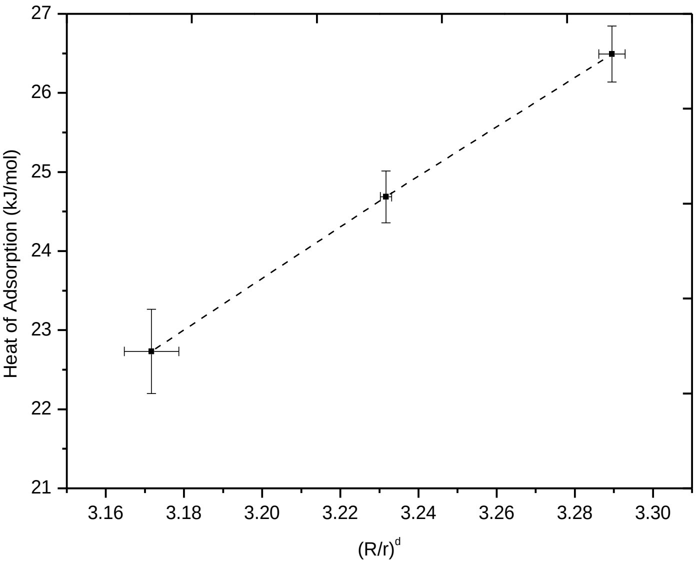

Figure 4.11 Variation of heat of adsorption of CO_2 versus $(R_n/r)^d$ for various depths of Marcellus shale. The solid line is a fit of the data to Eq. (4.6)

Figure 4.12 shows a plot of the natural logarithm of the pre-exponential factor for the surface diffusivity at a statistical monolayer coverage against the fractal dimension of the surface of the shale from the three depths of the Marcellus field described above. Figure 4.12 also shows a fit of the data to Eq. (4.4). It can be seen that the quality of fit is high (r^2=0.994) and thus the data are consistent with the fractal theory described in Section 4.2.1.

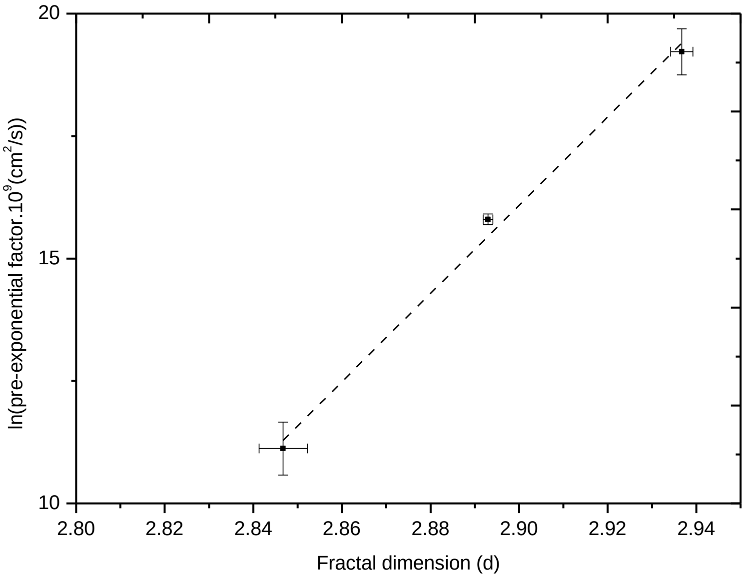

Figure 4.12 A plot of natural logarithm of the pre-exponential factor for the surace diffusivities for CO_2 against the fractal dimension on a variety of depths of Marcellus shale

Figure 4.13 shows a plot of the activation energy for the surface diffusivity at statistical monolayer coverage against the group $(R_n/r)^d$ for the shale sample from three depths of the Marcellus shale core. From Figure 4.13 it can be seen that a good fit of the experimental data was obtained to Eq. (4.6). It is noted that both the data for activation energy shown in Figure 4.13 and that for heat of adsorption in Figure 4.11 show a similar form of behaviour when plotted.

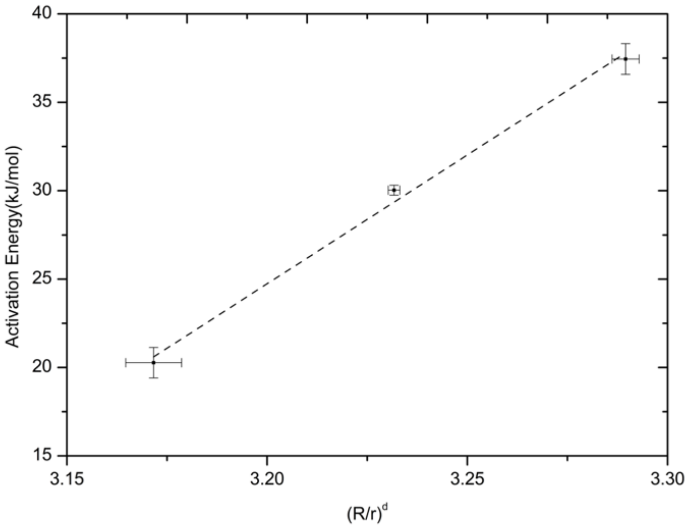

Figure 4.13 A plot of activation energies for the surface diffusivities of CO_2 against $(R_n/r)^d$ on different depths of Marcellus shale

Various past authors (Gilliland et al., 1974) have suggested that there is a linear relationship between these two enthalpy parameters, and the above findings are consistent with this proposal. This means that, if heat of adsorption has a linear relationship with $(R_n/r)^d$ and activation energy of surface diffusion, it then follows that the surface diffusion activation energy also has a linear relationship with $(R_n/r)^d$.

Figure 4.14 depicts a plot of the natural logarithm of the pre-exponential factor for the surface diffusivity at statistical monolayer coverage against the corresponding activation energy for surface diffusion on the shale samples. Figure 4.14 also shows a fit of the experimental data to a straight line of the form of Eq. (4.7).

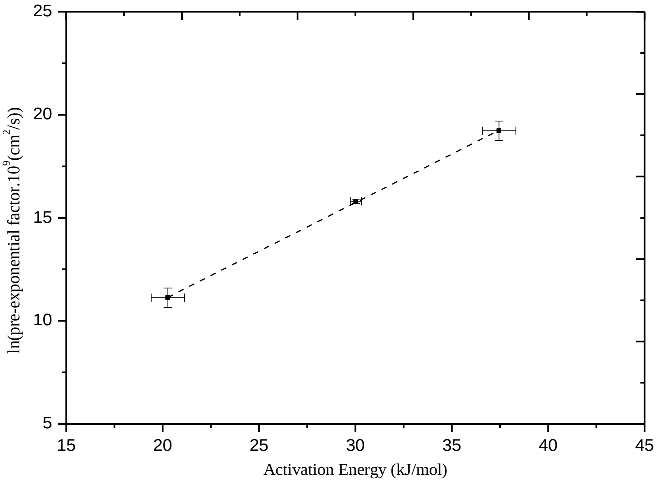

Figure 4.14 A plot of compensation effect of the Arrhenius parameters for the surface diffusivities of CO_2 *on Marcellus shale*

The results shown in Figure 4.14 suggest the occurrence of the theoretically predicted (Rigby, 2005) compensation effect for surface diffusion for CO_2. Moreover, it was determined that the activation energy for surface diffusivity for CO_2 produced a good fit for all three depths of Marcellus shale in accordance with the theoretical prediction, and hence the model is probably correct.

In summary, the results indicate that the data obtained for CO_2 surface diffusion on the Marcellus shale samples from different depths give outcomes consistent with the theoretical predictions. The fact that only one single fractal dimension for each shale was necessary to predict the surface diffusivity of CO_2 for such heterogeneous samples, may be a combination of two factors.

First, critical path analysis (Rigby, 2003a) suggests that the observed rate of mass transport processes in network-like structures, such as shale rocks, is controlled by a particular set of critical conductances. The critical conductance is the lowest value in the network of pathways through which the mass transport flux actually migrates. In a shale rock, these critical conductances would correspond to particular patches of the internal pore-space surface that had the critical value of surface diffusivity. These critical surface patches would be the regions of the rock through which the surface diffusion flux is necessarily funnelled. This is because conductances above the critical value have the most rapid mass transport and, therefore, they are not rate-limiting, while conductances below the critical value would not contribute appreciably to the flux and they are effectively bypassed. Hence, the observed surface diffusivity is that characteristic of the set of critical surface patches with intermediate surface diffusivity.

Second, previous work suggests that nitrogen is much more of a specific adsorbate than is commonly suspected (Watt-Smith et al., 2005). Even for supposedly relatively homogeneous materials, such as industrial sol-gel silicas, nitrogen has some tendency towards preferential adsorption, rather than being completely pervasively distributed across the whole surface (Watt-Smith et al., 2005). Therefore, pore structural parameters obtained from nitrogen sorption can be more heavily-weighted towards certain regions of the void space.

Hence, if the critical patches for surface diffusion are part of the pore space surface predominantly characterised by nitrogen sorption, then even for a relatively heterogeneous material the structural parameters obtained from gas sorption will be predictive of the observed surface diffusivity. These two pore space regions are likely to overlap because the above findings suggest regions with intermediate heat of adsorption will correspond to regions of intermediate surface diffusion activation energy. Further, it is frequently found for shales that most of the accessible void space is predominantly associated with one component, namely the carbonaceous pores, with only a relatively small fraction of accessible porosity associated with illite or quartz phases (Gu et al., 2016). Further, previous work (Rigby, 2003a) has indicated that for surface coverages around a statistical monolayer, due to surface heterogeneities and/or intermolecular interactions, adsorption on the surface is patchwise heterogeneous and surface coverages of the critical patches controlling mass transport approaches unity, irrespective of overall average surface coverage (at least for moderate partial coverages and above).

The combined diffusivity was calculated using the pore diameters attained through gas adsorption. The Bosanquet equation was applied in this calculation. The particle tortuosity was then calculated. Different values of tortuosity, ranging between 1.74 and 2.69, were obtained which are reasonable values for shale tortuosity given past results in the literature (Du and Nojabaei, 2020).

4.5 Summary

It has been found that Do's theory for combined pore and surface diffusion gives rise to good fits to data even for highly heterogeneous adsorbents such as shales, and, thence, the surface diffusivity can be effectively estimated. The technique of parameter determination was demonstrated using sorption data for CO_2 onto Marcellus shale. It has also been found that the experimental data shows that the surface geometry of the adsorbent determines the activation energy for CO_2 surface diffusion and the heat of adsorption. The activation energy and pre-exponential factor were both found to be dependent on the surface fractal dimension, and this led to an expected compensation effect. It has been found that the surface diffusion data for CO_2 on Marcellus shale from a variety of depths is consistent with the fractal theory developed by Rigby. The results confirm that the degree of structural heterogeneity of a shale surface determines the value of the Arrhenius parameters for surface diffusivity. Hence, the fractal theory for the structure-transport relation for surface diffusion can be used even for highly heterogeneous natural materials like shales.

5. Chapter Five: Evaluation of impact of surface diffusion on methane recovery via carbon dioxide injection in shale

5.1 Introduction

The world today is faced with a scarcity of conventional energy sources due to population growth and technological advancement (Lozano-Maya, 2016; Wang et al., 2017). The global demand of natural gas is predicted to rise by 35% by 2040, due to its relative environmental friendliness (EIA, 2020). In particular, gas shales are expected to contribute approximately 30% of the natural gas supply (EIA, 2020). The production potential of shale gas reservoirs, which are amenable to hydraulic fracturing and horizontal drilling techniques, has been scrutinized in order to overcome the depletion of conventional reservoirs and to supply the world with greater quantities of clean-burning energy (Yuan et al., 2015). As a result, there has been a paradigm shift in thinking towards unconventional gas that is now, to a large extent, changing the world energy landscape, leading to a rapid expansion of shale gas production, especially over the past decade. In particular, there has been an increase in supply from the shale resources in North America (Weijermars, 2014), namely the Marcellus Shale, as discussed in Chapter 4.

According to Pan and Connell (2015), shale gas production usually lasts for just under two years, while the free gas in large pores and fractures is mainly produced in the early stage of development. In the later production processes, the dominant source of gas is then adsorbed gas because the small pores in shale have slow desorption kinetics which restricts diffusion from the matrix (Yuan et al., 2014). Subsequently, shale gas production rate exhibits steep initial decline and gradually flattens out. Thence, there has been a growing interest in enhanced shale gas recovery (ESGR) via carbon dioxide (CO_2) injection. As highlighted in previous sections, the CO_2-ESGR injection technique does not just improve the production of CH_4 but also enables CO_2 sequestration. According to a number of studies, the main reason is the greater sorption affinity of CO_2 compared to that of CH_4 (Shi and Durucan, 2008; Busch et al., 2008)

In general, shales act as the seal, the reservoir, and/or the hydrocarbon source. The typical features of gas shales mainly include a small porosity, a very low permeability (ranging between 10^{-3} and 10^{-6} mD) and increased total organic carbon (TOC). As outlined in Section 2.3 of Chapter 2, bulk gas and adsorbed gas both exist in shale reservoirs simultaneously because of their unique nanoscale phenomena. Specifically, gas is stored as bulk gas within the pore space and as adsorbed gas on the internal shale matrix (Crosdale et al., 1998; Curtis, 2002; Pan and Wood, 2015). According to past studies, gases are adsorbed in the nanopores of clay minerals and organic matter, which make up the larger part of shale (Chalmers and Bustin, 2007; Ross and Bustin, 2007; Zhang et al., 2012). Notably, adsorbed gas is estimated to be up to 20%-80% of the total gas in place (OGIP) in five of United States shale formations, while a study conducted by Lu et al. (2015) for 24 Devonian shales found that adsorbed gas can average 61% of the total gas volume. A study conducted by Wang et al. (2016a) showed that, without the appropriate petrophysical corrections to commercial simulators (Eclipse, CMG, VIP) when considering gas adsorption, the original gas in place (OGIP) can be overestimated by approximately 50%.

In addition, shale-gas reservoirs (SGRs) have a gas mass-transfer process exhibiting a significant rate difference from that seen in conventional gas reservoirs. This kind of variation is ultimately attributed to the presence of organic matter and particular nano-scale phenomena. According to Xiong et al. (2017) and Firouzi et al. (2014) the diameter of organic pores is usually below 10 nm and accounts for 42% of the total volume. Moreover, the diameter of nanopores has the same order of magnitude as the gas molecular mean free path at reservoir conditions. The gas transfer regimes, occurring within the SGRs, include both bulk gas transfer and surface diffusion mechanisms (as highlighted in Section 2.4 of Chapter 2). The latter regime tends to have been overlooked by previous researchers, who have conducted reservoir simulations (Yu et al., 2016; Kim et al., 2017) to investigate the practical feasibility of use of CO_2 for gas extraction from shale reservoirs. Subsequently, gas production predicted may be significantly overestimated or underestimated. Further, Knudsen diffusion plays a significant role in mass transport within the nanopores of shale since it has the potential to contribute approximately 20% of the total produced gas at typical SGR conditions (Darabi et al., 2012). Experimental studies have also been made of transport and phase changes in fabricated nanofluidic models for shale rocks (Zhong et al., 2018; Jatukaran et al., 2019). However, while these model pore networks studied have included pore body-pore neck geometries, they are only 2D planar and thus miss the full three-dimensional connectivity of real rocks. These models also have only limited spatial extent and thus miss the impact of longer-range heterogeneities. Further, these experiments also only considered transport by Knudsen diffusion and viscous flow.

However, other experimental investigations have also indicated that surface diffusion is much more significant than the bulk gas transport where the pore network is not yet well-evolved within shale gas reservoirs (Rigby and Gladden, 1999; Rigby, 2003a). This means that, surface diffusion dominates in the microporous kerogen due to high surface area and the non-development of fractures within shales. It has also been shown that the surface diffusion of adsorbed gas and the Knudsen diffusion of the free gas, can increase the apparent permeability of the SGRs. Previous studies have indicated that the estimated apparent permeability may be several orders of magnitude higher than that of conventional hydrodynamic techniques (i.e. the Darcy and Klinkenberg models) (Holt, 2006; Rahmanian et al., 2010; Darabi et al., 2012). Thence, it is reasonable to say that the surface diffusion of adsorbed gas and the Knudsen diffusion of the free gas, can increase the apparent permeability of the SGRs and must be included to ensure accurate prediction of gas recovery, despite them generally being omitted in previous work.

In this study, a new dual permeability-dual porosity model of the Marcellus shale reservoir will be primarily generated based on existing geological data. The Langmuir isotherm is considered as a model for adsorption in different areas of Marcellus shale. Then, the bulk porosity, free gas saturation, and connate water saturation of the models are corrected, *a priori*, according to Wang's theory (2016b) to avoid overestimation of the volume of free gas and the original gas in place. Fracture height, fracture half-length, and fracture conductivity were the main fitting parameters used to obtain a good history match with gas field data (Yu et al., 2016). Thereafter, surface diffusion is implemented into a reservoir scale simulator. This was achieved by utilizing an established approach based on apparent permeability model that included surface diffusion (Wu et al., 2016). Most publications to date have used a theoretical model to predict surface diffusivity in a low-pressure condition (Hwang and Kammermeyer, 1966; Guo et al., 2008). In this study, the adsorbed-gas surface diffusivity in a low-pressure condition is estimated from gravimetric gas uptake experiments on Marcellus shale samples. In addition, Barnett and New Albany reservoir models are also generated from previous studies to investigate the significance of surface diffusion to CO_2 injection techniques in these locales. The fractal theory for surface diffusivity proposed, and tested, in Chapter 4 is applied, for the first time, to all reservoir models to permit the examination of the effects of degree of surface roughness on CH_4 production and CO_2 adsorption. Finally, a geostatistical approach is applied to assess the effect of larger-scale reservoir heterogeneity on gas production. The goal of this study is to provide insights into a better understanding of the effectiveness of surface diffusion on methane recovery via CO_2 injection techniques at shale reservoir scale.

5.2. Theory

5.2.1 Correction of petrophysical properties

Wang et al. (2016a, b) demonstrated a feasible approach to correct the petrophysical properties of shale gas reservoirs effectively within commercial reservoir simulators when considering gas adsorption. Figure 5.1 is a schematic depiction of the volumetric constituents of the nanopores within a typical shale matrix in both the petro-physical model and a commercial reservoir simulator. In commercial simulators, the volume of adsorbed gas is frequently treated as polymer, alkali or other chemical agents, or is often ignored. However, adsorbed gas comprises 20%-80% of the total gas in place and should not be overlooked as discussed in Section 5.1.

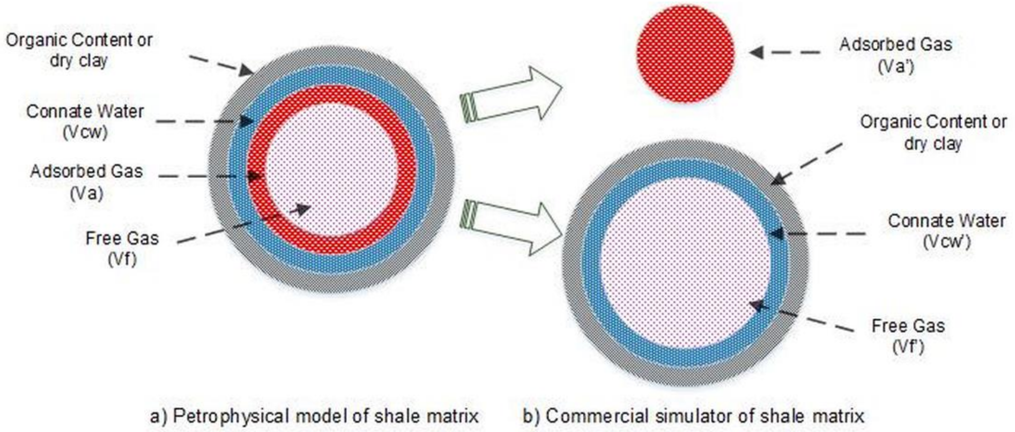

Figure 5.1 Schematic diagram illustrating the volume fractions of shale matrix in a) Wang et al. (2016a, b) petrophysical model and b) commercial reservoir simulator

As illustrated in Figure 5.1b, the total void volume (V_t’) is equal to the sum of the connate water volume (V_{cw}’) and the free gas volume (V_f’). In contrast, the total void volume (V_t) in the petrophysical model is equal to the sum of the connate water (V_{cw}), free gas (V_f), and gas adsorbed (V_a) (Figure 5.1a). Hence, the total void volumes (V_t’) and porosity (φ_t’) of both the petrophysical model and commercial simulator are expressed as:

$$V_t' = V_{cw}' + V_f' < V_t = V_{cw} + V_f + V_a \tag{5.1}$$

$$\phi_t' = \phi_{cw}' + \phi_f' = \phi_{cw} + \phi_f = \phi_t - \phi_a \tag{5.2}$$

where φ_{cw} and φ_{a} are the connate water porosity and adsorbed gas porosity, respectively. Eqs. (5.1) and (5.2) show that the free gas volume and porosity in the commercial simulator are overestimated, and, thus both the total void volume and porosity in the simulator should be less than that in Wang's petrophysical model of the shale matrix. Subsequently, bulk porosity, free gas saturation, and connate water saturation were corrected in order to accurately predict the gas production and reduce the error of OGIP. The theory behind the derivations will be given only briefly, since it is described extensively in previous work (Wang et al., 2016a).

Ambrose et al. (2012) proposed a new method for obtaining the storage capacities of both adsorbed and free gas. The storage capacities of free gas (G_f) and adsorbed gas (G_a) on the basis of Langmuir isotherm are:

$$G_a = V_L\left(\frac{P/Z}{P/Z+P_L}\right) \tag{5.3}$$

$$G_f = \frac{32.0368}{B_{gf}}\left[\frac{\phi_t(1-S_w)}{\rho_r} - \frac{1.318\times10^{-6}M}{\rho_{ga}}G_a\right] \tag{5.4}$$

where B_{gf} is the free gas volume factor, P_L is the Langmuir pressure, V_L is the Langmuir volume, S_w is the water saturation, ρ_r is the rock density, ρ_{ga} the adsorbed gas density and Z is the gas factor. Moreover, Ambrose et al. (2012) showed that the density of free gas and adsorbed gas is different in the shale matrix nanopore. Hence, the porosity ratio of free gas and adsorbed gas in the petrophysical model is:

$$\frac{\phi_{gf}}{\phi_{ga}} = \frac{V_{gf}}{V_{ga}} = \frac{G_f\rho_{ga}}{G_a\rho_{gf}} \tag{5.5}$$

Hence,

$$\phi_{ga} = \frac{\phi_{gf}G_a\rho_{gf}}{G_f\rho_{ga}} \tag{5.6}$$

At connate saturation, the total gas porosity is:

$$\phi_{gf} + \phi_{ga} = \phi_t(1-S_{wc}) \tag{5.7}$$

Substituting Eqs. (5.1) and (5.6) into Eq. (5.7), the corrected bulk porosity in the commercial simulator is:

$$\phi'_t = \phi_{gf} + \phi_{wc} = \phi_t - \frac{\phi_{gf} G_a \rho_{gf}}{G_f \cdot \rho_{ga}} \tag{5.8}$$

The connate water saturation and free gas saturation in the simulation model are:

$$S'_{\mathrm{wc}} = \frac{\phi_t S_{wc}}{\phi'_t} = \frac{G_f \rho_{ga} \phi_t S_{wc}}{G_f \rho_{ga} \phi_t - \phi_{gf} G_a \rho_{gf}} \tag{5.9}$$

$$S'_{gf} = \frac{G_f \rho_{ga} \phi_t (1 - S_{wc}) - \phi_{gf} G_a \rho_{gf}}{G_f \rho_{ga} \phi_t - \phi_{gf} G_a \rho_{gf}} \tag{5.10}$$

Consequently, the total porosity, water saturation and gas saturation used in the commercial reservoir simulator are calculated, *a priori*, according to Eqs. (5.8), (5.9), and (5.10) respectively. It should be mentioned that these equations have already been validated in previous studies using field data obtained from Marcellus and Barnett shale (Wang et al., 2016a).

5.2.2 Gas Transfer mechanisms for shale gas

Numerical simulations play a major role in comprehending and forecasting the production of gas and oil from reservoirs. In industry a range of commercial reservoir simulator packages are used. However, mass transport within reservoir models constructed with these commercial simulators is generally based upon Darcy's law, and, thence neglects certain gas transfer mechanisms that exist within the SGRs. As a result, the shale gas production forecasted can be overestimated, or underestimated, when the apparent permeability is not used. Previous studies have demonstrated (Wang et al., 2016b; Wu et al., 2016) that the Darcy flow permeability can be corrected for additional transport mechanisms via multipliers, which are functions of gas pressure and are input into the simulator model.

The mass flux for total fluid transfer, J_t, is given by (Wu et al., 2015; Wu et al., 2016; Huang et al., 2018):

$$J_t = J_b + J_s = J_{vs} + J_k + J_s \tag{5.11}$$

where J_b is the mass flux of the bulk gas transfer and J_s is the mass flux of the adsorbed gas surface diffusion. J_b includes the contributions from J_{vs} and J_k, which are the slip-flow flux and Knudsen diffusion flux, respectively. Substituting Eqs. (2.19) and (2.22), the bulk gas transfer in nanopores is:

$$
\begin{aligned}
J_t = &-\frac{1}{1+Kn}\zeta_{mb}\omega_s\omega_m\frac{r^2P}{8\mu RT}(1+\alpha Kn)\left(1+\frac{4Kn}{1-\psi Kn}\right)\frac{\mathrm{d}P}{\mathrm{d}l} \\
&-\frac{1}{1+1/Kn}\frac{2}{3}\zeta_{mb}\,\omega_s\omega_m r\delta^{D_f-2}\left(\frac{8}{\pi RTM}\right)^{0.5}\frac{\mathrm{d}P}{\mathrm{d}l}+J_s
\end{aligned}
\qquad (5.12)
$$

From Eq. (5.12), it can be observed that the adsorbed-gas flux and bulk-gas flux are determined from a simple sum, whereas the resultant gas flux in the bulk transfer phase is obtained by taking the weighted sum of Knudsen diffusion flux and slip-flow flux based on their respective contributions. Moreover, Eq. (5.12) demonstrates a correlation, for both the poromechanical and sorption-induced swelling responses, to the bulk gas flux, which varies with permeability during the development of SGRs (Wang et al., 2012).

5.2.3 Surface diffusion of adsorbed gas

Surface diffusion is of major importance in the overall gas mass transfer within the nanopores of shale reservoirs (Kang et al., 2011; Fathi and Akkutlu, 2014; Etminan et al., 2014; Xiong et al., 2017). Previous work has shown that it is more reasonable to investigate shale gas sorption via the Langmuir isotherm (Cui et al., 2009; Ambrose et al., 2010). As discussed in Section 2.4.4.1 of Chapter 2, Hwang and Kammermeyer (1966) and Guo et al. (2008) developed an analytical model which is widely used by various researchers to estimate the surface diffusion coefficient at low-pressure conditions. In this analytical model (hopping model), the equation of surface diffusivity is influenced by adsorbent, adsorbate and temperature.

However, this model overpredicts surface diffusivity at low pressure, which is an observation made by Do et al. (2001). In particular, Do et al.(2001) estimated surface diffusivities by analyzing kinetic data collected using three different kinetics methods: constant molar flow, the differential adsorption bed, and the differential permeation methods. The experimental results showed that the apparent surface diffusivity decreases very rapidly with molecular weight, and much more strongly than the inverse of the square root of molecular weight, as obtained by Hwang and Kammermeyer (1966) and Guo et al. (2008), and, thus this latter model will not be used.

Experimental measurements of kinetic gas uptake into a reference shale material were used to estimate the surface diffusivity of carbon dioxide at the limit of surface coverage tending to zero. As discussed in Section 4.2.3 of Chapter 4, the analysis of the experimental kinetic data was performed using the dual-diffusion model proposed by Do and Rice (1991). This analysis was used to obtain an estimate of the surface diffusivity at zero coverage for the reference surface. The sample particles used in this work have a roughly spherical shape and will be analysed as such in Section 5.3.1.

The difference in surface diffusion rates between different shales resulting from variation in surface roughness was determined using a fractal model. As was shown in Chapter 4, Section 4.2.3, for shales, both the pre-exponential factor and the activation energy for surface diffusivity are functions of the surface fractal dimension, and, thus the surface diffusivity on shales could be established from an equilibrium gas adsorption isotherm. Hence, the surface diffusivities for new surfaces can be obtained from measurements performed on a reference material and knowledge of the surface fractal dimension for the new surface.

The impact, on surface flow of surface occupancies above the zero limit, was obtained using the Chen and Yang (1991) model (as highlighted in Section 2.4.4.2 of Chapter 2). According to Eq. (4.18), D_{so} is initially estimated via gravimetric experiments using the dual-diffusion model and implemented in Eq. (2.27). Thereafter, in cases where the surface roughness for shales was other than that of the reference, the fractal model in Eq. (4.1) was applied to estimate D_{so}.

In order to simplify the treatment of the contribution of surface diffusion to flow in the reservoir simulations, the component of effective permeability resulting from surface diffusion will be estimated using the properties of carbon dioxide alone. This assumption means that the impact of surface diffusion on methane production estimated below is likely to be a lower limit, given the relatively higher mobility of methane compared with carbon dioxide. In order to estimate the contribution of surface diffusion to effective permeability a series of models were used. First, an estimate of the surface diffusivity at zero coverage on a reference shale was obtained using a dual-diffusion model to analyse low pressure gas uptake experiments. Second, if considering simulations in shales other than the reference, this zero-coverage surface diffusivity was adjusted for the influence of different surface roughness between shales using a fractal model. Third, where the pressure was such that the surface coverage was above zero the surface diffusivity was also adjusted accordingly using a model for the impact of surface occupancy on migration. The resultant surface diffusivity was then used to obtain the contribution of surface diffusion to the effective permeability for a particular shale.

5.2.3.1 Surface diffusion contribution to effective permeability

According to previous studies (Wu et al., 2015; Wu et al., 2016; Huang et al., 2018) the apparent permeability of adsorbed gas surface diffusion can be expressed as:

$$k_{\mathrm{s}} = -\frac{J_{\mathrm{s}} V_{\mathrm{std}} \mu}{M \mathrm{d}P/\mathrm{d}x} = \zeta_{\mathrm{ms}} D_{\mathrm{s}} \frac{C_{\mathrm{s}} V_{\mathrm{std}} \mu}{PM} \tag{5.13}$$

where

$$\zeta_{ms} = \frac{\phi}{\tau}\left[\left(1 - \frac{d_M}{r}\right)^{-2} - 1\right] \tag{5.14}$$

and

$$C_s = \frac{4\theta M}{\pi d_M^3 N_A} \tag{5.15}$$

$$\theta = \frac{P}{P_L + P} \tag{5.16}$$

where C_s is the adsorbed gas concentration; ζ_{ms} is the correction factor of surface diffusion of adsorbed gas; d_M is gas molecular diameter; and N_A is Avogadro's constant.

Eq. (5.13) is based on the combination of the Maxwell-Stefan method, which states that the driving force of surface diffusion is a chemical potential gradient, and the assumption that the gas behaves as an ideal gas (Krishna and van den Broeke, 1995; Do et al., 2001).

5.2.4 Apparent Permeability Model Flow Gas Transfer in Shale Nanopores

The gas transfer mechanisms discussed above include slip flow, Knudsen diffusion, and surface diffusion in the nanopores of SGRs. The sum of each gas flux mechanism comprises the total gas flux. While the adsorbed-gas flux and bulk-gas flux are determined from a simple sum, the slip-flow flux and Knudsen diffusion flux are determined from the weighted sum.

By Combining Eqs. (5.12) and (5.13), the apparent permeability for the total gas transport through shale nanopores, comprising of slip flow, Knudsen diffusion and surface diffusion, is expressed as:

$$k_t = k_{vs} + k_k + k_s \tag{5.17}$$

where

$$k_{vs} = \frac{1}{(1+Kn)} \zeta_{mb} \omega_m \omega_s \frac{r^2 (1+\alpha Kn)}{8} \left(1 + \frac{4Kn}{1-\psi Kn}\right) \tag{5.18}$$

$$k_k = \frac{1}{(1+1/Kn)} \zeta_{mb} \omega_m \omega_s \frac{2}{3} r \delta^{D_f - 2} \left(\frac{8RT}{\pi M}\right)^{0.5} \frac{\mu}{P} \tag{5.19}$$

$$k_s = \zeta_{ms} D_s \frac{C_s RT\mu}{P^2 M} \tag{5.20}$$

Eq. (5.17) has been validated through molecular simulation and experimental data (Wu et al., 2015; Wu et al., 2016). The model includes the effects of rarefaction, slippage, poromechanical response, nanopore structure (porosity, pore size, surface roughness, and tortuosity), and sorption-induced-swelling response on the bulk-gas transfer. It can successfully describe the contributions of each gas transfer mechanism taking into account the impact of Knudsen diffusion and slip-flow on bulk gas transfer. Notably, it includes the contribution of surface diffusion which is considered as an essential mechanism for transport in the nanopores of shale reservoirs.

5.3 Methods

5.3.1 Experimental Method

Marcellus Shale samples were used as the reference material for this study to estimate surface diffusion at a low-pressure condition. Dynamic measurements were made by using a gravimetric method. Kinetic gas uptake data were obtained from a gravimetric analyser (Hiden XEMIS) using a sensitive microbalance (see Figure 3.2), which measured the change in weight of a shale sample subjected to a step change in adsorbate concentration.

Marcellus shale samples were initially degassed at 383K overnight to remove the atmospheric moisture. Then, the sample is brought to the adsorption temperature (328K), chosen to be similar to the actual reservoir conditions used in the simulations. The reservoir temperature is achieved by immersing the adsorbent in an isothermal water bath. Thereafter, adsorption initiates where the adsorbent was exposed to adsorbate gas which passes through the ceramic tube. With sufficiently long adsorption times and monitoring of the sample weight change, constant mass was determined indicating that equilibrium had been attained. Then, the sample was degassed at elevated temperature in order to desorb the gas that was initially injected. By repeating this procedure for a series of various bulk concentrations, a series of uptake curves was generated. Lastly, the uptake curves were corrected for buoyancy effects.

5.3.2 Numerical Reservoir Simulation Method

In this study, the main tool that is used for simulating CO_2 injection is the GEM simulator, which is the CMG (Computer Modelling Group) advanced general equation-of-state compositional simulator (CMG-GEM, 2019). First, a single porosity (SP) model, as proposed by Yu et al. (2016) without considering the gas-desorption effect, was generated.

However, the model did not consider the natural fracture system which is crucial for CO_2 injection. Previous studies showed that, actually, a dual permeability model in unconventional reservoirs offers the best prediction of production performance, and yields more reliable outcomes for shale reservoir analysis (Ho, 2000; Moridis et al., 2010; Guo et al., 2018). Hence, for the base case, a dual porosity dual-permeability model (DP-DP) was developed by keeping constant the main parameters from the SP model (Table 5.1) and adding natural fracture porosity and permeability. Subsequently, flow via matrix and fractures to the production well, were considered. Once the DP-DP numerical model was history matched with existing field data, then the adsorption capacity from different areas of Marcellus shale was included (Table 5.2). The corrections presented in Section 5.2.1 were also applied to avoid overestimation of the volume of free gas and the original gas in place.

Table 5.1 Reservoir and fracture parameters for the Marcellus Shale well (Yu et al., 2016b)

Parameter	Value
Initial reservoir pressure, psi	5100
Reservoir Temperature, K	328
Reservoir permeability, nD	800
Reservoir porosity, upper layer	7.1%
Reservoir porosity, bottom layer	14.2%
Initial water saturation	10%
Total compressibility, psi^{-1}	3×10^{-6}

Number of stages	16
Cluster spacing, ft	50
Gas specific gravity	0.58
Fracture height, ft	95
Fracture conductivity, md-ft	3.5
Fracture half-length, ft	400
Total number of fractures	64

5.3.2.1 Basic Reservoir model

A commercial simulator (CMG-GEM) was used for the numerical modelling and the analysis of CO_2 injection into the shale reservoirs. The basic 3-dimensional DP-DP model for the Marcellus reservoir (Figure 5.2) was constructed via history matching with existing field scale gas production data published by Chief Oil and Gas LLC (Yu et al., 2016), using CMG-MOST (CMG-MOST, 2019) (please see Appendix B). Fracture half-length, fracture conductivity, and fracture height were the main tuning parameters used to obtain a good history match (Table 5.3). After extensive numerical simulations, the best match obtained for the cumulative gas production data has only 0.7% of average matching error (Figure 5.3). Similar to previous researchers, the flowing bottomhole pressure (BHP) (Yu et al., 2016) was utilised to constrain the reservoir simulation.

The field reservoir dimensions are 6,000 ft × 1,500 ft × 130 ft (i.e. length, width and thickness respectively), and there are two shale layers in the reservoir (the upper and the bottom layers) whose porosity values are 7.1 % and 14.2 %, respectively (Yu et al., 2016). Stimulation of the horizontal well is done in the bottom layer that contains 16 fracturing stages, as well as four perforation clusters in every stage with a cluster spacing of about 50 ft in total, such that the length of the well is approximately 3,900 ft. It is assumed that the reservoir is homogeneous, where the fractures are spaced evenly with stress independent permeability and porosity. It should be mentioned that the distance between production and injection wells is 775 ft and remains constant for all of the areas within the Marcellus reservoir.

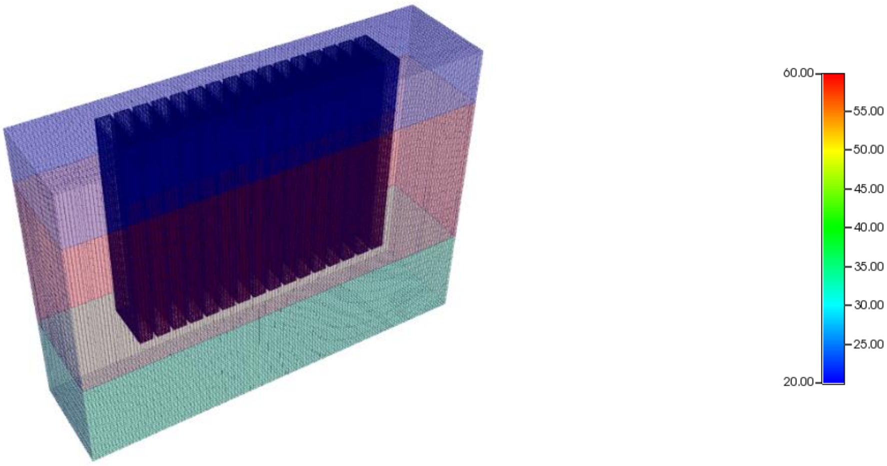

Figure 5.2 Schematic view of the DP-DP model of Marcellus shale reservoir. The dark blue area and the colour variation represent hydraulic fractures and reservoir thickness (ft), respectively. The scale bar is the reservoir thickness (ft)

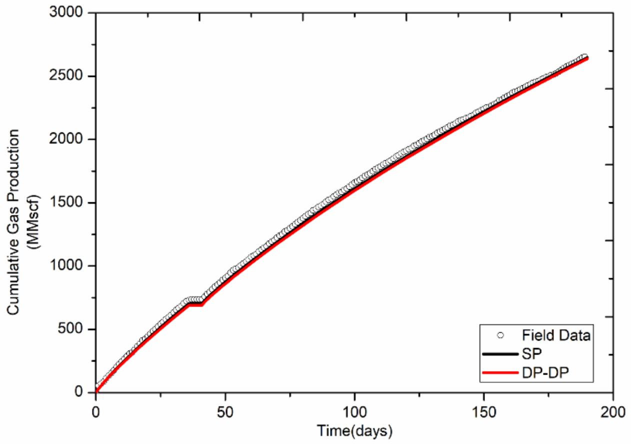

Figure 5.3 Comparison between field data (symbols) for cumulative gas production (Yu et al., 2016) and simulation data (lines) of SP model and DP-DP model.

In the subsequent simulation studies, gas adsorption capacity was considered in the DP-DP model for different areas of Marcellus shale. In particular, the shale samples investigated in this study are taken from the areas of Oatka, Canoga, Bedford, and Burlington (Dilmore et al., 2015). Since gas adsorption is to be considered, the petrophysical properties of the models are corrected according to the theory proposed by Wang et al. (2016b).

In order to correct the total porosity, water saturation, and gas saturation *a priori*, Eqs. (5.8), (5.9), and (5.10) were used, respectively. Figure 5.4 shows that, otherwise, gas production leads to an overestimated OGIP without applying formula corrections (Eqs. (5.8), (5.9), (5.10)) after

30 years. The results in Figure 5.4 are in agreement with similar findings by Wang et al. (2016b), where an overestimation of up to 50% of gas production was observed.

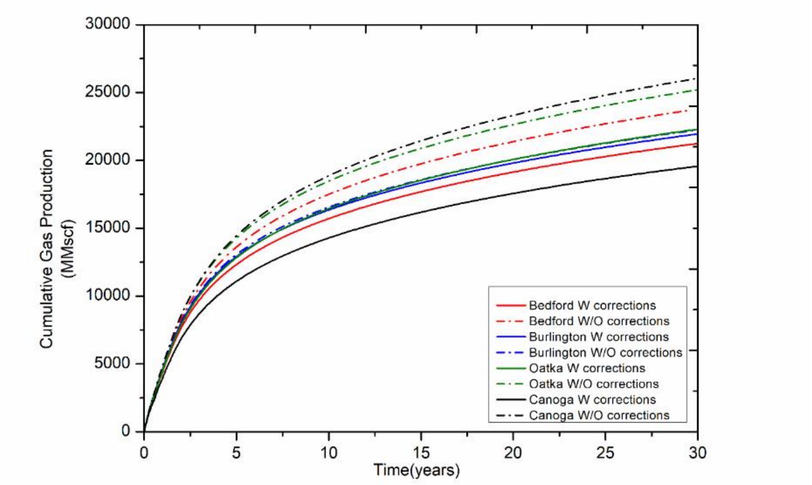

Figure 5.4 Comparison of predictions of cumulative gas production performance carried out both with(W) and without(W/O) corrections proposed by Wang et al. (2016b)

Competitive adsorption of CO_2 and CH_4 on the shales was described using a multi-component Langmuir isotherm. The parameters for this isotherm were obtained from pure component adsorption experiments. The Langmuir constants for CH_4 and CO_2 for the calculation of the competitive sorption mechanism were obtained from experiments on Marcellus shale cores (Dilmore et al., 2015). The shale samples were initially degassed at elevated temperatures (110 ^{o}C) to remove excess moisture and contaminants from the air. Since these experiments were performed at different temperatures from the reservoir simulation model, the combined Langmuir-Freundlich model 2 (Eq. (5.21)) was applied which has been shown to predict successfully the gas adsorption data at multiple temperatures (Fianu et al., 2018) (Figure 5.5 and Figure 5.6):

$$V = V_L \exp\left(\frac{-q_1}{T}\right)\left(\frac{b_i P^n}{1+b_i P}\right) \tag{5.21}$$

where

$$b_i = b_0 \exp\left(-\frac{\Delta H_{\text{ads}}}{RT}\right) \tag{5.22}$$

where ΔH_{ads} is the heat of adsorption, b_o is the pre-exponential factor, and q_1 a temperature-independent constant. The Langmuir constants of CH_4 and CO_2 for the calculation of the competitive sorption are presented in Table 5.2.

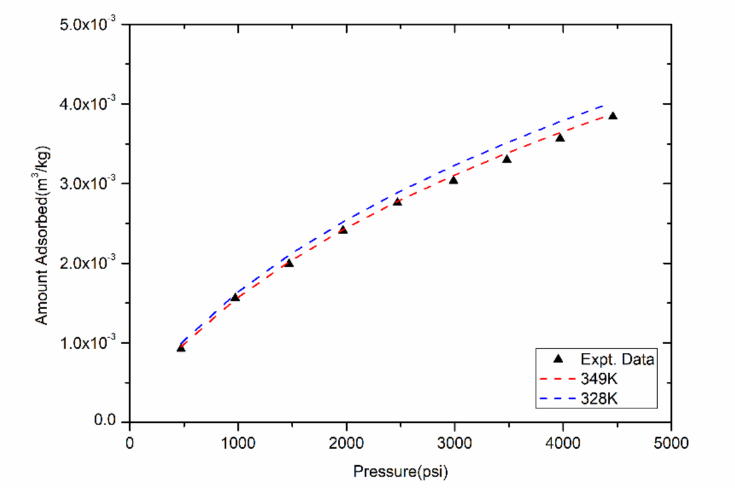

Figure 5.5 Experimentally (Expt.) measured adsorption data (symbols) for CH_4 on Oatka area of Marcellus shale at temperature of 349 K. Also shown (dashed lines) are fits of the combined Langmuir-Freundlich isotherm model

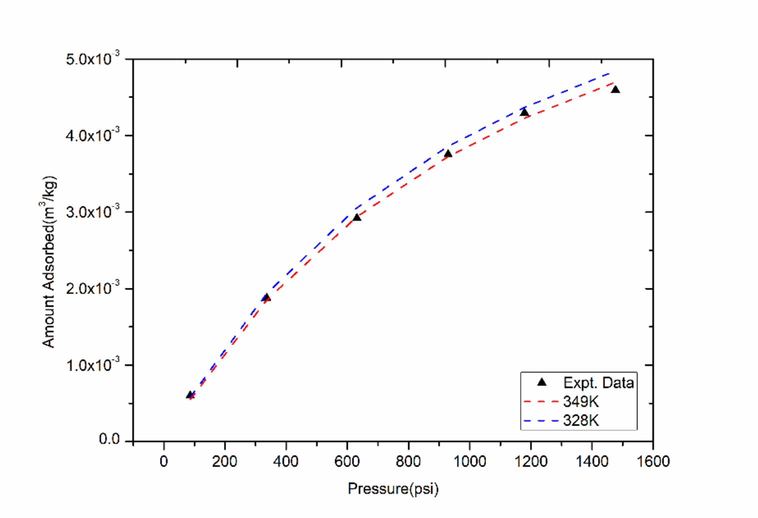

Figure 5.6 Experimentally (Expt.) measured adsorption data (symbols) for CO_2 on shale from the Oatka area of the Marcellus shale at temperature of 349 K. Also shown (dashed lines) are fits of the combined Langmuir-Freundlich isotherm model

Table 5.2 Parameters of the multicomponent Langmuir isotherm model for adsorption of CH_4 and CO_2 for shales taken from the various stated areas of the Marcellus shale reservoir

	CH_4			CO_2		
Region of Marcellus	P_L(psi)	V_L(scf/ton)	b_i(1/psi)	P_L(psi)	V_L(scf/ton)	b_i(1/psi)
Oatka	2833	209.0	0.000353	1155	283.5	0.000866
Bedford	1209	133.5	0.000827	1116	352.1	0.000896
Burlington	4771	26.3	0.000210	2951	93.1	0.000339
Canoga	1027	283.5	0.000974	326	360.0	0.003068

Once the gas adsorption capacities with the corrected petrophysical properties were implemented in the base case model (i.e. DP-DP without desorption), separate history matching was performed for all the different areas.

Previous studies have shown that fracture half-length, fracture height, and fracture conductivity are the key parameters to obtain a good history match at the early stage of gas production (Yu and Sepehrnoori, 2016; Yu et al., 2016). Thus, history matching was performed by tuning these three parameters. During the history-matching process both fracture height and half-length were reduced relative to the base case model (i.e. DP-DP with no desorption) for each sample (Table 5.3) from different locales. This observation is in agreement with past findings of previous researchers (Yu and Sepehrnoori, 2016; Yu et al., 2016) for different regions in Marcellus shale reservoir. As shown in Figure 5.7, a good match to the raw adsorption data was obtained using the Langmuir adsorption isotherm for the four samples from the different areas of the Marcellus reservoir.

Table 5.3 Optimised reservoir and fracture parameters obtained from history matching

	Regions of Marcellus				
Parameters	No desorption	Oatka	Bedford	Burlington	Canoga
Reservoir Temperature, K	328	328	328	328	328
Matrix permeability, nD	800	800	800	800	800
Fracture permeability, nD	1000	1000	1000	1000	1000
Fracture height, ft	95	70	80	78	80
Fracture half length, ft	350	235	325	325	350
Fracture conductivity, md-ft	3.5	1.5	4	3.7	4.6

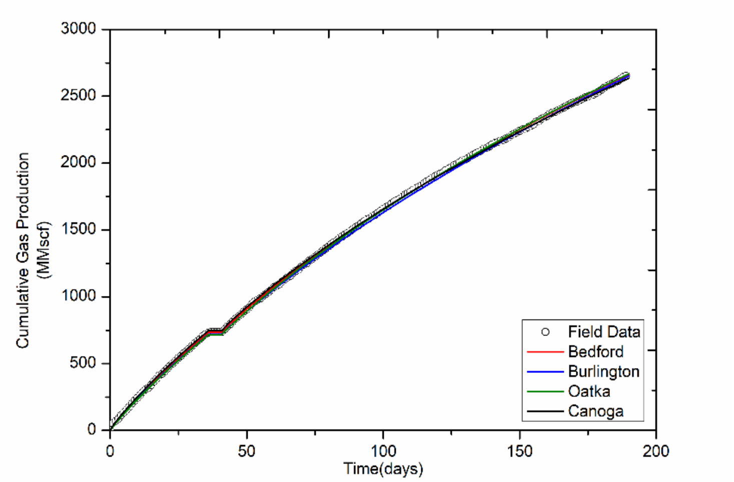

Figure 5.7 Comparison between field data (symbols) and simulation results, obtained with Langmuir isotherms, for cumulative gas production from different areas of Marcellus shale reservoir (lines)

5.4. Results and discussion

5.4.1 Surface diffusivity

Figure 5.8 shows the CO_2 equilibrium isotherm data for a representative sample of the Marcellus shale, obtained at the reservoir temperature (328K) via the aforementioned gravimetric method. The Langmuir isotherm fits the experimental data well for the reservoir temperature, and the parameters $C_{\mu s}$ and b, thereby obtained via nonlinear regression are given in Table 5.4.

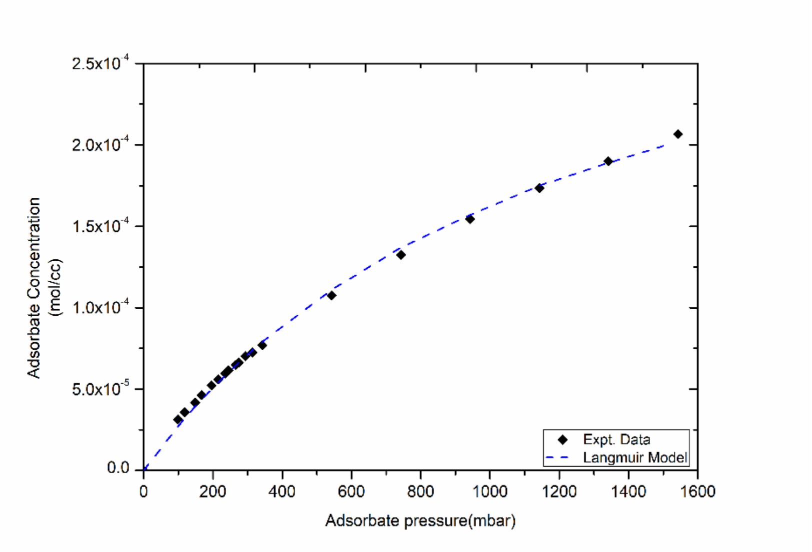

Figure 5.8 Equilibrum adsorption data for CO_2 on Marcellus shale at reservoir temperature of 328 K. Also shown (dashed line) a fit of the Langmuir isotherm model. The parameters are given in Table 5.4

The gravimetric kinetic uptake method was used to obtain the variation of fractional uptake of CO_2 with time at 328K for various bulk concentrations of CO_2 on Marcellus shale. The characteristic half time of the adsorption process was obtained by fitting a single exponential Linear Driving Force (LDF) model to the experimental data. The measured half-time was incorporated into Eq. (4.19) to estimate the surface diffusivity.

Figure 5.9 shows an example of a typical plot of a fit of the experimental data to the Linear Driving Force (LDF) model. Adsorption dynamics were measured at different ultimate bulk gas concentration steps for use in the Do model for surface diffusion.

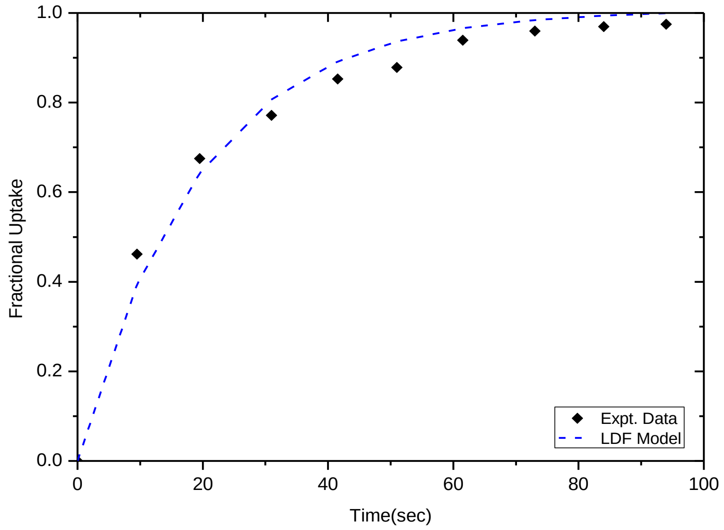

Figure 5.9 Experimentally measured (symbols) uptake curves and fits to the LDF mode (dashed line) for CO_2 on Marcellus shale at reservoir temperature of 328 K

The experimental uptake data was then fitted to the Do and Rice model (Do and Rice, 1991) for surface diffusion. It can be seen from Figure 5.10 that the agreement between the experimental data and the linear variation expected from the model of Do and Rice is good. Plotting the parameter Ω, from Eq. (4.19), versus the parameter Ξ (Eq. (4.20)), as shown in Figure 5.10, gave rise to a linear form for the data, and a fit to a straight line was used to determine the slope which corresponds to the group $(1-\varepsilon_M)D_{so}$.

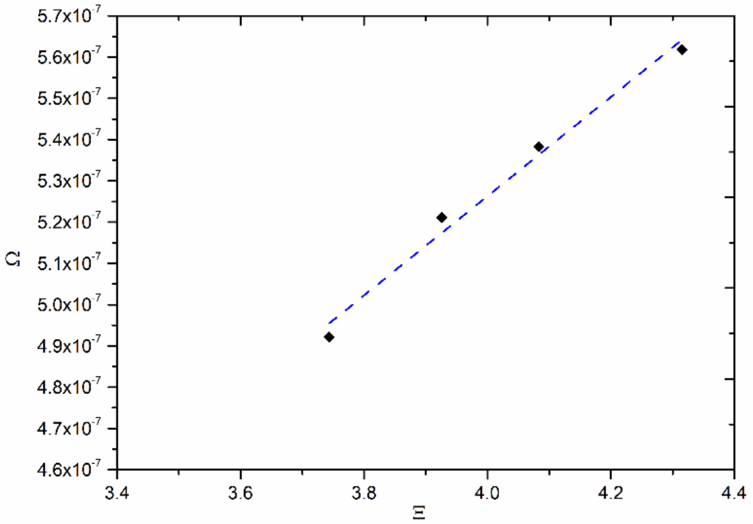

Figure 5.10 Plot of Ω versus Ξ for CO_2 for the Marcellus shale reservoir

Table 5.4 Langmuir isotherm and surface diffusivity parameters obtained from fit of the Do model to CO_2 uptake data for shale samples from Marcellus shale reservoir

Parameter	Value
Temperature(K)	328
$C_{\mu s}$ (mol/cm^3)	0.00036
b(cm^3/mol)	22188
ε_M	0.076
Ds_o(cm^2/sec)	1.30E-07

5.4.2 Simulation of CO_2 injection scenarios in Marcellus shale reservoir

A simplified segment, for each of the areas of Marcellus shale reservoir, was generated in order to reduce computational demands (Figure 5.12). Three different simulation cases have been compared in order to analyse the effects of different CO_2 injection methods in shale reservoirs, namely no-injection, CO_2 flooding, and CO_2 huff and puff scenarios.

In the case without CO_2 injection, both horizontal wells produce CH_4 for 30 years. Production was conducted by dropping the BHP gradually to 500 psi and maintaining that pressure for 30 years.

In the CO_2 flooding case, both horizontal wells produce shale gas for the first 5 years. After 5 years of production, one well is converted to a CO_2 injector well with a rate of 350 Mscf/day. After 6 years of CO_2 injection, the injector is shut-in, while the other well continues to produce CH_4 for the entire period of 30 years. It should be noted that the carbon dioxide injected is in a supercritical state due to the reservoir conditions.

In the huff and puff case, both horizontal wells produce CH_4 for 5 years, and then both wells are converted to CO_2 injectors with a rate of 640 Mscf/day for 2 months. After a 1 month soaking period, both wells are converted back to producers for 3 months. This cycle is repeated for 10 years and the overall amount of CO_2 injected is the same as for the CO_2 flooding case.

As can be seen from the findings shown in Figure 5.11(a-d), CH_4 production for the cases with CO_2 injection is higher than that of the models without CO_2 injection in all areas except for the Oatka area. The reason for this exception is probably due to the combination of a small fracture conductivity value, and the reduced fracture half-length, in Oatka.

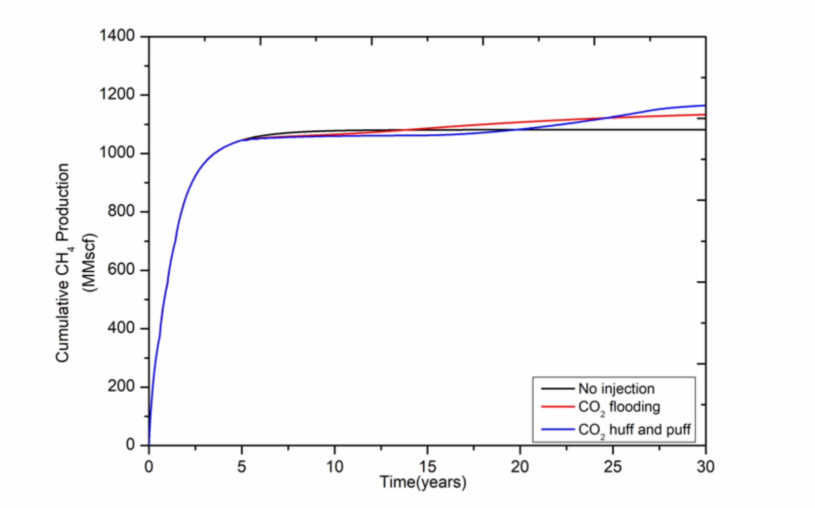
1400
1200
1000
800
600
400
200
0
Cumulative CH4 Production (MMscf)
0
5
10
15
20
25
30
Time(years)
No injection
CO2 flooding
CO2 huff and puff

(a)

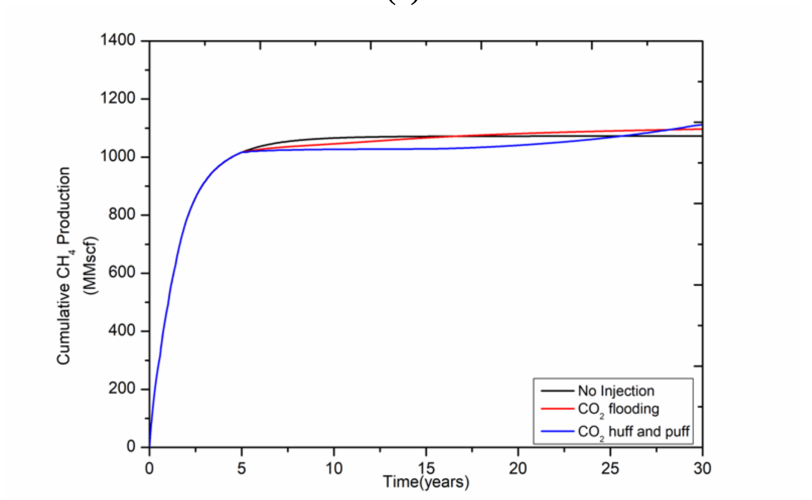
1400
1200
1000
800
600
400
200
0
Cumulative CH4 Production (MMscf)
0
5
10
15
20
25
30
Time(years)
No Injection
CO2 flooding
CO2 huff and puff

(b)

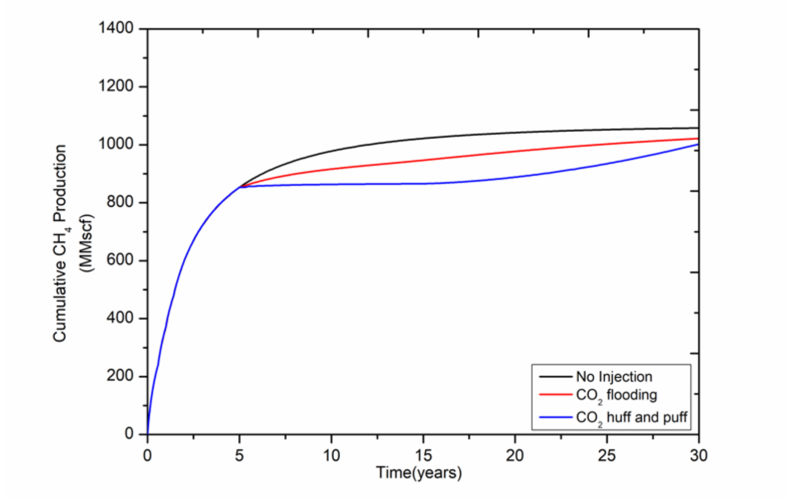
1400
1200
1000
800
600
400
200
0
Cumulative CH4 Production (MMscf)
0
5
10
15
20
25
30
Time(years)
No Injection
CO2 flooding
CO2 huff and puff

(c)

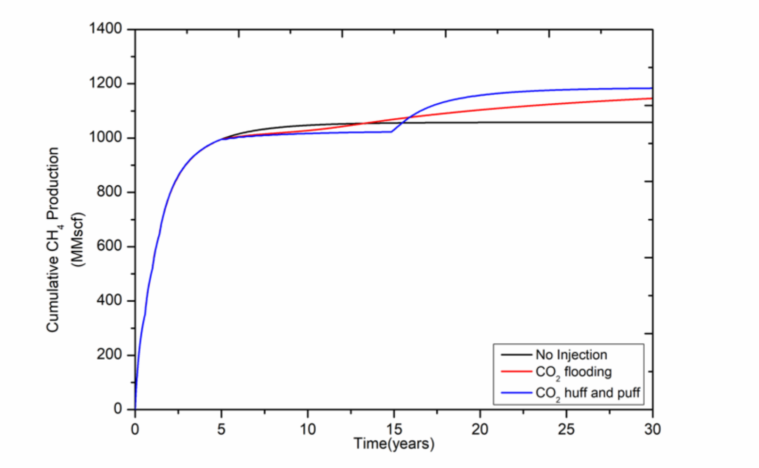

(d)

Figure 5.11 A comparison of the CH_4 production from the Marcellus shale reservoir with no CO_2 injection, CO_2 flooding, and huff and puff scenarios for the areas of (a) Bedford, (b) Burlington, (c) Oatka, and (d) Canoga

In the findings for the Bedford and Canoga areas (in Figure 5.11a,b), it can be observed that CH_4 production with CO_2 flooding starts approximately after 8 years. Despite the fact that the sample from the Burlington area has the lowest Langmuir *b* constant for CH_4, and thus it might be expected that CH_4 is more weakly bound to the shale there, the CH_4 production with CO_2 flooding starts approximately after 12 years. A potential reason, for this apparent anomaly, is a combination of the low fracture conductivity value, along with the low monolayer volume of CH_4 for the Burlington area, when compared to the samples from Bedford and Canoga areas. The cumulative gas production from the Bedford, Canoga, and Burlington areas were 4.8%, 8.3%, and 2.2%, respectively, higher than for the no CO_2 injection model at the end of production.

From Figure 5.11d, in the CO_2 huff and puff scenario, it can be observed that a steep increase of CH_4 production occurred once the cycles had been completed in the Canoga area. As shown in Figure 5.12, this steep increase is probably due to low reservoir pressure which results from the spread of CO_2 molecules through the reservoir. The CH_4 production for the remaining areas increases more steadily. The cumulative gas production from the Bedford, Canoga, and Burlington areas was 7.7%, 11.9%, and 3.7%, respectively, higher than for the no CO_2 injection case at the end of production.

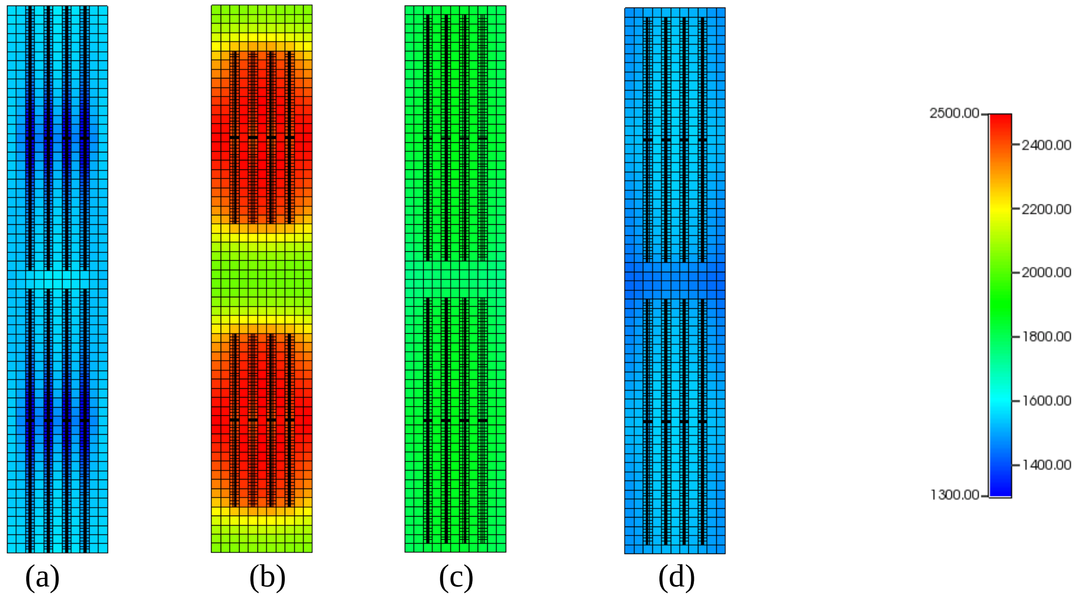

Figure 5.12 Distributions of pressure (psi) for the areas of a) Canoga b) Oatka, c) Burlington and d) Bedford of Marcellus shale reservoir at the end of simulation of CO_2 huff and puff after 30 years

5.4.3 Effects of Surface Diffusivity

One of the issues yet to be addressed in the literature is that only a few studies have implemented, into a reservoir simulator, an apparent permeability model that includes additional mass transfer mechanisms beyond Darcy flow (Wang and Marongiu-Porcu, 2015; Wang et al., 2016a; Feng et al., 2019). However, even these studies did not include all gas transfer mechanisms, especially surface diffusion, which may result in overestimating, or underestimating, gas production. To the best of our knowledge, this is the first study that extends the established model of Wu et al. (2016) for gas transport in nanopores of shale gas reservoirs to include surface diffusion and has implemented it into a reservoir simulator. The basic underlying apparent permeability model (Eq. (5.17)) has already been validated through experimental data and molecular simulation (Wu et al., 2016).

Models for the Barnett and New Albany shales have been generated to investigate the effect of CO_2 surface diffusion on CH_4 production compared with other areas from the Marcellus shale reservoir. Figure 5.13 shows the geological models of the Barnett and New Albany shale reservoirs used. The models were created based on the reservoir data of Kim et al. (2017) and Liu et al. (2013), respectively (Table 5.5). Similar to the approach of previous researchers, both models are segregated for computational efficiency. The parameters of the Langmuir isotherm for adsorption of CH_4 and CO_2 in the two shales implemented in these models have been estimated in previous studies (Table 5.6) (Strąpoć et al., 2010). Eq. (4.1) was applied in order to estimate the surface diffusion at the appropriate temperature of each reservoir.

Table 5.5 Reservoir and Fracture parameters for the Barnett and New Albany model.

Parameters	Barnett	New Albany
Reservoir Temperature, K	314	303
Porosity	0.029	0.12
Matrix permeability, nD	0.58	150
Natural fracture permeability, nD	7120	1000
Fracture height, ft	330	100
Fracture half length, ft	100	450
Fracture conductivity, md-ft	1	100

Table 5.6 Parameters of the Langmuir isotherm model for adsorption of CH_4 and CO_2 for shales taken from the Barnett and New Albany shale reservoir

	CH_4			CO_2		
Shale Reservoir	P_L(psi)	V_L(scf/ton)	b_i(1/psi)	P_L(psi)	V_L(scf/ton)	b_i(1/psi)
Barnett	1596	39.2	0.000627	1254	183.6	0.000797
New Albany	894	119.5	0.001119	1116	510	0.000896

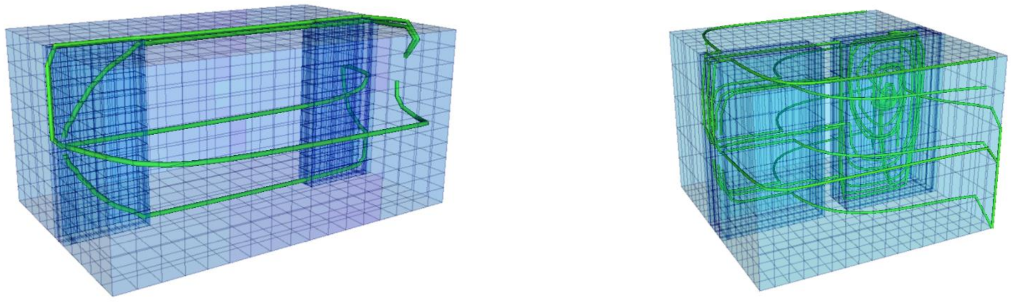
(a) (b)

Figure 5.13 Schematic views of the a) Barnett and b) New Albany shale reservoirs along with the movement of gas (shown by green lines) at the end of simulation with CO_2 flooding after 30 years. Dark blue areas represent hydraulic fractures

Eq. (5.17) was applied to determine the apparent permeability, via permeability multipliers which are functions of pressure, for the different areas of the Marcellus reservoir. Thereafter, evaluation of the impact of surface diffusion on methane recovery was investigated for models with pores in the micropore region (≤ 2 nm) where surface diffusion is more pronounced (Wu et al., 2015; Wu et al., 2016). The variation in typical pore sizes for porous matrices studied in this work is 0.5 nm, 1 nm, and 2 nm, and the surface diffusivity employed in the models was ultimately determined from the gravimetric experiments.

Assuming that the average pore radius is 0.5 nm, in certain regions of the Marcellus shale reservoir, such as the Canoga and Oatka areas, and in the New Albany reservoir, the cumulative CH_4 produced at the end of production, as predicted by the new reservoir simulator models presented here, can range between 0.91% and 1.8% higher than for the equivalent CO_2 injection model without considering surface diffusion (Table 5.7). However, as the average pore radius increases to 1 nm and 2 nm (Figure 5.14b,c), the cumulative CH_4 production declines significantly, which results in a smaller percentage of increase of CH_4 production due to surface diffusion.

Table 5.7 Change introduced to production increase percentage (PIP) by adding surface diffusion (SD) after 30 years of production, for the CO_2 flooding scenario. Surface diffusion is estimated via gravimetric experiments (GE) and fractal model (FM), assuming an average pore radius of 0.5 nm, 1 nm, 2 nm

Regions	PIP (%)					
	0.5nm		1nm		2nm	
	Change With SD (GE)	Change With SD (FM)	Change With SD (GE)	Change With SD (FM)	Change With SD (GE)	Change With SD (FM)
Oatka	1.549	2.996	0.201	0.416	0.040	0.105
Bedford	0.187	0.387	0.019	0.032	0.002	0.003
Burlington	0.340	0.688	0.031	0.075	0.013	0.017
Canoga	1.770	3.167	0.247	0.471	0.048	0.108
Barnett	0.151	0.268	0.025	0.043	0.006	0.010
New Albany	0.908	1.422	0.126	0.197	0.065	0.072

Further, the fractal surface diffusion model, implemented via Eqs. (4.18), (4.19) and (4.20), was used to investigate the impact of the particular morphology of the specific shale rock in the Marcellus reservoir on CH_4 production. It should be mentioned that the fractal dimension used in all the marine reservoirs (Marcellus, Barnett, New Albany) investigated is 2.9 and was obtained from the Frenkel-Halsey-Hill (FHH) model applied to N_2 adsorption data (Liu et al., 2018). For the fractal surface diffusion model in all regions, the production with surface diffusion is higher by up to 1.5%, thereby enhancing further the CH_4 production compared with the model with the experimental surface diffusivity (Table 5.7).

An improvement in cumulative gas production of the order of 1.5% could still yield 250 (MSCF) of additional gas. It has been reported that 250 (MSCF) could bring in additional revenue of up to $500,000 with an assumption of a gas price of $5 per thousand cubic feet and a CO_2 price of $20 per ton (Pei et al., 2015).

While the data are not shown, when, for comparison purposes, surface diffusivity was estimated for a shale surface with a low fractal dimension, the results for CH_4 production were similar to the models without surface diffusion. This is probably because a higher surface fractal dimension will enhance surface diffusion significantly. It should be noted that surface diffusion at similar pore radii was also investigated for the huff and puff scenario and the results for the cumulative CH_4 production were similar to those for CO_2 flooding.

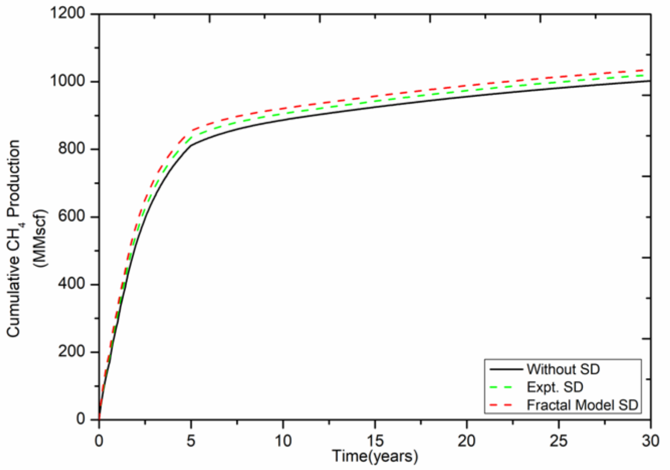

(a)

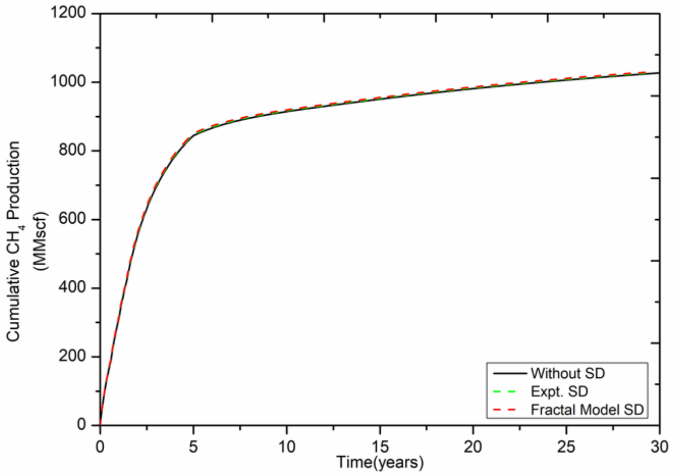

(b)

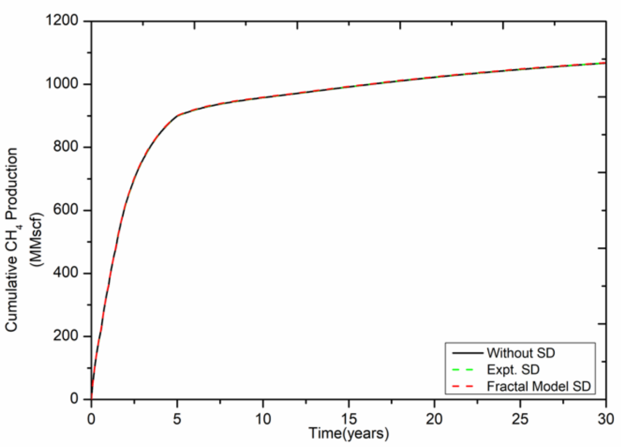

(c)

Figure 5.14 Cumulative CH_4 production with an average pore radius of a) 0.5 nm, b) 1 nm, and c) 2 nm for the Canoga area with CO_2 flooding scenario

From Table 5.7, it can be seen that the contribution of SD to PIP becomes less pronounced with an increase of typical pore radius in all the reservoirs examined. This result is reasonable considering that the smaller the pore radius, the greater the ratio of surface area per unit volume, and, thus the greater adsorbed-gas transfer volume via surface diffusion. In addition, it has been observed that the apparent permeability of surface diffusion decreases with an increase in pressure. From Eq. (5.20), the apparent permeability of surface diffusion is related not only to the surface-diffusion coefficient but also to the ratio of the adsorbed-gas concentration to the square of reciprocal pressure C_s/p^2. This means that, the ratio of the adsorbed-gas concentration to the square of reciprocal pressure is greater than the increase of the surface diffusion coefficient which results in a low surface diffusion flux.

Comparing the findings for the Bedford area of the Marcellus reservoir, and for the Barnett shale (Figure 5.15a) reservoir, to the corresponding findings for New Albany (Figure 5.15b) and the remaining areas of Marcellus shale reservoir (i.e. Canoga, Burlington, Oatka), it can be seen that surface diffusion does not make an important contribution to gas transfer, and, thus to CH_4 production (Table 5.7). The reason for this insignificant contribution of surface diffusion to CH_4 production in certain areas, is that the surface capacity in those areas is lower. Surface diffusion becomes more pronounced when the surface capacity is higher since this means a greater amount of adsorbed gas molecules. Hence, the values of the Langmuir capacity parameter play a critical role in determining the effectiveness of CO_2 injection and should be considered in shale gas reservoirs.

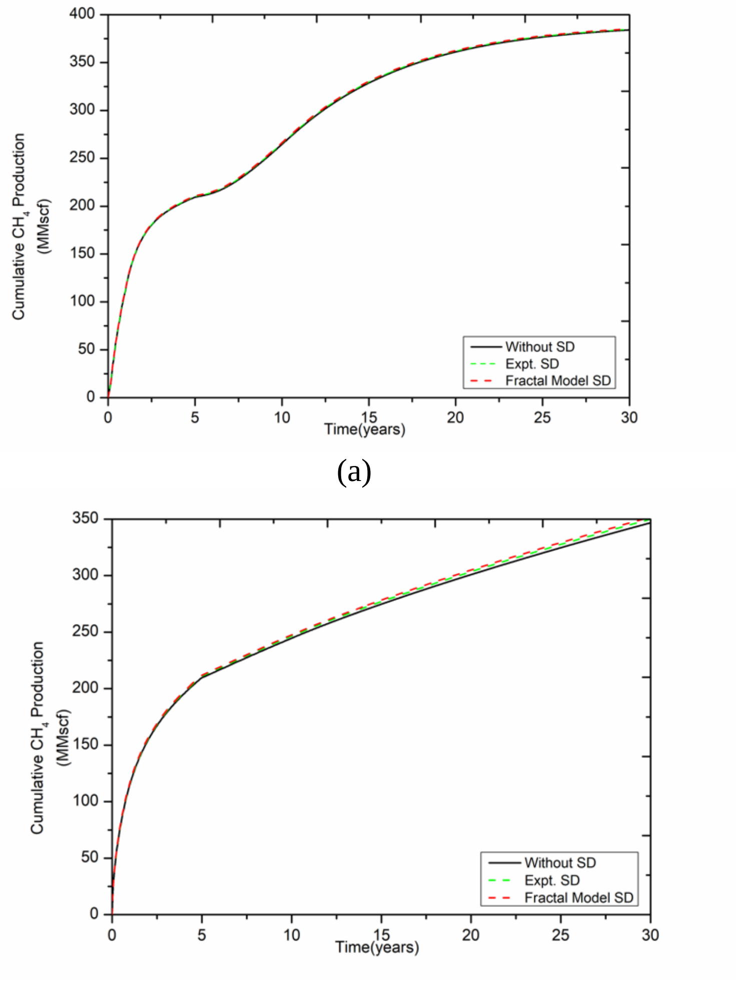

(a)

(b)

Figure 5.15 Cumulative CH_4 production, assuming an average pore radius of 0.5 nm for (a) Barnett and (b) New Albany shale reservoir, for the CO_2 flooding scenario

Table 5.8 shows the variation in the amount of adsorbed CO_2 molecules, for each of the CO_2 injection scenarios, when compared to the equivalent CO_2 injection models without considering surface diffusion. The results indicate that the effect of surface diffusion on the CO_2 amount adsorbed is not significant for the regions that have low surface capacity. The Canoga region of the Marcellus shale reservoir has the highest surface capacity and, in the flooding scenario, the amount of adsorbed CO_2 molecules may increase by up to 2.74% when surface diffusion is included and the average pore radius is 0.5 nm (Figure 5.16).

Figure 5.16 also shows the variation in the amount of adsorbed CO_2 for the huff and puff scenario. The results indicate that the relative increase in the amount of adsorbed CO_2 molecules for the models with surface diffusion compared to no surface diffusion, is similar to those for the CO_2 flooding scenario. It should be mentioned that, in the case of the CO_2 huff and puff scenario, the total amount of CO_2 molecules trapped in the reservoir is roughly half the amount of CO_2 molecules trapped in the flooding scenario. The reason for the observed difference between the two injection scenarios is that the CO_2 molecules cannot spread as far within the reservoir during the huff and puff method, since CO_2 is produced during the puff cycles.

Table 5.8 Change introduced to CO_2 adsorption increase percentage (AIP) molecules by adding surface diffusion (SD) after 30 years of production, for the CO_2 injection scenarios. Surface diffusion is estimated via fractal model (FM), assuming an average pore radius of 0.5 nm, and 1 nm

Regions	CO_2 AIP (%)			
	CO_2 flooding		CO_2 huff and puff	
	0.5 nm	1 nm	0.5 nm	1 nm
	Change With SD (FM)	Change With SD (FM)	Change With SD (FM)	Change With SD (FM)
Oatka	1.63	0.29	0.63	0.06
Bedford	0.48	0.47	0.53	0.26
Burlington	1.32	0.23	1.35	0.55
Canoga	2.74	1.06	0.73	0.71
Barnett	0.20	0.02	1.19	0.24
New Albany	1.22	0.29	2.04	1.41

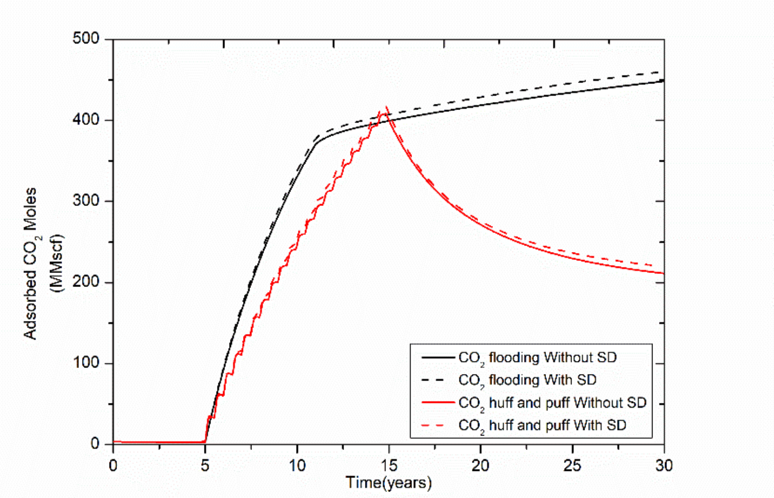

Figure 5.16 Effect of inclusion of surface diffusion (SD), assuming an average pore radius of 0.5 nm, on the amount of adsorbed CO_2 molecules for the Canoga area with CO_2 flooding and CO_2 huff and puff scenario

Table 5.9 shows the variation in the amount of desorbed CH_4 molecules for the various CO_2 injection scenarios compared to the equivalent CO_2 injection models without considering surface diffusion. In areas with high surface capacity, such as Canoga (Figure 5.17) and Oatka, when surface diffusion is applied, the amount of desorbed CH_4 molecules may increase by up to 2.3% in the flooding scenario. In the remaining areas, the effect of surface diffusion on the amount of CH_4 desorbed molecules is not significant. This result is similar to the effect of surface diffusion on the amount of CO_2 adsorbed molecules.

Figure 5.17 also shows the variation over time of the adsorbed amount of CH_4 for the Canoga area of the Marcellus shale reservoir during CO_2 huff and puff. In all reservoirs investigated, the difference between the corresponding amounts of CH_4 desorbed for the models with surface diffusion and without surface diffusion is similar to found for the CO_2 flooding scenario.

The results indicate that the amount of CH_4 desorbed is always higher in the case of the CO_2 flooding technique when compared to huff and puff, except for the case of the New Albany reservoir. A reason for the higher amount of CH_4 desorbed in the huff and puff scenario is the high fracture conductivity of the New Albany reservoir (Table 5.9) which exhibits a wider-spread of CH_4 molecules within the reservoir. In particular, the model that has the lowest fracture conductivity (Oatka) shows the largest difference in CH_4 amount desorbed amongst the various CO_2 injection techniques (i.e. CO_2 flooding and huff and puff).

Table 5.9 Change introduced to CH_4 desorption increase percentage (DIP)) molecules by adding surface diffusion (SD) after 30 years of production, for the CO_2 injection scenarios. Surface diffusion is estimated via fractal model (FM), assuming an average pore radius of 0.5 nm, and 1 nm

Regions	CH_4 DIP (%)			
	CO_2 flooding		CO_2 huff and puff	
	0.5 nm	1 nm	0.5 nm	1 nm
	Change With SD (FM)	Change With SD (FM)	Change With SD (FM)	Change With SD (FM)
Oatka	2.37	0.33	3.31	0.48
Bedford	0.51	0.05	0.77	0.04
Burlington	0.57	0.06	1.13	0.17
Canoga	2.29	0.33	2.61	0.36
Barnett	0.71	0.20	2.05	0.26
New Albany	1.46	0.21	1.32	0.19

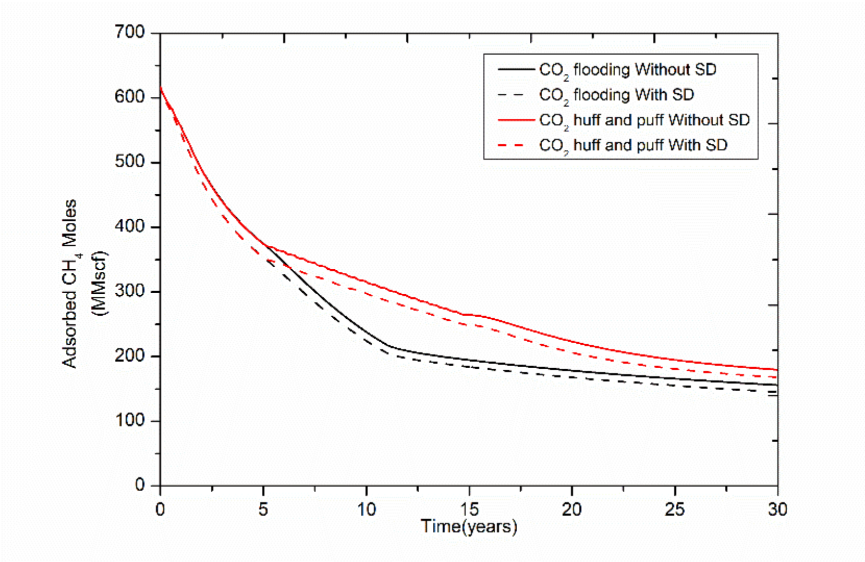

Figure 5.17 Effect of surface diffusion (SD), assuming an average pore radius of 0.5 nm, on comparison of remaining adsorbed CH_4 molecules for the Canoga area with a) CO_2 flooding and b) CO_2 huff and puff scenario

5.4.4 Effect of reservoir heterogeneity

Geostatistics is defined as a technique which takes into consideration spatial relationships of variables in estimating values of the variables at unsampled locations. Geostatistical modelling assumes that reservoir properties (i.e. porosity, permeability) are more similar at two nearby locations than for two locations distant from each other. In this work, a geostatistical approach was used for stochastically generating multiple permeability realizations to assess the effect of reservoir heterogeneity on gas production.

The observed statistical data on permeability, namely the variance and mean, are utilised in the stochastic method, in conjunction with correlation lengths representing model anisotropy in various directions. This means that this approach generated a relationship between permeability and distance, from a given site, and thus was capable of representing the natural variability of permeability. In addition, the geostatistical approach helps in quantifying uncertainty when describing the reservoir.

Hereafter, semivariogram modelling is used, which is mathematically defined as a measure of dissimilarity over distance. A semivariogram model expresses the generated permeability data and captures the correlation between the spatial variation of the permeability with distance. In particular, the spherical semivariogram is applied to describe the generated heterogeneity, since it has been shown to be the best fit to experimental variograms for shales (Yu et al., 2015;

Hosseini et al., 2019). From Figure 5.18 it can be seen that the semivariance *(γ)* increases as a function of separation distance (lag). For instance, γ shows smaller permeability values for paired samples which are closer together in space. However, the difference between permeability data increases with lag.

Discontinuities in the spatial distribution of permeability data within the reservoir are generated using the nugget effect. The nugget effect adds an amount of short-wavelength randomness to the solution from Geostatistics. In particular, a nugget is the vertical jump from the value of zero at the origin (0 lag) to the value of the variogram. More heterogeneity and increased discontinuities are caused by a larger value of the nugget.

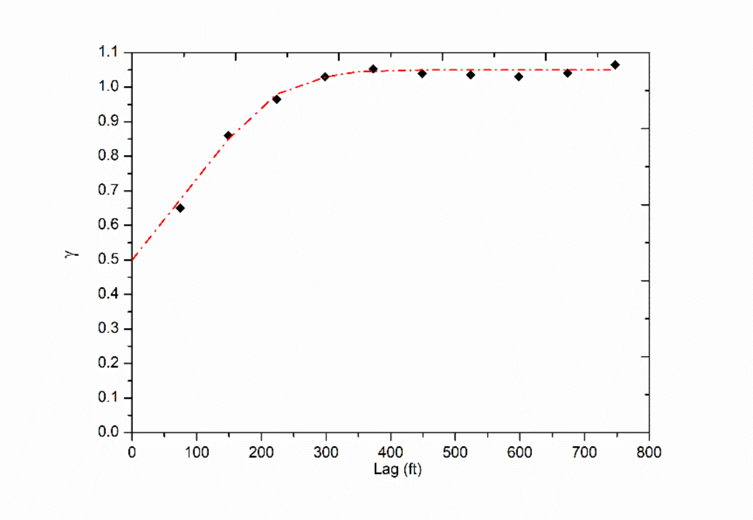

Figure 5.18 Spherical model (dashed line) with a nugget value of 0.5 fitted to the generated permeability data (symbols) for a semivariogram model. The semivariogram model represents the Canoga area of Marcellus shale reservoir

Figure 5.19 shows the comparison between methane gas production, with and without CO_2 injection, for cases of heterogeneous and homogeneous reservoir models for the Bedford area. Different nugget values of 0.001, 0.01 and 0.5 were used in this work to represent minimum, medium and maximum heterogeneity respectively (as shown in Figure 5.20). In the three heterogeneous reservoir model with different nugget values, the average permeability is similar to the base case of each reservoir.

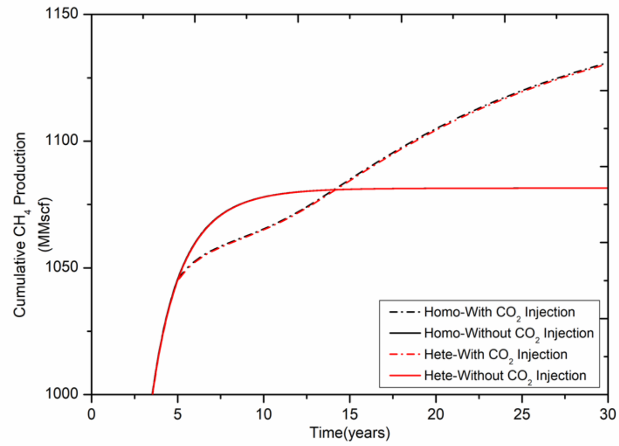

Figure 5.19 Effect of spatial heterogeneities in reservoir permeability on CH$_4$ production over time in cases with and without CO$_2$ injection for the area of Bedford (Homo:Homogeneous case, Hete:Heterogeneous case)

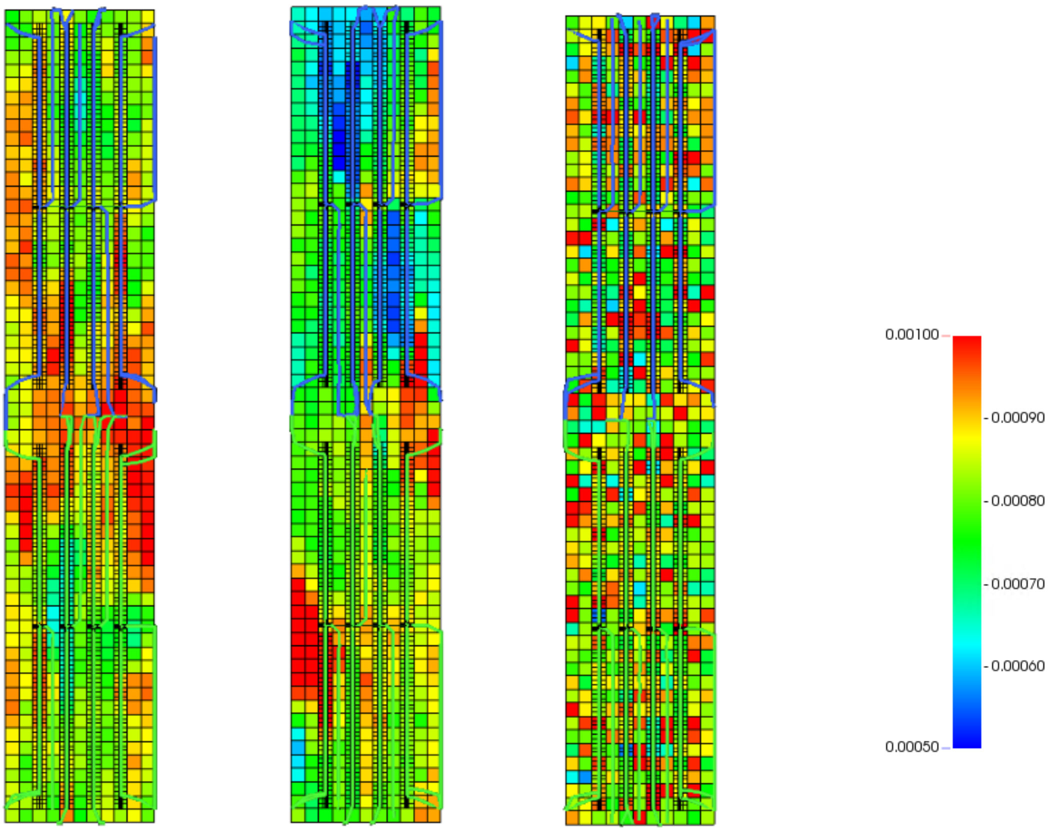

(a) (b) (c)

Figure 5.20 Maps of 2D sections through reservoir models with heterogeneity in the spatial distribution of permeability exhibiting either (a) minimum heterogeneity or (b) medium heterogeneity or (c) maximum heterogeneity along with the movement of gas (shown by the flowlines) with CO$_2$ flooding at the end of simulation. The scale bar is the permeability (mD). The size of individual lattice square is 25 ft in x and y direction, respectively

After a production period of 30 years, the incremental CH_4 production, for all the areas in the Marcellus shale reservoir considered in the heterogeneous case, is less than for the homogeneous base case. The overall percentages produced of original CH_4 in-place for minimum, medium and maximum levels of heterogeneity are lower compared to the homogeneous base case by approximately 0.8%, 1.2% and 1.5% respectively. Similarly to Marcellus shale reservoir, the CH_4 production from the New Albany shale for minimum, medium and maximum levels of heterogeneity are lower compared to the homogeneous base case by approximately 0.01%, 0.05% and 0.07% respectively. A reason for the reduction in the produced CH_4 in-place in the heterogeneous case, may be because of the slower mass transport rates than for the homogeneous case. This results in a greater amount of CO_2 trapped in the matrix which inhibits gas migration.

In contrast, the results for the Barnett shale reservoir shown in Figure 5.21 exhibit a small increase in CH_4 production in the case of heterogeneity in permeability. The data in Figure 5.21 shows that the CH_4 production values for minimum, medium and maximum degrees of heterogeneity in permeability are relatively higher than for the homogeneous base case by approximately 0.02%, 0.05% and 0.1% respectively. In contrast to the homogeneous base case model for the Barnett reservoir, adding heterogeneity enhances the CO_2 flow to the production well. It should be noted that Barnett shale has a lower overall permeability compared to the New Albany and Marcellus shale reservoirs. The new higher permeability sites introduced by the heterogeneous model assist mass transport relative to the uniformly low permeability in the homogeneous case thereby enhancing CH_4 production. The corresponding results for simulations of the impact of spatial heterogeneities in permeability on the performance of the huff and puff technique are similar to those for CO_2 flooding.

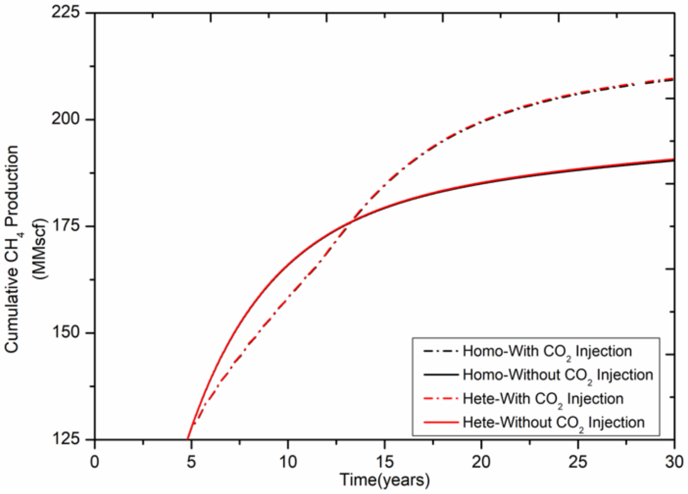

Figure 5.21 Effect of reservoir permeability on comparison on CH_4 production with and without CO_2 injection for Barnet shale reservoir (Homo:Homogeneous case, Hete:Heterogeneous case)

5.5 Summary

In the areas of Bedford, Canoga, and Burlington of the Marcellus shale reservoir, there is an increase of CH_4 production by CO_2 injection compared to no injection scenario due to high fracture conductivity. It has been shown that the surface diffusivity estimated from gravimetric experiments makes an important contribution to CH_4 production when the average pore radius is less than 2nm and should not be ignored. It has also been found that a high fractal dimension (2.9) may enhance CH_4 production when the average pore radius is less than 1nm. For example, when the average pore size is 0.5 nm, areas with high surface capacity show an increase up to 3.2% of cumulative gas production when surface diffusion is applied. This increase could bring a revenue by up to $1 million with an assumption of gas price $5 per thousand cubic feet and CO_2 price $20 per ton. In the remaining reservoirs, surface diffusion is not pronounced since the ratio of the adsorbed-gas concentration to the square of pressure is greater than the increase of surface diffusion coefficient.

The effect of surface diffusion on the amount of CO_2 molecules adsorbed and CH_4 molecules desorbed is not significant for the regions that have low surface capacity. However, for areas with high surface capacity, such as Canoga, adsorption of CO_2 and desorption of CH_4 molecules may increase by up to 2.74% and 2.3%, respectively, when compared to the models with no surface diffusion.

In all the areas investigated, geostatistical simulations showed that reservoir heterogeneity is not favourable for the CO_2 injection techniques, except the Barnett shale reservoir. The reason for this exception is probably due to the impact of high permeability heterogeneities in an otherwise low permeability of the reservoir (0.58 nD) which results in the CO_2 diffusion being more pronounced, and, thus enhancing CH_4 production.

6. Chapter Six: CO_2 Injection for Enhanced Oil Recovery and CO_2 Sequestration in Prinos Oil Reservoir

6.1 Introduction

A stable low oil price over a long period of time has forced oil companies to focus on potential techniques for enhanced oil recovery (EOR). It has been shown that around 40% of oil remains trapped in the reservoir after primary and secondary oil recovery (Mandal et al., 2010; Samanta et al., 2012; Ghosh et al., 2016; Bera et al., 2020). Previous studies have proposed gas injection as a cost-effective technology for EOR to extract the remaining oil (Kumar and Mandal, 2017; Pancholi et al., 2020).

The industrial revolution is one of the major contributors to the global warming (Falkowski et al., 2000; Le Quéré et al., 2014). It is widely accepted that the primary cause for very recent global warming is anthropogenic carbon dioxide (CO_2) emissions, which are mainly produced from fossil fuel combustion and industrial sources (Behrensmeyer, 2006).

The implementation of CO_2 enhanced oil recovery (CO_2-EOR) in oil and gas reservoirs is considered as a method to address the issue of increased anthropogenic CO_2 released into the atmosphere by sequestering CO_2 in oil reservoirs. Injection of CO_2 represents an opportunity not only to mitigate greenhouse gas emissions but also to simultaneously enhance or improve oil recovery factor (RF) due to high microscopic displacement efficiency of CO_2 (Bachu, 2000; Kovscek, 2002; Rubin et al., 2005). Typically, CO_2 injection may recover an additional 10-20% of the original oil in place (Yongmao et al., 2004) thereby prolonging the reservoir life for 15-20 years. The various CO_2-EOR techniques mainly include continuous CO_2 injection, CO_2-Water alternating gas (CO_2-WAG) injection under miscible or immiscible conditions, and CO_2 huff and puff (Han and Gu, 2014; Gong and Gu, 2015). However, previous studies have determined some distinct limitations that need to be taken into account (Li and Gu, 2014) when CO_2-EOR techniques are applied. For instance, continuous CO_2 injection produces an early CO_2 breakthrough (BT) due to viscous fingering and gravity overriding (Dellinger et al., 1984). In addition, the great amount of CO_2 injected into the oil reservoir increases the operating and capital costs of CO_2 supply, transportation, storage and compression (Holt et al., 2009). Moreover, the CO_2 huff and puff technique, which is best applied in tight reservoirs and fractured matrix formations, produces substantial amounts of the injected CO_2 (Abedini and

Torabi, 2014a; Abedini and Torabi, 2014b; Li and Gu, 2014). In particular, the injected CO_2 is produced simultaneously with oil, thereby increasing the cost related to CO_2 collection and separation. Economically speaking, the CO_2-WAG injection method reduces CO_2 consumption and the associated capital and operating costs.

The CO_2-WAG technique has been applied in over 90% of CO_2 injection projects (Merchant, 2017; Aghdam and Ghorashi, 2017; Afzali et al., 2018). This technique has various advantages, especially when it is implemented in light-oil reservoirs. Initially, the injected CO_2 and the light crude oil become miscible under reservoir conditions due to low minimum miscibility pressure (MMP) between them. Then, the CO_2-induced interfacial tension (IFT) and oil viscosity reduces, allowing the oil to expand and become better able to flow to the production wells. Once, water is injected, the reservoir pressure increases above the MMP. In addition, the water injection leads to effective control of the mobility of the injected CO_2 by reducing the gas relative permeability. Previous studies (Jaber and Awang, 2017; Karimaie et al., 2017) have shown that CO_2-WAG leads to a higher recovery factor when compared to waterflooding or continuous CO_2 flooding.

It should be noted that not all reservoirs are suitable for the application of CO_2-EOR techniques. A variety of factors, namely reservoir geology, viscosity, oil density, MMP need to be examined (Verma, 2015) before applying the CO_2-EOR technique. Generally, reservoirs having depths deeper than 3,000 ft, oil with API gravity more than 12, oil viscosity less than 500 cP and oil saturation more than 35% are the best suitable candidates for the implementation of the CO_2-EOR technique (Taber et al., 1997). According to a previous study of the U.S. CO_2 field applications, it was also suggested that CO_2 is best applied to sandstones with permeabilities greater than 10 mD (Yin, 2015). As will be shown in Section 6.2, the Prinos field (sandstone oil reservoir) in Greece is a suitable candidate for the implementation of CO_2-EOR processes. The main reasons are the petrophysical and fluid characteristics (i.e. API gravity, oil viscosity, oil saturation, depth).

In this chapter, a fluid characterization model was primarily constructed for the Prinos reservoir in northern Greece. The fluid characterization model was based on laboratory-measured data for live oil samples and existing laboratory experimental studies from the Prinos reservoir. Thereafter, the fluid characterization model was implemented into a reservoir simulator. The simulated reservoir model was history matched with real field scale oil production data. Afterwards, several CO_2-flooding injection strategies were investigated and compared with waterflooding, as a base case. The simulated CO_2-flooding injection strategies include continuous CO_2 injection and CO_2-WAG injection under miscible and immiscible conditions. Various CO_2-WAG ratios and reservoir heterogeneities were simulated to assess their impact on cumulative oil production and CO_2 storage efficiency in the Prinos reservoir. Subsequently, the results obtained were analyzed depending on the economic analysis for each case. As a result, this chapter will provide insights into the potential of CO_2-EOR techniques for the Prinos reservoir.

6.2 Reservoir Characterization and description

The Prinos sedimentary basin is the only geological area in Greece where oil and gas have been extracted for more than 40 years. The Prinos Oil Field is located offshore in the Gulf of Kavala of the North Aegean Sea (Figure 6.1). It covers an area of 6 km^2 and the sea depth is less than 50 metres (Proedrou and Papaconstantinou, 2004). The basin was explored in the 1970s and the first exploration well in the Prinos field was drilled in 1974. Crude oil production commenced in 1981, at initial rates of 9,000 Bopd. The field was formed by a low relief faulted anticline and the oil trapped was found from depths of 2450 to 2800m TVDSS (HHRM, 2018). The proven and probable (2P) reserves have been independently audited at 17.8 MMbls of oil, while the contingent (2C) resources are estimated to be 25 MMbls of oil. Of the total 54 wells drilled in the Prinos reservoir, 14 wells are currently producing and 4 are being injected with sea water.

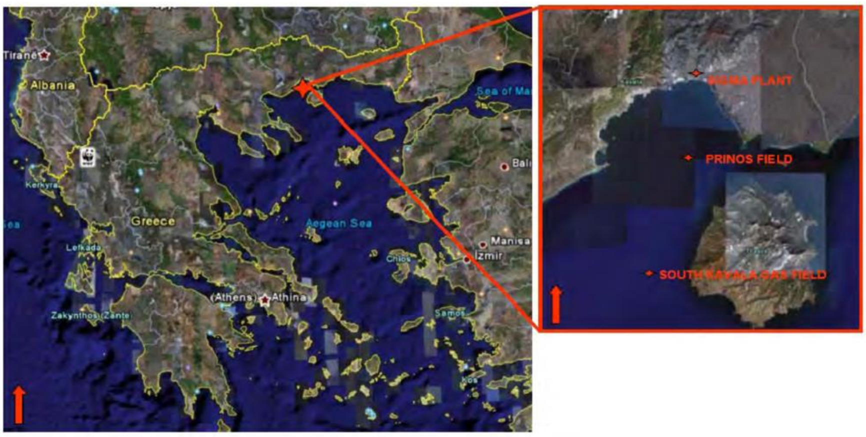

Figure 6.1 Geographic Location of Prinos oil field (Energean PLC, 2018)

It has been reported that cumulative production is approximately 110 million barrels of oil (MMbbls) (Energean PLC, 2018) and 600 Mcm^3 of natural gas. The average recovery factor is

38%. The reservoir is mainly composed of sandstones of Miocene Age with reservoir thickness of approximately 200 m.

Porosity ranges from 12% to 22%, and permeability can range up to 400 mD. The reservoir temperature is approximately 120 ^{o}C and the oil is considered medium (27-28 ^{o}API). It should be noted that both porosity and permeability decrease with increasing depth. The reason for this decrease is a combination of weight overlay, dolomitization and clay content (Proedrou and Papaconstantinou, 2004). The oil produced from the field is under-saturated and sour with a gas oil ratio (GOR) of 600 scf/bbl (Energean PLC, 2018). In addition, asphaltene precipitation occurs at pressures below 2,400 psi. Hence, the values of bottomhole pressures are being maintained above the asphaltene onset pressure. Stamataki and Magoulas (2000) reported that the H_2S content in the reservoir is about 60%(mole) in the gas phase, and the bubble point pressure varies from 1190 to 2060 psia. The initial formation volume factor (FVF) is approximately 1.40 reservoir barrels per stock tank barrel (RB/STB) and the in-situ viscosity ranges from 0.55 to 0.80 centipoise (cP) at initial conditions. Initial pressures in the reservoir were between 4,000 to 4,500 psia and seawater has been used for partial pressure support.

6.3 Materials Used and Experimental Methods

6.3.1 Materials

A crude oil sample was obtained from a vertical production well located in the Prinos offshore reservoir. The depth of the oil reservoir is between 2,300 m and 2,500 m. Due to commercial confidentiality reasons, a more detailed location cannot be disclosed. The average oil gravity and the sulfur content suggested by Energean PLC was approximately 26 ^{o}API and 3%, respectively. These values were confirmed by laboratory tests conducted at the University of Nottingham. In particular, the average oil gravity was around 25.4 ^{o}API and was estimated using a glass pycnometer following ASTM D5355-95. According to ASTM D4294-16, a calibrated energy-dispersive X-ray fluorescence spectrometer was used to measure the sulfur content. The sulphur content was approximately 3.03%, indicating that the crude oil is high sulphur or sour. Hence, these experimental results were in agreement with similar findings by Energean PLC.

6.3.2 Viscometer

The oil viscosity was measured using a co-axial cylinder type rotational viscometer, made by Brookfield company. For this research work, a small diameter spindle (22mm) was set to rotate inside a hollow cylinder which contained the oil. The amount of crude oil used in all the experiments was approximately 50 ml.

The viscosity at different temperatures was estimated by initially measuring the amount of torque required to rotate the spindle immersed in the oil (Table 6.1). This torque is quantified as a "shear stress". Keeping the shear rate constant, viscosity was estimated since it is defined as the ratio of shear stress to shear rate.

Table 6.1 Properties obtained from viscometer experiment for the Prinos oil

	Temperature (^{o}C)					
Property	28	80	100	120	135	150
Shear Rate (s^{-1})	186	186	186	186	186	186
Shear Stress (gr/cm × sec^2)	32.3	9.8	8	6.7	5.8	5.5
Viscosity (cP)	17.4	5.3	4.3	3.6	3.1	3

6.3.3 Thermogravimetric analysis

Thermogravimetric analysis (TGA) (SDT Q600) experiments were conducted to monitor and record the weight change of the crude oil, as a function of increasing temperature. The sample was initially immersed in an alumina crucible which was then placed in the sample holder. A controlled heating program was used to heat the crucible under a N_2 gas flow. The sample was heated with a constant heating rate (10^{o}C/min) from room temperature to a desired ultimate temperature of 700^{o}C. In particular, the purging gas (N_2) displaced the evolved vapour phase of the crude oil. Afterwards, the mass loss of the oil which resulted from evaporation and cracking reactions, was recorded at different temperatures. To generate the PVT data for the crude oil, the experimental True Boiling Point Curve was implemented into a fluid package, Aspen HYSYS software (HYSYS, 2020). The Peng-Robinson Equation of State (PR-EOS), available in Aspen HYSYS software as a fluid package, was then applied to fit the experimental True Boiling Point curve. From Figure 6.2, it can be seen that the PR-EOS fits the experimental data well. The PR-EOS was then used to form a raw crude oil blend from which the Energean oil pseudo-components were generated.

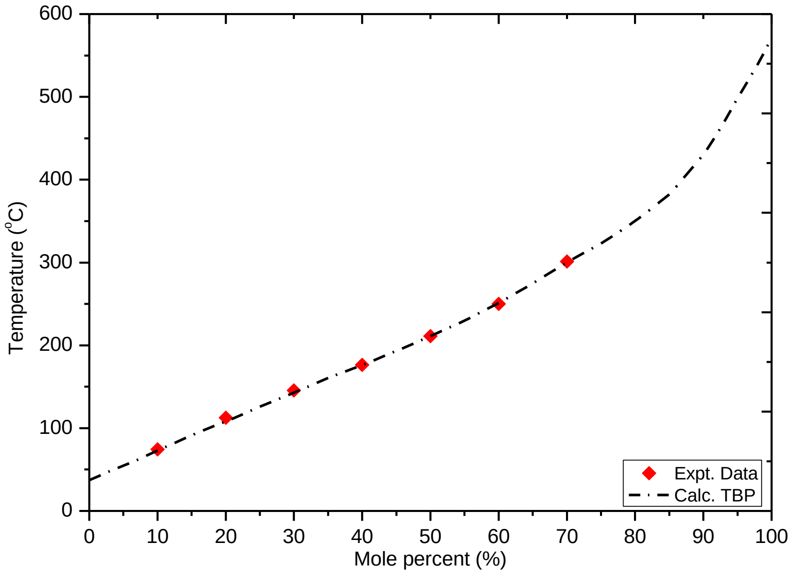

Figure 6.2 Experimental data (symbols) and calculated True Boiling Point (TBP) curve (dashed line) for Prinos Crude Oil

6.3.4 Fluid Characterization of Prinos

The offshore crude oil used in this work was supplied by Energean PLC. The oil sample is representative of the Prinos reservoir which was extracted via a vertical well, as described above. The CMG-WinProp phase behavior module was used to construct the fluid model for the Prinos oil reservoir. This module allows for component lumping, PVT matching, and modeling of laboratory experiments. As mentioned in Section 6.3.1, the average oil gravity is around 25.4 ^{o}API and the sulfur content is approximately 3.03%. Stamataki and Magoulas (2000) conducted laboratory experiments and presented that the bubble point pressure is 1190 psia, oil volume factor is 1.08-1.63 RB/STB, oil density is 47.4-52.1 lb/cft and GOR is 222-1192 scf/stb (Table 6.2). The crude oil composition was considered to consist of 6 pseudo components to ensure the accuracy of the calculation results in the numerical simulation. Since no experimental minimum miscible pressure (MMP) is reported for this oil, a typical variation seen for similar oils of between 2500 psi and 3500 psi will be examined (Jaber and Awang, 2017). Table 6.3 shows the mole fractions of the six pseudo-components along with the input data required for the Peng-Robinson equation-of-state (EOS). Table 6.4 lists the binary interaction parameters for oil components and Figure 6.3 shows the pressure temperature (P-T) phase diagram of crude oil. Once the fluid model was tuned via a regression technique to match the experimental values (please see Appendix C), it was implemented in the compositional reservoir simulator CMG-GEM. Afterwards, CMG-GEM was used to model and evaluate the effectiveness of the use of waterflooding and gas flooding processes for the Prinos oil reservoir.

Table 6.2 Fluid properties of Prinos oil

Variable Name	Value
^{0}API gravity of oil	25.4
Molecular Weight (g/mol)	146
Oil Viscosity at reservoir condition (cP)	1.72
Crude Oil density (kg/m^3)	849
Bubble point pressure (psi)	1190
Gas-Oil ratio (scf/stb)	970

Table 6.3 Compositional Data for the Peng-Robinson EOS in the Prinos reservoir

Component	Content (%)	Critical Pressure (atm)	Critical Temperature (K)	Critical Volume (m^3/kgmole)	Molar Weight (g/gmole)	Acentric factor	Parachor Coefficient
CO_2	3.24	72.8	304.2	0.094	44.01	0.23	78
N_2	0.06	33.5	126.2	0.09	28.01	0.04	41
H_2S-C_1	47.12	82.4	348.5	0.099	31.96	0.09	79.7
C_2-C_4	10.76	41.4	417.6	0.211	46.12	0.15	154.5
C_5-C_6	6.91	33.7	417.9	0.324	78.85	0.26	238.7
C_7^+	31.91	20.8	801.9	0.891	219.31	0.69	702.4

Table 6.4 Binary interaction parameters for oil components from the Prinos reservoir

Component	CO_2	N_2	H_2S-C_1	C_2-C_4	C_5-C_6	C_7^+
CO_2	0	0	0.131	0.123	0.115	0.151
N_2	0	0	0.118	0.074	0.107	0.120
H_2S-C_1	0.131	0.118	0	0.071	0.056	0.009
C_2-C_4	0.123	0.074	0.071	0	0.005	0.051
C_5-C_6	0.115	0.107	0.056	0.005	0	0.025
C_7^+	0.151	0.120	0.009	0.051	0.025	0

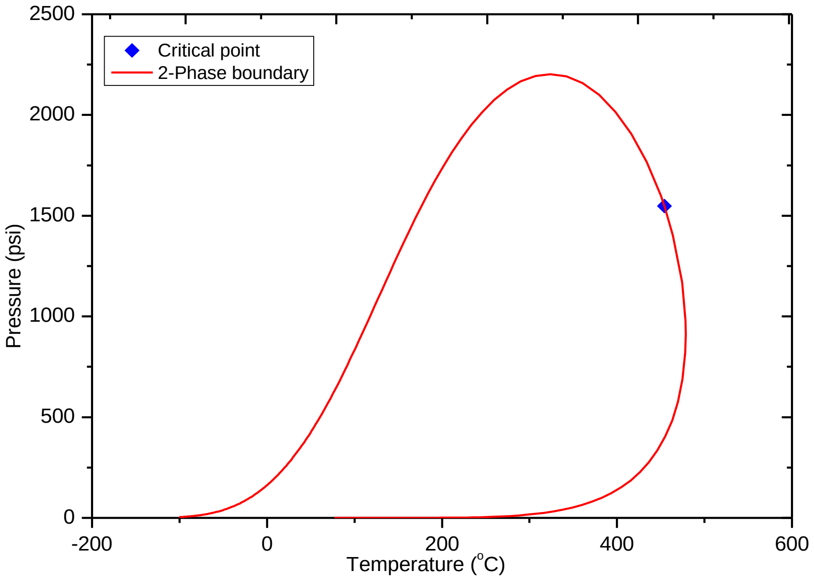

Figure 6.3 Pressure-Temperature phase diagram of crude oil from Prinos reservoir

6.4 Results and Discussion

6.4.1 Basic Reservoir Model

For the base case, a conventional single porosity (SP) reservoir model was constructed in CMG-GEM, as shown in Figure 6.4. The dimensions for the reservoir were 500 m × 400 m ×200 m, which corresponds to length, width, and thickness, respectively. The grid block size was set to 50 m × 40 m × 40 m in the x, y, z directions, respectively. For the basic 3-dimensional SP model, a waterflooding technique was applied. The Prinos reservoir history matching was conducted to match 6 years (2014-2020) of real field scale oil production data using CMG-

MOST (please see Appendix D). Crude oil production data, water injection data and bottom hole pressure were provided by Energean PLC. Initial water saturation was 20% (HHRM, 2018). The assumed oil/water and oil/gas relative permeability curves, shown in Figure 6.5, are based on previous published data (Yu et al., 2017). The rock compressibility was selected based on typical values in sandstone reservoirs (Guliyev, 2018). History matching was performed by tuning reservoir parameters, namely porosity and permeability. As done by previous researchers the flowing bottomhole pressure (BHP) (Yu et al., 2016) data in Figure 6.6, was utilized to constrain the reservoir simulation.

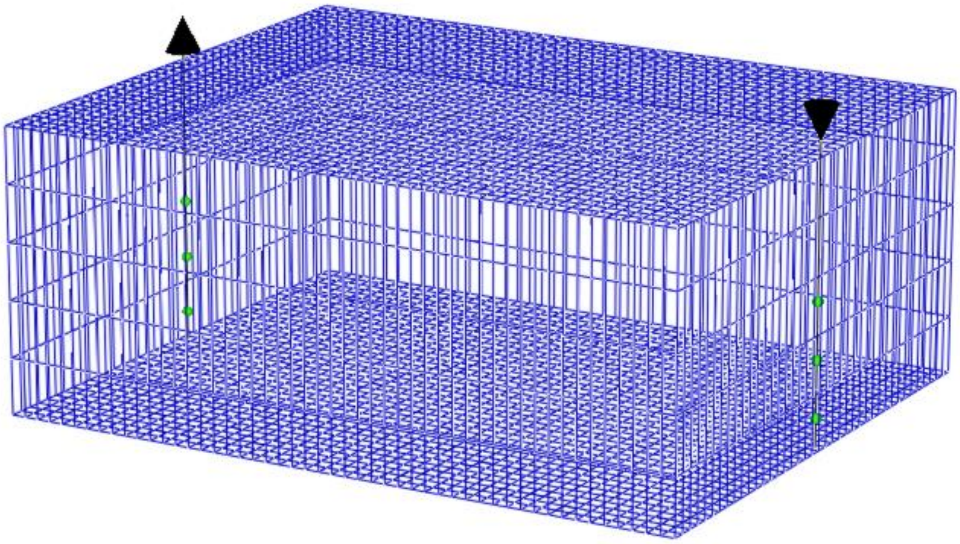

Figure 6.4 Schematic view of the single porosity model of Prinos oil

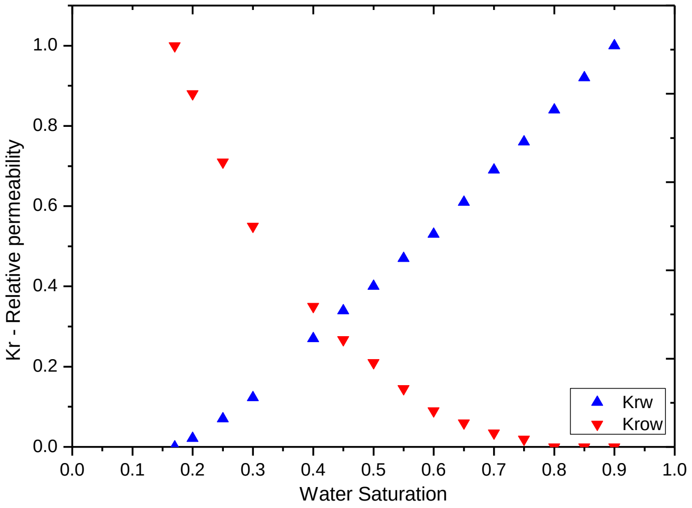

(a)

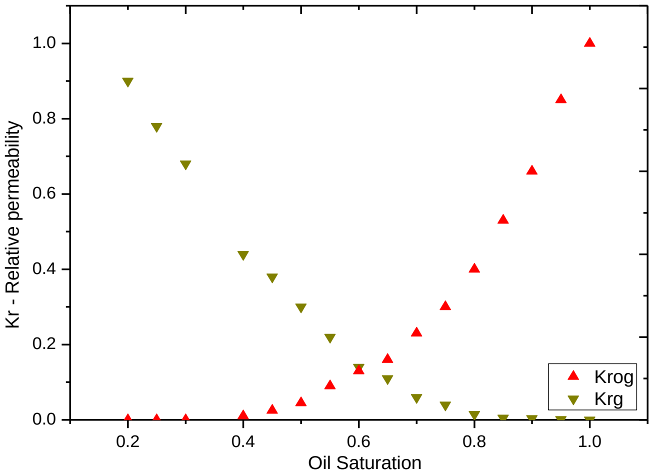

(b)

Figure 6.5 Relative permeability curves for the Prinos oil (a) Water-Oil relative permeability curve, (b) Oil-Gas relative permeability curve

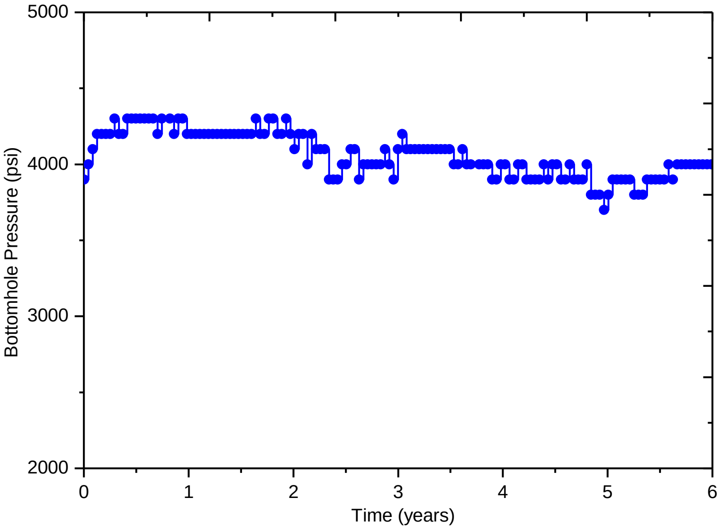

Figure 6.6 Flowing bottomhole pressure of the Prinos production well

The porosity obtained was 18%, and the permeability was found to be 100 mD, which are within the reasonable range of typical values of Prinos reservoir as explained in Section 6.2. Table 6.5 summarizes the detailed properties for the numerical reservoir simulation study. As shown in Figure 6.7 a good history match was obtained.

Table 6.5 Reservoir rock properties of Prinos reservoir

Reservoir Parameters	Value
Reservoir depth (m)	2300-2500
Pay thickness (m)	200
Initial reservoir pressure (psi)	4060
Reservoir temperature (°C)	120
Reservoir porosity (%)	18
Reservoir permeability (mD)	100
Initial water saturation (%)	20
Rock compressibility (psi^{-1})	1.03×10^{-5}

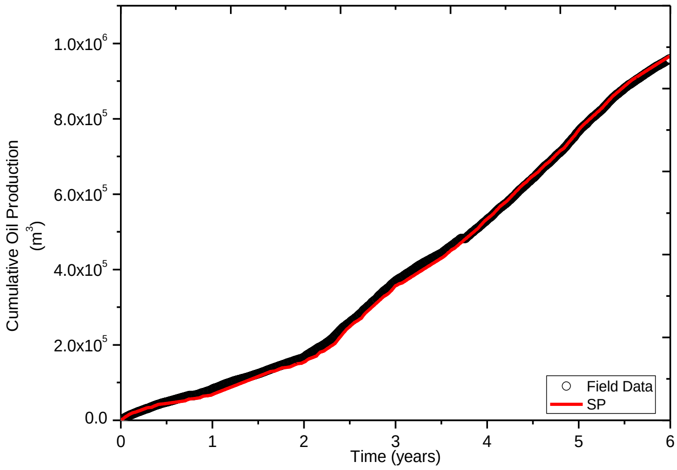

Figure 6.7 Comparison between field data (symbols) for cumulative oil production and simulation data (line) of single porosity (SP) model

6.4.2 Miscibility

The CO_2 injection processes can be classified as miscible or immiscible. The minimum miscibility pressure (MMP) is the minimum pressure, for a given specific temperature, where miscibility occurs (El-Maghraby et al., 2011). Slim-tube experiments are typically conducted to determine the MMP accurately. However, slim tube experiments are costly and time consuming. In the absence of slim-tube experiments, numerical models using the Peng-Robinson equation of state (EOS) and correlations are applied to determine the MMP. Previous studies (Verma, 2015) have shown that mathematical models using EOS analysis are a more rigorous procedure for calculating MMP and provide more accurate results than correlations (Ahmadi and Johns, 2011; Verma, 2015).

In this work, the MMP was estimated via the multiple-mixing-cell method (Ahmadi and Johns, 2011), utilizing the CMG-Winprop simulator. The multiple-mixing method is a numerical model which relies upon conducting P/T flash calculations using the EOS. In particular, the crude oil of the Prinos reservoir, was represented by a 6 component model (Table 6.3), namely: CO_2, N_2, H_2S-C_1, C_2-C_4 ,C_5-C_6 , and a lumped pseudo C_7^+ fraction.

In order to achieve miscibility between CO_2 and the reservoir oil, the MMP needs to be lower than the reservoir pressure (i.e. 3770 psi). Since slim-tube experiments have not been conducted to estimate the MMP in the Prinos reservoir, typical values of MMP from the literature were assumed for the miscible and immiscible processes (Yellig and Metcalfe, 1980; Alston et al., 1985; Glaso, 1985; Yuan et al., 2004). In the CO_2 injection case under miscible conditions, the experimental MMP value was assumed to be 2750 psi, which is a reasonable value for medium oil reservoirs (Jaber and Awang, 2017). In the CO_2 injection case under immiscible conditions, the experimental MMP value was assumed to be 5500 psi which is considered the upper bound of the typical range (Hassan et al., 2019).

The parameters of the Peng-Robinson EOS were tuned via a regression technique to match the experimental MMP values under miscible and immiscible conditions (i.e. 2750 psi, 5500 psi), at reservoir temperature (120^{o}C). In particular, the volume shift, acentric factor, Omega A, and Omega B parameters in the Winprop model for Prinos crude oil were adjusted.

Figure 6.8 shows that the recovery factor for CO_2-WAG injection under miscible conditions is 2.14% higher than for CO_2-WAG under immiscible conditions. In particular, the miscibility between reservoir oil and CO_2, results in a lowering of the interfacial tension between oil and CO_2, and swelling of the crude oil. The swelling of the crude oil is due to the mass transfer of the injected CO_2 into the oil (condensation gas-drive process) (Merchant, 2010). Once the injected CO_2 had dissolved into the oil, oil viscosity and density were lowered, increasing the oil recovery factor. In the subsequent simulation studies, the MMP to CO_2 was taken as 2750 psi.

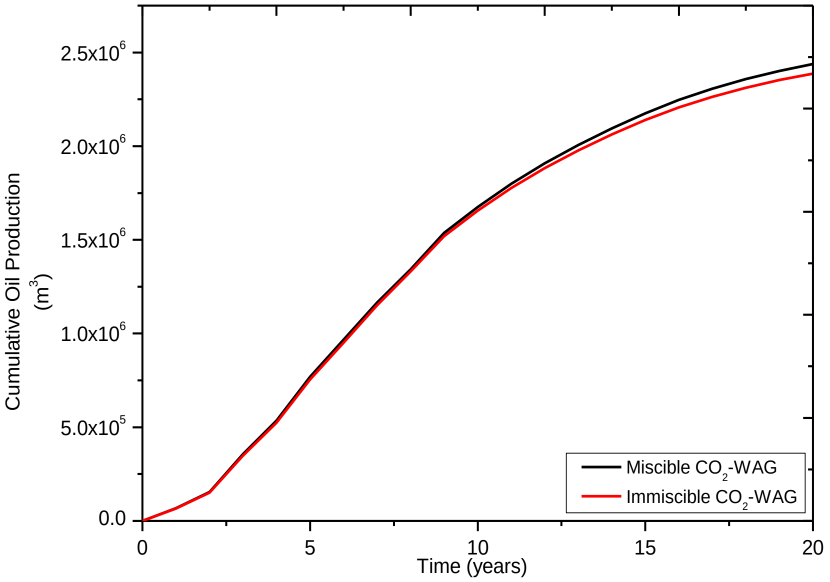

Figure 6.8 Comparison between CO_2-WAG case under miscible conditions (miscible CO_2-WAG) for cumulative oil production and immiscible conditions (immiscible CO_2-WAG)

6.4.3 Economic Analysis

Previous studies (Jaber and Awang, 2017; Arnaut et al., 2021) have shown that a variety of EOR methods were technically feasible but not economically justifiable. In this study, economic calculations were based on criteria to select the best development strategy for the Prinos field. In particular, one of the most widely used economic criteria is the net present value (NPV). NPV is defined as the aggregate of all future project cash flows (i.e. inflows, outflows) where each future cash flow must be discounted back to a common point in time. NPV is considered as a measure of profit and it comprises the time value of money. Hence, NPV was obtained by calculating the present value of all the future cash flows. According to previous studies (Fukai et al., 2016; Jaber and Awang, 2017), a fixed discount rate of 12% per annum was considered acceptable to obtain the present value of future cash flows. The discount rate accounts for the time-dependent value of money and risk associated with a future investment. In this study, the discount rate of 12% used for all the economic calculations is within the range of discount rates used in the Advanced Resources International (ARI) studies. Table 6.6 depicts a sensitivity analysis of the discount rate for the miscible CO_2-WAG scenario, where the CO_2 injection rate and the water injection rate were kept constant at 0.2Mt/yr and 2500 m^3/day, respectively.

Table 6.6 Sensitivity Analysis of the discount rate for the miscible CO_2-WAG scenario

Discount rate (%)	NPV ($MM)
8	385.86
10	339.64
12	300.89
14	268.10
16	240.12

The future cash flows included the gross revenue of the produced oil and gas minus the operational expenditure (OPEX) and capital expenditure (CAPEX).

The NPV was estimated using the following formula (Abdus and Ganesh, 1994; Nwaozo, 2006):

$$NPV = \sum_{t=0}^{n} \frac{NCF_t}{(1+i)^t} \quad (6.1)$$

where

$$NCF_t = Revenue - CAPEX - OPEX \quad (6.2)$$

where NCF_t is the revenue at time t, t is the time in years, and i is the discount rate.

Despite the fact that the Prinos field is located offshore it is a great candidate for application of EOR processes for various reasons. First, the reservoir exists at a shallow burial depth and at a short distance from the Greek mainland. Second, a coal fired power plant exists on the mainland and CO_2 can be transported via pipeline to the field (190km). Thence, the costs of CO_2 capture, pipeline maintenance, and CO_2 transportation were reduced (Kouzoukas et al., 2011). In addition, royalties and taxes were neglected in the economic analysis since the oil fields are owned and developed by the Greek Government.

In the case of waterflooding, operational costs included water handling and reinjection (Jaber and Awang, 2017), lifting cost (King et al., 2011), and gas processing costs of the produced gas (EIA, 2016). In the case of CO_2 injection, operational costs included lifting cost, gas processing costs of the produced gas, CO_2 transportation and capture cost (Kouzoukas et al., 2011), operation and maintenance cost of CO_2 recycling (Jaber and Awang, 2017), and CO_2 compression and injection (Gozalpour et al., 2005; Ghani et al., 2015; Fukai et al., 2016). When CO_2-WAG was conducted, operational costs were obtained both from the waterflooding and from the CO_2 injection cases.

The capital cost included the injection well drilling, completion and tie in of the well, and the CO_2 compressor. Since, the field has already conducted primary and secondary flooding (i.e. waterflooding) it was assumed that the water injection wells were converted to CO_2 injection wells. The reason for this is that reworking in the existing well field with the current infrastructure will be significantly cheaper than drilling a new well for CO_2-EOR (McCoy, 2008).

Similar to the approach of previous researchers (Jaber and Awang, 2017; King et al., 2011; Iwashaki et al., 2004), the prices of oil, gas and CO_2 were assumed to be constant over the project life. The initial capital investment is also included in the NPV. Table 6.7 shows the economical parameters used in this study.

Table 6.7 Economic Analysis Parameters for the Prinos Reservoir

Parameter	Value
Interest Rate(%)	12
Oil Price ($/stb)	55
Gas Price ($/Mscf)	2.5
CO_2 Capture($/Mscf)	1
Well drilling (MM$/well)	2.5
Completions and tie in (MM$/well)	2
Water injection Facilities (MM$/well)	17
CO_2 compressor ($MM)	1.6
Oil Lift ($/stb)	0.25
Gas processing cost($/Mscf)	0.25
Water handling ($/stb)	0.37
Water reinjection ($/stb)	0.56
CO_2 transportation($/Mscf)	0.13
CO_2 compression and injection($/Mscf)	0.5
CO_2 recycled($/Mscf)	0.3

6.4.4 Comparison of simulated development scenarios

In the Prinos reservoir model, reservoir simulations have been performed to compare the efficiency of different injection techniques for cumulative oil production. Specifically, three different cases were simulated, namely waterflooding, continuous CO_2 flooding, and CO_2-WAG injection under miscible conditions. In all three cases the base case model in Section 6.4.1 was applied for the first 6 years. Afterwards, production forecasting was conducted by dropping the BHP at 6 years to 3770 psi and maintaining that pressure for 14 years. It should be noted that the BHP is higher than the asphaltene-onset pressure (AOP) which inhibits asphaltene precipitation (Energean PLC, 2018). Asphaltene precipitation may lead to clogging of the reservoir and the reduction of cumulative oil production. In addition, the selected BHP is greater than the minimum miscibility pressure (MMP) to ensure a miscible condition in the oil reservoir.

In the waterflooding case, water was injected at a constant rate of 2500 m^3/d via a vertical well. Approximately 12.8 MMm^3 of water was injected at the end of the simulation. The total oil production and recovery factor were around 2.18 MMm^3 and 51% respectively.

In the CO_2 flooding case, continuous pure CO_2 was injected was injected at a constant rate of 0.2 Mt/yr via the aforementioned vertical well into the reservoir. Approximately 2.8 Mt of CO_2 was injected by the end of the simulation. Figure 6.9 shows that CO_2 flooding shows less cumulative oil production than the waterflooding case. In particular, the total oil production and recovery factor were around 194000 m^3 and 45% respectively. In total, 1.6 Mt of CO_2 has been stored in the reservoir at the end of the simulation which is equal to 51% of the total CO_2 injected.

Hereafter, reservoir simulations have been conducted to determine the impact of CO_2-WAG on cumulative oil production. CO_2-WAG involves a cyclic injection process whereby water injection and CO_2 injection are carried out alternately over a number of cycles until the end of the simulation. Figure 6.9 shows miscible CO_2-WAG injection where the CO_2 injection rate has been kept constant at 0.2 Mt/yr, similarly to the CO_2 flooding case. The water injection rate has been kept constant at 2500 m^3/day. The simulation results show higher cumulative oil production in the CO_2-WAG case at the end of the simulation when compared to the waterflooding and continuous CO_2 flooding. In particular, the recovery factor for the miscible CO_2-WAG injection was around 57%. Consequently, the NPV in the waterflooding and continuous CO_2 injection cases, were 3.6% and 19.1%, respectively, lower than for the miscible CO_2-WAG case (Table 6.8). The reason is that the CO_2-WAG case comprises increasing volumetric sweep efficiency compared to waterflooding and the enhanced microscopic displacement efficiency of CO_2 injection. A total of about 1.2 Mt CO_2 will be stored in the reservoir at the end of production. This means that approximately 38% of the injected CO_2 can be stored in the reservoir at the end of the production period.

In the CO_2-WAG injection case, the CO_2 injection rate was decreased to 0.1Mt/yr to reduce the cost of the CO_2 injection project. The results showed an increase up to 1% of the oil recovery factor when compared to the waterflooding case (Table 6.8).

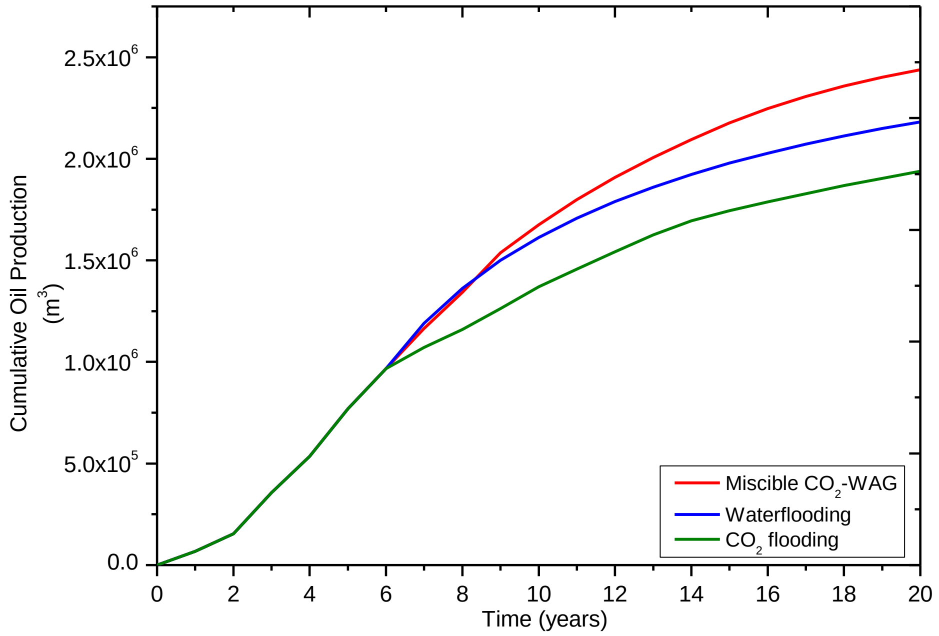

Figure 6.9 A comparison of the cumulative oil production with CO_2-WAG under miscible conditions, Waterflooding and continuous CO_2 flooding

Table 6.8 Net Present Value (NPV) and oil Recovery Factor (RF) for different development scenarios for the Prinos reservoir

Process	Oil Recovery Factor (%)	NPV ($MM)
Waterflooding	51	290.472
CO_2 flooding with CO_2 rate 0.2Mt/yr	45	252.677
CO_2-WAG with CO_2 rate 0.1Mt/yr	52	283.011
CO_2-WAG with CO_2 rate 0.2Mt/yr	57	300.887

6.4.4.1 Miscibility rather than pressure support

A consideration of the oil saturation in the CO_2-WAG and Waterflooding model grid site will enable the determination of whether the oil produced is from developed miscibility or pressure support. Figure 6.10 shows the simulated oil saturation variation in a selected grid cell for the Prinos reservoir during CO_2-WAG and Waterflooding techniques. The grid cell was located midway between the producer and the injector at the top of Prinos reservoir. In the waterflooding case, oil saturation remained unchanged for the first 9 years. After water breakthrough in the grid cell, oil saturation dropped gradually to around 0.45. In the CO_2-WAG injection case, oil saturation remained unchanged for the first 7 years. After CO_2 breakthrough in the grid cell, oil saturation dropped steeply to residual oil saturation (i.e. 0.15). This observation is in agreement with similar findings by Karimaie et al. (2017), where CO_2 segregates to the top of the reservoir and oil saturation decreases to almost zero.

Figure 6.11 shows that the average reservoir pressure in the waterflooding case is higher than that of the CO_2 injection case. This means that the increase in oil production in the CO_2-WAG injection case is due to miscibility rather than pressure support.

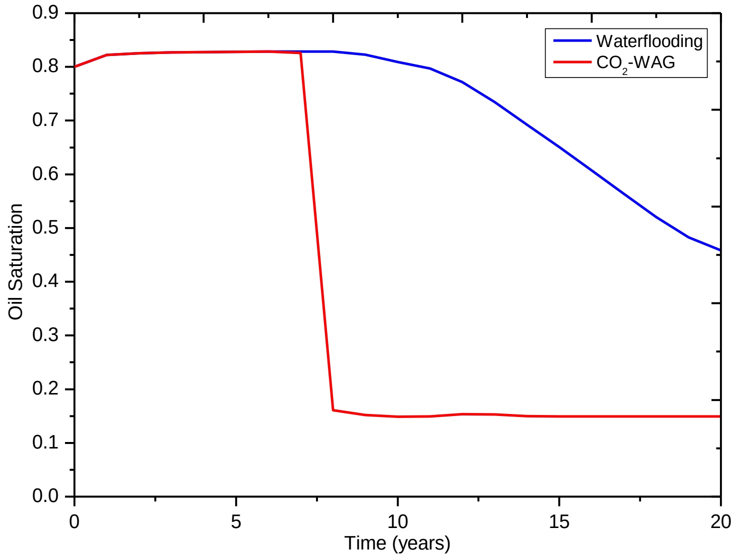

Figure 6.10 A comparison of oil saturation from the Prinos reservoir with Waterflooding and CO_2-WAG injection

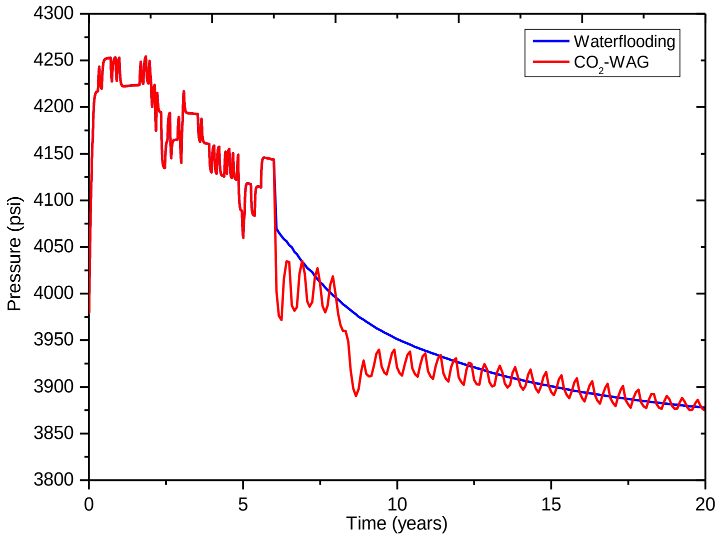

Figure 6.11 A comparison of reservoir pressure from the Prinos reservoir with Waterflooding and CO_2-WAG injection

6.4.5 Effect of CO_2-WAG cycles

Previous studies (Han and Gu, 2014; Karimaie et al., 2017) have shown that the initialization of CO_2-WAG injection is an important factor when designing a CO_2-WAG process. Hence, various simulations were conducted to determine the most optimal time to initiate the CO_2-WAG process after the base case model. Four different starting CO_2-WAG injection periods were investigated such as year 6, 9, 12, and 15. As can be seen from Figure 6.12, the most optimal time to initiate the CO_2-WAG injection is year 6; after the waterflooding base case.

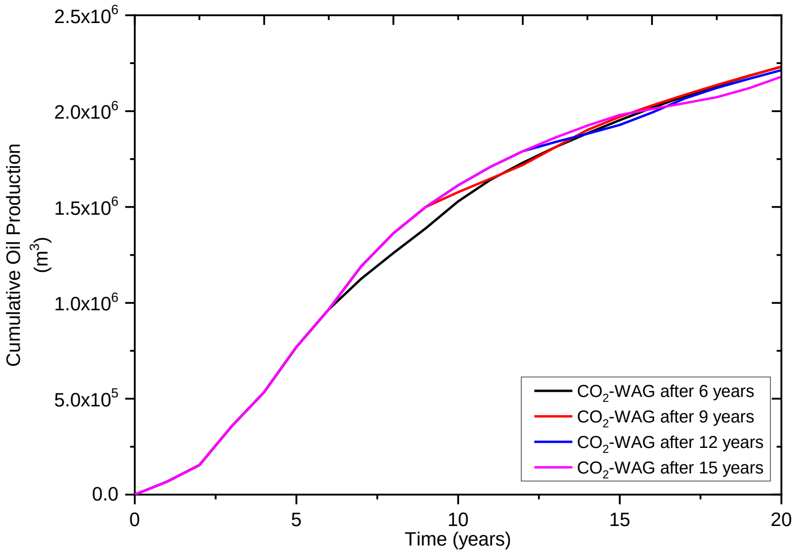

Figure 6.12 A comparison of the cumulative oil production from the Prinos reservoir with WAG injection after 6, 9, 12 and 15 years

6.4.6 Effect of CO_2-WAG injection rate

A sensitivity analysis was conducted to determine the optimal CO_2-WAG cycle time. Various time intervals were considered such as 30, 60, 90 and 120 days. As can be seen from Figure 6.13, CO_2-WAG cycle time does not have a significant impact on cumulative oil production (~0.02%). Thence, 90 days of CO_2-WAG cycle time was considered for this study.

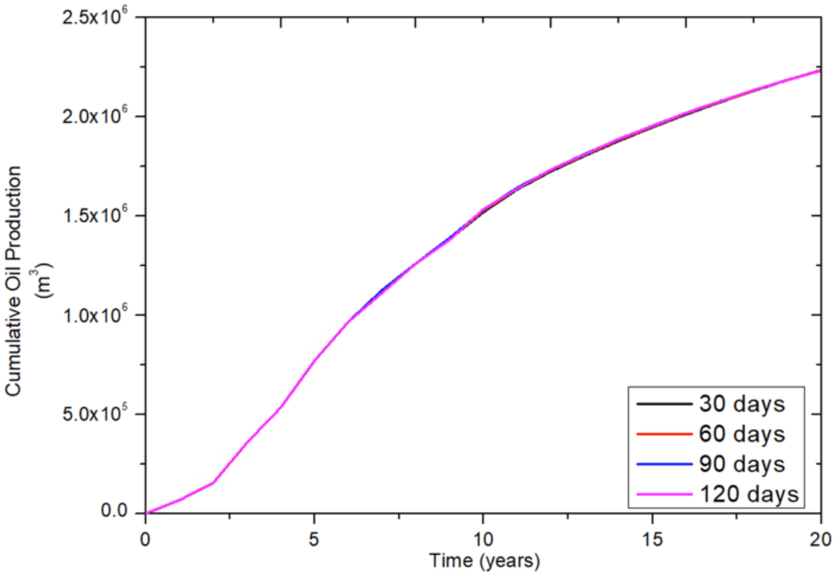

Figure 6.13 A comparison of the cumulative oil production from the Prinos reservoir with CO_2-WAG injection cycles of 30, 60,90 and 120 days

6.4.7 Effect of CO_2-WAG Slug Ratio

Economic analysis was conducted to investigate the impact of CO_2-WAG ratio on cumulative oil production. As can be seen from Table 6.9, the NPV in the case with a CO_2-WAG cycle of 1:1 under miscible conditions (Case A_m) was increased by up to 5 million dollars compared to the CO_2-WAG cycle of 1:1 under immiscible conditions (Case A_{im}). The reason for this increase in NPV in Case A_m is due to the increase of the oil recovery factor (1%). In Case A_m, the injected CO_2 dissolves in the reservoir oil which results in swelling of oil. Thereafter, viscosity and density were lowered, thereby improving the oil mobility, and, thus the oil recovery factor.

In addition, various injected CO_2-WAG ratios (CO_2/water) were examined (Figure 6.14). In the cases with CO_2-WAG ratio of 2:1(Case B) and CO_2-WAG ratio of 3:1(case D), the CO_2 slugs were greater than water slugs.

In cases B and D, the oil recovery factors were 18% and 21%, respectively, higher than for the Case A_m. While the oil RF (%) in Case D was higher than for the case B, the NPV was lower (Table 6.9). The reason for this NPV decrease in Case D was due to the operational costs (i.e. recycling) of CO_2.

In addition, cases with CO_2 slug size (volume) lower than water slug size were examined, i.e. a CO_2-WAG ratio of 1:2 (Case C) and CO_2-WAG ratio of 1:3 (Case E). In Cases C and E, the oil recovery factor was 15.8% and 15.9%, respectively, higher than for the Case A_m. From Table 6.9, it can also be seen that the NPV for the Cases C and E was increased by approximately 6.3%, respectively, compared to the Case A_m. Moreover, the NPV difference between Cases C and E is not significantly great ($0.035M). Hence, the CO_2 injection rate has a greater impact on the cumulative oil production when compared to the water injection rate in the CO_2-WAG case. These results indicate that Case B is considered as the optimum NPV case since it yields a high oil recovery factor and lower operational costs for CO_2.

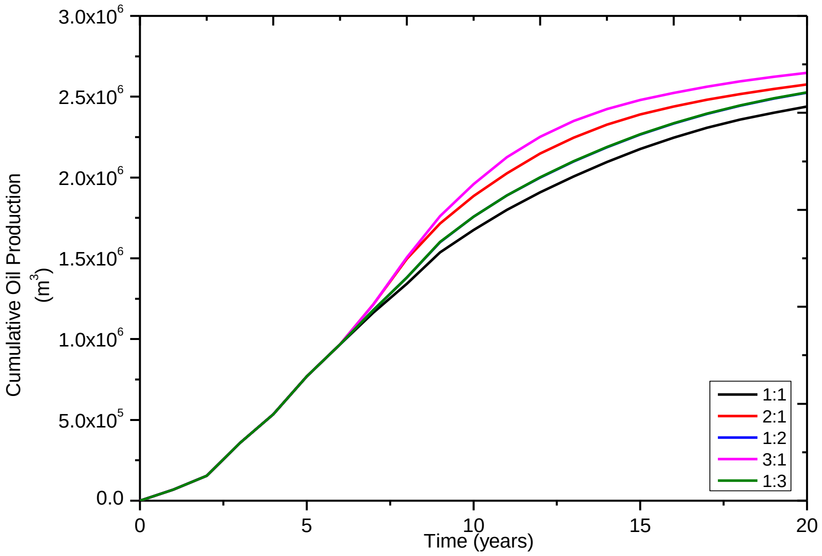

Figure 6.14 Effect of CO_2-WAG slug ratio of 1:1, 2:1, 1:2, 3:1 and 1:3 on the cumulative oil production for the Prinos reservoir

Table 6.9 Net Present Value (NPV) and oil Recovery Factor (RF) for different water alternating gas (CO_2-WAG) scenarios for the Prinos reservoir

Slug ratio (CO_2/Water)	Oil Recover Factor (%)	NPV ($MM)
1:1 miscible (Case A_m)	57	300.887
1:1 immiscible (Case A_{im})	56	295.202
2:1 (Case B)	60	313.73
1:2 (Case C)	59	308.643
3:1 (Case D)	62	313.725
1:3 (Case E)	59	308.745

6.4.8 Effect of CO_2-WAG Cycles on Storage Mechanisms

Previous investigations (Ampomah et al., 2016) have shown that the CO_2 stored within the reservoir can be affected by changes in CO_2-WAG ratio. In this work the CO_2 storage efficiency is given by the expression:

$$E = \frac{\text{Stored } CO_2}{\text{Maximum volumetric } CO_2 \text{ sequestration}} \times 100 \qquad (6.3)$$

where the stored CO_2 mass was estimated from numerical simulations and the total potential storage of CO_2 was estimated from the static geologic model. In particular, the maximum theoretical volumetric CO_2 sequestration capacity of the Prinos reservoir can be expressed as:

$$Q = (A) * (T) * (\varphi) * (\rho) * (1 - S_w) \qquad (6.4)$$

where A is the field area (ft^2), T is the producing interval thickness (ft), φ is the average reservoir porosity (%) and ρ is the density of CO_2 (lb/ft^3) at reservoir temperature and pressure and S_w is the initial water saturation (%).

From Table 6.10, it can be seen that the CO_2 storage efficiency in the Case A_{im} may decrease by approximately 1% compared to Case A_m. A potential reason for this decrease is that in Case $A_{im,}$ the CO_2 free gas was produced via the free gas channel to the production well and the injected CO_2 did not mix with the reservoir oil. In contrast, in Case $A_{m,}$ the injected CO_2 was dissolved in the oil, which meant that better CO_2 storage efficiency was achieved.

In addition, the high volume of CO_2 led to an increase in the CO_2 stored. For example, in the Cases B and D the CO_2 stored was 1.55Mt and 1.75Mt, respectively. Hence, in the Cases B and D the CO_2 storage efficiency may increase by up to 11% and 17%, respectively, when compared to the case with a CO_2-WAG cycle of 1:1 (Case A). As shown in Figure 6.15, increasing the total volume of injected CO_2, the average reservoir pressure also increases. Subsequently, the CO_2 storage mechanism of capillary trapping and dissolution trapping in the reservoir increases. This observation comes in agreement with past findings of previous researchers (Ampomah et al., 2016; Lei et al., 2016).

In the Cases C and E the CO_2 stored was 0.99Mt and 0.98Mt, respectively. The CO_2 storage efficiency from cases C and E are lower compared to Case A by approximately 7% and 7.2% respectively. Hence, high water volume decreases the storage amount of CO_2. This result is reasonable considering that the greater the water volume injected, the greater the average pressure (Figure 6.16), the greater the cumulative oil produced, and, thus the greater CO_2 produced.

Table 6.10 CO_2 sequestration for a variety of CO_2-WAG slug ratios

Slug ratio (CO_2/Water)	CO_2 stored (Mt)	CO_2 storage efficiency (%)
1:1 miscible (Case A_m)	1.21	38.3
1:1 immiscible (Case A_{im})	1.18	37.4
2:1 (Case B)	1.55	49
1:2 (Case C)	0.99	31.3
3:1 (Case D)	1.75	55.4
1:3 (Case E)	0.98	31.1

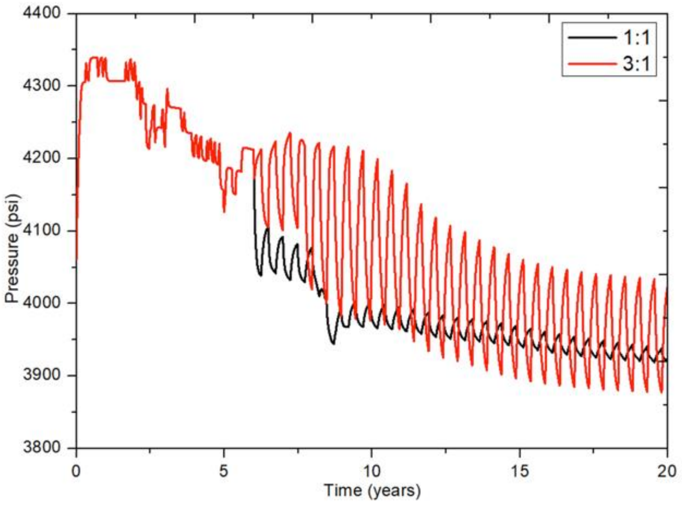

Figure 6.15 Effect of CO_2-WAG slug ratio of 1:1, and 3:1 on the average field pressure for the Prinos reservoir

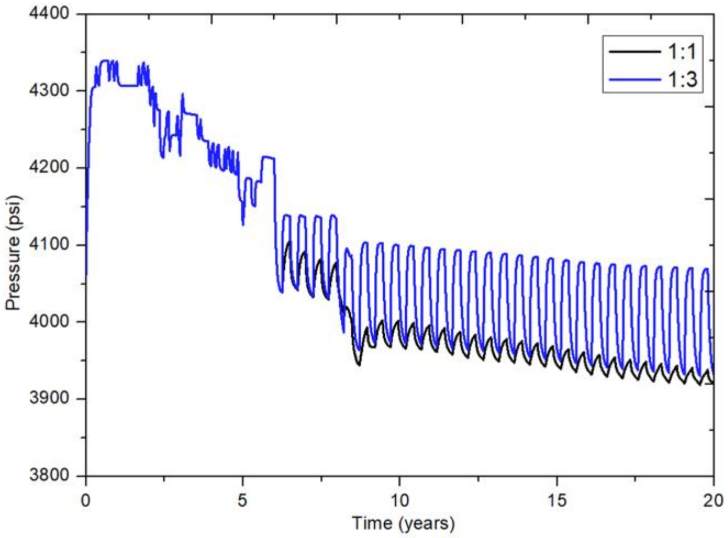

Figure 6.16 Effect of CO_2-WAG slug ratio of 1:1, and 1:3 on the average field pressure for the Prinos reservoir

6.4.9 Effect of Reservoir Heterogeneity

In this work, the potential impact of reservoir permeability heterogeneity was investigated for the Prinos reservoir. Due to the absence of detailed geological information on the spatial variation of permeability, a geostatistical approach was applied. As was shown in Chapter 5, Section 5.4.4, geostatistical modelling is one of the most widely used techniques for efficient reservoir simulation and characterization. CMG software was utilized as the 3D modelling package to define the petrophysical properties (i.e. permeability) of the Prinos reservoir. Multiple permeability realizations were generated to determine the effect of reservoir heterogeneity on oil recovery factor, NPV and CO_2 storage efficiency. The nugget effect was implemented within the reservoir to generate discontinuities in the spatial distribution of permeability data. As shown in Figure 6.17(a-c) different nugget values of 0.01, 0.1 and 0.5 were applied to represent minimum, medium and maximum heterogeneity respectively. It should be noted that the average permeability in the three heterogeneous reservoir models is similar to the average permeability of the homogeneous reservoir model (i.e. 100mD).

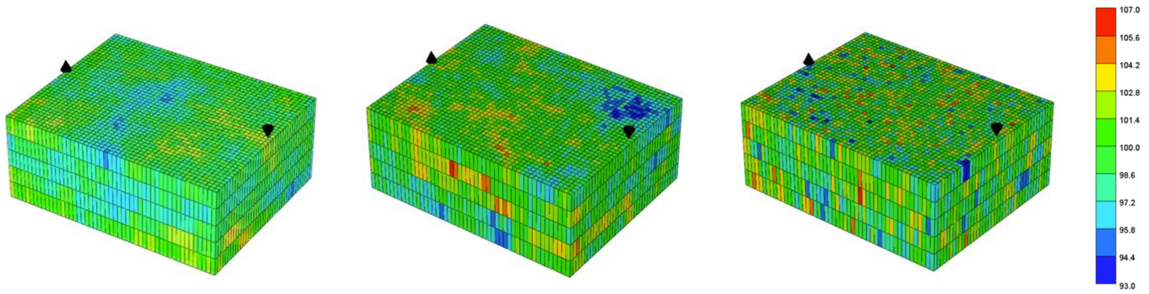

(a) (b) (c)

Figure 6.17 Distributions of reservoir permeability heterogeneity exhibiting (a) minimum heterogeneity, (b) medium heterogeneity, (c) maximum heterogeneity for the Prinos oil reservoir. The scale bar is the permeability (mD)

Hereafter, a spherical semivariogram was applied to describe the generated permeability heterogeneity. Figure 6.18(a-c) shows that the difference between permeability data increases with distance (lag).

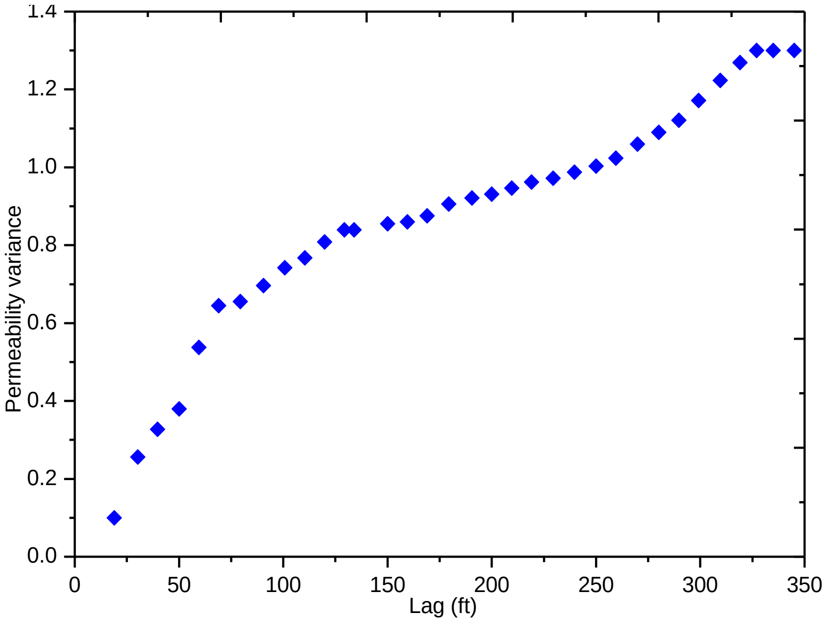

(a)

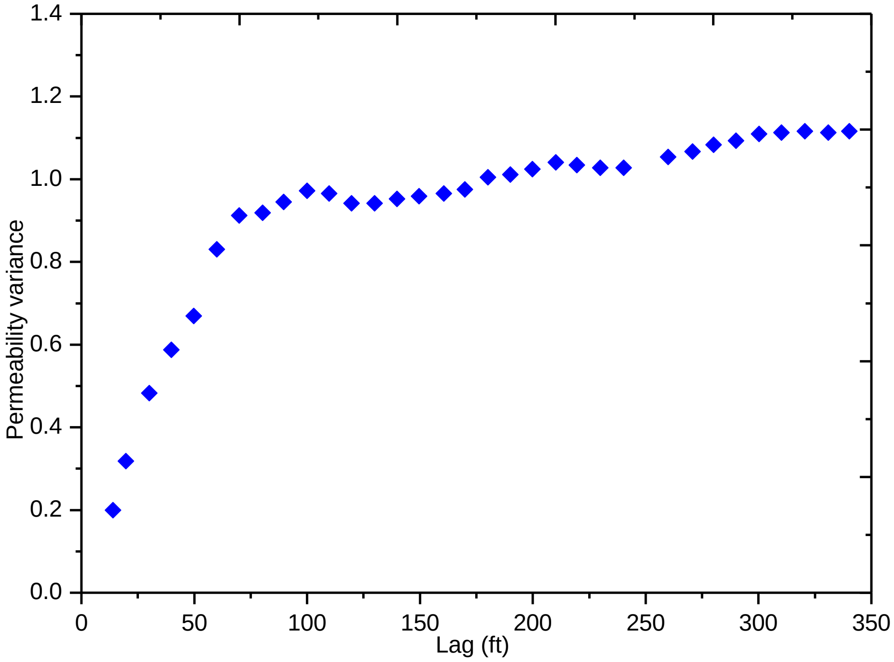

(b)

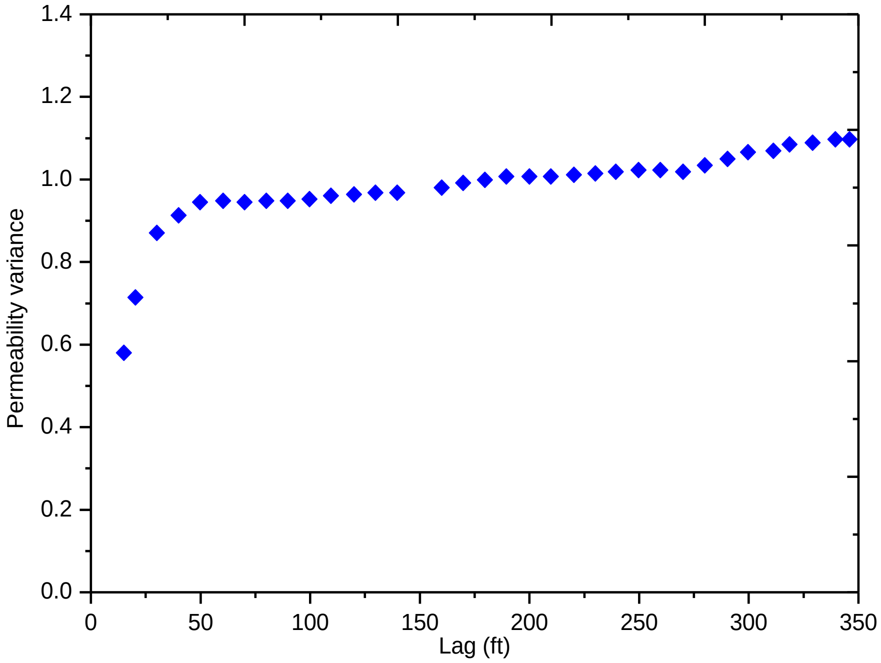

(c)

Figure 6.18 Permeability variance for the reservoir heterogeneous models with a nugget value of (a) 0.01, (b) 0.1, and (c) 0.5

As shown in Table 6.11, the CO_2 storage efficiency for minimum, medium and maximum levels of heterogeneity are greater compared to the homogeneous base case by approximately 140t, 220t and 650t respectively. As a result, the CO_2 storage efficiency increases with increasing permeability heterogeneity, which is an observation made by previous researchers (Al-Khdheeawi et al., 2017; Anderson et al., 2018).

In the case of a homogeneous reservoir, the density difference between CO_2 molecules and reservoir oil enhances mobility of CO_2 molecules towards the top of the reservoir. In contrast, reservoir heterogeneity slows down the migration of CO_2 molecules towards the top of the reservoir and CO_2 spreads laterally (Bondor, 1992; Kovscek, 2002; Flett et al., 2005). Subsequently, CO_2 dissolution within the reservoir oil is increased, leading to greater storage potential.

Simulation results showed that the CO_2 injected, and CO_2 produced in the heterogeneous cases were lower than the homogeneous case. This means that CO_2 cost (i.e. CAPEX and OPEX) in the heterogeneous case was lower than the homogenous case. This observation comes in agreement with similar findings by Lengler et al. (2010) for CO_2 storage in the Ketzin reservoir. However, the NPV in the maximum heterogeneity case showed a decrease by approximately $325,000 compared to the homogeneous case. The reason for this NPV decrease was the oil RF which is directly related to NPV. Table 6.11 also shows that oil RF may decrease by up to 0.02% with increasing permeability heterogeneity due to reduction of CO_2 mobility and greater trapping of CO_2 molecules. In summary, reservoir heterogeneity may have a positive effect on CO_2 storage efficiency, whereas it negatively affects the oil RF.

Table 6.11 Oil recovery factor (RF), Net present value (NPV) and CO_2 sequestration for the homogeneous and heterogeneous scenarios

Reservoir Model	RF (%)	NPV ($MM)	CO_2 stored (Mt)	CO_2 storage Efficiency (%)
Homogeneous	57.163	300.89	1.2098	38.257
Minimum Heterogeneity	57.155	300.87	1.2099	38.261
Medium Heterogeneity	57.149	300.82	1.21	38.263
Maximum Heterogeneity	57.147	300.56	1.2104	38.277

6.5 Summary

This chapter has shown the impact of various CO_2-EOR injection cases compared to the waterflooding case, as the base model. Simulation results showed that the continuous CO_2 flooding case is not favorable for the Prinos reservoir since the NPV decreased by 13% compared to the waterflooding case.

In all the CO_2/water ratios investigated, simulation results showed that CO_2-WAG injection case is favorable for the Prinos reservoir. In particular, CO_2 injection rate had a greater impact on the oil RF when compared to the water injection rate. The optimum CO_2/water ratio at CO_2-WAG injection was the 2:1 ratio since it yields the highest NPV ($313.73 million) due to low operational costs of CO_2 and high oil recovery factor.

The effect of miscibility is a significant factor for the NPV and should not be overlooked. For instance, CO_2-WAG injection under miscible conditions increased by up to $5 million compared to the CO_2-WAG injection under immiscible conditions.

It has also been shown that CO_2 storage efficiency is greatly affected by CO_2-WAG ratio. When the CO_2/water ratio is 3:1 the CO_2 storage efficiency may increase by up to 17% compared to the CO_2/water ratio 1:1. In contrast, high water volume may decrease the CO_2 stored by up to 7.2%.

Geostatistical simulations showed that increasing reservoir permeability heterogeneity was favorable for the CO_2 storage efficiency, whilst it had a negative impact on oil RF. Hence, NPV was affected. For instance, the NPV for reservoir models with maximum permeability heterogeneity may decrease by up to 0.11% (i.e. $325,000), respectively, when compared to the homogeneous base case model. The reason for this decrease was due to reduction of CO_2 mobility and greater trapping of CO_2 molecules.

7. Chapter Seven: Conclusion and Future Work

7.1 Conclusion

In this dissertation, CO_2 injection techniques were investigated in conventional and unconventional reservoirs. A key issue affecting the efficiency of such processes is the transport of CO_2 within the porous rock. A fractal theory for the structure-transport relation for surface diffusivity of molecules on heterogeneous surfaces was expanded and applied to experimental data on the surface diffusion of CO_2 upon shales. Gas (N_2 and CO_2) sorption experimental methods (volumetric and gravimetric analysis) offered an insight into the application of the fractal theory on different shale samples. The experimental results revealed that the value of Arrhenius parameters for surface diffusivity, at a monolayer coverage, can be determined through the degree of structural heterogeneity of a shale surface. Hence, the fractal theory can effectively predict, *a priori*, surface diffusivity parameters for such structurally and chemically heterogeneous natural samples like shales. Therefore, it is concluded that this theory enables the optimization of the designs of CO_2 injection in field applications since surface diffusion is of major importance in the apparent permeability, and, thus, in the gas flow mechanisms.

The experimental values of surface diffusivity were then implemented into an apparent permeability model within a reservoir simulator to investigate the impact of surface diffusion on methane recovery via CO_2 injection techniques (CO_2 flooding, CO_2 huff and puff) at various shale gas reservoirs with different properties. The results showed that surface diffusion plays a significant role in increasing CH_4 production when the average pore radius is less than 2 nm. The reason for this significant contribution of surface diffusion is that the smaller the pore radius, the greater the ratio of surface area per unit volume, and, thus the greater adsorbed-gas transfer volume via surface diffusion. However, in areas where the surface capacity is low, the surface diffusion becomes less pronounced.

The proposed fractal model was additionally applied to all reservoir models to examine the effects of degree of surface roughness on CH_4 production and CO_2 adsorption. It revealed that high surface fractal dimension can potentially enhance CH_4 production and should not be neglected, especially when the average pore radius is less than 1nm. In areas with high surface fractal dimension (2.9), the adsorption of CO_2 and desorption of CH_4 molecules both show substantial increases, when compared to models with no surface diffusion. In all the reservoirs examined, geostatistical reservoir simulations showed that reservoir heterogeneity is not favourable to methane recovery via CO_2 injection techniques where the CO_2 diffusion was not pronounced.

Application of CO_2 injection techniques were also studied in the Prinos reservoir to optimize the oil recovery factor, and, thence, the NPV. In contrast to the shale gas reservoirs, continuous CO_2 injection is not efficient for the Prinos reservoir due to viscous fingering and gravity overriding. However, the CO_2-WAG injection technique was more favorable for the Prinos reservoir. The reason was that the CO_2-WAG technique increases the reservoir pressure above the MMP and effectively controls the mobility of the injected CO_2, leading to higher volumetric sweep efficiency. The effects of CO_2/water ratio, miscibility and reservoir heterogeneity at WAG injection are significant factors for the NPV, as well as the CO_2 storage efficiency and should not be overlooked.

7.2 Future Work

Even though the results and conclusions from this thesis provide valuable information for our understanding of gas adsorption behavior, thermodynamics, fractal theory, kinetics in shale and CO_2 injection in unconventional as well as conventional reservoirs, these topics are far from being exhaustive.

For the proposed fractal theory for surface diffusion, the following future research should be considered:

1. Extension of the fractal theory to different shale types, as well as coal samples, exhibiting a wide range of surface fractal dimensions.
2. Measurement of the surface diffusivity parameter via Nuclear Magnetic Resonance (NMR) to establish the fractal theory.
3. Experimental investigation of impact of water on the kinetics of CO_2 molecules in shale and coal since water can displace the adsorbed phase of methane due to the high affinity of water.
4. Applicability of the fractal theory on a multi-component gas adsorption system.

For the numerical model of CO_2 injection for enhanced gas recovery in shale reservoirs, the following future research should be considered:

1. Examination of the mass transfer processes in CH_4 recovery and CO_2 sequestration assuming a greater range of pore radius in the matrix.
2. Evaluation of the Langmuir capacity parameters in determining the efficiency of transport of CO_2 via surface diffusion.
3. Validation of gas adsorption behavior in different scales of pore via the robust theoretical background of molecular simulation.
4. Evaluation of the impact of surface diffusion on CH_4 recovery via CO_2 injection in coal reservoirs.

For the numerical reservoir simulations of CO_2 injection for enhanced oil recovery in the Prinos reservoir, the following future research should be considered:

1. Investigation of the effects of fault reactivation and CO_2 migration during CO_2 injection.
2. Examination of the local grid refinement to improve predictions and reduce simulation run-time.
3. Optimization of the vertical and lateral distance between injectors.
4. Investigation of the comparison between WAG and thermal methods in Prinos oil reservoirs.

Apart from the foregoing future work suggested, preliminary experimental work was conducted to investigate the application of the fractal theory to both shale and coal samples over a wide range of fractal dimension (please see Appendix E).

References

Abdus, S. and Ganesh, C.T. 1994. *Integrated Petroleum Reservoir Management: A Team Approach* [Online]. [Accessed 6 April 2021]. Available from: https://books.google.gr/books/about/Integrated_Petroleum_Reservoir_Managemen.html.

Abedini, A. and Torabi, F. 2014a. Oil recovery performance of immiscible and miscible CO2 Huff-and-puff processes. *Energy and Fuels*. 28(2), pp.774–784.

Abedini, A. and Torabi, F. 2014b. On the CO2 storage potential of cyclic CO2 injection process for enhanced oil recovery. *Fuel*. 124, pp.14–27.

Afzali, S., Rezaei, N. and Zendehboudi, S. 2018. A comprehensive review on Enhanced Oil Recovery by Water Alternating Gas (WAG) injection. *Fuel*. 227, pp.218–246.

Aghdam, K.A. and Ghorashi, S.S. 2017. *Critical Parameters Affecting Water Alternating Gas (WAG) Injection in an Iranian Fractured Reservoir* [Online]. Research Institute of Petroleum Industry (RIPI). [Accessed 6 April 2021]. Available from: http://jpst.ripi.ir.

Aguilera, R. 2014. Flow Units: From Conventional to Tight-Gas to Shale-Gas to Tight-Oil to Shale-Oil Reservoirs. *SPE Reservoir Evaluation & Engineering*. 17(02), pp.190–208.

Ahmadi, K. and Johns, R.T. 2011. Multiple-mixing-cell method for MMP calculations *In*: *SPE Journal*. Society of Petroleum Engineers, pp.733–742.

Akkutlu, I.Y. and Fathi, E. 2012. Multiscale Gas Transport in Shales With Local Kerogen Heterogeneities. *SPE Journal*. 17(04), pp.1002–1011.

Al-Khdheeawi, E.A., Vialle, S., Barifcani, A., Sarmadivaleh, M. and Iglauer, S. 2017. Impact of reservoir wettability and heterogeneity on CO2-plume migration and trapping capacity. *International Journal of Greenhouse Gas Control*. 58, pp.142–158.

Alba-Simionesco, C., Coasne, B., Dosseh, G., Dudziak, G., Gubbins, K.E., Radhakrishnan, R. and Sliwinska-Bartkowiak, M. 2006. Effects of confinement on freezing and melting. *Journal of Physics: Condensed Matter*. 18(6), pp.R15–R68.

Alexander, P. and Gladden, L.F. 1997. A kinetic description of sorbate motion in zeolites using 2H n.m.r. *Zeolites*. 18(1), pp.38–43.

Alston, R.B., Kokolis, G.P. and James, C.F. 1985. CO2 minimum miscibility pressure: a correlation for impure CO2 streams and live oil oil systems. *Society of Petroleum Engineers journal*. 25(2), pp.268–274.

Alvarado, V. and Manrique, E. 2010. Enhanced oil recovery: An update review. *Energies*. 3(9), pp.1529–1575.

Ambrose, R.J., Hartman, R.C., Diaz-Campos, M., Akkutlu, I.Y. and Sondergeld, C.H. 2012. Shale gas-in-place calculations Part I: New pore-scale considerations *In*: *SPE Journal*. Society of Petroleum Engineers, pp.219–229.

Ambrose, R.J., Hartman, R.C., Diaz Campos, M., Akkutlu, I.Y. and Sondergeld, C. 2010. New Pore-scale Considerations for Shale Gas in Place Calculations *In*: *SPE Unconventional Gas Conference* [Online]. Society of Petroleum Engineers. [Accessed 27 June 2018]. Available from: http://www.onepetro.org/doi/10.2118/131772-MS.

Ampomah, W., Balch, R., Cather, M., Rose-Coss, D., Dai, Z., Heath, J., Dewers, T. and Mozley, P. 2016. Evaluation of CO2 Storage Mechanisms in CO2 Enhanced Oil Recovery Sites: Application to Morrow Sandstone Reservoir. *Energy and Fuels*. 30(10), pp.8545–8555.

Anderson, J., Bachu, S., Bashir Nimir, H., Basu, B., Bradshaw, J., Deguchi, G., Gale, J., Von Goerne, G., Heidug, W., Holloway, S., Kamal, R., Keith, D., Lloyd, P., Rocha, P., Senior, B., Thomson, J., Torp, T., Wildenborg, T., Wilson, M., Zarlenga, F. and Zhou, D. 2018. *IPCC Special Report on Carbon dioxide Capture and Storage*.

Appau, P.O., Dankwa, O.K. and Brantson, E.T. 2019. A comparative study between finite difference explicit and implicit method for predicting pressure distribution in a petroleum reservoir. *International Journal of Engineering, Science and Technology*. 11(4), pp.23–40.

Arnaut, M., Vulin, D., Lamberg, G.J.G. and Jukić, L. 2021. Simulation analysis of co2-eor process and feasibility of co2 storage during eor. *Energies*. 14(4), p.1154.

Arri, L.E., Yee, D., Morgan, W.D. and Jeansonne, M.W. 1992. Modeling Coalbed Methane Production With Binary Gas Sorption *In*: *SPE Rocky Mountain Regional Meeting* [Online]. Society of Petroleum Engineers. [Accessed 21 June 2019]. Available from: http://www.onepetro.org/doi/10.2118/24363-MS.

Avnir, D., Farin, D. and Pfeifer, P. 1984. Molecular fractal surfaces. *Nature*.

Ayirala, S.C. and Rao, D.N. 2006. Comparative evaluation of a new MMP determination technique *In*: *Proceedings - SPE Symposium on Improved Oil Recovery*. OnePetro, pp.349–363.

Aziz, K. and Settari, A. 1979. Petroleum Reservoir Simulation *In*: *Applied Science Publishers.* [Online]. [Accessed 17 June 2021]. Available from: https://books.google.gr/books/about/Petroleum_reservoir_simulation.html?id=GJ5TAAAAMAAJ&redir_esc=y.

Bachu, S. 2000. Sequestration of CO2 in geological media: Criteria and approach for site selection in response to climate change. *Energy Conversion and Management*. 41(9), pp.953–970.

Bahadori, A. 2018. *Fundamentals of Enhanced Oil and Gas Recovery from Conventional and Unconventional Reservoirs*. Elsevier Inc.

Barrer, R.M. 1987. *Flow into and through Zeolite Beds and Compactst* [Online]. [Accessed 10 April 2019]. Available from: https://pubs.acs.org/sharingguidelines.

Behrensmeyer, A.K. 2006. Climate Change and Human Evolution. *Science (Washington)*. 311, pp.476–478.

Bellani, J., Verma, H.K., Khatri, D., Makwana, D. and Shah, M. 2021. Shale gas: a step toward sustainable energy future. *Journal of Petroleum Exploration and Production*., pp.1–15.

Bera, A., Agarwal, J., Shah, M., Shah, S. and Vij, R.K. 2020. Recent advances in ionic liquids as alternative to surfactants/chemicals for application in upstream oil industry. *Journal of Industrial and Engineering Chemistry*. 82, pp.17–30.

Bhatia, J., Srivastava, J.P., Sharma, A. and Sangwai, J.S. 2014. Production performance of water alternate gas injection techniques for enhanced oil recovery: Effect of WAG ratio, number of WAG cycles and the type of injection gas. *International Journal of Oil, Gas and Coal Technology*. 7(2), pp.132–151.

Bolis, V. 2013. Fundamentals in Adsorption at the Solid-Gas Interface. Concepts and Thermodynamics *In*:, pp.3–50. [Accessed 27 June 2018]. Available from: http://link.springer.com/10.1007/978-3-642-11954-5_1.

Bondor, P.L. 1992. Applications of carbon dioxide in enhanced oil recovery. *Energy Conversion and Management*. 33(5–8), pp.579–586.

Bougre, E.S. and Gamadi, · T D 2021. Enhanced oil recovery application in low permeability formations by the injections of CO2 , N2 and CO2/N2 mixture gases. *Journal of Petroleum Exploration and Production*. 11(4), pp.1–9.

BP 2020. *BP energy outlook* [Online]. [Accessed 1 July 2021]. Available from: https://ieefa.org/bp-energy-outlook-sees-global-fossil-fuel-demand-falling-for-first-time-this-year/.

Brunauer, S., Emmett, P.H. and Teller, E. 1938. Adsorption of Gases in Multimolecular Layers. *Journal of the American Chemical Society*. 60(2), pp.309–319.

Busch, A., Alles, S., Gensterblum, Y., Prinz, D., Dewhurst, D.N., Raven, M.D., Stanjek, H. and Krooss, B.M. 2008. Carbon dioxide storage potential of shales. *International Journal of Greenhouse Gas Control*. 2(3), pp.297–308.

Bustin, R.. and Clarkson, C.. 1998. Geological controls on coalbed methane reservoir capacity and gas content. *International Journal of Coal Geology*. 38(1–2), pp.3–26.

Chalmers, G.R.L. and Marc Bustin, R. 2007. On the effects of petrographic composition on coalbed methane sorption. *International Journal of Coal Geology*. 69(4), pp.288–304.

Cheah, K.Y., Alexander, P. and Gladden, L.F. 1997. Investigation of coking phenomena in zeolite HY using deuterium NMR. *Applied Catalysis A: General*. 148(2), pp.387–403.

Chen, Y.D. and Yang, R.T. 1991. Concentration dependence of surface diffusion and zeolitic diffusion. *AIChE Journal*. 37(10), pp.1579–1582.

Choi, J.-G., Do, D.D. and Do, H.D. 2001. Surface Diffusion of Adsorbed Molecules in Porous Media: Monolayer, Multilayer, and Capillary Condensation Regimes.

Christensen, J.R., Stenby, E.H. and Skauge, A. 1998. Review of WAG field experience *In*: *Proceedings of the SPE International Petroleum Conference & Exhibition of Mexico*. Soc Pet Eng (SPE), pp.357–370.

Cipolla, C.L., Lolon, E.P., Erdle, J.C. and Rubin, B. 2010. Reservoir Modeling in Shale-Gas Reservoirs. *SPE Reservoir Evaluation & Engineering*. 13(04), pp.638–653.

Civan, F., Rai, C.S. and Sondergeld, C.H. 2011. Shale-Gas Permeability and Diffusivity Inferred by Improved Formulation of Relevant Retention and Transport Mechanisms. *Transport in Porous Media*. 86(3), pp.925–944.

Clarkson, C.R., Solano, N., Bustin, R.M., Bustin, A.M.M., Chalmers, G.R.L., He, L., Melnichenko, Y.B., Radliński, A.P. and Blach, T.P. 2013. Pore structure characterization of North American shale gas reservoirs using USANS/SANS, gas adsorption, and mercury intrusion. *Fuel*. 103, pp.606–616.

CMG-GEM 2019. *Compositional and Unconventional Reservoir Simulator*, Calgary, Computer Modelling Group Ltd.

CMG-MOST 2019. *Intelligent Optimization & Analysis Tool Reservoir Simulator*, Calgary, Computer Modelling Group Ltd.

Cooke, C.E. 1973. Conductivity of fracture proppants in multiple layers. *JPT, Journal of Petroleum Technology*. 25(09), pp.1101–1107.

Crank, J. 1975. *The Mathematics of Diffusion* [Online]. Clarendon press Oxford. [Accessed 4 December 2018]. Available from: http://www.eng.lbl.gov/~shuman/Next/Materials%26Components/Xe_damage/Crank-The-Mathematics-of-Diffusion.pdf.

Crosdale, P.J., Beamish, B.B. and Valix, M. 1998. Coalbed methane sorption related to coal composition. *International Journal of Coal Geology*. 35(1–4), pp.147–158.

Cui, X., Bustin, A.M.M. and Bustin, R.M. 2009. Measurements of gas permeability and diffusivity of tight reservoir rocks: Different approaches and their applications. *Geofluids*. 9(3), pp.208–223.

Cuiec, L., Bourbiaux, B. and Kalaydjian, F. 1994. Oil recovery by imbibition in low-permeability chalk. *SPE Formation Evaluation*. 9(3), pp.200–208.

Curtis, J.B. 2002. Fractured shale-gas systems. *AAPG Bulletin*. 86(11), pp.1921–1938.

Daigle, H., Ezidiegwu, S. and Turner, R. 2015. Determining Relative Permeability In Shales By Including The Effects Of Pore Structure On Unsaturated Diffusion And Advection *In*: *SPE Annual Technical Conference and Exhibition* [Online]. Society of Petroleum Engineers. [Accessed 15 June 2020]. Available from: http://www.onepetro.org/doi/10.2118/175019-MS.

Darabi, H., Ettehad, A., Javadpour, F. and Sepehrnoori, K. 2012. Gas flow in ultra-tight shale strata. *Journal of Fluid Mechanics*. 710, pp.641–658.

David Martin, F. and Taber, J.J. 1992. Carbon dioxide flooding. *JPT, Journal of Petroleum Technology*. 44(4), pp.396–410.

Dellinger, E.S., Patton, J.T. and Holbrook, S.T. 1984. CO2 Mobility control. *Society of Petroleum Engineers journal*. 24(2), pp.191–196.

Dilmore, R., Bruner, K., Wyatt, C., Romanov, V., Goodman, A., Hedges, S., McIntyre, D., Crandall, D., Gill, M., Disenhof, C., Jinesh, J., Lopano, C., Aminian, K., Zamirian, M., Mashayekhi, A., Sanguinito, S., Mroz, T. and Soeder, D. 2015. Experimental Characterization of Marcellus Shale Outcrop Samples, and Their Interactions with Carbon Dioxide and Methane. U.S. *Department of Energy, National Energy Technology Laboratory, Morgantown, WV NETL Technical Report Series.*

Do, D.D. and Wang, K. 1998. A new model for the description of adsorption kinetics in heterogeneous activated carbon. *Carbon*. 36(10), pp.1539–1554.

Do, D.D. 1998. *Adsorption Analysis: Equilibria and Kinetics* [Online]. Imperial College Press. [Accessed 23 June 2020]. Available from: https://www.worldscientific.com/worldscibooks/10.1142/p111.

Do, D.D. 1990. Hierarchy of rate models for adsorption and desorption in bidispersed structured sorbents. *Chemical Engineering Science*. 45(5), pp.1373–1381.

Do, D.D. and Rice, R.G. 1991. A simple method of determining pore and surface diffusivities in adsorption studies. *Chemical Engineering Communications*. 107(1), pp.151–161.

Do, H.D., Do, D.D. and Prasetyo, I. 2001. On the surface diffusion of hydrocarbons in microporous activated carbon. *Chemical Engineering Science*. 56(14), pp.4351–4368.

Du, F. and Nojabaei, B. 2020. Estimating diffusion coefficients of shale oil, gas, and condensate with nano-confinement effect. *Journal of Petroleum Science and Engineering*. 193, p.107362.

Dubinin, M.M. 1975. Physical Adsorption of Gases and Vapors in Micropores. *Progress in Surface and Membrane Science*. 9, pp.1–70.

Dubinin, M.M. 1960. The Potential Theory of Adsorption of Gases and Vapors for Adsorbents with Energetically Nonuniform Surfaces. *Chemical Reviews*. 60(2), pp.235–241.

EIA 2021. Greenhouse gases' effect on climate. U.S. Energy Information Administration. *U.S. Department of Energy, Washington, D.C.* [Online]. [Accessed 9 July 2021]. Available from: https://www.eia.gov/energyexplained/energy-and-the-environment/greenhouse-gases-and-the-climate.php.

EIA 2020. International Energy Outlook. *U.S. Department of Energy, Washington, D.C.* [Online]. [Accessed 1 July 2021]. Available from: www.eia.gov.

EIA 2010. Schematic geology of natural gas resources. *U.S. Department of Energy, Washington, D.C.* [Online]. [Accessed 9 July 2021]. Available from: http://www.eia.gov/oil_gas/natural_gas/%0Aspecial/ngresources/ngresources.html.

EIA 2016. Trends in U.S. Oil and Natural Gas Upstream Costs. *U.S. Department of Energy, Washington, D.C.* [Online]. [Accessed 6 April 2021]. Available from: www.eia.gov.

EIA 2017. Utica Shale Play. *U.S. Dep. Energy, Washington, D.C.* [Online]. [Accessed 30 August 2021]. Available from: www.eia.gov.

El-Maghraby, R.M., Pentland, C.H. and Blunt, M.J. 2011. Coreflood measurements of CO2 trapping *In*: *Proceedings - SPE Annual Technical Conference and Exhibition*. Society of Petroleum Engineers (SPE), pp.4285–4290.

Energean PLC 2018. https://www.energean.com/. [Accessed 6 April 2021]. Available from: https://www.energean.com/.

Energy, I.O. 2008. US Department of Energy. *US Department of Energy*. [Online]. [Accessed 24 May 2021]. Available from: https://www.researchgate.net/deref/http%3A%2F%2Fwww.%2520fossil.energy.gov%2Fprograms%2Foilgas%2Feor%2Findex.html.

Etebar, S. 1995. Captain innovative development approach *In*: *Offshore Europe Conference - Proceedings*. Society of Petroleum Engineers (SPE), pp.115–123.

Etminan, S.R., Javadpour, F., Maini, B.B. and Chen, Z. 2014. Measurement of gas storage processes in shale and of the molecular diffusion coefficient in kerogen. *International Journal of Coal Geology*. 123, pp.10–19.

Evans, R., Marconi, U.M.B. and Tarazona, P. 1986. Capillary condensation and adsorption in cylindrical and slit-like pores. *Journal of the Chemical Society, Faraday Transactions 2: Molecular and Chemical Physics*. 82(10), pp.1763–1787.

Evans, R., Marini Bettolo Marconi, U. and Tarazona, P. 1985. Fluids in narrow pores: Adsorption, capillary condensation, and critical points. *The Journal of Chemical Physics*. 84(4), pp.2376–2399.

Evans, R. and Tarazona, P. 1984. Theory of condensation in narrow capillaries. *Physical Review Letters*. 52(7), pp.557–560.

Evans, R.D. and Civan, F. 1994. *Characterization of non-Darcy multiphase flow in petroleum bearing formation. Final report* [Online]. Pittsburgh, PA, and Morgantown, WV. [Accessed 21 June 2019]. Available from: http://www.osti.gov/servlets/purl/10142377-nIwwlt/native/.

Fandrich, R., Gu, Y., Burrows, D., Moeller, K. 2006. Modern SEM-based mineral liberation analysis. *International Journal of mineral processing*. 84(2007), pp.310-320.

Falkowski, P., Scholes, R.J., Boyle, E., Canadell, J., Canfield, D., Elser, J., Gruber, N., Hibbard, K., Hogberg, P., Linder, S., Mackenzie, F.T., Moore, B., Pedersen, T., Rosental, Y., Seitzinger, S., Smetacek, V. and Steffen, W. 2000. The global carbon cycle: A test of our knowledge of earth as a system. *Science*. 290(5490), pp.291–296.

Fan, W., Sun, H., Yao, J., Fan, D. and Zhang, K. 2018. A new fractal transport model of shale gas reservoirs considering multiple gas transport mechanisms, multi-scale and heterogeneity. *Fractals*. 26(6), pp.1850096.

Fathi, E. and Akkutlu, I.Y. 2014. Multi-component gas transport and adsorption effects during CO 2 injection and enhanced shale gas recovery.

Feng, X., Ma, F., Zhao, H., Liu, G. and Guo, J. 2019. Gas Multiple Flow Mechanisms and Apparent Permeability Evaluation in Shale Reservoirs. *Sustainability*. 11(7), pp.2114.

Fianu, J., Gholinezhad, J. and Hassan, M. 2018. Comparison of Temperature-Dependent Gas Adsorption Models and Their Application to Shale Gas Reservoirs. *Energy and Fuels*. 32(4), pp. 4763–4771.

Firoozabadi, A. and Aziz, K. 1986. Analysis and correlation of nitrogen and lean-gas miscibility pressure. *SPE Reservoir Engineering (Society of Petroleum Engineers)*. 1(6), pp.575–582.

Firouzi, M., Rupp, E.C., Liu, C.W. and Wilcox, J. 2014. Molecular simulation and experimental characterization of the nanoporous structures of coal and gas shale. *International Journal of Coal Geology*. 121, pp.123–128.

Flett, M.A., Gurton, R.M. and Taggart, I.J. 2005. Heterogeneous saline formations: Long-term benefits for geo-sequestration of greenhouse gases *In*: *Greenhouse Gas Control Technologies*. Elsevier Ltd, pp.501–509.

Forchheimer, P.Z. 1901. Wasserbewegungdurch Boden. *Zeitschrift des Vereins Deutscher Ingenieure,*. 45, pp.1781–1788.

Fukai, I., Mishra, S. and Moody, M.A. 2016. Economic analysis of CO2-enhanced oil recovery in Ohio: Implications for carbon capture, utilization, and storage in the Appalachian Basin region. *International Journal of Greenhouse Gas Control*. 52, pp.357–377.

Fumagalli, A., Zonca, S. and Formaggia, L. 2017. Advances in computation of local problems for a flow-based upscaling in fractured reservoirs. *Mathematics and Computers in Simulation*. 137, pp.299–324.

Geertsma, J. 1974. Estimating the coefficient of inertial resistance in fluid flow through porous media. *Soc Pet Eng AIME J*. 14(5), pp.445–450.

Ghani, A., Khan, F. and Garaniya, V. 2015. Improved oil recovery using CO2 as an injection medium: a detailed analysis. *Journal of Petroleum Exploration and Production Technology*. 5(3), pp.241–254.

Ghedan, S. 2009. Global Laboratory Experience of CO2-EOR Flooding *In*: *Reservoir Characterization & Simulation Conference* [Online]. EAGE Publications, cp-170-00075. [Accessed 21 May 2021]. Available from: https://www.earthdoc.org/content/papers/10.3997/2214-4609-pdb.170.spe125581.

Ghosh, B., Sun, L. and Osisanya, S. 2016. Smart-Water EOR Made Smarter A Laboratory Development. *In*: *International Petroleum Technology Conference, Bangkok, Thailand*. Available from: https://doi.org/10.2523/IPTC-18988-MS

Gilliland, E.R., Baddour, R.F., Perkinson, G.P. and Sladek, K.J. 1974. *Diffusion on Surfaces. I. Effect of Concentration on the Diffusivity of Physically Adsorbed Gases* [Online]. UTC. [Accessed 12 September 2018]. Available from: https://pubs.acs.org/sharingguidelines.

Giovambattista, N., Rossky, P.J. and Debenedetti, P.G. 2009. Phase Transitions Induced by Nanoconfinement in Liquid Water. *Physical Review Letters*. 102(5), p.050603.

Glaso, O.S. 1985. Generalized minimum miscibility pressure correlation. *Society of Petroleum Engineers journal*. 25(6), pp.927–934.

Godec, M., Koperna, G., Petrusak, R. and Oudinot, A. 2013. Potential for enhanced gas recovery and CO2 storage in the Marcellus Shale in the Eastern United States. *International Journal of Coal Geology*. 118, pp.95–104.

Gong, B., Qin, G., Douglas, C. and Yuan, S. 2011. Detailed modeling of the complex fracture network of shale gas reservoirs *In*: *Society of Petroleum Engineers - SPE Middle East Unconventional Gas Conference and Exhibition 2011, UGAS*. OnePetro, pp.370–378.

Gong, Y. and Gu, Y. 2015. Experimental Study of Water and CO2 Flooding in the Tight Main Pay Zone and Vuggy Residual Oil Zone of a Carbonate Reservoir. *Energy and Fuels*. 29(10), pp.6213–6223.

Gozalpour, F., Ren, S.R. and Tohidi, B. 2005. CO2 EOR and storage in oil reservoirs. *Oil and Gas Science and Technology*. 60(3), pp.537–546.

Greaves, M., Xia, T.X. and Turta, A.T. 2008. Stability of THAI^{TM} process-theoretical and experimental observations. *Journal of Canadian Petroleum Technology*. 47(9), pp.65–73.

Greaves, M., Xia, T.X., Turta, A.T. and Ayasse, C. 2000. Recent Laboratory Results of THAI and Its Comparison with Other IOR Processes *In*: *Society of Petroleum Engineers (SPE)*. Society of Petroleum Engineers (SPE).

Green, D. and Willhite, P. 1998. *Enhanced Oil Recovery* [Online]. [Accessed 21 May 2021]. Available from: https://pdf.wecabrio.com/enhanced-oil-recovery-green-willhite.pdf.

Groen, J.C., Peffer, L.A.. and Pérez-Ramírez, J. 2003. Pore size determination in modified micro- and mesoporous materials. Pitfalls and limitations in gas adsorption data analysis. *Microporous and Mesoporous Materials*. 60(1–3), pp.1–17.

Gu, X., Mildner, D.F.R., Cole, D.R., Rother, G., Slingerland, R. and Brantley, S.L. 2016. Quantification of Organic Porosity and Water Accessibility in Marcellus Shale Using Neutron Scattering. *Energy and Fuels*. 30(6), pp.4438–4449.

Guliyev, A. 2018. '*Pore compressibility of reservoir sandstones from integrated laboratory experiments'*, PhD thesis, Colorado University, Colorado.

Guo, C., Wei, M. and Liu, H. 2018. Study of gas production from shale reservoirs with multi-stage hydraulic fracturing horizontal well considering multiple transport mechanisms D. A. Lightfoot, ed. *PLOS ONE*. 13(1), p.e0188480.

Guo, L., Peng, X. and Wu, Z. 2008. Dynamical characteristics of methane adsorption on monolith nanometer activated carbon. *Huagong Xuebao*. 59(11), pp.2726–2732.

Hall, F.E., Chunhe, Z., Gasem, K.A.M., Robinson, R.L. and Dan, Y. 1994. Adsorption of Pure Methane, Nitrogen, and Carbon Dioxide and Their Binary Mixtures on Wet Fruitland Coal *In*: *SPE Eastern Regional Meeting* [Online]. Society of Petroleum Engineers. [Accessed 21 June 2019]. Available from: http://www.onepetro.org/doi/10.2118/29194-MS.

Han, L. and Gu, Y. 2014. Optimization of miscible CO2 water-alternating-gas injection in the bakken formation. *Energy and Fuels*. 28(11), pp.6811–6819.

Hassan, A., Elkatatny, S. and Abdulraheem, A. 2019. Intelligent Prediction of Minimum Miscibility Pressure (MMP) During CO2 Flooding Using Artificial Intelligence Techniques. *Sustainability*. 11(24), p.7020.

Haul, R. 1982. S. J. Gregg, K. S. W. Sing: Adsorption, Surface Area and Porosity. 2. Auflage, Academic Press, London 1982. 303 Seiten, Preis: $ 49.50. *Berichte der Bunsengesellschaft für physikalische Chemie*. 86(10), pp.957–957.

Havlin, S. and Ben-Avraham, D. 1987. Diffusion in disordered media. *Advances in Physics*. 36(6), pp.695–798.

Hawthorne, S.B., Gorecki, C.D., Sorensen, J.A., Steadman, E.N., Harju, J.A. and Melzer, S. 2013. Hydrocarbon Mobilization Mechanisms from Upper, Middle, and Lower Bakken Reservoir Rocks Exposed to CO2. *Society of Petroleum Engineers - SPE Canadian Unconventional Resources Conference 2013 - Unconventional Becoming Conventional: Lessons Learned and New Innovations*. 2, pp.920–928.

Heller, R. and Zoback, M. 2014. Adsorption of methane and carbon dioxide on gas shale and pure mineral samples. *Journal of Unconventional Oil and Gas Resources*. 8(C), pp.14–24.

HHRM 2018. Prinos Concession. [Accessed 6 April 2021]. Available from: https://www.greekhydrocarbons.gr/en/PrinosConcession_en.html.

Hitchcock, I., Malik, S., Holt, E.M., Fletcher, R.S. and Rigby, S.P. 2014. Impact of Chemical Heterogeneity on the Accuracy of Pore Size Distributions in Disordered Solids. *ACS, Journal of Physical Chemistry*.118(35) pp.20627-20638

Ho, C.K. 2000. *Dual Porosity vs. Dual Permeability Models of Matrix Diffusion in Fractured*

Rock [Online]. Sandia National Laboratories. [Accessed 18 November 2020]. Available from: https://digital.library.unt.edu/ark:/67531/metadc724039/.

Holdaway, K. 2014. *Harness Oil and Gas Big Data with Analytics: Optimize Exploration and Production with Data-Driven Models*. Wiley.

Holm, L.R.W. and Josendal, V.A. 1982. Effect of oil composition on miscible-type displacement by carbon dioxide. *Society of Petroleum Engineers journal*. 22(1), pp.87–98.

Holm, L.W. 1987. Evolution of the carbon dioxide flooding processes. *JPT, Journal of Petroleum Technology*. 39(11), pp.1337–1342.

Holm, L.W. and Josendal, V.A. 1974. Mechanisms of oil displacement by carbon dioxide. *Journal of Petroleum Technology*. 26(12), pp.1427–1438.

Holt, J.K. 2006. Fast Mass Transport Through Sub-2-Nanometer Carbon Nanotubes. *Science*. 312(5776), pp.1034–1037.

Holt, T., Lindeberg, E. and Wessel-Berg, D. 2009. EOR and CO2 disposal - Economic and capacity potential in the North Sea *In*: *Energy Procedia*. Elsevier, pp.4159–4166.

Hong, L., Jain, J., Romanov, V., Lopano, C., Disenhof, C., Goodman, A., Hedges, S., Soeder, D., Sanguinit, S. and Dilmore, R. 2016. An investigation of factors affecting the interaction of CO2 and CH4 on shale in Appalachian Basin. *Journal of Unconventional Oil and Gas Resources*. 14, pp.99–112.

Hosseini, E., Gholami, R. and Hajivand, F. 2019. Geostatistical modeling and spatial distribution analysis of porosity and permeability in the Shurijeh-B reservoir of Khangiran gas field in Iran. *Journal of Petroleum Exploration and Production Technology*. 9(2), pp.1051–1073.

Huang, S., Wu, Y., Cheng, L., Liu, H., Xue, Y. and Ding, G. 2018. Apparent permeability model for shale gas reservoirs considering multiple transport mechanisms. *Geofluids*. 2018.

Hwang, S. and Kammermeyer, K. 1966. Surface diffusion in microporous media. *The Canadian Journal of Chemical Engineering*. 44(2), pp.82–89.

HYSYS 2020. A Property Methods and Calculations. [Accessed 16 September 2020]. Available from: https://www.aspentech.com/en/products/pages/aspen-hysys-dynamics.

Istchenko, C.M. and Gates, I.D. 2014. Well/wormhole model of cold heavy-oil production with sand. *SPE Journal*. 19(2), pp.260–269.

Iwashaki, S., Kamijo, T., Takashina, T. and Tanaka, H. 2004. Large Scale Flue Gas CO2 Recovering / CO2 Cost and Total System for CO2 Enhanced Oil Recovery. *In: Technical Review Mitsubishi heavy Industries Ltd.* 11(4), pp. 50-59

Jaber, A.K. and Awang, M.B. 2017. Field-scale investigation of different miscible CO2-injection modes to improve oil recovery in a clastic highly heterogeneous reservoir. *Journal of Petroleum Exploration and Production Technology*. 7(1), pp.125–146.

Jarrell, P., Fox, C., Stein, M. and Webb, S. 2002. *Practical aspects of* CO_2 *flooding*. Society of Petroleum Engineers.

Jatukaran, A., Zhong, J., Abedini, A., Sherbatian, A., Zhao, Y., Jin, Z., Mostowfi, F. and

Sinton, D. 2019. Natural gas vaporization in a nanoscale throat connected model of shale: multi-scale, multi-component and multi-phase. *Lab on a Chip*. 19(2), pp.272–280.

Jayasekera, A.J. and Goodyear, S.G. 1999. The Development of Heavy Oil Fields in the U.K. Continental Shelf: Past, Present and Future *In*: *Society of Petroleum Engineers (SPE)*. Society of Petroleum Engineers (SPE).

Johns, R.T., Dindoruk, B. and Orr, F.M. 1993. Analytical theory of combined condensing/vaporizing gas drives. *SPE Advanced Technology Series*. 1(2), pp.7–16.

Kang, S.M., Fathi, E., Ambrose, R.J., Akkutlu, I.Y. and Sigal, R.F. 2011. Carbon Dioxide Storage Capacity of Organic-Rich Shales. *SPE Journal*. 16(04), pp.842–855.

Karacan, C.Ö. and Mitchell, G.D. 2003. Behavior and effect of different coal microlithotypes during gas transport for carbon dioxide sequestration into coal seams. *International Journal of Coal Geology*. 53(4), pp.201–217.

Karimaie, H., Nazarian, B., Aurdal, T., Nøkleby, P.H. and Hansen, O. 2017. Simulation Study of CO2 EOR and Storage Potential in a North Sea Reservoir *In*: *Energy Procedia*. Elsevier Ltd, pp.7018–7032.

Karimi-Fard, M. and Durlofsky, L.J. 2016. A general gridding, discretization, and coarsening methodology for modeling flow in porous formations with discrete geological features. *Advances in Water Resources*. 96, pp.354–372.

Karniadakis, G., Beskok, A. and Aluru, N. 2005. *Microflows and Nanoflows: Fundamentals and Simulation* [Online]. [Accessed 17 November 2020]. Available from: https://books.google.co.uk/books/about/Microflows_and_Nanoflows.html?id=JRSYpC8OwsgC.

Kazemi, H., Gilman, J.R. and Elsharkawy, A.M. 1992. Analytical and numerical solution of oil recovery from fractured reservoirs with empirical transfer functions. *SPE Reservoir Engineering (Society of Petroleum Engineers)*. 7(2), pp.219–227.

Kazemi, H., Vestal, C.R. and Shank, G.D. 1978. Efficient multicomponent numerical simulator. *Soc Pet Eng AIME J*. 18(5), pp.355–368.

Keeling, C.D., Whorf, T.P., Wahlen, M. and Plicht, J. van der 1995. Interannual extremes in the rate of rise of atmospheric carbon dioxide since 1980. *Nature*. 375(6533), pp.666–670.

Kim, J., Maiti, A., Lin, L.-C., Stolaroff, J.K., Smit, B. and Aines, R.D. 2013. New materials for methane capture from dilute and medium-concentration sources. *Nature Communications*. 4(1), p.1694.

Kim, T.H., Cho, J. and Lee, K.S. 2017. Evaluation of CO2 injection in shale gas reservoirs with multi-component transport and geomechanical effects. *Applied Energy*. 190, pp.1195–1206.

King, C., Coleman, S., Cohen, S. and Gülen, G. 2011. The economics of an integrated CO2 capture and sequestration system: Texas Gulf Coast case study *In*: *Energy Procedia*. Elsevier Ltd, pp.2588–2595.

Köfinger, J., Hummer, G. and Dellago, C. 2008. Macroscopically ordered water in nanopores. *Proceedings of the National Academy of Sciences of the United States of America*. 105(36), pp.13218–22.

Koga, K., Gao, G.T., Tanaka, H. and Zeng, X.C. 2001. Formation of ordered ice nanotubes inside carbon nanotubes. *Nature*. 412(6849), pp.802–805.

Kong, X., Delshad, M. and Wheeler, M. 2015. A Numerical Study of Benefits of Adding Polymer to WAG Processes for a Pilot Case *In*: *SPE Reservoir Simulation Conference* [Online]. [Accessed 21 May 2021]. Available from: https://onepetro.org/spersc/proceedings-abstract/15RSS/2-15RSS/D022S002R015/183451.

Kouzoukas, N., Ziogou, F. and Gemeni, V. 2011. Cost of pipeline-based CO2 transport and geological storage in saline aquifers in Greece *In*: *Energy Procedia*. Elsevier Ltd, pp.2978–2983.

Kovscek, A.R. 2002. Screening criteria for CO2 storage in oil reservoirs. *Petroleum Science and Technology*. 20(7–8), pp.841–866.

Krishna, R. and van den Broeke, L.J.P. 1995. The Maxwell-Stefan description of mass transport across zeolite membranes. *The Chemical Engineering Journal and The Biochemical Engineering Journal*. 57(2), pp.155–162.

Kruk, M., Antochshuk, V., Jaroniec, M. and Sayari, A. 1999. New approach to evaluate pore size distributions and surface areas for hydrophobie mesoporous solids. *Journal of Physical Chemistry B*. 103(48), pp.10670–10678.

Kumar, S. and Mandal, A. 2017. A comprehensive review on chemically enhanced water alternating gas/CO2 (CEWAG) injection for enhanced oil recovery. *Journal of Petroleum Science and Engineering*. 157, pp.696–715.

Lambert, M.R., Marino, S.D., Anthony, T.L., Calvin, M.W., Gutierrez, S. and Smith, D.P. 1996. Implementing CO2 floods: No more delays! *In*: *Society of Petroleum Engineers - Permian Basin Oil and Gas Recovery Conference, OGR 1996*. Society of Petroleum Engineers, pp.361–368.

Landers, J., Gor, G.Y. and Neimark, A. V. 2013. Density functional theory methods for characterization of porous materials. *Colloids and Surfaces A: Physicochemical and Engineering Aspects*. 437, pp.3–32.

Langmuir, I. 1918. The adsorption of gases on plane surfaces of glass, mica and platinum. *Journal of the American Chemical Society*. 40(9), pp.1361–1403.

Langmuir, I. 1916. The constitution and fundamental properties of solids and liquids. Part I. Solids. *Journal of the American Chemical Society*. 38(11), pp.2221–2295.

Lastoskie, C., Gubbins, K.E. and Quirke, N. 1993. Pore size heterogeneity and the carbon slit pore: a density functional theory model. *Langmuir*. 9(10), pp.2693–2702.

Lei, H., Yang, S., Zu, L., Wang, Z. and Li, Y. 2016. Oil Recovery Performance and CO2 Storage Potential of CO2 Water-Alternating-Gas Injection after Continuous CO2 Injection in a Multilayer Formation. *Energy and Fuels*. 30(11), pp.8922–8931.

Lengler, U., De Lucia, M. and Kühn, M. 2010. The impact of heterogeneity on the distribution of CO2: Numerical simulation of CO2 storage at Ketzin. *International Journal of Greenhouse Gas Control*. 4(6), pp.1016–1025.

Li, X. and Elsworth, D. 2015. Geomechanics of CO2 enhanced shale gas recovery. *Journal of Natural Gas Science and Engineering*. 26, pp.1607–1619.

Li, Y. -K and Nghiem, L.X. 1986. Phase equilibria of oil, gas and water/brine mixtures from a cubic equation of state and henry's law. *The Canadian Journal of Chemical Engineering*. 64(3), pp.486–496.

Li, Y., Wang, Z., Pan, Z., Niu, X., Yu, Y. and Meng, S. 2019. Pore structure and its fractal dimensions of transitional shale: A cross-section from east margin of the Ordos Basin, China. *Fuel*. 241, pp.417–431.

Li, Z. and Gu, Y. 2014. Soaking effect on miscible CO2 flooding in a tight sandstone formation. *Fuel*. 134, pp.659–668.

Ligero, E.L. and Schiozer, D.J. 2014. Miscible WAG-CO2 light oil recovery from low temperature and high pressure heterogeneous reservoir *In*: *SPE Latin American and Caribbean Petroleum Engineering Conference Proceedings*. Society of Petroleum Engineers (SPE), pp.526–538.

Liu, D., Li, Y., Yang, S. and Agarwal, R.K. 2019. CO2 sequestration with enhanced shale gas recovery . *Energy Sources, Part A: Recovery, Utilization, and Environmental Effects*., pp.1–11.

Liu, F., Ellett, K., Xiao, Y. and Rupp, J.A. 2013. Assessing the feasibility of CO2 storage in the New Albany Shale (Devonian-Mississippian) with potential enhanced gas recovery using reservoir simulation. *International Journal of Greenhouse Gas Control*. 17, pp.111–126.

Liu, J., Xie, L., Yao, Y., Gan, Q., Zhao, P. and Du, L. 2019. Preliminary Study of Influence Factors and Estimation Model of the Enhanced Gas Recovery Stimulated by Carbon Dioxide Utilization in Shale. *ACS Sustainable Chemistry and Engineering*. 7(24), pp.20114–20125.

Liu, J., Yao, Y., Liu, D., Cai, Y. and Cai, J. 2018. Comparison of pore fractal characteristics between marine and continental shales. *Fractals*. 26(2), p.1840016.

Liu, S., Sun, B., Xu, J., Li, H. and Wang, X. 2020. Study on Competitive Adsorption and Displacing Properties of CO2Enhanced Shale Gas Recovery: Advances and Challenges. *Geofluids*. 2020.

Louk, K., Ripepi, N., Luxbacher, K., Gilliland, E., Tang, X., Keles, C., Schlosser, C., Diminick, E., Keim, S., Amante, J. and Michael, K. 2017. Monitoring CO2 storage and enhanced gas recovery in unconventional shale reservoirs: Results from the Morgan County, Tennessee injection test. *Journal of Natural Gas Science and Engineering*. 45, pp.11–25.

Lowell, S. 2004. *Characterization of porous solids and powders : surface area, pore size, and density*. Kluwer Academic Publishers.

Lowell, S., Shields, J.E., Thomas, M.A. and Thommes, M. 2004. Gas Adsorption *In*:, pp.5–10. [Accessed 26 June 2018]. Available from: http://link.springer.com/10.1007/978-1-4020-2303-3_2.

Lozano-Maya, J.R. 2016. Looking through the prism of shale gas development: Towards a holistic framework for analysis. *Energy Research and Social Science*. 20, pp.63–72.

Lu, X., Jin, D., Wei, S., Zhang, M., Zhu, Q., Shi, X., Deng, Z., Guo, W. and Shen, W. 2015. Competitive adsorption of a binary CO_2–CH_4 mixture in nanoporous carbons: effects of edge-functionalization. *Nanoscale*. 7(3), pp.1002–1012.

Lyons, W. 1996. *Standard Handbook of Petroleum and Natural Gas Engineering*. Elsevier.

Majumder, M., Chopra, N., Andrews, R. and Hinds, B.J. 2005. Enhanced flow in carbon nanotubes. *Nature*. 438(7064), pp.44–44.

Mandal, A., Samanta, A., Bera, A. and Ojha, K. 2010. Characterization of oil-water emulsion and its use in enhanced oil recovery. *Industrial and Engineering Chemistry Research*. 49(24), pp.12756–12761.

Manger, E. 1963. Porosity and bulk density of sedimentary rocks. *Geological Survey Bull*. 1114-E(55).

Manrique, E., Thomas, C., Ravikiran, R., Izadi, M., Lantz, M., Romero, J. and Alvarado, V. 2010. EOR: Current status and opportunities *In*: *Proceedings - SPE Symposium on Improved Oil Recovery*. Society of Petroleum Engineers (SPE), pp.1584–1604.

Mattax, C.C. and Kyte, J.R. 1962. Imbibition Oil Recovery from Fractured, Water-Drive Reservoir. *Society of Petroleum Engineers Journal*. 2(02), pp.177–184.

Mayfield, P.L.J. and Do, D.D. 1991. Measurement of the Single-Component Adsorption Kinetics of Ethane, Butane, and Pentane onto Activated Carbon Using a Differential Adsorption Bed. *Industrial and Engineering Chemistry Research*. 30(6), pp.1262–1270.

Mccoy, S.T. 2008. *The Economics of CO2 Transport by Pipeline and Storage in Saline Aquifers and Oil Reservoirs*.

Mengal, S.A. and Wattenbarger, R.A. 2011. Accounting For Adsorbed Gas in Shale Gas Reservoirs *In*: *SPE Middle East Oil and Gas Show and Conference* [Online]. Society of Petroleum Engineers. [Accessed 21 June 2019]. Available from: http://www.onepetro.org/doi/10.2118/141085-MS.

Merchant, D. 2017. Enhanced Oil Recovery - The history of CO2 Conventional WAG Injection Techniques developed from lab in the 1950’s to 2017 *In*: *Carbon Management Technology Conference, CMTC 2017: Global CCUS Innovation Nexus*. AIChE, pp.712–734.

Merchant, D.H. 2010. Life beyond 80: A look at conventional WAG recovery beyond 80% HCPV injection in CO2 tertiary floods *In*: *Society of Petroleum Engineers - SPE International Conference on CO2 Capture, Storage, and Utilization 2010*. OnePetro, pp.182–195.

Miller, M.S. 1974. Stratigraphy and coal beds of Upper Mississippian and Lower Pennsylvanian rocks in southwestern Virginia: Virginia Division of Mineral Resources. *Bulletin*., p.211.

Milliken, K.L., Rudnicki, M., Awwiller, D.N. and Zhang, T. 2013. Organic matter–hosted pore system, Marcellus Formation (Devonian), PennsylvaniaGeohorizon. *AAPG Bulletin*. 97(2), pp.177–200.

Moridis, G.J., Blasingame, T.A. and Freeman, C.M. 2010. Analysis of mechanisms of flow in fractured tight-gas and shale-gas reservoirs *In*: *SPE Latin American and Caribbean Petroleum Engineering Conference Proceedings*. Society of Petroleum Engineers (SPE), pp.1310–1331.

Muggeridge, A., Cockin, A., Webb, K., Frampton, H., Collins, I., Moulds, T. and Salino, P. 2014. Recovery rates, enhanced oil recovery and technological limits. *Philosophical*

Transactions of the Royal Society A: Mathematical, Physical and Engineering Sciences. 372(2006).

Myers, A.L. and Monson, P.A. 2014. Physical adsorption of gases: the case for absolute adsorption as the basis for thermodynamic analysis. *Adsorption*. 20(4), pp.591–622.

NETL 2013. Modern Shale Gas Development in the United States: An Update.

NETL 2010. Permanence and Safety of CCS | netl.doe.gov. [Accessed 21 May 2021]. Available from: https://netl.doe.gov/coal/carbon-storage/faqs/permanence-safety.

Nuttal, B.C., Eble, C., Bustin, R.M. and Drahovzal, J.A. 2005. Analysis of Devonian black shales in kentucky for potential carbon dioxide sequestration and enhanced natural gas production *In*: *Greenhouse Gas Control Technologies* [Online]. Elsevier Ltd, pp.2225–2228. [Accessed 9 February 2021]. Available from: https://linkinghub.elsevier.com/retrieve/pii/B9780080447049503062.

Nwaozo, J. 2006. *Dynamic optimization of a waterflood reservoir*.

Ojha, S.P., Misra, S., Tinni, A., Sondergeld, C. and Rai, C. 2017. Pore connectivity and pore size distribution estimates for Wolfcamp and Eagle Ford shale samples from oil, gas and condensate windows using adsorption-desorption measurements. *Journal of Petroleum Science and Engineering*. 158, pp.454–468.

Oren, P.E., Billotte, J. and Pinczewski, W. V. 1992. Mobilization of waterflood residual oil by gas injection for water-wet conditions. *SPE Formation Evaluation*. 7(1), pp.70–78.

Orr, F.M., Silva, M.K. and Lien, C.L. 1983. Equilibrium phase compositions of CO2/crude oil mixtures. Comparison of continuous multiple-contact and slim-tube displacement tests. *Society of Petroleum Engineers journal*. 23(2), pp.281–291.

Pan, Z. and Connell, L.D. 2015. Reservoir simulation of free and adsorbed gas production from shale. *Journal of Natural Gas Science and Engineering*. 22, pp.359–370.

Pan, Z. and Wood, D.A. 2015. Coalbed methane (CBM) exploration, reservoir characterisation, production, and modelling: A collection of published research (2009–2015). *Journal of Natural Gas Science and Engineering*. 26, pp.1472–1484.

Pancholi, S., Negi, G.S., Agarwal, J.R., Bera, A. and Shah, M. 2020. Experimental and simulation studies for optimization of water–alternating-gas (CO2) flooding for enhanced oil recovery. *Petroleum Research*. 5(3), pp.227–234.

Peaceman, D.W. 1978. Interpretation of Well-Block Pressures in Numerical Reservoir Simulation. *Society of Petroleum Engineers Journal*. 18(03), pp.183–194.

Pei, P., Ling, K., He, J. and Liu, Z. 2015. Shale gas reservoir treatment by a CO2-based technology. *Journal of Natural Gas Science and Engineering*. 26, pp.1595–1606.

Pellenq, R.J.-M., Coasne, B., Denoyel, R.O. and Coussy, O. 2009. Simple Phenomenological Model for Phase Transitions in Confined Geometry. 2. Capillary Condensation/Evaporation in Cylindrical Mesopores. *Langmuir*. 25(3), pp.1393–1402.

Peng, D.Y. and Robinson, D.B. 1976. A New Two-Constant Equation of State. *Industrial and Engineering Chemistry Fundamentals*. 15(1), pp.59–64.

Perera, M.S.A., Gamage, R.P., Rathnaweera, T.D., Ranathunga, A.S., Koay, A. and Choi, X. 2016. A Review of CO2 -Enhanced oil recovery with a simulated sensitivity analysis.

Energies. 9(7), p.481.

Petropoulos, J.H. and Papadokostaki, K.G. 2012. May the Knudsen equation be legitimately, or at least usefully, applied to dilute adsorbable gas flow in mesoporous media? *Chemical Engineering Science*. 68(1), pp.392–400.

Pfeifer, P. and Liu, K.-Y. 1997. Multilayer adsorption as a tool to investigate the fractal nature of porous adsorbents. *Studies in Surface Science and Catalysis*. 104, pp.625–677.

Prats, M. 1982. *Thermal recovery*. SPE of AIME,New York, NY.

Proedrou, P. and Papaconstantinou, M.C. 2004. Prinos Basin - A model for oil exploration. *Bulletin of the Geological Society of Greece*. 36(1), p.327.

Pruess, K. and Narasimhan, T.N. 1985. Practical method for modeling fluid and heat flow in fractured porous media. *Society of Petroleum Engineers journal*. 25(1), pp.14–26.

Le Quéré, C., Moriarty, R., Andrew, R.M., Peters, G.P., Ciais, P., Friedlingstein, P., Jones, S.D., Sitch, S., Tans, P., Arneth, A., Boden, T.A., Bopp, L., Bozec, Y., Canadell, J.G., Chevallier, F., Cosca, C.E., Harris, I., Hoppema, M., Houghton, R.A., House, J.I., Jain, J.K., Johannessen, T., Kato, E., Keeling, R.F., Kitidis, V., Klein Goldewijk, K., Koven, C., Landa, C., Landschützer, P., Lenton, A., Lima, I.D., Marland, G., Mathis, J.T., Metzl, N., Nojiri, Y., Olsen, A., Ono, T., Peters, W., Pfeil, B., Poulter, B., Raupach, M.R., Regnier, P., Rödenbeck, C., Saito, S., Salisbury, J.E., Schuster, U., Schwinger, J., Séférian, R., Segschneider, J., Steinhoff, T., Stocker, B.D., Sutton, A.J., Takahashi, T., Tilbrook, B., Van Der Werf, G., Viovy, N., Wang, Y.-P., Wanninkhof, R., Wiltshire, A. and Zeng, N. 2014. Global carbon budget 2014. *Earth Syst. Sci. Data Discuss*. 6, pp.1–90.

Rahmanian, M., Solano, N. and Aguilera, R. 2010. Storage and output flow from shale and tight gas reservoirs *In*: *Society of Petroleum Engineers Western North American Regional Meeting 2010 - In Collaboration with the Joint Meetings of the Pacific Section AAPG and Cordilleran Section GSA*. Society of Petroleum Engineers, pp.1038–1058.

Rao, D. 2001. Gas injection EOR - a new meaning in the new millennium. *Journal of Canadian Petroleum Technology*. 40(2), pp.11–19.

Ravikovitch, P.I., Vishnyakov, A., Russo, R. and Neimark, A. V. 2000. Unified approach to pore size characterization of microporous carbonaceous materials from N2, Ar, and CO2 adsorption isotherms. *Langmuir*. 16(5), pp.2311–2320.

Riekert, L. 1971. *Rates of Sorption and Diffusion of Hydrocarbons in Zeolites* [Online]. [Accessed 21 June 2019]. Available from: https://aiche.onlinelibrary.wiley.com/doi/pdf/10.1002/aic.690170237.

Rigby, S.P. 2003a. A Model for the Surface Diffusion of Molecules on a Heterogeneous Surface. *Langmuir*.

Rigby, S.P. 2002. Fractal Theory for the Compensation Effect Observed in a Surface Diffusion Process Studied Using Deuteron NMR.

Rigby, S.P. 1999. NMR and modelling studies of structural heterogeneity over several lengthscales in amorphous catalyst supports. *Catalysis Today*. 53(2), pp.207–223.

Rigby, S.P. 2005. Predicting surface diffusivities of molecules from equilibrium adsorption isotherms. *Colloids and Surfaces A: Physicochemical and Engineering Aspects*. 262(1–

3), pp.139–149.

Rigby, S.P. 2003b. Structure-transport relationships in the surface diffusion of molecules over heterogeneous surfaces within porous catalysts. *Catalysis in Application [Papers presented at the International Symposium on Applied Catalysis]*., pp.170–177.

Rigby, S.P. and Gladden, L.F. 1999. *The prediction of transport properties of porous media using fractal models and NMR experimental techniques* [Online]. [Accessed 3 September 2018]. Available from: https://ac.els-cdn.com/S000925099800517X/1-s2.0-S000925099800517X-main.pdf.

Rogers, J.D. and Grigg, R.B. 2000. A literature analysis of the WAG injectivity abnormalities in the CO2 process *In*: *SPE - DOE Improved Oil Recovery Symposium Proceedings*. Society of Petroleum Engineers (SPE).

Rojas, G.A., Zhu, T., Dyer, S.B., Thomas, S. and Ali, S.. F. 1991. Scaled Model Studies of CO2 Floods. *SPE Reservoir Engineering*. 6(02), pp.169–178.

Ross, D.J.K. and Bustin, R.M. 2007. Shale gas potential of the Lower Jurassic Gordondale Member, northeastern British Columbia, Canada. *Bulletin of Canadian Petroleum Geology*. 55(1), pp.51–75.

Rouquerol, F., Rouquerol, J. (Jean) and Sing, K.S.W. 1999. *Adsorption by powders and porous solids : principles, methodology, and applications*. Academic Press.

Roux, L. 2021. Density - A contentious issue in the evaluation and determination of Resources and Reserves in coal deposits. *Journal of the Southern African Institute of Mining and Metallurgy*. 121(5), pp.227–250.

Rubin, B. 2010. Accurate simulation of non-darcy flow in stimulated fractured shale reservoirs *In*: *Society of Petroleum Engineers Western North American Regional Meeting 2010 - In Collaboration with the Joint Meetings of the Pacific Section AAPG and Cordilleran Section GSA*. Society of Petroleum Engineers, pp.19–34.

Rubin, E., Meyer, L. and Coninck, H. 2005. *Carbon Dioxide Capture and Storage* [Online]. [Accessed 6 April 2021]. Available from: https://www.ipcc.ch/report/carbon-dioxide-capture-and-storage/.

Sakhaee-Pour, A. and Li, W. 2016. Fractal dimensions of shale. *Journal of Natural Gas Science and Engineering*. 30, pp.578–582.

Samanta, A., Bera, A., Ojha, K. and Mandal, A. 2012. Comparative studies on enhanced oil recovery by alkali-surfactant and polymer flooding. *Journal of Petroleum Exploration and Production Technology*. 2(2), pp.67–74.

Sanchez, L., Astudillo, A., Rodriguez, F., Morales, J. and Rodriguez, A. 2005. Nitrogen injection in the Cantarell complex: results after four years of operation *In*: *Proceedings of the Latin American and Caribbean Petroleum Engineering Conference*. Society of Petroleum Engineers (SPE).

Schneider, P. and Smith, J.M. 1968. Adsorption rate constants from chromatography. *AIChE Journal*. 14(5), pp.762–771.

Seaton, N.A., Walton, J.P.R.B. and quirke, N. 1989. A new analysis method for the determination of the pore size distribution of porous carbons from nitrogen adsorption measurements. *Carbon*. 27(6), pp.853–861.

Shah, A., Fishwick, R., Wood, J., Leeke, G., Rigby, S. and Greaves, M. 2010. A review of novel techniques for heavy oil and bitumen extraction and upgrading. *Energy and Environmental Science*. 3(6), pp.700–714.

Shi, J.-Q. and Durucan, S. 2008. Modelling of Mixed-Gas Adsorption and Diffusion in Coalbed Reservoirs *In*: *SPE Unconventional Reservoirs Conference* [Online]. Society of Petroleum Engineers. [Accessed 21 June 2019]. Available from: http://www.onepetro.org/doi/10.2118/114197-MS.

Shindo, Y., Hakuta, T., Yoshitome, H. and Inoue, H. 1983. Gas diffusion in microporous media in knudsen's regime. *Journal of Chemical Engineering of Japan*. 16(2), pp.120–126.

Sigmund, P.M. 1976. Prediction of Molecular Diffusion At Reservoir Conditions. Part II - Estimating the Effects Of Molecular Diffusion And Convective Mixing In Multicomponent Systems. *Journal of Canadian Petroleum Technology*. 15(03).

Sigmund, P.M., Kerr, W. and MacPherson, R.E. 1984. A Laboratory and Computer Model Evaluation of Immiscible CO2 Flooding in a Low-Temperature Reservoir *In*: *All Days* [Online]. SPE. [Accessed 21 May 2021]. Available from: https://onepetro.org/SPEIOR/proceedings/84EOR/All-84EOR/Tulsa, Oklahoma/66693.

Sing, K.S.W. 1985. Reporting physisorption data for gas/solid systems with special reference to the determination of surface area and porosity (Recommendations 1984). *Pure and Applied Chemistry*. 57(4), pp.603–619.

Slatt, R.M. and O'Brien, N.R. 2011. Pore types in the Barnett and Woodford gas shales: Contribution to understanding gas storage and migration pathways in fine-grained rocksGeohorizon. *AAPG Bulletin*. 95(12), pp.2017–2030.

Speight, J. 2014. The Chemistry and Technology of Petroleum -. *CRC Press*. [Online]. [Accessed 10 June 2021]. Available from: https://www.routledge.com/The-Chemistry-and-Technology-of-Petroleum/Speight/p/book/9781439873892.

Speight, J.G. 1999. *The chemistry and technology of petroleum: Third edition, revised and expanded* [Online]. CRC Press. [Accessed 24 May 2021]. Available from: http://www.taylorandfrancis.com.

Stalkup, F.I. 1987. Displacement behavior of the condensing/vaporizing gas drive process. *SPE Annual Technical Conference and Exhibition*.

Stamataki, S. and Magoulas, K. 2000. Prediction of phase equilibria and volumetric behavior of fluids with high concentration of hydrogen sulfide. *Oil and Gas Science and Technology*. 55(5), pp.511–522.

Strąpoć, D., Mastalerz, M., Schimmelmann, A., Drobniak, A. and Hasenmueller, N.R. 2010. Geochemical constraints on the origin and volume of gas in the New Albany Shale (Devonian–Mississippian), eastern Illinois Basin. *AAPG Bulletin*. 94(11), pp.1713–1740.

Stumm, W. and Morgan, J. 1996. Aquatic Chemistry: Chemical Equilibria and Rates in Natural Waters. *Wiley*.

Sylvester, P.J. 2012. Use of the Mineral Liberation Analyzer (MLA) for Mineralogical Studies of Sediments and Sedimentary Rocks. *Mineralogi*.pp. 1-16.

Taber, J.J. and Martin, F.D. 1983. Technical Screening Guides for the Enhanced Recovery of Oil *In*: *SPE Annual Technical Conference and Exhibition*.

Taber, J.J., Martin, F.D. and Seright, R.S. 1997. EOR Screening Criteria Revisited - Part 2: Applications and Impact of Oil Prices. *SPE Reservoir Engineering (Society of Petroleum Engineers)*. 12(3), pp.199–204.

Taber, J.J. and Seright, R.S. 1992. Horizontal injection and production wells for EOR or waterflooding *In*: *Proceedings of the 1992 Permian Basin Oil and Gas Recovery Conference*. Publ by Soc of Petroleum Engineers of AIME, pp.227–239.

Tang, X., Ripepi, N., Luxbacher, K. and Pitcher, E. 2017. Adsorption Models for Methane in Shales: Review, Comparison, and Application. *Energy & Fuels*. 31(10), pp.10787–10801.

Tewari, R.D., Riyadi, S., Kittrell, C., Kadir, F.B.A., Bakar, M.A., Othman, T.R.B.T. and Banu, N. 2010. Maximizing the oil recovery through Immiscible Water Alternating Gas (IWAG) in mature offshore field *In*: *Society of Petroleum Engineers - SPE Asia Pacific Oil and Gas Conference and Exhibition 2010, APOGCE 2010*. OnePetro, pp.931–941.

Thomas, G.W. 1977. *Principles of hydrocarbon reservoir simulation* [Online]. [Accessed 18 June 2021]. Available from: https://www.Principles-hydrocarbon-reservoir-simulation-Thomas/dp/8251901898.

Thomas, S. and Farouq Ali, S.M. 1999. Status and assessment of chemical oil recovery methods. *Energy Sources*. 21(1–2), pp.177–189.

Thommes, M. and Cychosz, K.A. 2014. Physical adsorption characterization of nanoporous materials: Progress and challenges. *Adsorption*. 20(2–3), pp.233–250.

Thommes, M., Kaneko, K., Neimark, A. V, Olivier, J.P., Rodriguez-Reinoso, F., Rouquerol, J. and Sing, K.S.W. 2015. IUPAC Technical Report Physisorption of gases, with special reference to the evaluation of surface area and pore size distribution (IUPAC Technical Report). *Pure Appl. Chem*.

Thompson, J.M., Okouma Mangha, V. and Anderson, D.M. 2011. Improved Shale Gas Production Forecasting Using a Simplified Analytical Method-A Marcellus Case Study *In*: *North American Unconventional Gas Conference and Exhibition* [Online]. Society of Petroleum Engineers. [Accessed 21 June 2019]. Available from: http://www.onepetro.org/doi/10.2118/144436-MS.

Turta, A.T., Chattopadhyay, S.K., Bhattacharya, R.N., Condrachi, A. and Hanson, W. 2005. Current status of the commercial in situ combustion (ISC) projects and new approaches to apply ISC *In*: *Canadian International Petroleum Conference 2005, CIPC 2005*. Petroleum Society of Canada (PETSOC).

Turta, A.T. and Singhal, A.K. 2004. Overview of short-distance oil displacement processes. *Journal of Canadian Petroleum Technology*. 43(2), pp.29–38.

Tzimas, E., Georgakaki, A., Cortes, G. and Peteves, S.D. 2005. *Enhanced Oil Recovery using Carbon Dioxide in the European Energy System* [Online]. [Accessed 24 May 2021]. Available from: http://ie.jrc.cec.eu.int/.

Venaruzzo, J.L., Volzone, C., Rueda, M.L. and Ortiga, J. 2002. Modified bentonitic clay minerals as adsorbents of CO, CO2 and SO2 gases. *Microporous and Mesoporous Materials*. 56(1), pp.73–80.

Verma, M.K. 2015. *Fundamentals of Carbon Dioxide-Enhanced Oil Recovery (CO 2-EOR): a supporting document of the assessment methodology for hydrocarbon recovery using CO2-EOR associated with carbon sequestration* [Online]. [Accessed 6 April 2021]. Available from: http://dx.doi.org/10.3133/ofr20151071.

Wang, H.Y. and Marongiu-Porcu, M. 2015. A unified model of matrix permeability in shale gas formations *In*: *Society of Petroleum Engineers - SPE Reservoir Simulation Symposium 2015*. Society of Petroleum Engineers, pp.103–122.

Wang, J., Liu, H., Yu, W., Cao, F. and Sepehrnoori, K. 2016a. Necessity of porosity correction before simulation and re-understanding of the effects of gas adsorption on production in shale gas reservoirs. *Journal of Petroleum Science and Engineering*. 139, pp.162–170.

Wang, J., Liu, H., Zhang, H., Luo, H., Cao, F., Jiao, Y. and Sepehrnoori, K. 2016b. How to correct the petro-physical properties for simulating shale gas production using current commercial simulators? *In*: *Proceedings - SPE Annual Technical Conference and Exhibition*. Society of Petroleum Engineers (SPE).

Wang, J., Yuan, Q., Dong, M., Cai, J. and Yu, L. 2017. Experimental investigation of gas mass transport and diffusion coefficients in porous media with nanopores. *International Journal of Heat and Mass Transfer*. 115, pp.566–579.

Wang, S., Elsworth, D. and Liu, J. 2012. A mechanistic model for permeability evolution in fractured sorbing media. *Journal of Geophysical Research: Solid Earth*. 117(6).

Wang, X., Jiang, Z., Jiang, S., Chang, J., Zhu, L., Li, X. and Li, J. 2019. Full-scale pore structure and fractal dimension of the Longmaxi shale from the southern Sichuan basin: Investigations using FE-SEM, gas adsorption and mercury intrusion porosimetry. *Minerals*. 9(9).

Warren, J.E. and Root, P.J. 1963. The Behavior of Naturally Fractured Reservoirs. *Society of Petroleum Engineers Journal*. 3(03), pp.245–255.

Watt-Smith, M.J., Edler, K.J. and Rigby, S.P. 2005. An experimental study of gas adsorption on fractal surfaces. *Langmuir*. 21(6), pp.2281–2292.

Weijermars, R. 2014. US shale gas production outlook based on well roll-out rate scenarios. *Applied Energy*. 124, pp.283–297.

Wu, K., Li, X., Guo, C., Wang, C. and Chen, Z. 2016. A unified model for gas transfer in nanopores of shale-gas reservoirs: Coupling pore diffusion and surface diffusion *In*: *SPE Journal*. Society of Petroleum Engineers, pp.1583–1611.

Wu, K., Li, X., Wang, C., Yu, W. and Chen, Z. 2015. Model for surface diffusion of adsorbed gas in nanopores of shale gas reservoirs. *Industrial and Engineering Chemistry Research*. 54(12), pp.3225–3236.

Xia, T.X. and Greaves, M. 2002. Upgrading Athabasca tar sand using Toe-to-Heel air injection. *Journal of Canadian Petroleum Technology*. 41(8), pp.51–57.

Xia, T.X., Greaves, M. and Turta, A. 2005. Main mechanism for stability of THAI - Toe-to-heel air injection. *Journal of Canadian Petroleum Technology*. 44(1), pp.42–48.

Xiong, J., Liu, X., Liang, L. and Zeng, Q. 2017. Methane Adsorption on Carbon Models of the Organic Matter of Organic-Rich Shales. *Energy & Fuels*. 31(2), pp.1489–1501.

Yang, F., Ning, Z. and Liu, H. 2014. Fractal characteristics of shales from a shale gas reservoir in the Sichuan Basin, China. *Fuel*. 115, pp.378–384.

Yeh, Y.T. and Yang, R.T. 1989. Diffusion in zeolites containing mixed cations. *AIChE Journal*. 35(10), pp.1659–1666.

Yellig, W.F. and Metcalfe, R.S. 1980. Determination and prediction of CO2 minimum miscibility pressures. *JPT, Journal of Petroleum Technology*. 32(1), pp.160–168.

Yi, J., Akkutlu, I.Y., Karacan, C.Ö. and Clarkson, C.R. 2009. Gas sorption and transport in coals: A poroelastic medium approach. *International Journal of Coal Geology*. 77(1–2), pp.137–144.

Yin, M. 2015. *CO_2 miscible flooding application and screening criteria CO miscible flooding application and screening criteria* [Online]. [Accessed 6 April 2021]. Available from: https://scholarsmine.mst.edu/masters_theseshttps://scholarsmine.mst.edu/masters_theses/7423.

Yongmao, H., Zenggui, W., Binshan, J., Yueming, C. and Xiangjie, L. 2004. Laboratory Investigation of CO2 Flooding *In*: *All Days* [Online]. SPE. [Accessed 6 April 2021]. Available from: https://onepetro.org/SPENAIC/proceedings/04NAICE/All-04NAICE/Abuja, Nigeria/71137.

Yu, W., Al-Shalabi, E.W. and Sepehrnoori, K. 2014. A sensitivity study of potential CO2 injection for enhanced gas recovery in Barnett Shale reservoirs *In*: *Society of Petroleum Engineers - SPE USA Unconventional Resources Conference 2014*. Society of Petroleum Engineers, pp.610–625.

Yu, W., Lashgari, H.R., Wu, K. and Sepehrnoori, K. 2015. CO2 injection for enhanced oil recovery in Bakken tight oil reservoirs. *Fuel*. 159, pp.354–363.

Yu, W. and Sepehrnoori, K. 2018. CO2 Injection for Enhanced Oil Recovery in Tight Oil Reservoirs *In*: *Shale Gas and Tight Oil Reservoir Simulation* [Online]. Elsevier, pp.333–376. [Accessed 22 May 2019]. Available from: https://linkinghub.elsevier.com/retrieve/pii/B9780128138687000080.

Yu, W. and Sepehrnoori, K. 2016. Sensitivity study and history matching and economic optimization for marcellus shale *In*: *Society of Petroleum Engineers - SPE/AAPG/SEG Unconventional Resources Technology Conference*. Society of Petroleum Engineers.

Yu, W., Sepehrnoori, K. and Patzek, T.W. 2016. Modeling Gas Adsorption in Marcellus Shale With Langmuir and BET Isotherms. *SPE Journal*. 21(02), pp.589–600.

Yu, W., Weijermars, R., Xu, Y., Wu, K. and Sepehrnoori, K. 2017. Impact of well interference on shale oil production performance: A numerical model for analyzing pressure response of fracture hits with complex geometries *In*: *Society of Petroleum Engineers - SPE Hydraulic Fracturing Technology Conference and Exhibition 2017*. Society of Petroleum Engineers, pp.196–220.

Yuan, H., Johns, R.T., Egwuenu, A.M. and Dindoruk, B. 2004. Improved MMP Correlations for CO2 Floods Using Analytical Gas Flooding Theory [Accessed 6 April 2021]. Available from: https://onepetro.org/SPEIOR/proceedings-abstract/04IOR/All-04IOR/SPE-89359-MS/71216.

Yuan, J., Luo, D. and Feng, L. 2015. A review of the technical and economic evaluation techniques for shale gas development. *Applied Energy*. 148, pp.49–65.

Yuan, W., Pan, Z., Li, X., Yang, Y., Zhao, C., Connell, L.D., Li, S. and He, J. 2014. Experimental study and modelling of methane adsorption and diffusion in shale. *Fuel*. 117, pp.509–519.

Zgrablich, G. 1997. Chapter 7. Surface diffusion of adsorbates on heterogeneous substrates *In*: Elsevier, pp.373–449. [Accessed 15 June 2020]. Available from: https://linkinghub.elsevier.com/retrieve/pii/S0167299197800705.

Zhang, P.Y., Huang, S., Sayegh, S. and Zhou, X.L. 2004. Effect of CO2 impurities on gas-injection EOR processes *In*: *Proceedings - SPE Symposium on Improved Oil Recovery*. Society of Petroleum Engineers (SPE).

Zhang, T., Ellis, G.S., Ruppel, S.C., Milliken, K. and Yang, R. 2012. Effect of organic-matter type and thermal maturity on methane adsorption in shale-gas systems. *Organic Geochemistry*. 47, pp.120–131.

Zhang, X., Liu, Qingwang, Fan, Z. and Liu, Qicheng 2019. An in situ combustion process for recovering heavy oil using scaled physical model. *Journal of Petroleum Exploration and Production Technology*. 9(4), pp.2681–2688.

Zhao, G. and Wang, C. 2019. Influence of CO2 on the adsorption of CH4 on shale using low-field nuclear magnetic resonance technique. *Fuel*. 238, pp.51–58.

Zhong, J., Abedini, A., Xu, L., Xu, Y., Qi, Z., Mostowfi, F. and Sinton, D. 2018. Nanomodel visualization of fluid injections in tight formations. *Nanoscale*. 10(46), pp.21994–22002.

Appendices

Appendix A: Peng-Robinson equation of state

The PR-EOS model, mainly used in petroleum industry, is applied to calculate the fugacity coefficient of the components in the gas phase. In terms of the *z* factor the PR-EOS is expressed in cubic polynomial form as:

$$z^3 - (1 - B)z^2 + (A - 3B^2 - 2B)z - (AB - B^2 - B^3) = 0 \tag{A.1}$$

The cubic z-factor equation is solved by trial and error. In cases where the real root is more than one, then the correct root is selected according to the lowest normalized Gibbs energy. The parameter *A* and *B*, which are functions of pressure and temperatures can be expressed as:

$$A = a\frac{p}{(RT)^2} \tag{A.2}$$

and

$$B = b\frac{p}{RT} \tag{A.3}$$

The parameters *a* and *b* are given by:

$$a = 0.45724\frac{R^2T_c^2}{p_c}[1 + (0.37469 + 1.54226\omega - 0.26992\omega^2)(1 - T_r^{0.5})]^2 \tag{A.4}$$

and

$$b = 0.0778\frac{RT_c}{p_c} \tag{A.5}$$

where T_c is the critical temperature, P_c is the critical pressure and ω is the acentric factor.

The parameters *A* and *B* use the linear mixing rule to corelate the properties of the pure components to the properties of the mixtures such that:

$$A = \sum_{i=1}^{N} \sum_{j=1}^{N} y_i y_j A_{ij} \tag{A.6}$$

and

$$B = \sum_{i=1}^{N} y_i B_i \tag{A.7}$$

with

$$A_{ij} = (1 - k_{ij})\sqrt{A_i A_j} \tag{A.8}$$

where k_{ij} is the binary interaction parameter.

Appendix B: Sensitivity Analysis of Marcellus shale reservoir

Sensitivity analysis was conducted to determine the sensitivity of parameters in Marcellus shale reservoir. These parameters include matrix permeability, fracture permeability, fracture porosity, fracture permeability, rock compressibility and fracture half length. Figure B.1 gives a visual representation of the parameter sensitivity. Parameters with higher percentage values on the plot can be considered to be more sensitive to parameter value changes than parameters with a low value.

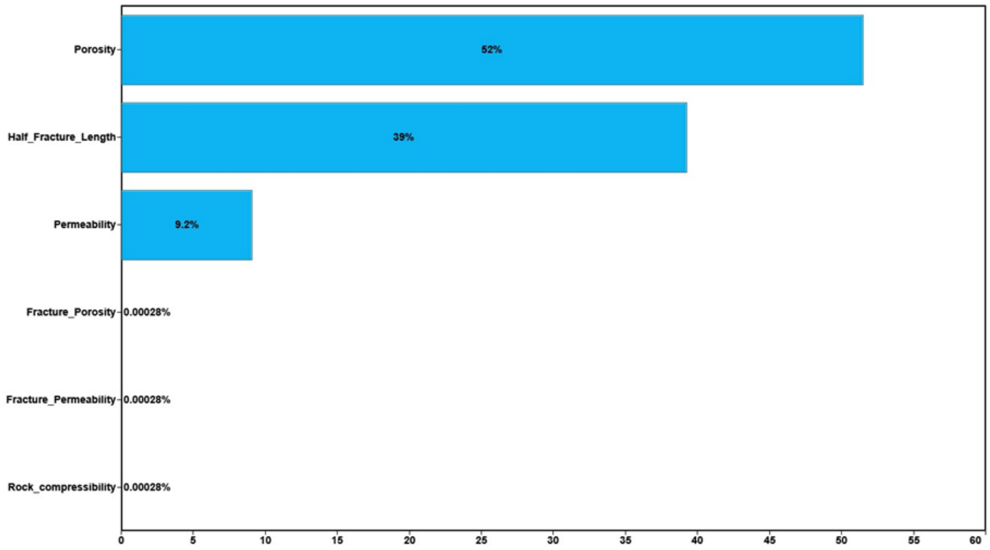

Figure B.1 Sensitivity Analysis for the Marcellus shale reservoir

Appendix C: Fluid Characterisation model of Prinos oil reservoir

Figures C.1 - C.3 represent the fluid model of Prinos reservoir which was tuned via a regression technique to match the experimental values.

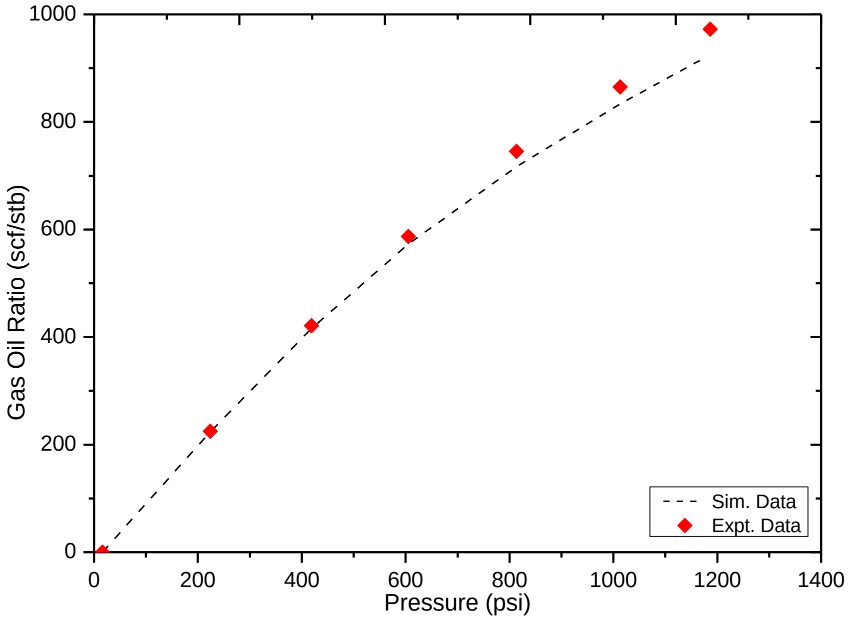

Figure C.1 Experimentally measured (symbols) (Stamataki and Magoulas, 2000) *and simulation data (dashed line) of the Gas Oil Ratio for the Prinos oil*

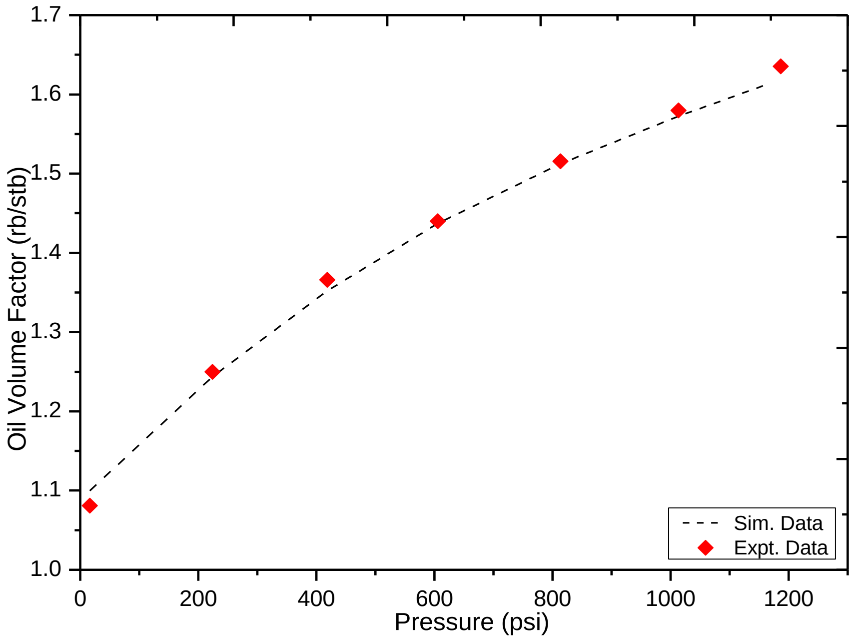

Figure C.2 Experimentally measured (symbols) and simulation data (dashed line) of the oil volume factor for the Prinos oil

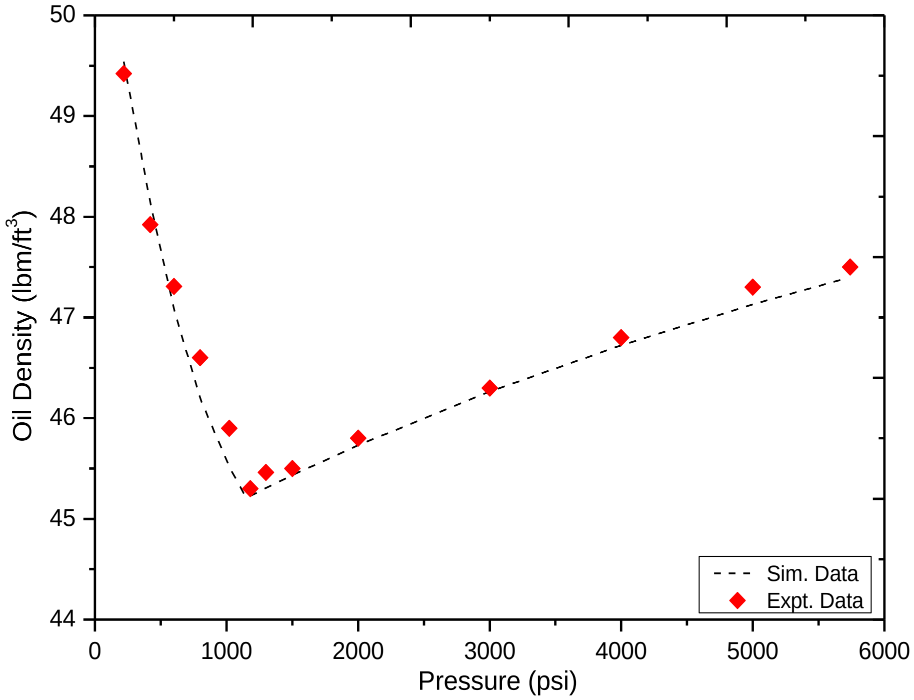

Figure C.3 Experimentally measured (symbols) and simulation data (dashed line) of the Prinos oil density

Appendix D: Sensitivity Analysis of Prinos oil reservoir

Sensitivity analysis was conducted to determine the sensitivity of parameters in Prinos reservoir. These parameters include grid thickness, permeability, porosity, initial pressure and rock compressibility. As explained in Appendix B, the higher the percentage, the more sensitive the parameter (Figure D.1).

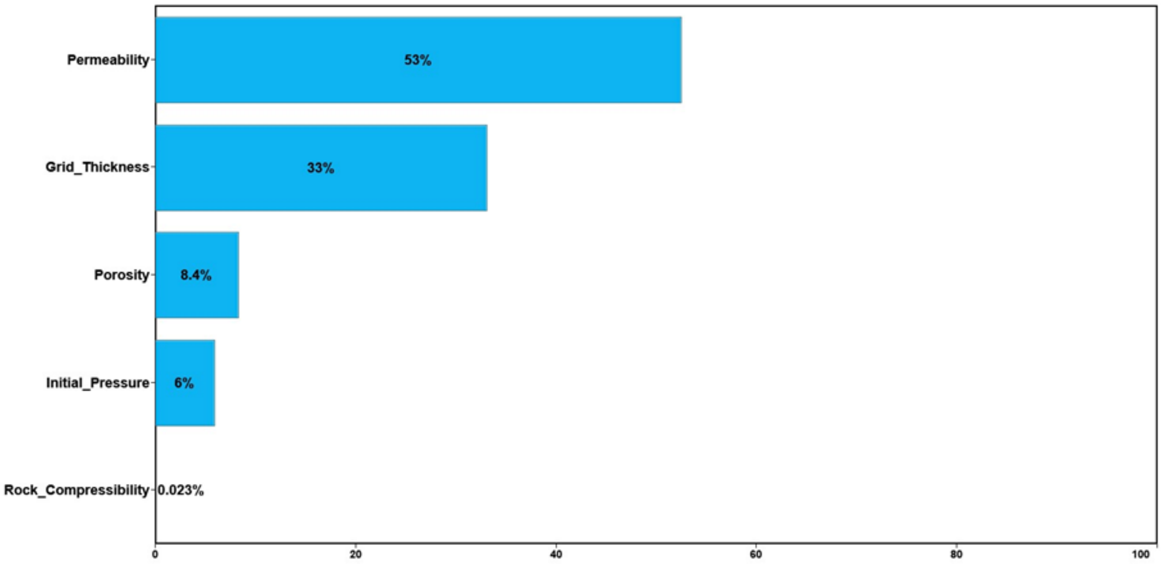

Figure D.1 Sensitivity Analysis for the Prinos oil reservoir

Appendix E: Characterisation of Utica shale and Pocahontas coal

E.1 Materials Used

Three core shale samples from the Utica Formation were obtained during exploratory drilling of a borehole located in the Appalachian basin, Ohio, USA. The core samples were collected from three different depths: 5860-5863 ft, 5875-5878 ft and 6102-6106 ft. The Utica shale lies within a total area of greater than 115,000 square miles and extends across four states: New York, Ohio, West Virginia and Pennsylvania. The depth ranges between 2000 and 8000 ft in Ohio, having an average thickness of less than 100 ft to approximately 500 ft (EIA, 2017). In specific, the Utica formation is thickest in western Ohio (200-300 ft), and it generally thins to the southern Ohio (~100 ft).

The blocks of coal utilized in this study were obtained from the Pocahontas (Poca) coal seam located in Buchanan County, Western Virginia, USA. The core samples were collected from two different depths: 1297-1299 ft and 1413-1414 ft. The Poca formation extends from the top of the Mississippian Bluestone Formation to the base of the New River Formation where the depth ranges between 1000 and 2000 ft. Throughout most of its extent, the formation is around 700 ft thick (Miller, 1974).

E.2 Volumetric Analysis

Gas sorption was conducted using a Micromeritics 3Flex volumetric analyser. Each shale and coal specimen was ground and sieved using 0.15-0.18 mm metal sifters. All samples were degassed for 16 hours at 110 °C for 16 h using a VacPrep Degasser. The adsorbates used were N_2 at 77 K, and CO_2 at 273 K. Similar to Marcellus shale samples in Chapter 4, the meso- and macro-porosity was determined via the carbon slit pore model of NLDFT kernel using N_2 adsorption data. Afterwards, the microporosity was obtained via the CO_2-DFT kernel using CO_2 adsorption data. In addition, the determination of the bulk density was obtained using helium pycnometry. The physical parameters of the shale and coal samples are shown in E.1*Table E.1*.

Table E.1 Results of Utica shale and Poca coal characterisation

Sample name	Depth(ft)	BET(m^2/g)	Fractal dimension (d)	TOC(%)	Illite(%)	Calcite(%)	Porosity(%)
Utica	5860-5863	2.3 ± 0.04	2.547 ± 0.001	2.33	39.75	9.7	2.53
	5875-5878	1.7 ± 0.04	2.534 ± 0.007	1.27	21.69	25.29	-
	6102-6106	1.5 ± 0.04	2.614 ± 0.006	0.39	0.84	75.43	-
Poca	1297-1299	0.2 ± 0.05	2.543 ± 0.007	69.8	0.21	0.19	-
	1413-1414	0.8 ± 0.03	2.565 ± 0.004	70.23	0.22	0.16	5.06

Figure E.(a,b), shows the N_2 adsorption isotherms for Utica shale (5860-5863ft) and Poca coal (1413-1414ft), respectively. From Figure E.1 (a,b) and Table E.1, it can be observed that Utica shale (5860-5863 ft) has greater BET surface area compared to Poca coal (1413-1414 ft). A potential reason that the BET surface area is higher in Utica shales may be the main inorganic compositions of shale (illite,quartz and calcite). According to previous studies (Venaruzzo et al., 2002; Slatt and O'Brien, 2011; Milliken et al., 2013) these inorganic compositions (clays) contribute significantly to the inner surface area. Hence, clay types (illite) and inorganic minerals (calcite), are of major importance on gas adsoprtion capacity, leading to higher BET surface area. Gas sorption isotherms of the remaining Utica shale and Poca coal samples, can be found in Appendix F.

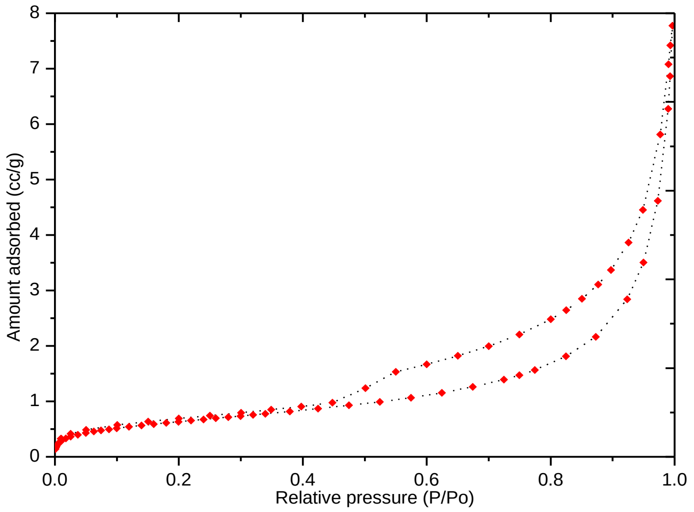

(a)

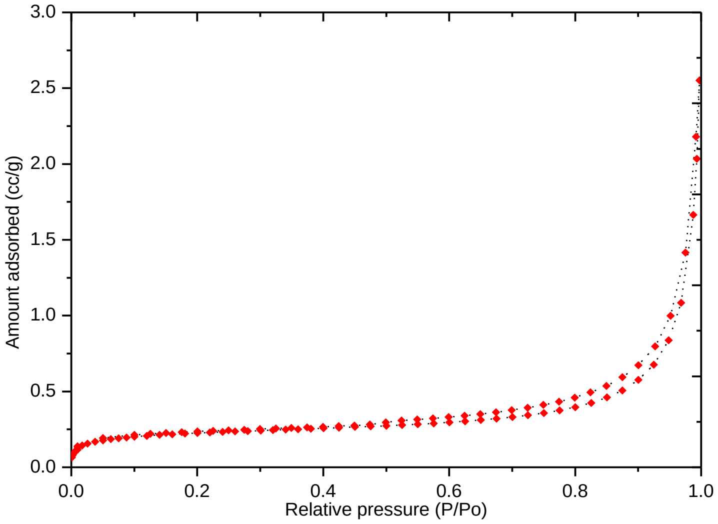

(b)

Figure E.1 Adsorption isotherms for N_2 on a) Utica shale (5860-5863 ft) b)Poca coal (1413-1414 ft)

According to Figure E.2(a,b), the adsorption isotherms for carbon dioxide on Utica shale (5860-5863 ft) and Poca coal (1413-1414 ft), respectively, show that the micropore surface area of coal is much larger than those of shale. The reason for this great difference in micropore surface area, is the abundance of micropores in the organic matter of coal (Figure E.3). Thus, the porosity of Poca coal is greater compared to Utica shale (Table E.1).

It should be noted that the skeletal densities for the Utica shale (5860-5863 ft) and Poca coal (1413-1414 ft) samples were obtained from helium pycnometry and the values are equal to 2.70 g/cm^3 and 1.41 g/cm^3, respectively. These density values are in agreement with past findings of Manger (1963) for shales, and Roux (2021) for coals.

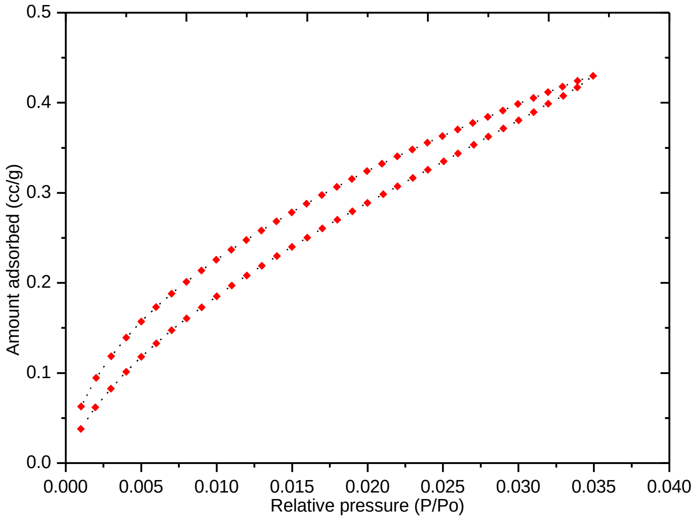

(a)

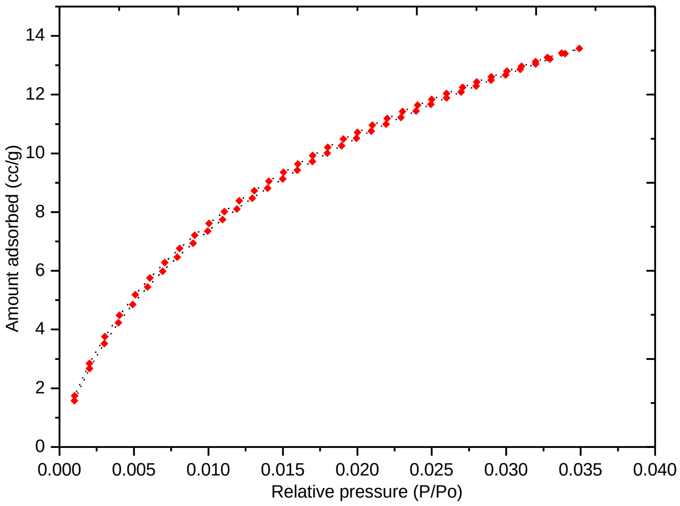

(b)

Figure E.2 Adsorption isotherms for CO_2 on a) Utica shale (5860-5863 ft) b)Poca coal (1413-1414 ft)

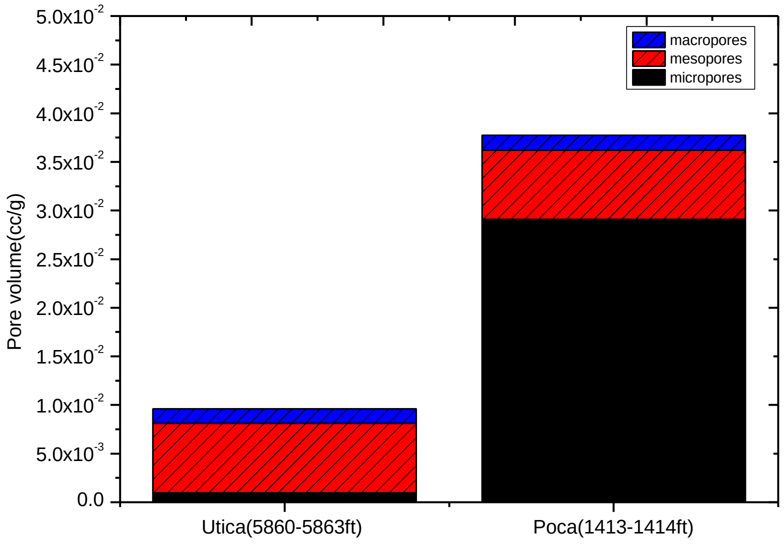

Figure E.3 Pore size distribution of Utica shale (5860-5863 ft) and Poca coal (1413-1414 ft)

Figure E.4(a,b), show examples of a fractal FHH plot obtained using one of the sets of nitrogen adsorption isotherm data given in Figure E.1(a,b). The surface fractal dimension obtained from such fits (using Eqs. (2.13) and (2.15)) to all the nitrogen isotherm data above a statistical monolayer coverage are given in Table E.1. In contrast to the surface fractal dimension of Marcellus shale samples in Chapter 4 (Table 4.3), the surface fractal dimension of Utica shales and Poca coal samples do not tend to decline with increasing depth. The remaining fractal FHH plots can be found can be found in Appendix F.

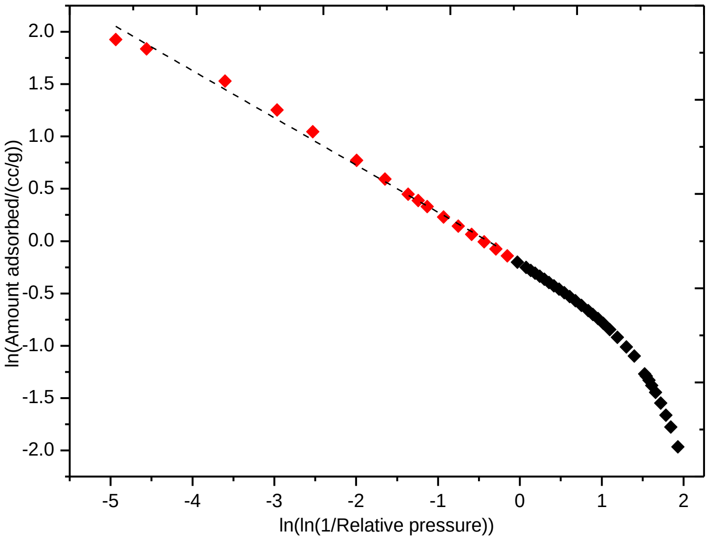

(a)

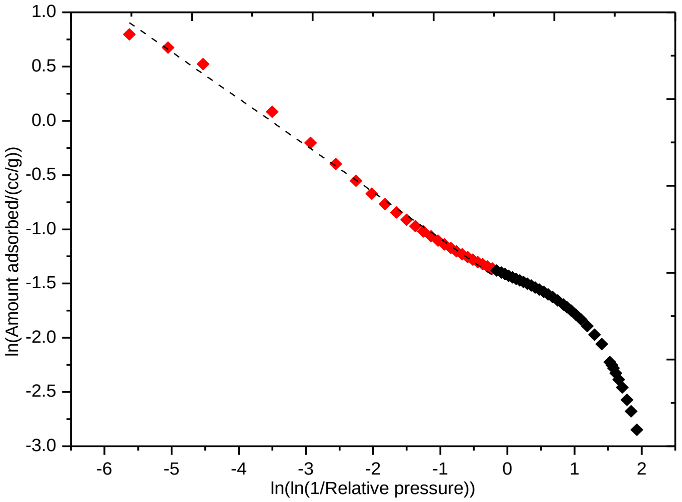

(b)

Figure E.4 Fit of Fractal FHH (dashed line) to the adsorption isotherm data(symbols) for nitrogen on a) Utica shale (5860-5863 ft), b) Poca coal (1413-1414 ft)

E.3 Gravimetric Analysis

Kinetic gas (CO_2) uptake data were obtained from a gravimetric analyser (Hiden XEMIS) using a sensitive microbalance. The detailed procedure for the experiment is outlined in Section 4.4.4. Examples of the isotherm data for carbon dioxide on Utica shale and Poca coal, can be seen in Figure E.5(a,b). Similar to Chapter 4 (Figure 4.7), the local adsorption equilibrium is reached quickly. Subsequently, the isotherm data were reasonably fitted to a Langmuir isotherm expression by using a non-linear regression technique for the selected temperatures of 10 ^oC, 20 ^oC, and 30 ^oC. Table E.2 shows the Langmuir parameters, $C_{\mu s}$ and b, which were obtained from this non-linear regression for the three temperatures. From Figure E.5(a,b), it can be seen that the Langmuir isotherm fits the experimental data well for the three temperatures.

Table E.2 Langmuir isotherm parameters for CO_2 on Utica shale and Poca coal derived from isotherms measured at the indicated different temperatures

Sample name	Depth(ft)	Property	Temperature(^{o}C)		
			10	20	30
Utica	5860-5863				
		$C_{\mu s}$ (mol/cm^3)	0.001034	0.000931	0.000836
		b(cm^3/mol)	33268	27648	22835
Poca	1413-1414				
		$C_{\mu s}$ (mol/cm^3)	0.000078	0.000068	0.000075
		b(cm^3/mol)	36075	35864	28261

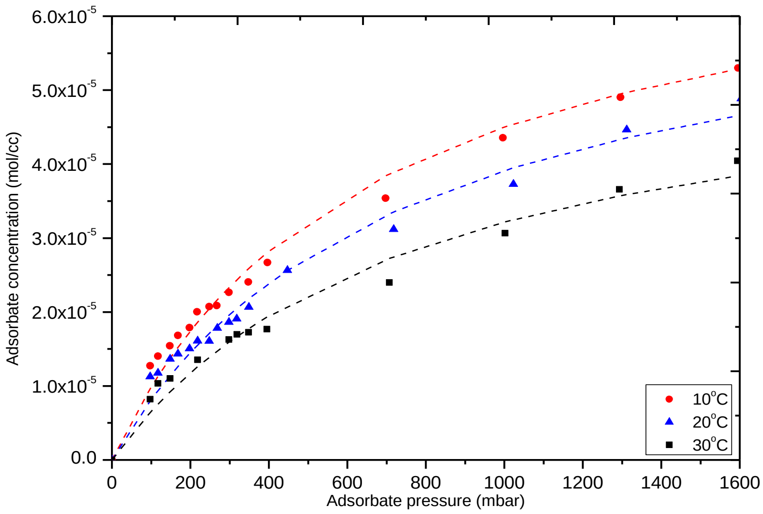

(a)

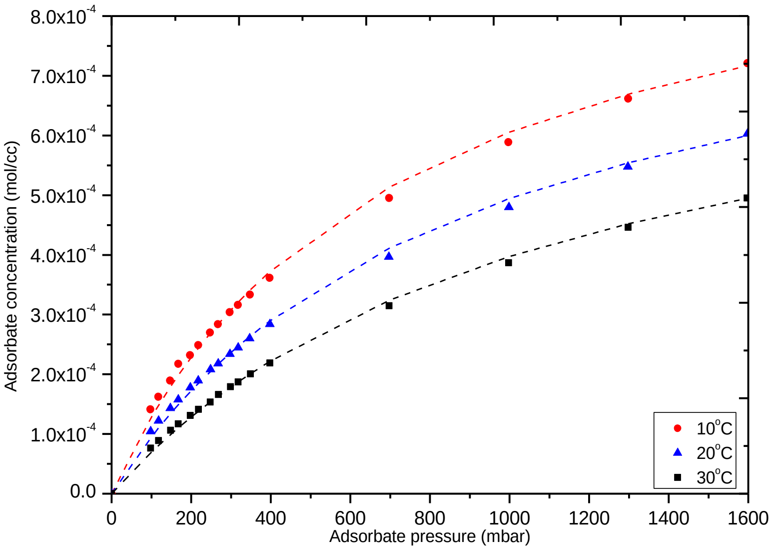

(b)

Figure E.5 Isotherms for CO_2 adsorption onto a) Utica shale from 5860-5863ft b) Poca coal 1413-1414ft measured at 10°C, 20°C, 30°C using Xemis apparatus. The lines are fits to the Langmuir isotherm model using parameters given in Table E.2

Figure E.6 shows the experimental fractional uptakes at three similar bulk concentrations of CO_2 for Poca coal (1413-1414 ft) samples. These spherical particles of coal have a radius of 0.00825 cm. It can be seen that the half-time is decreasing with temperature for all three bulk concentrations. These results are in agreement with past findings of Chapter 4 for spherical particles on Marcellus shale. Hence, given the same concentration of the bulk gas at the initial stages, it is considered that when the temperature is higher, the adsorption equilibrium time will be shorter.

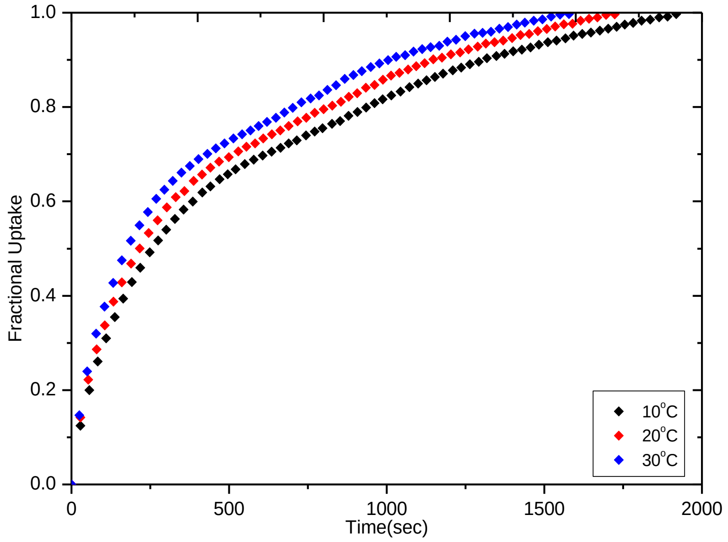

Figure E.6 Plot of fractional uptake of CO_2 onto Poca coal (1413-1414 ft) at three different temperatures

Figure E.7 shows an example of the fractional uptake of CO_2 on Poca coal (1413-1414 ft). A single exponential Linear Driving Force (LDF) model was used in order to fit the experimental data and thereby obtain the rate constant to find the half time of adsorption (Do, 1998). The measured half-times were ultimately used in Eq. (4.19) to estimate the surface diffusion.

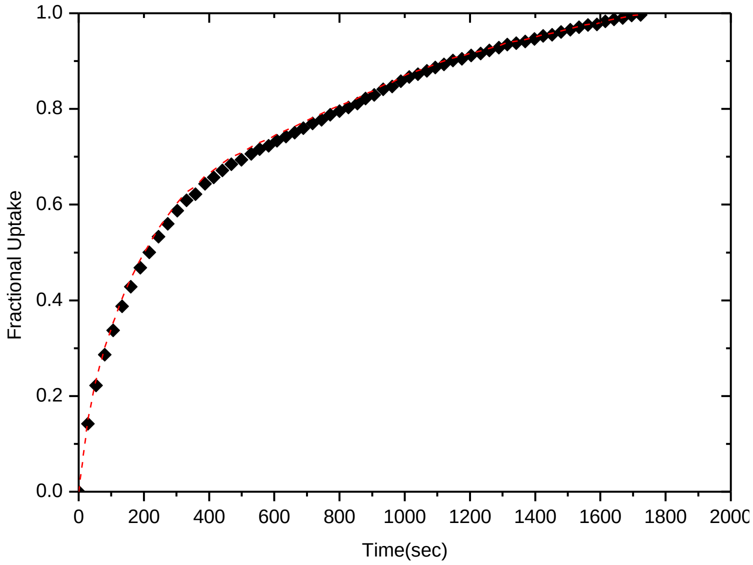

Figure E.7 Experimentally measured (symbols) uptake curves, and fits to the LDF model (lines) for Poca coal (1413-1414 ft)

The effectiveness of the Do technique (1991) for surface diffusion parameter determination was tested with the sorption data for CO_2 into Utica shale and Poca coal samples. Adsorption dynamics were measured at different bulk gas concentration steps but for the same range as explained in Section 4.4.4. From Figure E.8(a,b), it can be observed that the agreement between the experimental data and the linear variation expected from the model of Do and Rice (1991) is good. Plotting the parameter Ω from Eq. (4.19), versus the parameter Ξ (Eq. 4.20), as shown in Figure E.8(a,b), gave rise to a straight line for both shale and coal samples. As outlined in Section 4.2.2, the slope and the intercept correspond to $(1-\varepsilon_M)D_s$ and $\varepsilon_M D_p$, respectively.

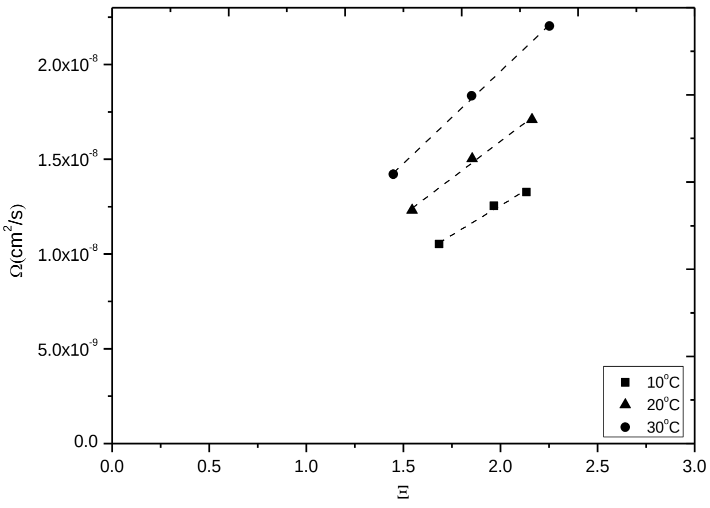

(a)

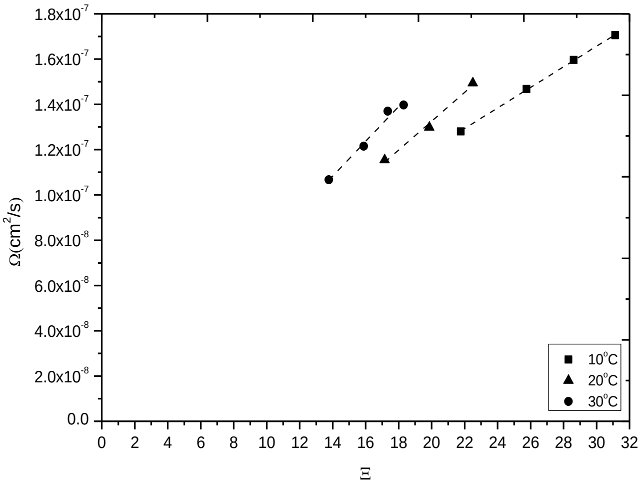

(b)

Figure E.8 Plot of the term Ω versus Ξ given in eq. 4.18 for a) Utica shale (5860-586 3ft) b) Poca coal (1413-1414 ft)

The results shown in Figure E.8(a,b), suggest that the CO_2 sorption data on Utica shale and Poca coal sample in the laboratory have indicated a good fit to the theoretical uptake model. Hence, this finding supports the implementation of Do's theory (1991) to heterogeneous systems (i.e. shale, coal) exhibiting fractal dimension down to ~2.54, in which surface diffusion and pore diffusion may be obtained within the system.

The values of the surface diffusivities obtained in this work are $\sim 10^{-8}$ cm^2/s. It should be mentioned that these results are consistent with previous studies in the literature (Karacan and Mitchell, 2003), for CO_2 in coal. However, direct measurement of heat release is also needed to examine if the heat of adsorption for surface diffusion of CO_2 is determined by the surface geometry of the adsorbent. As outlined in Chapter 4, Section 4.3.3, measurement of the heat of adsorption via the iQ-calorimeter in shale and coal is feasible. Therefore, more experimental work is needed on both shale and coals to establish the fractal theory and effectively predict, *a priori*, surface diffusivity parameters.

Appendix F: Characterisation of Utica shale and Pocahontas coal

Figure F.1(a-c) shows the nitrogen adsorption isotherms for Utica shale (5875-5878ft), Utica shale (6102-6106ft) and Poca coal (1297-1299ft), respectively. From Figure F.1(a-c), it can be observed that Utica shales have greater BET surface area compared to Poca coal (1297-1299ft). As highlighted in Appendix E, a potential reason that the BET surface area is higher in Utica shales is main inorganic compositions of shale (illite, quartz and calcite) which contribute significantly to the inner surface area.

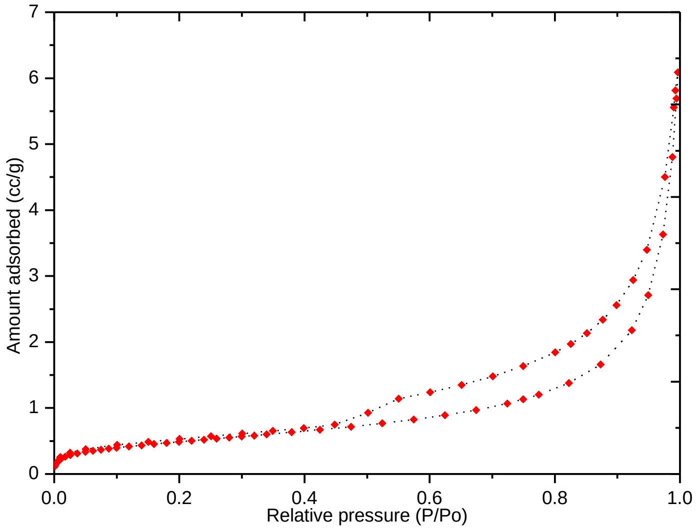

(a)

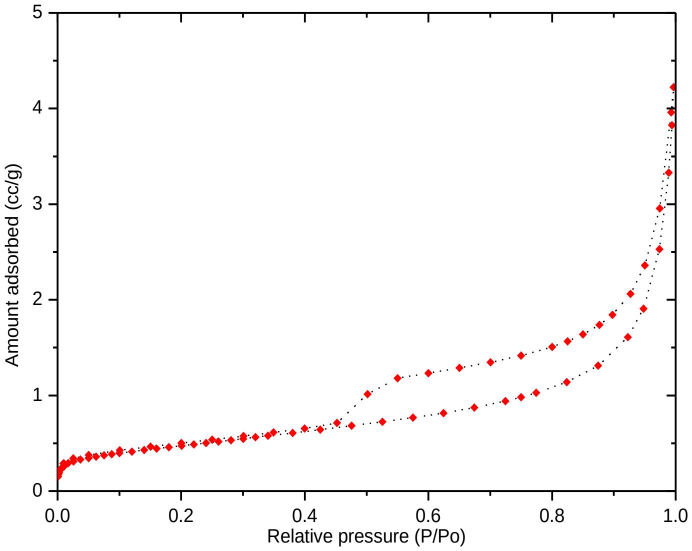

(b)

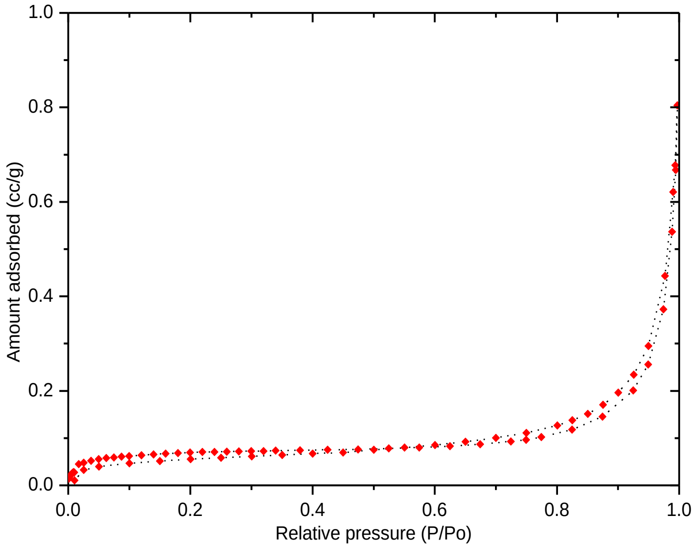

(c)

Figure F.1 Adsorption isotherms for N_2 on a) Utica shale (5875-5878 ft), b) Utica shale (6102-6106 ft), c)Poca coal (1297-1299 ft)

Figure F.2(a-c) shows the carbon dioxide adsorption isotherms for Utica shale (5875-5878ft), Utica shale (6102-6106ft) and Poca coal (1297-1299ft), respectively. From Figure F.2(a-c), it can be observed that the micropore surface area of coal is much larger than those of shales. These results are similar to those reported in Appendix E, and the reason for this great difference in micropore surface area, is the abundance of micropores in the organic matter of coal.

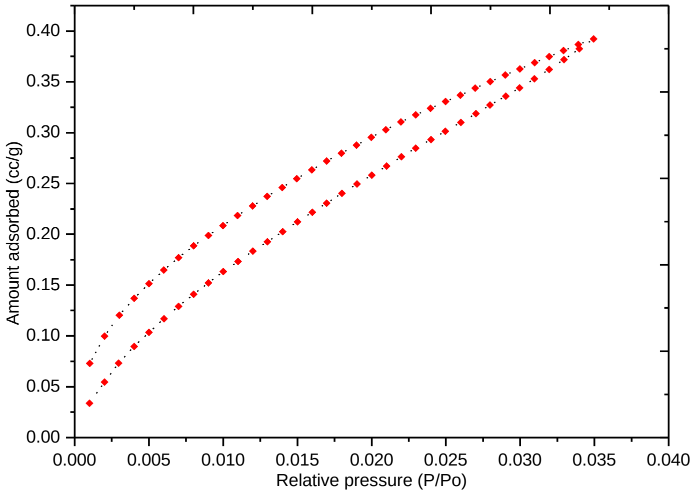

(a)

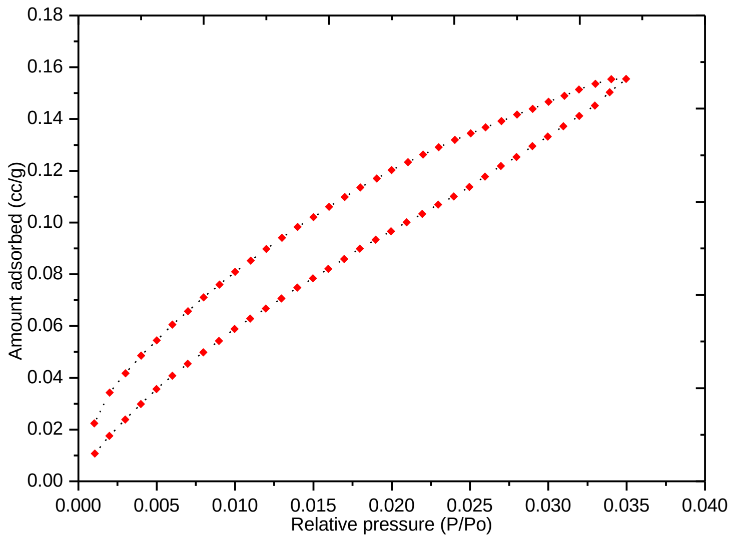

(b)

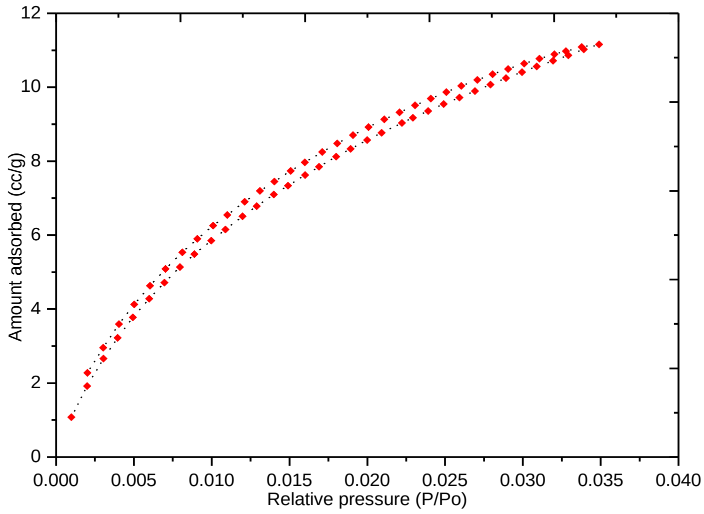

(c)

Figure F.2 Adsorption isotherms for CO_2 on a) Utica shale (5875-5878 ft), b) Utica shale (6102-6106 ft), c)Poca coal (1297-1299 ft)

Figure F.3(a-c) shows examples of a fractal FHH plot obtained using one of the sets of nitrogen adsorption isotherm data given in F.1(a-c). The surface fractal dimension obtained from such fits (using Eqs. (2.13) and (2.15)) to all the nitrogen isotherm data above a statistical monolayer coverage are given in Table E.1 of Appendix E.

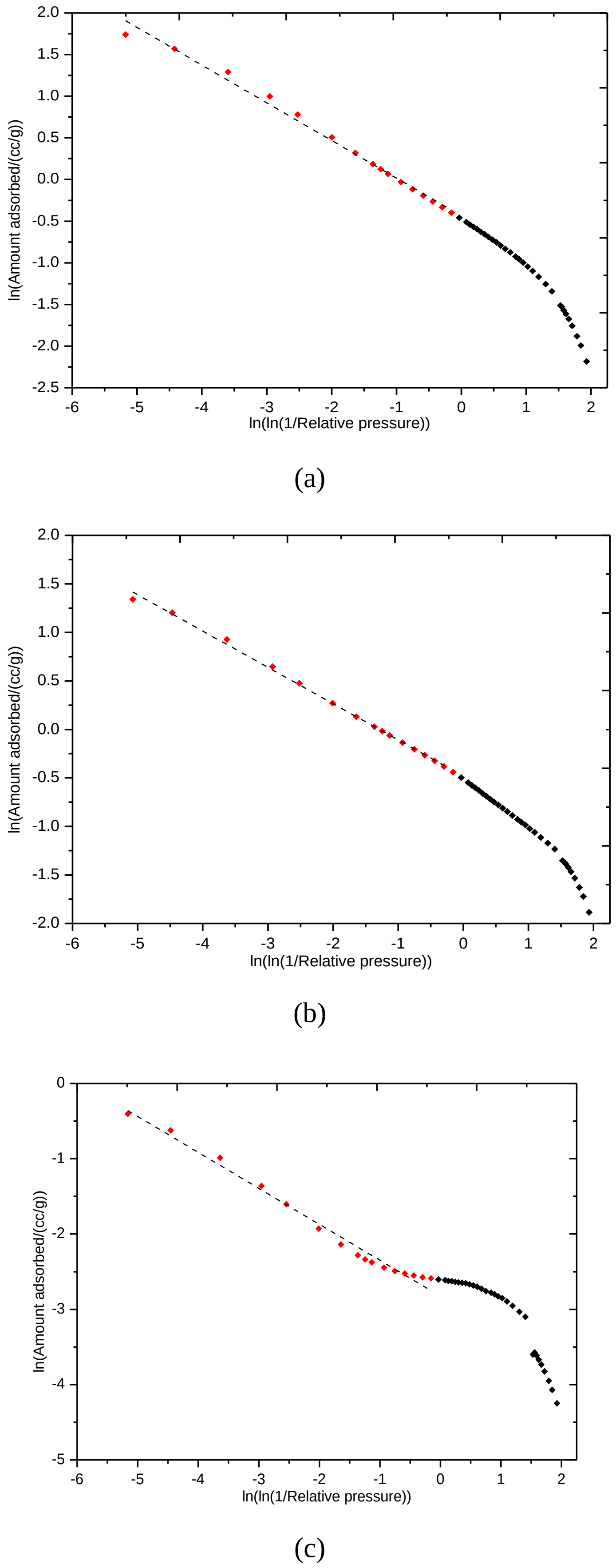

Figure F.3 Fit of Fractal FHH (dashed line) to the adsorption isotherm data(symbols) for nitrogen on a) Utica shale (5875-5878 ft), b) Utica shale (6102-6106 ft), c)Poca coal (1297-1299 ft)

The Scanning Electron Microscopy-Mineral Liberation Analyzer (SEM-MLA) was applied to evaluate the inorganic minerals of Utica shale samples. From Figure F.4, it can be seen that minerals which comprise heavier components (i.e. pyrite) backscatter more of the incident electrons of the SEM and seem brighter in the backscattered electron (BSE) image. However, minerals with lighter components (i.e. quartz) backscatter less electrons and seem darker.

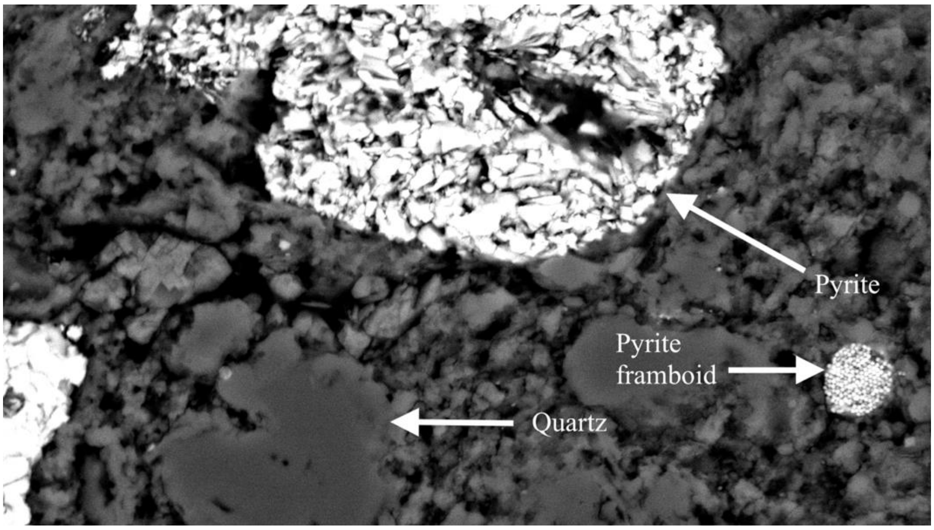

Figure F.4 Scanning Electron Microscopy image for the Utica Shale sample (6102-6106 ft)